DOE/ER-0045/15

BRASKI

Alloy Development for Irradiation Performance

Semiannual Progress Report
For Period Ending September 30, 1985

U.S. Department of Energy
Office of Fusion **Energy**

Printed in the United States of America Available from
National Technical Information Service
U S Department of Commerce
5285 Port Royal Road, Springfield. Virginia 22161
NTIS price codes — Printed Copy *A10* Microfiche A01

DOE/ER-0045/15
Distribution
Category
UC-20, 20c

ALLOY DEVELOPMENT FOR IRRADIATION PERFORMANCE
SEMIANNUAL PROGRESS REPORT FOR PERIOD ENDING SEPTEMBER 30. 1985

ARGONNE NATIONAL LABORATORY

AUBURN UNIVERSITY

GA TECHNOLOGIES, INC.

McDONNELL DOUGLAS ASTRONAUTICS COMPANY

MASSACHUSETTS INSTITUTE OF TECHNOLOGY

NAVAL RESEARCH LABORATORY

OAK RIDGE NATIONAL LABORATORY

WESTINGHOUSE HANFORD COMPANY

Date Published: February 1986

Prepared by
OAK RIDGE NATIONAL LABORATORY
Oak Ridge, Tennessee 37831
operated by
MARTIN MARIETTA ENERGY SYSTEMS, INC.
for the
U. S. DEPARTMENT OF ENERGY
Under Contract No. DE-AC05-840R21400

Reports previously issued in this series are as follows:

DOE/ET-0058/1	Period Ending March 31, 1978
DOE/ET-0058/2	Period Ending June 30, 1978
DOE/ET-0058/3	Period Ending September 30, 1918
DOE/ET-0058/4	Period Ending December 31, 1978
DOE/ET-0058/5	Period Ending March 31, 1979
DOE/ET-0058/6	Period Ending June 30, 1979
DOE/ET-0058/7	Period Ending September 30, 1979
DOE/ER-0045/1	Period Ending December 31, 1979
DOE/ER-0045/2	Period Ending March 31, 1980
DOE/ER-0045/3	Period Ending June 30, 1980
DOE/ER-0045/4	Period Ending September 30, 1980
DOE/ER-0045/5	Period Ending December 31, 1980
DOE/ER-0045/6	Period Ending March 31, 1981
DOE/ER-0045/7	Period Ending September 30, 1981
DOE/ER-0045/8	Period Ending March 31, 1982
DOE/ER-0045/9	Period Ending September 30, 1982
DOE/ER-0045/10	Period Ending March 31, 1983
DOE/ER-0045/11	Period Ending September 30, 1983
DOE/ER-0045/12	Period Ending March 31, 1984
DOE/ER-0045/13	Period Ending September 30, 1984
DOE/ER-0045/14	Period Ending March 31, 1985

This report is the twenty-second in a series of Technical Progress Reports on "*Alloy* ***Development for Irmdiation Performance"*** (ADIP), which is one element of the Fusion Reactor Materials Program, conducted in support of the Magnetic Fusion Energy Program of the U.S. Department of Energy. Other elements of the Materials Program are

- *Damage Analysis* ***and Fundamental Studies (DAFS)***
- ***Plasma-Materials Intemction (PMI)***
- *Special-Purpose* ***Materials (SPM)***
- ***High Heat*** *Flux* ***Components***

The first seven reports in this series are numbered DOE/ET-0058/1 through 7. This report is the fifteenth in a new numbering sequence that begins with DOE/ER-0045/1.

The ADIP program element is a national effort composed of contributions from a number of National Laboratories and other government laboratories, universities, and industrial laboratories. It was organized by the Materials and Radiation Effects Branch, Office of Fusion Energy, DOE, and a Task Group on *Alloy* ***Development for Irmdiation Performance,*** which now operates under the auspices of the Reactor Technologies Branch. The purpose of this series of reports is to provide a working technical record of that effort for the use of the program participants, for the fusion energy program in general, and for the Department of Energy.

This report is organized along topical lines with Chapters 3 through 8 devoted to the various alloy classes that are currently under investigation. Thus the work of a given laboratory may appear at several different places in the report. The materials compatibility and environmental effects work on all alloy classes is collected together in Chapter 9. The Table of Contents is annotated for the convenience of the reader.

This report has been compiled and edited under the guidance of the Chairman of the Task Group on ***Alloy Development for Irradiation Performance.*** A. F. Rowcliffe, Oak Ridge National Laboratory, and his efforts and those of the supporting staff of ORNL and the many persons who made technical contributions are gratefully acknowledged. T. C. Reuther, Reactor Technologies Branch, is the Department of Energy Counterpart to the Task Group Chairman and has responsibility for the ADIP Program within DOE.

G. M. Haas, Chief
Reactor Technologies Branch
Office of Fusion Energy

CONTENTS

1 ANALYSIS AND EVALUATION STUDIES

1.1 MATERIALS HANDBOOK FOR FUSION ENERGY SYSTEMS - J. W. Davis (McDonnell Douglas Astronautics Company - St. Louis Division)

1.1.1 ADIP Task

Task Number I.A.l, Define material property requirements and make structural life predictions.

1.1.2 Objective

To provide a consistent and authoritative source of material property data for use by the fusion community in concept evaluation, design, and performance/verification studies of the various fusion energy systems. A second objective is the early identification of areas in the materials data base where insufficient information or voids exist.

1.1.3 Summary

The July release of the 10th publication package of the Materials Handbook for Fusion Energy Systems to the approximately 90 handbook users represented the achievement of a number of milestones. First and foremost, the release of these 30 data pages represents the first step towards reducing the backlog of over 100 data sheets awaiting publication. Second it represents the initiation of the handbook into the world of computer generation and subsequent support services that can be provided via the MFE computer network.

1.1.4 Progress and Status

The primary thrust over the past six months has been directed towards breaking the logjam of data pages that have been piling up for the past several months. The release of the 10th publication package in July and the 11th in December is the first step in that direction. The 10th publication package was not as ambitious as originally hoped but it did contain roughly 20 data pages on the 12Cr-1Mo ferritic steel known as HT-9. The 11th publication package is a complete revamping of the G-10CR data sheets and adds three new materials to a newly designated chapter called Electrical Insulators. What made these publication packages unusual is that with the exception of the text pages, the data sheets were developed entirely on the MFE computer network which, because of its excellent graphics packages, allowed us to go directly to printing making the publication more efficient. The use of the MFE computer network also greatly increases the flexibility of the handbook with regard to its ability to provide greater user support. This support can be provided in a variety of ways. For example, if a project, such as the compact ignition tokamak, requires an advanced copy of a data curve prior to its publication in the handbook, an advance copy can be directed via the MFE network to a terminal located on or close to the project. This technique has been successfully demonstrated between MDAC and UCLA and is available as a service to any DOE/OFE supported project. The only limitation is that the user needs to know the site designation and the data sheets have to be in a form that they can be transmitted by the computer. A second capability that is currently being developed is to provide material property comparison curves to those handbook users involved in material trade studies. Currently we can provide up to six different curves on a data sheet. This capability allows the project to be able to have a consistent and direct comparison of materials properties without having to cross-plot the data or worry about the consistency of the data sets. Ultimately it is hoped to have the bulk of the handbook on the network where it can provide additional services. While the type of additional support has not been thoroughly thought out it may be desirable in the future to allow users direct access to the handbook computer files where they can instantly obtain the latest data and then maintain a hard copy of only the supporting documentation. At that point it might be possible to treat the handbook as a data base management file so that the user could query the computer with regard to the specific property, temperature range of interest, and material and the computer would give the user the desired information.

1.1.5 Conclusions

With the release of the 10th and 11th publication packages the data page backlog is beginning to approach a manageable level. In addition, with the handbook beginning to show forward progress, new data sheets are starting to be submitted. The first of these is in the area of magnet support cases and copper alloys. During the next six months, a supporting documentation volume of the handbook will be released along with a 12th data package containing information on copper alloys.

2 TEST MATRICES, EXPERIMENT DESCRIPTIONS, AND MICROSTRUCTURAL DEVELOPMENT

2.1 NEUTRON DOSIMETRY AND DAMAGE CALCULATIONS FOR ORR-6J-TEST, HFIR-RE-HAFNIUM TEST, AND THE HFIR-RE1 AND RE2 EXPERIMENTS

L. R. Greenwood (Argonne National Laboratory)

2.1.1 ADIP/DAFS Tasks

ADIP Tasks I.A.2 - Define Test Matrices and Procedures.
DAFS - Task II.A.2 - Fission Reactor Dosimetry.

2.1.2 Objective

To characterize neutron irradiation experiments in terms of neutron fluence, spectra, and damage parameters (dpa, gas production, transmutation).

2.1.3 *Summary*

Results are reported for a test of the 6J Japanese experiment in the Oak Ridge Research Reactor. Maximum fast fluxes above 0.1 MeV were $2.0 \times 10^{14} n/cm^2-s$ producing about 4.5 dpa per year in 316 stainless steel.

Analysis has been completed for the hafnium shield tests in the removable beryllium positions of the High Flux Isotopes Reactor (ORNL). The shield reduces the thermal flux by 90%, the epithermal flux by 50%, and the fast flux by only 5%. Yearly helium production in 316 stainless steel is thus reduced by a factor of 26 with little effect on displacement damage production. These new spectral analyses have been used to reanalyze previously reported results from the RB1 and RB2 materials irradiations in HFIR; the damage rates have been increased by 20-30%.

The status of all dosimetry experiments is summarized in Table 2.1.1.

Table 2.1.1. Status of Dosimetry Experiments

Facility/Experiment		Status/Comments
ORR	- MFE 1	Completed 12/79
	- MFE 2	Completed 06/81
	- MFE 4A1	Completed 12/81
	- MFE 4A2	Completed 11/82
	- MFE 4B	Completed 04/84
	- MFE 4A3, 4B2	Samples received 11/85
	- TBC 07	Completed 07/80
	- TRIO-Test	Completed 07/82
	- TRIO-1	Completed 12/83
	- HF Test	Completed 03/84
	- J6 Test	Completed 07/85
	- J6, J7	Irradiations in Progress
HFIR	- CTR 32	Completed 04/82
	- CTR 31. 34, 35	Completed 04/83
	- T2, RB1	Completed 09/83
	- T1, CTR 39	Completed 01/84
	- CTR 40-45	Completed 09/84
	- CTR 30, 36, 46	Completed 03/85
	- RB2	Completed 06/85
	- CTR 47-56	Irradiations in Progress
	- JP 1	Analysis in Progress
	- JP3	Samples received 11/85
	- JP 2-8	Irradiations in Progress
	- Hf Test	Completed 09/85
Omega West	- Spectral Analysis	Completed 10/80
	- HEDL1	Completed 05/81
	- HEDL2	Samples Sent 04/85
	- LANL 1	Completed 08/84
EER II	- X287	Completed 09/81
IPNS	- Spectral Analysis	Completed 01/82
	- LANL 1 (Hurley)	Completed 06/82
	- Hurley	Completed 02/83
	- Coltman	Completed 08/83

2.1.4.1 Dosimetry Measurements for the ORR-6J Prototype Experiment

Analysis has been completed for the prototype 6J Japanese experiment in the Oak Ridge Research Reactor. The experiment was conducted in the C7 position from September 6, 1984 to January 21, 1985 for a net exposure of 82.096 MWH. The experiment contained specimens at two different temperatures, 60°C and 200°C and four dosimetry tubes were located in each temperature region. These two temperature regions were concentric, the 200°C being on the inside of the 60°C region and the regions extended from about 2.4 cm above midplane to -17.9 cm below midplane.

Each dosimetry tube contained four wires of 0.1% Co-Al, Fe, Ti. and Ni. Each wire was segmented into eight 1" pieces for gamma counting. Selected vertical gradients are shown in Fig. 2.1.1. All of the vertical gradients were fit by a simple polynomial function:

$$F(z) = a(1 + bz + cz^2) \qquad (1)$$

where a is the midplane value and z is the height above midplane (in centimeters). The b and c coefficients were determined by least-squares analysis. All of the data is well-described by eq. (1) using $b = -8.31 \times 10^{-3}$ and $c = -8.85 \times 10^{-4}$. There may be a small difference between the thermal and fast vertical flux gradients; however, this effect is at most only a few percent and no significant spectral difference is indicated.

The maximum flux position was determined to be at -4.7 cm below mid-plane. The activity rates at this location are listed in Table 2.1.2. These rates were then used as input to the STAY'SL computer code to adjust the neutron flux Spectrum at each location. These adjusted fluxes are listed in Table 2.1.3. Flux gradients can be determined using the data in Table 1-3 and Equation (1); however, we should note that since the maximum flux position is at -4.7 cm below midplane, the "a" terms in Equation (1) are actually 2% less than the values listed in Tables 2.1.2 or 2.1.3.

The horizontal flux gradients are in all cases less than 20%. The fast flux gradients are less than 14%; however, there is a drop in thermal flux of about 10-20% between the two different temperature regions presumably due to absorption in the extra material. If we consider the two temperature regions separately, then the horizontal flux gradients are only about 10% in each region. In all cases the flux is higher in the north and east sides and lowest on the west side.

Damage and gas production rates were computed using the SPECTER computer code. Results are listed for the highest flux position (east side, 60°C, -4.7 cm below midplane) in Table 2.1.4. These values correspond to a total fluence of 5.88×10^{21} n/cm^2 and 1.99×10^{21} n/cm^2 above 0.1 MeV. Since most of the damage terms are linear with the fluence. damage rates at any other location can be determined by scaling with the fast fluence (>.1 MeV) in Table 2.1.3 followed by the use of Equation (1). In any case, the results would be within about 30% of the values in Table 2.1.4. The only exception to this is for the thermal helium production in nickel which roughly scales with the square of the thermal fluence.

Similar dosimetry experiments are now in progress for the J6 and J7 irradiations in ORR. Samples are now being analyzed for the JP1 irradiation in HFIR.

Table 2.1.2. Maximum Activation Rate for ORR-6J-Test

Values at -4.7 cm below midplane normalized to 30 MW; data corrected for burnup; accuracy ±2%

Wire #	Location	Temp., °C	Activation Rate (atom/atom-s) $^{59}Co(n,\gamma)^{60}Co$ *10^{-9}	$^{58}Fe(n,\gamma)^{59}Fe$ *10^{-10}	$^{54}Fe(n,p)^{54}Mn$ *10^{-11}	$^{46}Ti(n,p)^{46}Sc$ *10-12
1	E	60°	6.84	1.98	1.20	1.57
2	N	60°	6.78	1.90	1.26	1.67
3	W	60°	6.31	1.73	1.14	1.47
4	S	60°	6.72	1.88	1.17	1.50
5	W	200°	5.65	1.63	1.14	1.46
6	S	200°	5.86	1.69	1.13	1.46
7	E	200°	5.69	1.72	1.18	1.55
8	N	200°	5.72	1.65	1.21	1.55

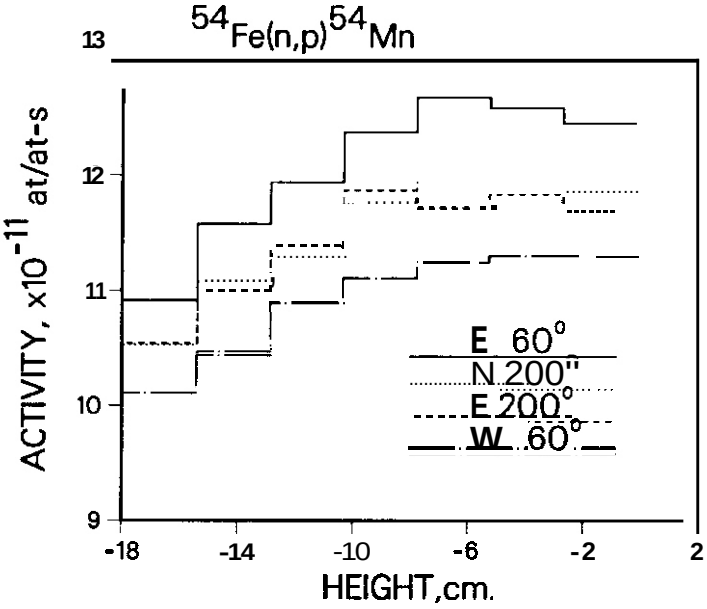

Fig. 2.1.1. Vertical Activity Gradients Measured for the $^{54}Fe(n,p)^{54}Mn$ Reaction Indicative of the Fast Neutron Flux (0.1 MeV). Gradients at all Other Locations Fall within the Range of Data Displayed.

Table 2.1.3. Flux Values for ORR-6J-Test

Values at maximum, 5 cm below midplane; accuracy ±10%

			Flux, x10^{14} n/cm^2-s		
Wire #	Location	Temp, °C	Thermal[a]	>0.1 MeV	Total
	E	60	2.01	1.99	5.97
2	N	60	1.97	2.03	5.99
3	W	60	1.82	1.85	5.49
4	S	60	1.95	1.93	5.80
5	W	200	1.65	1.79	5.14
6	S	200	1.71	1.80	5.26
7	E	200	1.68	1.85	5.27
8	N	200	1.66	1.86	5.27

[a]Thermal flux <0.5 eV for maxwellian at 95°C.

Table 2.1.4. Damage Parameters for ORR-6J-Test

Maximum values at east side. 60°C, 4.7 Cm below midplane. Other locations scale with fast flux in Table I-3 and Eq. (1). Values correspond to a fast fluence of 1.99×10^{21} n/cm^2.

Element		DPA	He, appm,
Al		2.68	1.22
Ti		1.71	0.92
V		1.90	0.044
Cr		1.70	0.30
Mn		1.82	0.25
Fe		1.51	0.52
Co		1.74	0.25
	Fast	1.59	7.34
Ni	Thermal	0.10	56.03
	Total	1.69	63.37
Cu		1.46	0.45
Nb		1.45	0.097
Mo		1.07	-
316 SS[a]		1.56	8.63

[a] 316 SS: Fe(.645), Ni(.13), Cr(.18), Mn(.019), Mo(.026)

2.1.4.2 Hafnium Shielding Tests in HFIR-RB Positions and Reanalysis of the HFIR-RB1, RB2 Experiments

Hafnium-shielding experiments have been completed in the removable beryllium (RB) positions in the High Flux Isotopes Reactor (HFIR) at ORNL. The purpose of these tests is to validate the design of a hafnium core piece for the RB positions. Hafnium is used to reduce the thermal/ epithermal flux ("spectrum tailoring") in order to reduce helium production in nickel-bearing materials (stainless steel) during lengthy fusion materials irradiations. Without the hafnium, the helium-to-displacement ratio will surpass the fusion first-wall value within a year. Thus. the idea is to first irradiate without hafnium, building up the helium content, and then to switch to the hafnium liner so that more damage can be accumulated without excessive helium. Similar experiments have been successfully conducted in the Oak Ridge Research Reactor.[1,2] Two fusion experiments (RB1 and RB2) have also been reported in HFIR.

The experiments were conducted in several different RB positions both with and without hafnium liners on August 3, 1985 for 1-hour at a reduced power level of 11 MW. Twelve different dosimetry materials were irradiated at six different vertical positions in each experimental assembly. These dosimeters were encapsulated in an aluminum tube measuring 1/8" OD by 21 7/8" in length. These tubes were inserted into the center of each hafnium and/or aluminum assembly which measured 1.24" OD. The reduced power level permitted us to use fissionable monitors and reduced the gamma heating. A full-power (100 MW) test is now in progress for one reactor cycle (22 days).

Two separate 1-hour irradiations were conducted. First. only aluminum assemblies were irradiated at 10.8 MW in positions RB-1 and RB-5; then an aluminum assembly was irradiated at 11.0 MW in RB5 along with a hafnium assembly in position RB1. The first irradiation provided a normal baseline operating condition for HFIR. whereas the second allowed us to measure the hafnium effect and to observe any tilting of the flux gradients due to the presence of the hafnium. Unfortunately one of the dosimetry tubes was not fully inserted into the aluminum capsule (RB5), and hence, one of the two baseline runs was lost. However, there does not appear to be any significant difference between the two positions (RB1 and RB5) so that one baseline measurement is adequate for this comparison.

The measured activities are listed in Table 2.1.5. As can be seen. there are only small differences between the two aluminum capsules and all of the fast (threshold) reaction rates, as expected. The presence of the hafnium depresses the thermal/epithermal reactions by factors of 3-10, depending on the energy response of each reaction.

The measured reaction rates were used to adjust the neutron flux spectra at each location as calculated by R. Lillie (ORNL) using the least-squares adjustment code STAY'S L. Uncertainties in the reaction rates are listed in Table 2.1.5, the neutron fluxes were assumed to have a uncertainty of 20%. and cross-section variances are taken from ENDF/B-V. Gaussian covariances were assumed in all cases. The adjusted fluxes are listed in Table 2.1.6. In both cases the adjusted flux spectra agree rather well with the calculations. Some caution is. however, required in the hafnium-shielded case since the calculated group structure was too coarse in the resonance region. For example. the 197 Au (n,γ) resonance does not coincide with those in hafnium and thus, the resonance shielding is not very large for this reaction. Unless finer group calculations are performed, very large errors will occur for this reaction. Consequently, some modifications were required in the input calculated spectrum to avoid these resonance pitfalls. However, these have no effect on the fast flux or dosage.

The bare and hafnium-shielded flux spectra are shown in Figure 2.1.2. The deep valleys centered around 1 eV and 300 eV are due to resonances in hafnium. The thermal flux is depressed about a factor of 8, while the fast flux is only depressed about 5%. Comparison of the two aluminum irradiations (no hafnium) show that the fast flux agrees within 1.5% and that the thermal/epithermal flux differs by about 5%. This difference is presumably due to a slight tilting of the flux gradients due to the presence of hafnium. In other words, the reactor power must be slightly increased overall to compensate for the depression near the hafnium assembly in order to maintain a net power level of 100 MW. Vertical flux gradients were measured at all three RB positions at 6 different vertical heights. Selected results are shown in Figs. 2.1.3 and 2.1.4. In all cases the data can be described by a single polynomial as follows:

$$f(z) = a(1 + bz + cz^2) \qquad (1)$$

where z = height in cm, f is the value of the flux or damage rate at height z, and a_3 is the midplane value (Table 2.1.6 or 2.1.7). The best fit to the bare (no-Hf) data gives b = 1.975×10^{-3} and c = -1.083×10^{-3} for the fast reactions and b = -1.625×10^{-3} and c = -1.280×10^{-3} for the thermal reactions. In the hafnium case, the thermal effect is quite striking and we can see in Fig. 2.1.3 that the flux rises near the end (.30 cm) as we emerge from; the hafnium shield. For this case, the fitting procedure gives b = 3.00×10^{-4} and c = -1.18×10^{-3}. All of these parameter sets are similar and the differences are negligible between -20 cm to +10 cm above midplane.

Table 2.1.5. Measured Reaction Rates for HFIR-RB-Hf Tests

Values normalized to 11.0 MW power level; accuracy ±2%

Reaction	Activation Rate, at/at-s		
	Al-RB1	Hf-RB1	Al-RB5
Thermal Reactions:			
$^{58}Fe(n,\gamma)^{59}Fe(10^{-11})$	9.75	1.14	10.50
$^{59}Co(n,\gamma)^{60}Co(10^{-9})$*	3.12	0.490	3.27
$^{63}Cu(n,\gamma)^{64}Cu(10^{-10})$	3.37	0.392	3.68
$^{64}Zn(n,\gamma)^{65}Zn(10^{-11})$	6.19	1.15	6.61
$^{176}Lu(n,\gamma)^{177}Lu(10^{-7})$*	3.22	0.390	3.45
$^{197}Au(n,\gamma)^{198}Au(10^{-8})$*	1.74	0.493	1.85
$^{238}U(n,\gamma)^{239}Np(10^{-10})$	7.28	2.69	8.36
$^{237}Np(n,\gamma)^{238}Np(10^{-8})$	1.63	0.265	1.73
Fast Reactions:			
$^{46}Ti(n,p)^{46}Sc(10^{-13})$	2.38	2.25	2.37
$^{47}Ti(n,p)^{47}Sc(10^{-13})$	3.74	3.53	3.81
$^{48}Ti(n,p)^{48}Sc(10^{-15})$	5.98	5.75	6.03
$^{54}Fe(n,p)^{54}Mn(10^{-12})$	1.72	1.58	1.73
$^{58}Ni(n,p)^{58}Co(10^{-12})$	2.32	2.16	2.36
$^{55}Mn(n,2n)^{54}Mn(10^{-15})$	5.31	4.99	5.29
$^{93}Nb(n,2n)^{92m}Nb(10^{-14})$	1.04	0.966	1.08
$^{237}Np(n,fission)(10^{-11})$	5.43	4.60	5.75
$^{238}U(n,fission)(10^{-12})$	7.88	7.65	8.15

* Dilute elements alloyed with aluminum.

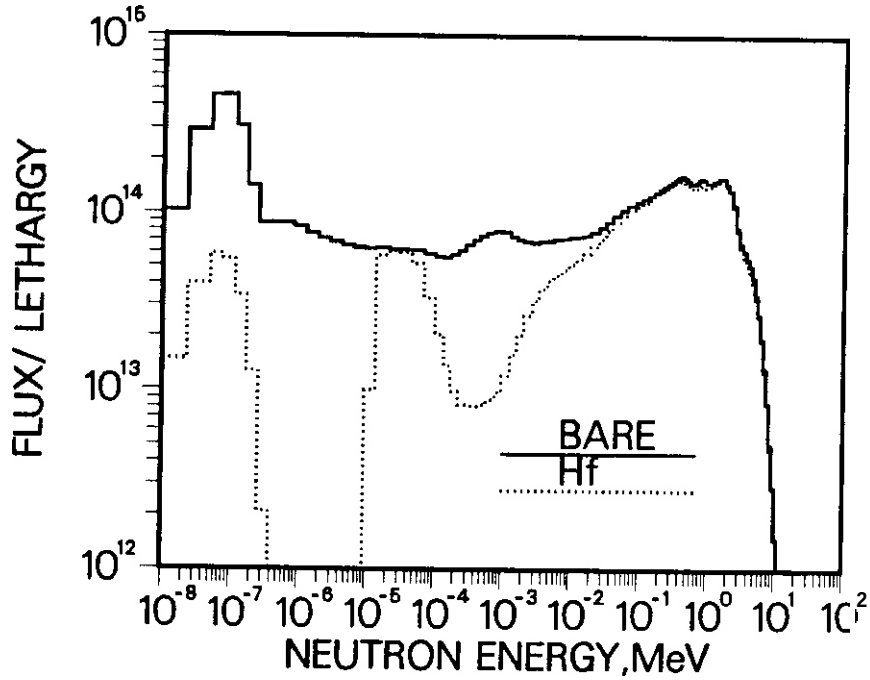

Fig. 2.1.2. Comparlson of STAY'SL-Adjusted Bare and Hafnium-Shielded Neutron Flux Spectra Measured in the RB1 Position of HFIR. The Large Dips around 1 and 30 eV are Caused by Hafnium Resonances.

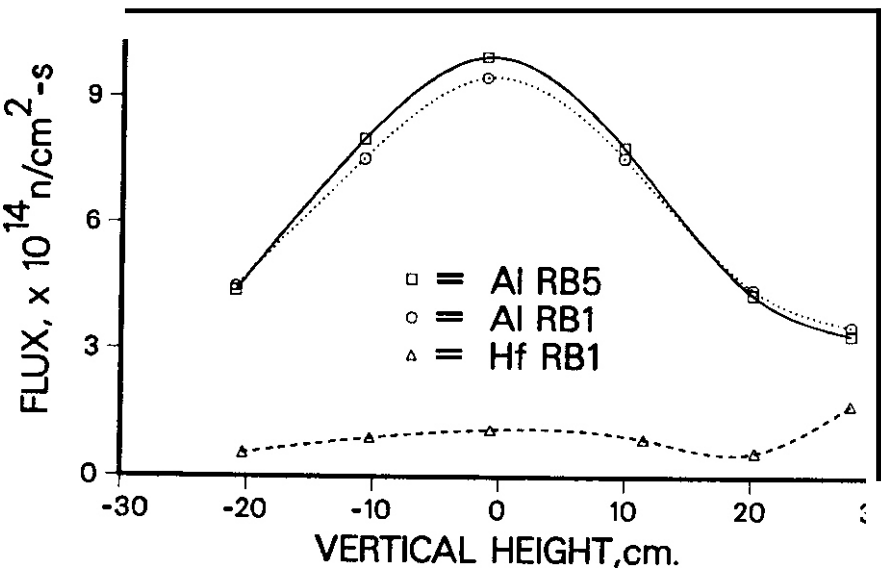

Fig. 2.1.3. Vertical Gradients are Shown for the Thermal Neutron Flux Measured With and Without Hafnium in Positions RBI and RB5 of HFIK.

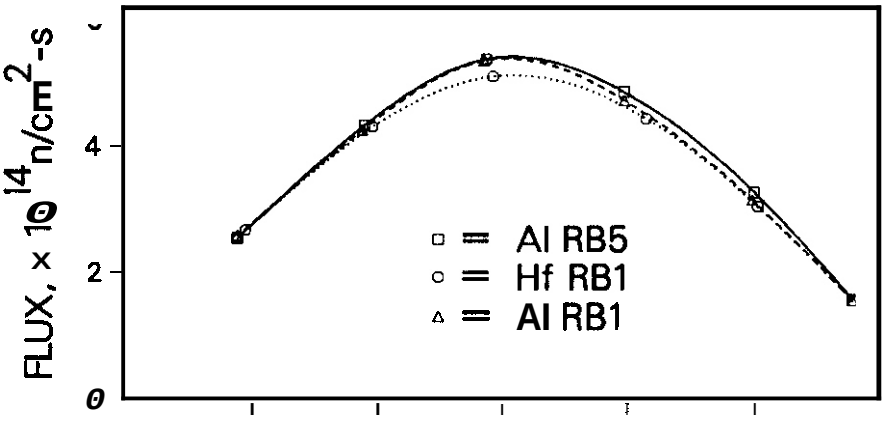

Fig. 2.1.4. Vertical Fast Flux (>.1 MeV) Gradients are Shown for Positions RB1 and RB5 of HFIR. Clearly, the Hafnium Shield has Little Effect on the Fast Flux.

Table 2.1.6. Adjusted Neutron Fluxes for HFIR-RB-Hf Test Midplane Values Normalized to 100 MW

	Neutron Flux, x 10^{14} n/cm^2-s		
Energy	RB1	RB1 (Hf)	RB5
Total	23.4	10.2	24.5
Thermal (2.5 eV)[a]	9.44	1.10	9.90
Intermediate	8.75	4.03	9.09
Fast (>.1 MeV)	5.27	5.02	5.35

[a]Thermal maxuellian at 120°C.

At larger distances there is clearly a spectral shift since the thermal flux falls more rapidly than the fast flux. At 20 cm above midplane the thermal to fast ratio is about 30% lower than at midplane. Within the hafnium shield the thermal vertical gradient is slightly shallower than without the shield; however. the fast flux gradient is about the same either way.

Damage and gas production rates were calculated with the SPECTER' computer code and the results are listed in Table 2.1.7. Both calculations are for position RB1 and the differences are mainly due to the difference in the fast Flux of about 1.51. The calculations in Table 2.1.7 were done for a 1 year (365 FPD) irradiation. The hafnium shield reduces the helium production in stainless steel From 688 appm to 26.1 appm, a factor of about 26. Of course. this is Only valid for the above conditions and must be done for each case considering possible burnout of the hafnium as well. In any case, it is evident that the hafnium, indeed, reduces the thermal helium effect without sacrificing the fast damage production as desired.

2.1.4.3 Reanalysis of the HFIR-RB1, RB2 Experiments

L. R. Greenwood (Argonne National Laboratory)

The hafnium tests in the removable beryllium (RB) positions of HFIR described in section 5.1 allowed us to perform detailed spectral measurements using short-lived activities. fissionable materials, and thermal shields. These techniques cannot be used in long materials irradiations and we must rely on a select number of dosimeters to adjust a previously determined neutron spectrum. Furthermore. new calculations of the neutron flux spectrum in the RB positions have recently been performed by D. Lillie (ORNL). Upon consideration of all of this new data, it was apparent that our previous measurements for the RB1[2] and RB2[3] experiments in HFIR should be reanalyzed. The results of this reanalysis are given below.

Table 2.1.8 lists revised neutron fluences and damage parameters for the RB1 and RB2 experiments. The flux and damage gradients can be determined by the following polynomial equation:

$$f(z) = a(1+bz+cz^2) \qquad (1)$$

where a = midplane value in Table 2.1.8, b = -2.48×10^{-3}, c = -9.76×10^{-4}, and z is the height in cm. This equation cannot be used to describe damage and helium production in copper, nickel, or stainless steel and calculations for the latter are given in Table 2.1.9.

The present results indicate a substantial increase in the fast flux and damage rates for both experiments. The flux above 0.1 MeV has been increased by about 30% for RB1 and 80% for RB2; however. the thermal flux and flux above about 1–2 MeV are not very different than before. In other words, most of the flux increase has occurred between about 0.1 to 1 MeV where our monitors are not very sensitive. If we compare damage rates this spectral change becomes more apparent since damage for 316 SS has only increased by 17% for RB1 and 33% for RB2. Helium rates actually show a decline since the very fast flux (>5 MeV) which produces helium by (n,α) rections is actually less than before. For iron, the helium has been reduced by 23% for RB1 and 10% for RB2. For nickel and stainless steel, the thermal helium effect has also been reduced primarily due to differences in the epithermal energy region.

2.1.5 Conclusions

The J6 and J7 expeirments are now in progress in ORR; samples are expected shortly from the MFE 4A and 4B spectral-tailoring experiments in ORR. Analysis is in progress for the JP1 and JP3 experiments in HFIR and samples have been received from the full cycle hafnium test in HFIR.

2.1.6 References

1. L. R. Greenwood and R. K. Smither, Hafnium Core Piece Test in ORR-MFE4, Damage Analysis and Fundamental Studies Quarterly Progress Report, DOE/ER-0046/17, pp. 5-10, May 1984.

2. L. R. Greenwood. Fission Reactor Dosimetry: HFIR–RB2, ibid., DOE/ER-0046/22, pp. 5-7, August 1985.

3. L. R. Greenwood and R. K. Smither, ANL/FPP/TM-197, SPECTER: Neutron Damage Calculations for Materials Irradiations, January 1985.

Table 2.1.7. Damage Parameters for HFIR-RB-Hf Test
Midplane values in RB1 at 100 MW

Element		Damage/year[a]			
		Bare		Hf Covered	
		DPA	He, appm	DPA	He, appm
Al		19.3	4.67	18.5	4.49
Ti		11.3	4.19	10.3	4.00
V		13.1	0.16	12.0	0.15
Cr		11.0	1.11	10.3	1.11
Mn[b]		12.9	0.91	11.1	0.94
Fe		9.7	2.06	9.2	1.91
Co[b]		13.5	0.91	10.3	0.94
Ni	Fast	11.0	31.0	10.1	29.0
	^{59}Ni	9.2	5247.0	0.3	160.0
	Total	20.2	5278.0	10.4	189.0
Cu	Fast	9.8	1.75	9.2	1.69
	^{65}Zn	(0.01	5.31	(0.01	0.02
	Total	9.8	1.06	9.2	1.71
Nb		9.8	0.39	9.4	0.31
Mo		7.7	-	7.2	-
316SS[c]		11.3	688.0	9.5	26.1

[a] 365 FPD assuming no burnout of Hf.
[b] Thermal neutron self-shielding may reduce damage in Mn, Co.
[c] 316SS: Fe(0.645), Ni(0.13), Cr(0.18), Mn(0.019), Mo(0.026).

Table 2.1.8. Revised Fluence and Damage Parameters for HFIR-RB1 and RB2 Experiments

Values at midplane; use eqn (1) for gradients

Energy	Neutron Fluence, x 10^{22} n/cm^2-s RB1	RB2
Total	4.62	9.30
Thermal (<.5 eV)[a]	2.15	4.19
Intermediate	1.55	3.21
Fast (>.1 MeV)	0.91	1.90

Element		RB1 DPA	RB1 He, appm	RB2 DPA	RB2 He, appm
Al		11.07	2.93	23.1	5.84
Ti		6.48	2.41	13.5	4.92
V		7.52	0.10	15.7	0.20
Cr[b]		6.11	0.71	13.2	1.42
Mn[b]		7.51	0.61	15.6	1.21
Fe[b]		5.52	1.27	11.5	2.52
Co[b]		8.37	0.61	17.1	1.20
Ni	Fast	6.30	18.	13.1	36.
	^{59}Ni	6.53	3705.	17.4	9868.
	Total	12.83	3723.	30.5	9904.
	Fast	5.57	1.09	11.6	2.2
	^{65}Zn	<0.01	3.33	0.04	18.6
	Total	5.57	4.42	11.6	20.8
Nb		5.50	0.24	11.5	0.47
Mo		4.30	-	9.0	-
316 SS[c]		6.62	485.	14.3	1289.

[a] Thermal maxwellian at 60°C.
[b] Thermal self-shielding may reduce damage for Mn, Co.
[c] 316 SS = Fe (.645), Ni (.13), Cr (.18), Mn (.019), Mo (.026).

Table 2.1.9. Revised Heium and DPA Rates for 316 SS for HFIR-RB1 and RB2 Experiments

Helium includes ^{59}Ni and fast reactions
Damage includes extra thermal kick (He/567)

Height, cm	RB1 He, appm	RB1 DPA	RB2 He, appm	RB2 DPA
0	485	6.52	1289	14.3
3	478	6.55	1274	14.2
6	459	6.35	1232	13.7
9	427	6.05	1161	13.1
12	383	5.62	1059	12.2
15	328	5.07	931	11.0
18	265	4.40	776	9.6
21	196	3.63	596	1.9
24	124	2.74	399	6.0

2.2 PROPOSED NEW IRRADIATION FACILITIES IN HFIR — K. R. Thorns, B. H. Montgomery. and C. D. West (Oak Ridge National Laboratory)

2.2.1 ADIP Task

ADIP Task 1.A.2, Define Test Matrices and Test Procedures

2.2.2 Objective

The objective of this work is to provide the capability to perform instrumented irradiation experiments in the target region of the High Flux Isotope Reactor (HFIR) and to increase the size and number of irradiation facilities in the removable beryllium (RB) reflector region of the HFIR.

2.2.3 *Summary*

A project is presently under way to improve and increase the irradiation facility capabilities in the HFIR. These improvements will permit the installation of two instrumented experiments in the target region of the HFIR by the fourth quarter of FY 1986. Additionally, the number of large RB positions will be increased from four to eight, and their diameter will be increased from 35 *to* 48 mm. This phase of the project is scheduled to be completed by May 1987.

2.2.4 Background and Description

A Laboratory-wide ad hoc committee was formed to consider and recommend changes and improvements to the Laboratory's facilities for materials irradiation testing. The committee determined (ORNL/TM-9709) that in seeking to reestablish ORNL's position as a world leader in irradiation experiments, it is clear that the HFIR, already an outstanding facility in many respects, is a better starting point than the ORR, which is surpassed in all respects by a number of other reactors.

The basic improvements needed at the HFIR are clearly evident when one examines the existing facilities. The highest flux positions in the target or flux trap region cannot be instrumented and are very small. The RB positions are few and much smaller than those in most general purpose reactors. The proposed reactor modifications address these issues.

Figure 2.2.1 is a diagrammatic side view of the HFIR fuel elements and target region. A structure known as the target tower extends upward from the target region almost 2.5 m (8 ft) to the quick-access hatch, a removable plug in the center of the reactor pressure vessel lid. The quick-access hatch is pierced in the center to admit a hydraulic rabbit tube. The committee proposed that a new quick-access hatch be made, pierced with three access holes on an equilateral triangle. Two of the three penetrations, to be provided with suitable flanges, seals, and hold-down clamps, will provide access to the target region for instrumentation ducts. The third penetration will be for the existing hydraulic tube facility. Because the rather complicated target tower assembly provides support and guidance for the hydraulic tube, it too must be redesigned and rebuilt.

With these modifications, two small target capsules of 16-mm diam may be instrumented. By occupying up to seven target positions, capsules up to 25-mm diam could be accommodated (Fig. 2.2.2). If desired, it would also be possible to incorporate a shield (e.g., of tungsten) to reduce the

ORNL DWG 85 4661 ETD

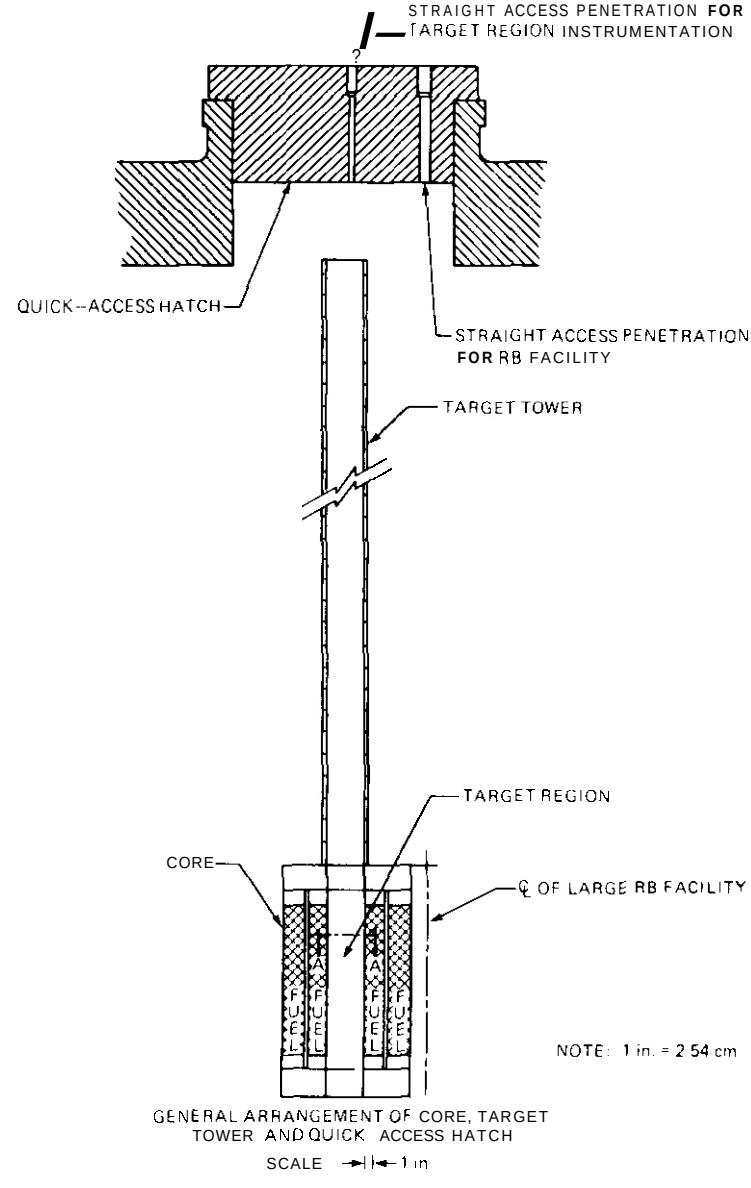

Fig. 2.2.1. Side view of HFIR core.

gamma heating rate in the capsule and permit the irradiation of larger specimens while maintaining acceptable temperature gradients within the samples. Alternatively, it would be possible selectively to absorb thermal neutrons (by using, e.g., a cadmium or hafnium shield) to provide spectral tailoring, but the effect of the shields on core life and on other uses of the reactor has yet to be fully assessed.

There are presently four 37-mm-diam irradiation positions in the RB region of the reactor [Fig. 2.2.3(a)]. The committee proposed that the four be replaced by eight larger holes capable of accepting 48-mm-diam capsules [Fig. 2.2.3(b)]. The change will increase the total experimental volume available within irradiation capsules at these positions by a factor of 3 to 4. The new positions are referred to as the RB Star (RB*) facilities, and they can accommodate most of the work presently accomplished in the ORR core with a twofold to threefold increase in fast neutron flux.

To provide straightline instrumentation access to the RB* facilities, other components of the HFIR, mounted above the RB and the core, must also be redesigned and rebuilt. Specifically, the upper-track assembly and the shroud flange (which are part of the control plate location and drive system) must be modified. It is also proposed that additional penetrations be made in the quick-access hatch to provide straightline access to the RB* positions for instrumentation. The straightline access will also permit rotation and vertical relocation of capsules during the course of an experiment, as well as making experiments interchangeable.

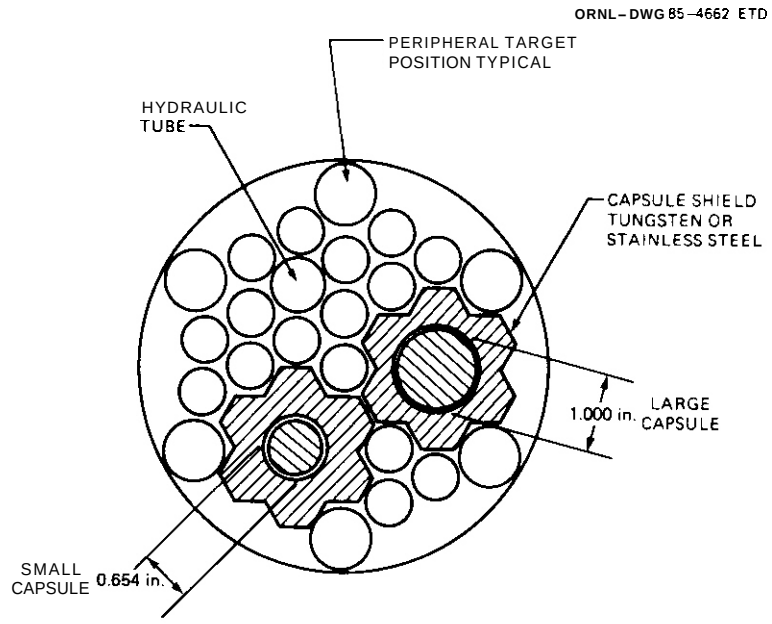

Fig. 2.2.2. The HFIR target region with two capsules.

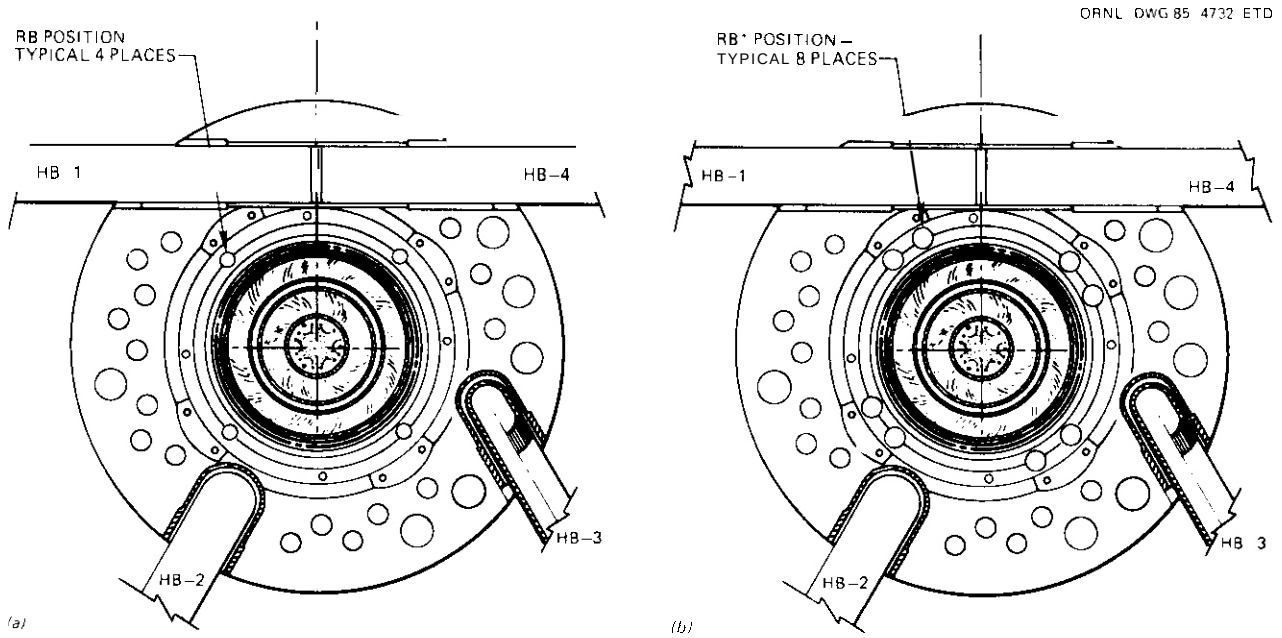

Fig. 2.2.3. The RB and RB* positions.

2.2.5 Progress and Status

Conceptual design work proving feasibility and methods of achieving the recommended modifications has been completed. The detail design of the target tower and access hatch is about 70% complete.

It is expected that some experimenters will wish to include spectral tailoring with their RB* experiments, and it is important to understand the effects of such neutron absorbers on the core life, beam tube

flux, and the RE* facility flux. Preliminary, though not very convincing, calculations were carried out which made it clear that the reactor operators and experimenters do not presently have available any satisfactory way of calculating and predicting the effects of loading new materials into the vicinity of the core. Consequently, an experimental program was undertaken to determine the effects of placing a 3.8-mm-thick hafnium sleeve in the present RE positions. A series of low power (100 kW) runs were made to determine the effects on beam tube fluxes. The results of these runs are summarized in Table 2.2.1., which compares flux levels with a base case in which the usual iridium loadings were placed in all RE positions except RE-3. As the table shows, all combinations of hafnium position and beam tube use except one (RE-3 and HE-2) are acceptable showing a beam tube flux loss of 6% or less.

Table 2.2.1. Effect of hafnium on beam tube flux[a]

	Percent change in thermal flux at beam tubes[b]			
	HE1	HE2	HE3	HE4
Hafnium Position				
RB1[c]	-3	0	+1	+2
RB3	+4	—13%	+1	+4
RB5[c]	+1	-1	-6	+2
RB7[c]	+1	0	+2	—4

[a]Measured at reactor Dower of 100 kW.

[b]The base case had the usual iridium (isotope production) capsules at all RE positions except R3.

[c]The iridium in these positions was replaced by the hafnium sleeve to make the measurement.

Following the low-power beam tube runs, a pair of moderate power (—11 MW) dosimetry runs were made to characterize the spectrum and flux levels inside the hafnium tube. The results of these runs, analyzed by L. R. Greenwood of ANL, are reported elsewhere' in this report. An additional, full-cycle, flux run was completed and dosimetry shipped to L. R. Greenwood.

Determining the effects of the hafnium on core lifetime has been complicated by the installation of two other experiments in RE positions and the addition of other poisons for the isotope production program. However, based on the observed shortening of the cycle in which the full-cycle dosimetry runs were made in addition to subsequent cycles, it appears that the hafnium tube caused a 0.9 (±0.3) day or about 4% reduction in expected core lifetime.

2.2.6 Reference

1. L. R. Greenwood, "Neutron Dosimetry and Damage Calculations for ORR6J Test, HFIR-RB-Hafnium Test and HFIR-RE-I and RE-2 Experiments," Sect. 2.1, this report.

2.3 PHASE I HFIR CAPSULES — IRRADIATION AND POSTIRRADIATION EXAMINATION — J. L. Scott, M. L. Grossbeck (Oak Ridge National Laboratory), and M. P. Tanaka (Japan Atomic Energy Research Institute, assigned to ORNL)

2.3.1 ADIP Task

ADIP Task I.A.2, Define Test Matrices and Test Procedures.

2.3.2 Objectives

The objective of this work is to carry out the postirradiation examination (PIE) of U.S./Japan capsules JP-1 to -8 irradiated in the High Flux Isotope Reactor (HFIR) for the purpose of investigating the irradiation response of Japanese and U.S. structural alloys to high levels of atomic displacement and helium content.

2.3.3 *Summary*

Capsules JP-1 and -3 have been disassembled and specimen testing is under way. Irradiation of capsules JP-2 and JP-4 to -8 is continuing.

2.3.4 Progress and Status

The U.S./Japan Phase I HFIR testing program consists of eight target capsules to be irradiated to peak damage levels of approximately 30 and 50 dpa. The test matrix and the damage levels in capsule JP-1, which has completed its irradiation campaign, were reported previously.[1-3] Capsule JP-3 was removed from HFIR May 28, 1985, after an exposure of 34,019 MWd. The exposure levels of the specimens in JP-3 are given in Table 2.3.1. Irradiation of the other six capsules is continuing. Present damage levels of JP-2 and JP-4–8 are given in Table 2.3.2. Results to date of postirradiation testing of JP-1 and JP-3 are reported below.

Table 2.3.1. Displacements per atom and helium contents in JP-3 capsule[a]

Position	Distance from HFIR center-line (cm)	Alloy	Specimen type	Identification	Displacements per atom (dpa)	Helium content (at. ppm)
1	23.20	PCA	Tensile	EL30	16.00	1020
2	18.76	PCA	Tensile	EL34	22.32	1559
3	14.31	PCA	Tensile	EC29	27.28	1981
4	9.59	PCA	Fatigue	EC152	31.07	2298
5	4.58	316	Fatigue	AA8	32.60	2019
6	0.00	J316	TEM		33.40	2142
7	4.58	JPCA	Fatigue	FE5	33.30	7447
8	9.59	JPCA	Fatigue	FE6	30.95	2258
9	14.31	JPCA	Tensile	TB7	27.17	1950
10	18.76	JPCA	Tensile	TB8	22.23	1541
11	23.20	JPCA	Tensile	TB9	15.95	1019

[a]MWd: 34,019.

Capsule	Reactor exposure[c,d] (MWd)	Level (dpa)		Capsule	Reactor exposure[c,d] (MWd)	Level (dpa)	
		Present[c]	Goal[d]			Present[c]	Goal[d]
JP-1[e]	33,644	33.03	30	JP-5	30,451	29.85	50
JP-2	51,198	50.37	50	JP-6	30,451	29.85	30
JP-3[e]	34,019	33.40	30	JP-7	28,343	27.75	30
JP-4	40,810	40.14	50	JP-8	28,343	27.75	50

2.3.4.1 Postirradiation Examination of Capsule JP-1

The upper and lower ends of capsule JP-1 were cut off with an abrasive cutoff wheel. The inner and outer containments were cut axially the entire length and removed. The appearance of the specimen holders is shown in Fig. 2.3.1. Everything was bright and shiny, indicating no water leakage into the capsule. The flux monitors, which were located at the top of holders 3, 5, 6, 9, and 11, were identified and shipped to L. R. Greenwood for analysis. The specimens were removed from their holders by cutting the retainer rings and prying apart the half shells.

Pictures of the specimens are shown in Figs. 2.3.2 and 2.3.3; exposure levels are given in Table 2.3.2. Figure 2.3.2 shows the four hourglass fatigue specimens and the holder containing TEM disks. The latter operated at 300°C while all the fatigue specimens operated at 430°C. There was a slight discoloration of the fatigue specimens due to surface oxidation. Even though the capsule is filled with helium, some outgassing occurs during the initial heatup in the reactor, leading to superficial oxidation at the higher specimen temperatures. Somewhat greater oxidation was observed on tensile specimens that operated at 500°C, as is shown in Fig. 2.3.3. The two center specimens were irradiated at 500°C. The 300 and 400°C specimens were bright and shiny after irradiation.

YP001

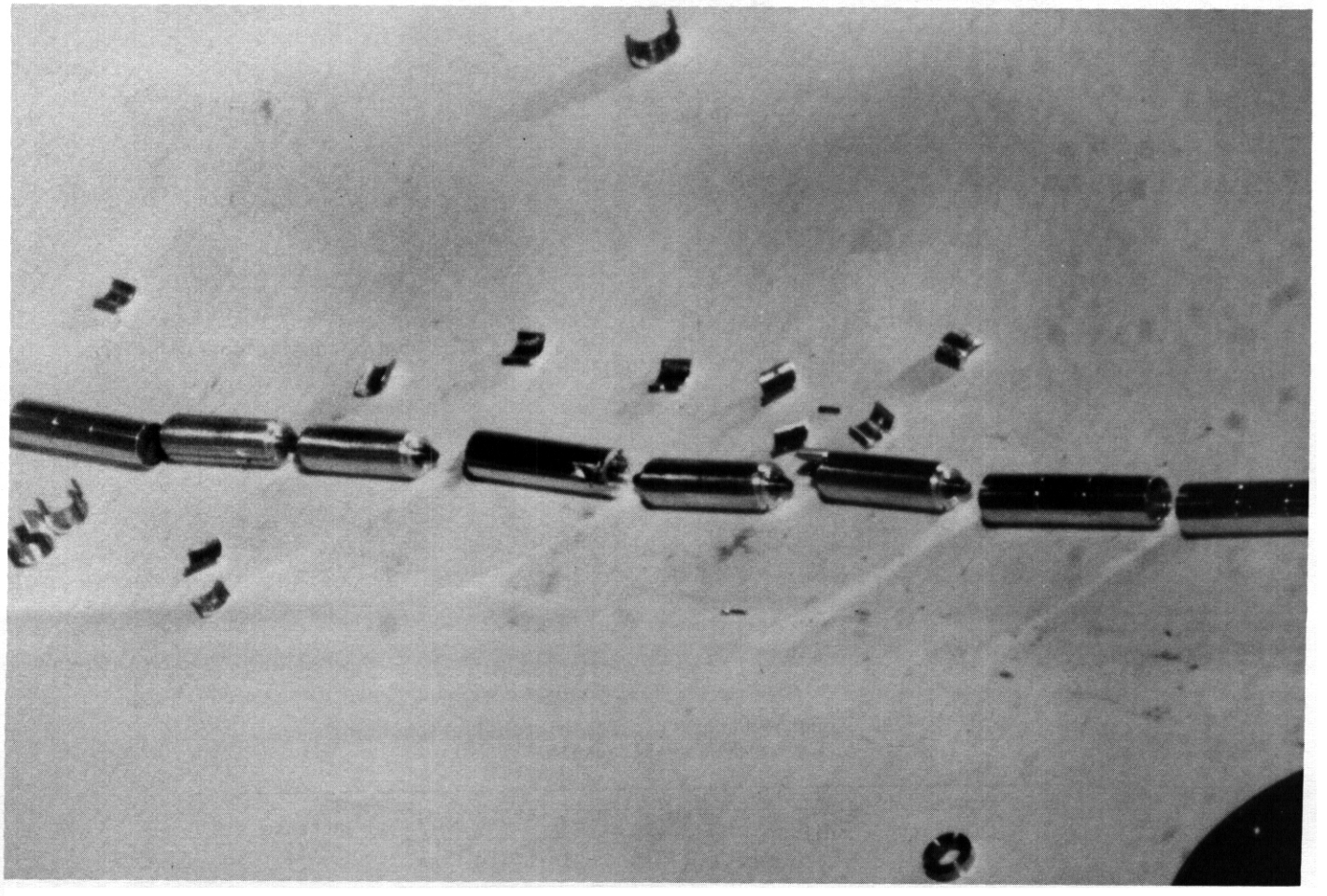

Fig. 2.3.1. Picture of JP-1 specimen holders during capsule disassemblv.

Length measurements of the tensile specimens were made after irradiation by use of a micrometer. Results are shown in Table 2.3.3. If one assumes that the dimensional changes are isotropic, volume increases are three times the lenath increases.

Immersion densities of the irradiated tensile specimens were measured together with standards and controls on a precision analytical balance. Results are shown in Table 2.3.4. If one compares these results with those in Table 2.3.3, one finds that swelling data obtained from length changes overestimate the true volume increases. Furthermore, the amount of swelling was small in all cases.

In other hot cell work, the TEM disks have been sorted. and equipment is being prepared for tensile and fatigue testing.

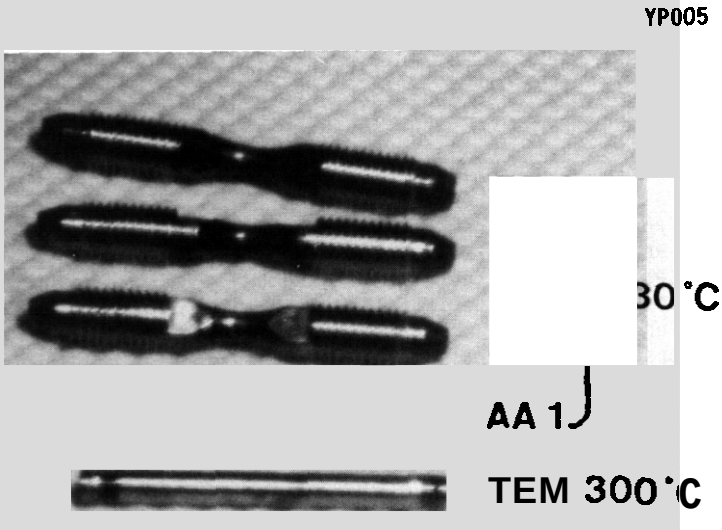

Fig. 2.3.2. Hourglass fatigue specimens and JEM disk holder from JP-1.

Fig. 2.3.3. Submini tensile specimens from JP-1.

Table 2.3.3. Length changes of submini tensile specimens in HFIR JP-1 capsule

Specimen number	Alloy	Conditiona	Irradiation temperature (°C)	Length (mm)		Increase
				Initial	Final	
EL15	PCA	83	300	39.34	39.35	0.02
EL21	PCA	B3	400	39.34	39.46	0.31
EL28	PCA	83	500	39.34	39.47	0.33
TB1	JPCA	PS2	500	39.39	39.50	0.28
TB2	JPCA	PS2	400	39.38	39.48	0.25
TE1	JPCA	PC2	300	39.37	39.46	0.23

aB3 — SA at 1100°C + 8 h at 800°C + 25% CW.
PS2 — SAat 1100°C.
PC2 — PS2 + 15% CW.

Table 2.3.4 Immersion densities of submini tensile specimens

Specimen number	Immersion density (g/cm^3)	$\frac{\Delta V}{V_0} = \frac{\Delta \rho}{\rho_f}$ (%)	Specimen number	Immersion density (g/cm^3)	$\frac{\Delta V}{V_0} = \frac{\Delta \rho}{\rho_f}$ (%)
ELA(control)	8.00275	0	TB1	7.96426	0.302
EL15	8.00174	0.013	TB2	7.97893	0.117
EL21	7.997 13	0.070	TE13(control)	7.97907	0
EL28	7.96327	0.496	TE1	7.98480	0.072
TB13(control)	7.98829	0			

2.3.4.2 Postirradiation Examination of Capsule JP-3

Capsule JP-3 has been disassembled. The specimens had the same appearance as those in capsule JP-1. Length measurements of tensile specimens are shown in Table 2.3.5. This is as far as testing has proceeded at this time.

Table 2.3.5. Length changes of submini tensile specimens in HFIR JP-3 capsule

Specimen number	Alloy	Condition[a]	Irradiation temperature (°C)	Length (mm)		Increase (%)
				Initial	Final	
EL30	PCA	83	*300*	39.34	39.39	0.14
EL34	PCA	B3	400	39.34	39.52	0.47
EC29	PCA	A3	500	39.35	39.43	0.20
TB7	JPCA	PS2	500	39.41	39.45	0.10
TB8	JPCA	PS2	400	39.40	39.46	0.15
TB9	JPCA	PS2	*300*	39.40	39.43	0.08

[a]A3 — SA at 1100°C t 25% CW.
83 — SA at 1100°C + 8 h at 800°C t 25% CW.
PS2 — SA at 1100°C.

2.4.5 References

1. A. F. Rowcliffe, M. L. Grossbeck, and S. Jitsukawa, "The U.S./Japan Collaborative Testing Program in HFIR and ORR," pp. 38–43 in *ADIP Semiannu. Prog. Rep. March 31, 1984,* DOE/ER-0045/12, U.S. DOE, Office of Fusion Energy.

2. A. F. Rowcliffe, M. L. Grossbeck, M. Tanaka, and S. Jitsukawa, "The U.S./Japan Collaborative Testing Program in HFIR and ORR: Specimen Matrices for HFIR Irradiation," pp. 61-62 in *ADIP Semiann. Prog. Rep. Sept. 30, 1984,* DOE/ER-0045/13, U.S. DOE, Office of Fusion Energy.

3. J. L. Scott and M. P. Tanaka. "Preparation for Postirradiation Examination of U.S./Japan HFIR Capsules, pp. 10–11 in *ADIP Semiannu. prog. Rep. March 31, 1985,* DOE/ER-0045/14, U.S. DOE, Office of Fusion Energy.

2.4 DESCRIPTION OF THE U.S.-JAPAN SPECTRAL-TAILORING EXPERIMENT IN ORR — J. L. Scott, L. K. Mansur, M. L. Grossbeck, E. H. Lee, K. Farrell, L. L. Horton, A. F. Rowcliffe (Oak Ridge National Laboratory), M. P. Tanaka (Japan Atomic Energy Research Institute, assigned to ORNL), and H. Hishinuma (Japan Atomic Energy Research Institute)

2.4.1 ADIP Task

ADIP Task I.A.2, Define Test Matrices and Test Procedures.

2.4.2 Objectives

The primary objective of this experiment is to study the response of U.S. and Japanese fusion structural alloys to high fluences with a helium/dpa ratio similar to that expected in a fusion reactor. In addition, the experiment is used to study fundamental radiation processes under well-controlled conditions.

2.4.3 *Summary*

The final test matrix for the two spectral-tailoring capsules MFE-6J and -7J was established. Specimens were loaded into the two capsules and irradiation testing has begun. The test matrix includes conventional U.S. and Japanese structural alloys and a series of base research alloys that will provide a basic understanding of alloy response to the fusion reactor environment.

2.4.4 Progress and Status

A basic description of the MFE-6J and -7J capsules and the experimental objectives were provided in the previous semiannual progress report.[1] Alloy compositions were also tabulated. This report contains a description of the specimens and the test matrix for the two capsules. The assembly of the capsules and the operating experience are described in Sect. 2.5 of this report. The final test matrix given in Table 2.4.1 has been modified slightly from that given in the previous progress report. The adjustments were made to optimize the use of available space in the capsules. Specimen descriptions and loading lists are given in the following sections.

Table 2.4.1. Test matrix for the MFE-6J and -7J capsules

Specimen type	Source	Number of specimens			
		60°C	200°C	330°C	400°C
Pressurized tubes	ORNL	32	16	39	33
	JAERI	6	10	6	6
Tube blanks	ORNL	6	6	6	6
	JAERI	3	3	3	3
SS1 tensiles	ORNL	29	34	11	13
	JAERI	70	59	72	64
SS3 tensiles	ORNL	43	44	16	22
	HEDL	35	35	30	30
Grodzinski fatigue	JAERI	56	24	56	40
Crack growth	JAERI	18	18	10	10
	HEDL	18	18	0	0
Rod tensiles	JAERI	0	0	4	0
Hourglass fatigue	JAERI	0	0	0	5
Disk packets	ORNL	4	4	8	9
	HEDL	0	0	4	4
	JAERI	5	7	6	6

2.4.4.1 Pressurized Tubes

Irradiation creep is being investigated through the use of pressurized-tube specimens. This technique, which was used in the earlier spectral-tailoring capsules MFE-4A and -4B,[2] has proven successful at ORNL,[3] HEDL,[4] and at KRZ Karlsruhe.[5] The design of the pressurized tube is shown in Fig. 2.4.1. After fabrication, the tube is placed in a pressure chamber that has a glass window. The chamber is pressurized with helium and the pinhole in the end cap is laser welded shut. Weld parameters are chosen so as to give a full-penetration weld. The Japanese tubes in MFE-6J and -7J were fabricated at HEDL and have a different end cap weld.

To obtain irradiation creep data, the pressurized tubes are periodically removed from the reactor and the diameter profiles are measured. The average diameter of the central three-fifths of each tube is used in the creep analysis. A correction for swelling is made based on density measurements of 6.35-mm-long tube specimens prepared with no end caps. Since the tubes are pressurized at a series of different pressures, the effect of stress at constant fluence can be determined for each alloy. The fluence dependence can be determined through the periodic examination of all the tubes. The test matrix and hoop stresses for each tube are presented in Table 2.4.2.

ORNL-DWG 78-7704R

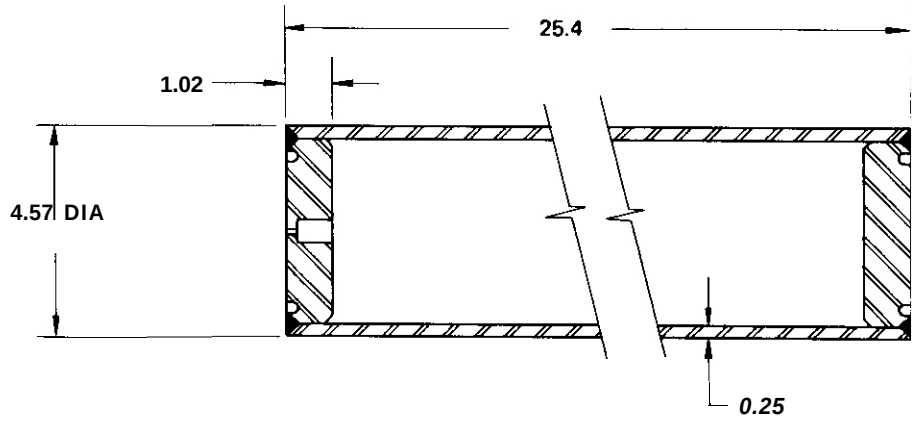

Fig. 2.4.1. Pressurized tube design — alldimensions are in millimeters.

Table 2.4.2. Test matrix for pressurized tubes in MFE-6J and -75 capsules

Alloy	Condition	Source	60°C		200°C		330°C		400°C	
			Identification	Stress (MPa)	Identification	Stress (MPa)	Identification	Stress (MPa)	Identification	Stress (MPa)
PCA	20% CW	ORNL	FA-1	0	FA-2	0	FA-1	0	FA-2	0
PCA	20% CW	ORNL	FA-51	50	FA-59	50	FA-33	50	FA-01	50
PCA	20% CW	ORNL	FA-36	100	FA-48	100	FA-19	100	FA-32	100
PCA	20% CW	ORNL	FA-53	150	FA-62	200	FA-27	200	FA-10	200
PCA	20% CW	ORNL	FA-58	200	-----	---	FA-34	200	FA-05	300
PCA	20% CW	ORNL	FA-24	200	-----	---	FA-08	300	FA-12	400
PCA	20% CW	ORNL	----	---	-----	---	FA-28	400	-----	---
HT-9	a	ORNL	SA28-1	0	SA28-2	0	SA-1	0	SA-2	0
HT-9	a	ORNL	SA-54	100	SA-21	200	SA-09	50	SA-58	50
HT-9	a	ORNL	SA-49	200	SA-30	400	SA-56	100	SA-37	100
HT-9	a	ORNL	SA-17	200	----	---	SA-05	200	SA-32	200
HT-9	a	ORNL	SA-41	280	----	---	SA-16	200	SA-53	300
HT-9	a	ORNL	SA-55	280	----	---	SA-01	300	SA-03	400
HT-9	a	ORNL	SA-24	300	----	---	SA-33	300	SA-31	400
			-----	---	----	---	SA-38	400	-----	---
1B	SA	ORNL	CA-1	0	CA-2	0	CA-1	0	CA-2	0
1B	SA	ORNL	C3-A4	5	C1-A6	5	C1-A0	5	C5-A2	5
1B	SA	ORNL	C1-A3	10	C2-A6	10	C4-A1	10	C3-A6	10
1B	SA	ORNL	C3-A0	30	C4-A9	30	C3-A1	20	C4-A2	20
1B	SA	ORNL	C3-A5	30	-----	---	C1-A9	27	C2-A4	30
1B	SA	ORNL	C3-A9	60	-----	---	C4-A6	30	C3-A2	40
1B	SA	ORNL	----	---	-----	---	C4-A3	40	C1-A1	40
28	SA	ORNL	CB-1	0	CB-2	0	CB-1	0	CB-2	0
2B	SA	ORNL	C2-B8	5	C3-B2	5	C5-B3	5	C4-B4	5
28	SA	ORNL	C2-B6	10	C1-B3	10	C4-89	10	c3-84	10
28	SA	ORNL	C2-B5	30	C3-B1	30	C4-B5	20	C4-32	20
28	SA	ORNL	C2-B9	30	----	---	C3-B3	20	C4-B0	30
2B	SA	ORNL	C1-B6	50	----	---	C5-B1	30	C5-BO	30
28	SA	ORNL	C3-B0	50	----	---	C3-B9	30	C4-86	40
28	SA	ORNL	C1-B5	60	----	---	C5-B5	40	-----	---
38	SA	ORNL	cc-1	0	cc-2	0	CC-1	0	cc-2	0
38	SA	ORNL	C1-C9	50	c4-co	20	C1-C5	10	C1-C0	10
38	SA	ORNL	C4-C2	100	C1-C8	50	C2-C9	20	C3-C4	20
38	SA	ORNL	C3-C1	150	C3-CO	100	C1-C2	50	C3-C6	50
3B	SA	ORNL	C2-C5	150	-----	---	C3-C7	100	C2-C7	50
38	SA	ORNL	-----	---	-----	---	C3-C8	100	C4-C3	100
38	SA	ORNL	-----	---	-----	---	C4-C9	150	-----	---
36	SA	ORNL	-----	---	-----	---	C3-C3	150	-----	---

Table 2.4.2. (continued).

Alloy	Condition	Source	60°C		200°C		330°C		400°C	
			Identification	Stress (MPa)	Identification	Stress (MPa)	Identification	Stress (MPa)	Identification	Stress (MPa)
SA	SA	ORNL	S1A5-1	0	S1-A5	0	SXAX-1	0	SXAX-2	0
SA	SA	ORNL	S3-A7	10	S3-A5	20	S2-A3	10	S1-A0	10
SA	SA	ORNL	S1-A9	20	S2-A7	80	S2-A6	20	01	20
SA	SA	ORNL	S2-A5	20	----	---	S1-A6	50	S2-A4	50
SA	SA	ORNL	S2-A2	50	----	---	S3-A0	50	S2-A0	80
SA	SA	ORNL	S1-A8	100	----	---	S1-A2	80	81-A1	100
SA	SA	ORNL	-----	---	----	---	S1-A7	100	-----	---
J-316	SA	JAERI	3S13-1	0	3S13-2	0	3S11-1	0	3S11-2	0
J-316	SA	JAERI	35-01	100	38-00	80	38-04	100	38-03	100
J-316	SA	JAERI	3S-08	180	3S-02	100	38-07	120	38-06	130
J-316	SA	JAERI	-----	---	38-05	130	-----	---	-----	---
J-316	SA	JAERI	-----	---	38-10	150	-----	---	-----	---
J-316	20% CW	JAERI	3C12-1	0	3C12-2	0	3C10-1	0	3C10-2	0
J-316	20% CW	JAERI	3C-11	100	3C-05	200	3C-03	200	3C-04	200
J-316	20% CW	JAERI	3C-08	200	3C-09	300	3C-06	350	3C-07	400
JPCA	SA	JAERI	PS14-1	0	PS14-2	0	PS11-1	0	PS11-2	0
JPCA	SA	JAERI	PS-01	100	PS-00	100	PS-03	100	PS-04	100
JPCA	SA	JAERI	PS-08	180	PS-02	130	PS-10	150	PS-07	150
JPCA	SA	JAERI	-----	---	PS-05	160	-----	---	-----	---
JPCA	SA	JAERI	-----	---	PS-09	180	-----	---	-----	---

[a]Tempered martensite.

2.4.4.2 Tensile Specimens

The tensile test matrix for MFE-6J and -7J consists of SS-1-type specimens from ORNL and JAERI, SS-3-type specimens from ORNL and HEOL, and a few so-called submini specimens, normally used in HFIR, from JAERI. The specimen dimensions are given in Figs. 2.4.2 through 2.4.4. The test matrix is given in Tables 2.4.3 through 2.4.6.

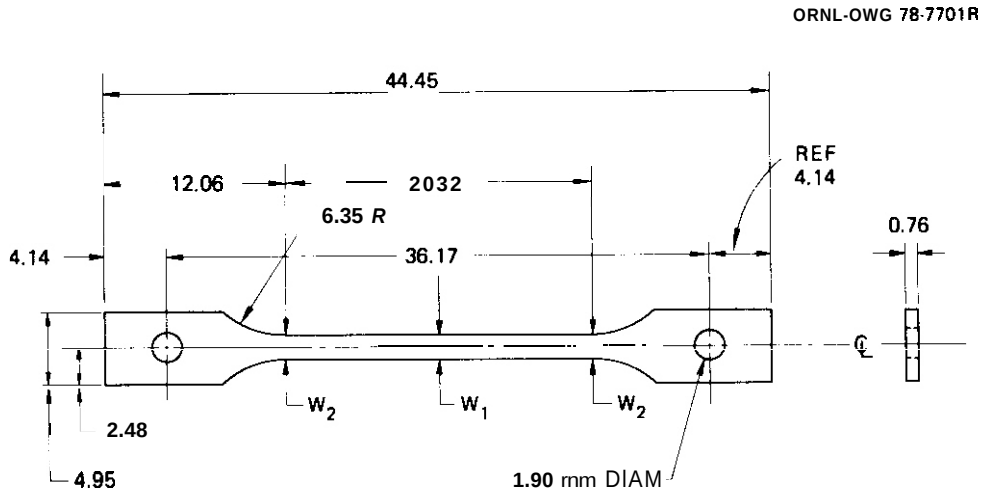

Fig. 2.4.2. SS-1 tensile specimens.

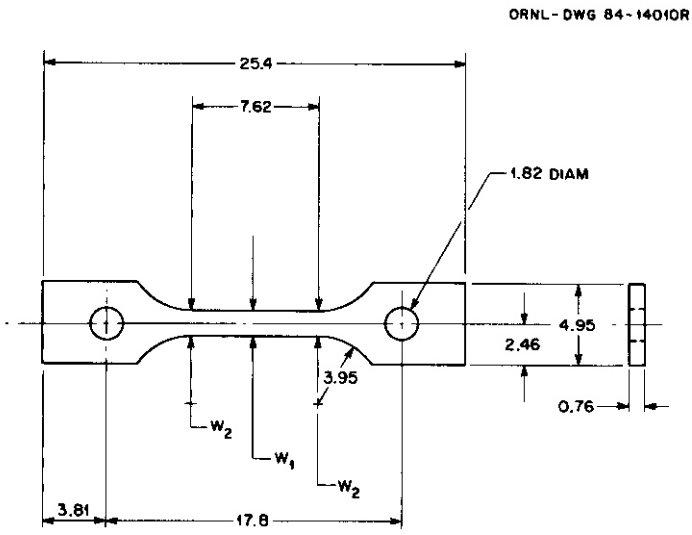

Fig. 2.4.3. SS-3 tensile specimens.

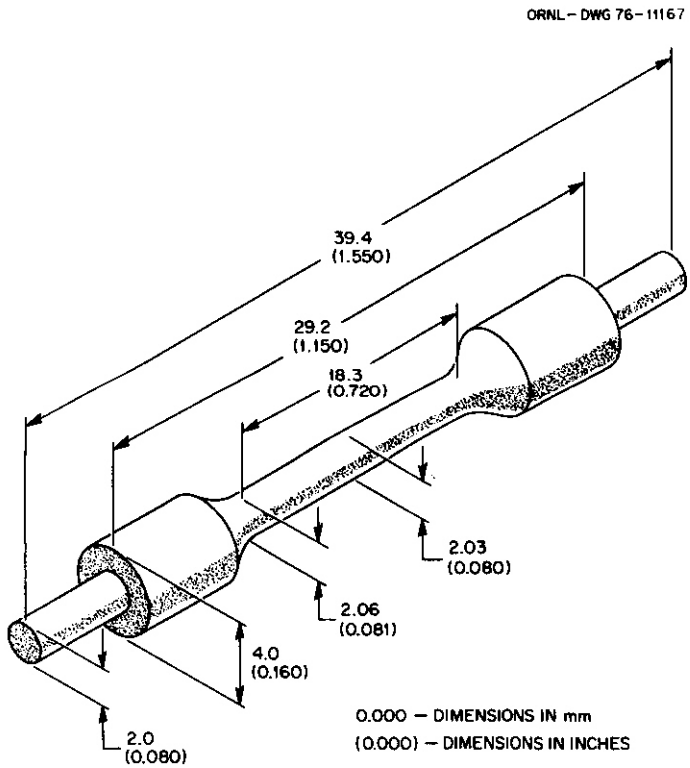

Fig. 2.4.4. HFIR submini tensile specimen.

2.4.4.3. Fatigue Specimens

The fatigue specimens, provided by JAERI, are of two types — Grodzinski sheet specimens and HFIR-type hourglass specimens. The former specimens, shown in Fig. 2.4.5, can be used for tensile-tensile fatigue or bend testing, and the latter, shown in Fig. 2.4.6, are tested in the full tension-compression mode. The fatigue test matrix is given in Table 2.4.1.

Table 2.4.3. ORNL SS-1 tensile test matrix in MFE-6J and -7J capsules

Alloy	Condition	dpa	Specimen Identification			
			60°C	200°C	330°C	400°C
316 SS	SA	10	AM-09	AM-04	AM-06	AM-12
316 SS	SA	10	AM-05	AM-10	AM-07	AM-08
316 SS	20% CW	10	01-16	AM-22	AM-26	AM-25
316 SS	20% CW	10	01-25	AM-28	AM-14	AM-13
316 SS	20% CW	10	07-23	B5-5	AB-107	B1-17
316 SS	20% CW	10	C1-5	AB-26	01-15	C1-10
316 SS	20% CW	10	B4-7	B1-5	07-15	05-12
316 SS	20% CW	10	AM-18	C1-17	B5-10	07-21
316 SS	20% CW	10	AM-15	B7-9	04-12	B7-2
316 SS	20% CW	10	----	04-23	C1-23	04-10
316 SS	20% CW	10	----	----	07-22	04-21
316 SS	20% CW	10	----	----	----	B5-23
316 SS	20% CW	10	----	----	----	AB-87
B1	SA	30	B1-08	01-07	-----	-----
02	SA	30	B2-08	02-07	-----	-----
03	SA	30	03-08	03-07	-----	-----
B5	SA	30	05-08	05-07	-----	-----
06	SA	30	06-08	06-07	-----	-----
07	SA	30	07-08	07-07	-----	-----
B9	SA	30	B9-08	09-07	-----	-----
B10	SA	30	B10-08	810-07	-----	-----
B11	SA	30	B11-08	B11-07	-----	-----
012	SA	30	B12-08	B12-07	-----	-----
013	SA	30	B13-08	B13-07	-----	-----
E-1	SA	30	El-08	El-07	-----	-----
E-2	SA	30	E2-08	E2-07	-----	-----
E-3	SA	30	E3-08	E3-07	-----	-----
E-4	SA	30	E4-08	E4-07	-----	-----
E-5	SA	30	E5-08	E5-07	-----	-----
E-6	SA	30	E6-08	E6-07	-----	-----
E-8	SA	30	E8-08	E8-07	-----	-----
E-9	SA	30	E9-08	E9-07	-----	-----
E-10	SA	30	EIO-08	E10-07	-----	-----
E-11	SA	30	-----	Ell-07	-----	-----
E-12	SA	30	-----	E12-07	-----	-----
E-13	SA	30	-----	E13-07	-----	-----
E-14	SA	30	-----	E14-07	-----	-----

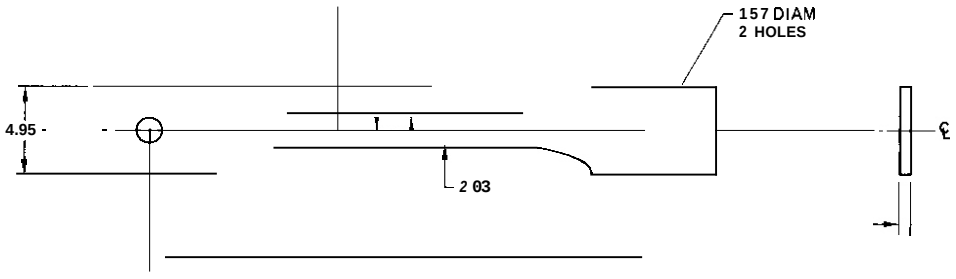

Table 2.4.4. Test matrix of ORNL *SS-3* tensile specimens in MFE-6J and -7J capsules

Alloy	Condition	dpa	Specimen identification			
			60°C	200°C	330°C	400°C
PCA	25% CW	10	----	EK-33	-----	-----
PCA	25% CW	10	EK-18	EK-34	-----	-----
PCA	25% CW	10	EK-19	EK-35	-----	-----
PCA	25% CW	10	EK-20	EK-36	-----	-----
PCA	25% CW	20	EK-21	EK-37	-----	-----
PCA	25% CW	20	EK-22	EK-38	-----	-----
PCA	25% CW	20	EK-23	EK-39	-----	-----
PCA	25% CW	20	EK-25	EK-40	-----	-----
PCA	25% CW	30	EK-26	EK-41	-----	-----
PCA	25% CW	30	EK-27	EK-42	-----	-----
PCA	25% CW	30	EK-28	EK-43	-----	-----
PCA	25% CW	30	EK-31	EK-46	-----	-----
316	20% CW	10	AE-01	AE-19	-----	-----
316	20% CW	10	AE-02	AE-20	-----	-----
316	20% CW	10	RE-04	AE-22	-----	-----
316	20% CW	10	AE-05	AE-23	-----	-----
316	20% CW	20	AE-06	AE-25	-----	-----
316	20% CW	20	AE-07	AE-26	-----	-----
316	20% CW	20	AE-08	AE-28	-----	-----
316	20% CW	20	AE-12	AE-31	-----	-----
316	20% CW	30	AE-13	AE-32	-----	-----
316	20% CW	30	AE-14	AE-34	-----	-----
316	20% CW	30	AE-15	AE-35	-----	-----
316	20% CW	30	AE-17	AE-37	-----	-----
PCA	25% CW	30	EC-10	EC-00	-----	-----
PCA	25% CW	30	EC-11	EC-03	-----	-----
PCA	25% CW	30	EC-12	EC-06	-----	-----
PCA	25% CW	30	EC-13	EC-08	-----	-----
PCA	25% CW	30	EC-14	EC-09	-----	-----
PCA	25% CW		EC-15	EC-21	-----	-----
PCA	83	30	EL-04	EL-00	-----	-----
PCA	83	30	EL-07	EL-03	-----	-----
PCA-20	25% CW	30	HV-09	HV-00	-----	-----
PCA-20	25% CW	30	HV-11	HV-02	-----	-----
PCA-20	25% CW	30	HV-12	HV-03	-----	-----
PCA-20	25% CW	30	HV-15	HV-04	-----	-----
PCA-20	25% CW	30	HV-16	HV-07	-----	-----
PCA-20	25% CW	30	HV-17	HV-08	-----	-----
PCMA-6	20% CW	30	MH-09	MH-01	-----	-----
PCMA-6	20% CW	30	MH-10	MH-02	-----	-----
PCMA-6	20% CW	30	MH-11	MH-05	-----	-----
PCMA-6	20% CW		MH-12	MH-06	-----	-----
PCMA-6	20% CW	30	MH-13	MH-07	-----	-----
PCMA-6	20% CW	30	MH-16	MH-08	-----	-----
Zr-1	Annealed	10	----	-----	1-01	-----
Zr-1	Annealed	10	----	-----	1-02	-----
Zr-1	Annealed	10	----	-----	1-03	-----
Zr-81	Annealed	10	----	-----	B-101	-----
Zr-B1	Annealed	10	----	-----	B-102	-----
Zr-B1	Annealed	10	----	-----	B-103	-----
Zr-B2	Annealed	10	----	-----	B-201	-----
Zr-B2	Annealed	10	----	-----	B-202	-----
Zr-B2	Annealed	10	----	-----	B-203	-----
Zr-4	Annealed	10	----	-----	52-1	-----
Zr-4	Annealed	10	----	-----	52-2	-----
Zr4-Li3	Annealed	10	----	-----	6701	-----
Zr4-Li3	Annealed	10	----	-----	6702	-----

Table 2.4.4. (continued).

Alloy	Condition	dpa	Specimen identification			
			60°C	200°C	330°C	400°C
Fe-Ni-Cr	Annealed	10	----	-----	871	-----
Fe-Ni-Cr-Li2	Annealed	10	----	-----	6901	-----
Fe-Ni-Cr-Li2	Annealed	10	----	-----	6902	-----
Ni-1Si	Annealed	10	----	-----	----	2701
Ni-1Si	Annealed	10	----	-----	----	2702
Ni-1Ti	Annealed	10	----	-----	----	3001
Ni-1Ti	Annealed	10	----	-----	----	3002
Ni-1Al	Annealed	10	----	-----	----	2901
Ni-1Al	Annealed	10	----	-----	----	2902
Ni-8Si	Annealed	10	----	-----	----	2801
Ni-8Si	Annealed	10	----	-----	----	2802
Fe-Ni-Cr(1Si)	Annealed	10	----	-----	----	7101
Fe-Ni-Cr(1Si)	Annealed	10	----	-----	----	7102
Fe-Ni-Cr(1Ti)	Annealed	10	----	-----	----	7301
Fe-Ni-Cr(1Ti)	Annealed	10	----	-----	----	7302
Fe-Ni-Cr(1Al)	Annealed	10	----	-----	----	7201
Fe-Ni-Cr(1Al)	Annealed	10	----	-----	----	7202
Fe	Annealed	10	----	-----	----	75-1
Fe	Annealed	10	----	-----	----	75-2
Fe-Li2	Annealed	10	----	-----	----	77-1
Fe-Li2	Annealed	10	----	-----	----	77-2
Fe-Lo8	Annealed	10	----	-----	----	8101
Fe-LoB	Annealed	10	----	-----	----	8102
Fe-HiB	Annealed	10	----	-----	----	8201
Fe-Hi8	Annealed	10	----	-----	----	8202

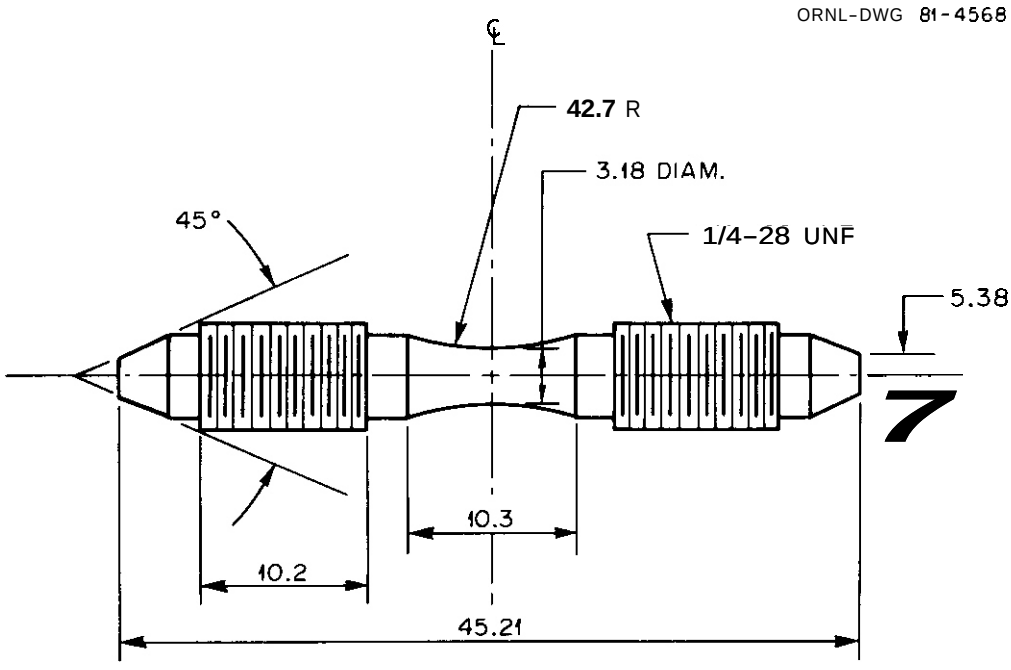

Fig. 2.4.6. Hourglass fatigue specimen. All dimensions are in millimeters.

Table 2.4.5. Test matrix of HEOL *SS-3* tensile specimens in MFE-6J and -7J capsules

Alloy	Condition[a]	dpa	Specimen identification			
			60°C	200°C	330°C	400°C
VO-2262	A	10	TE-15	TE-17	TE-11	TE-13
VO-2262	A	20	----	----	TE-12	TE-14
VO-2262	A	30	TE-16	TE-18	-----	-----
VO-2267	C	10	TL-15	TL-19	TL-11	t1-13
VO-2267	C	10	TL-16	TL-20	-----	-----
VO-2267	C	20	TL-17	TL-21	TL-12	t1-14
VO-2267	C	30	TL-18	TL-22	-----	-----
VO-2264	B	10	TM-15	TM-19	TM-11	TM-13
VO-2264	B	10	TM-16	TM-20	-----	-----
VO-2264	B	20	TM-17	TM-21	-----	-----
VO-2264	B	30	TM-18	TM-22	TM-12	TM-14
VO-2265	C	10	TN-15	TN-19	TN-11	TN-13
VO-2265	C	10	TN-16	TN-20	-----	-----
VO-2265	C	20	TN-17	TN-21	-----	-----
VO-2265	C	30	TN-18	TN-22	TN-12	TN-14
VO-2266	C	10	TP-15	TP-19	TP-11	TP-13
VO-2266	C	10	TP-16	TP-20	-----	-----
VO-2266	C	20	TP-17	TP-21	-----	-----
VO-2266	C	30	TP-18	TP-22	TP-12	TP-14
VO-2268	C	10	TR-09	TR-10	TR-11	TR-15
VO-2268	C	10	TR-19	TR-22	TR-12	TR-16
VO-2268	C	20	TR-20	TR-23	TR-13	TR-17
VO-2268	C	30	TR-21	TR-24	TR-14	TR-18
VO-2269	C	10	TU-07	TU-10	TU-11	TU-15
VO-2269	C	10	TU-19	TU-22	TU-12	TU-16
VO-2269	C	20	TU-09	TU-23	TU-13	TU-17
VO-2269	C	30	TU-21	TU-24	TU-14	TU-18
VO-2754	D	10	TW-11	TW-14	----	----
VO-2754	0	20	TW-12	TW-16	----	----
VO-2754	D	30	TW-13	TW-17	----	----
V0-2754	D	10	----	TW-15	----	----
YO-2755	D	10	TX-11	TX-15	----	----
VO-2755	0	10	TX-12	-----	----	----
VO-2755	D	20	TX-13	TX-16	----	----
YO-2755	0	30	TX-14	TX-17	----	----
?IC-19	A	10	TZ-19	TZ-22	TZ-11	TZ-15
uc-19	A	20	----	-----	TZ-13	TZ-17
uc-19	A	30	TZ-21	TZ-23	TZ-14	TZ-18
uc-19	A	10	----	-----	TZ-12	TZ-16
VO-2702	D	10	----	----	TT-11	TT-15
VO-2702	D	10	----	----	TT-12	TT-16
VO-2702	D	20	----	----	TT-13	TT-17
VO-2702	D	30	----	----	TT-14	TT-18
YO-2700	D	10	----	----	TF-11	TF-15
VO-2700	D	10	----	----	TF-12	TF-16
YO-2700	D	20	----	----	TF-13	TF-17
VO-2700	0	30	----	----	TF-14	TF-18

[a]A = 900°C/20 h/WQ + 950°C/20 min/WQ + 650°C/2 h/AC.
8 = 1000°C/20 h/AC + 1100°C/5 min/AC + 700°C/2 h/AC.
C = 1000°C/20 h/AC + 1100°C/10 min/AC + 700°C/2 h/AC.
D = 1000°C/20 h/AC + 1100°C/5 min/AC + 650°C/2 h/AC.

Table 2.4.6. JAERI tensile test matrix in MFE-6J and -7J capsules

Alloy	Condition	dpa	Specimen identification			
			60°C	200°C	330°C	400°C
JPCA	15% CW	10	DL-36	DL-3	DL-7	d1-19
JPCA	15% CW	10	DL-37	DL-4	DL-8	d1-20
JPCA	15% CW	10	DL-38	DL-5	DL-9	d1-21
JPCA	15% CW	10	----	DL-6	DL-10	d1-22
JPCA	15% CW	10	----	DL-45	DL-11	d1-73
JPCA	15% CW	10	----	DL-46	DL-12	d1-24
JPCA	15% CW	20	DL-39	DL-47	DL-13	d1-25
JPCA	15% CW	20	DL-40	DL-48	DL-14	d1-26
JPCA	15% CW	20	DL-41	DL-49	DL-15	d1-27
JPCA	15% CW	30	DL-42	DL-50	DL-16	DL-28
JPCA	15% CW	30	DL-44	DL-52	OL-17	d1-29
JPCA	15% CW	30	----	DL-53	DL-18	d1-30
5316	20% CW	10	FL-31	FL-39	FL-13	f1-1
J316	20% CW	10	FL-32	FL-40	FL-14	f1-2
J316	20% CW	10	FL-33	FL-42	FL-15	f1-3
J316	20% CW	10	----	FL-43	FL-16	f1-4
J316	20% CW	10	----	FL-44	FL-17	f1-5
J316	70% CW	10	----	FL-55	FL-18	f1-6
J316	20% CW	20	FL-34	FL-46	FL-19	f1-7
J316	20% CW	20	FL-35	FL-47	FL-20	f1-8
J316	20% CW	20	FL-36	FL-50	FL-71	f1-9
J316	20% CW	30	FL-37	FL-51	FL-22	FL-10
J316	20% CW	30	FL-38	FL-52	FL-23	f1-11
J316	20% CW	30	----	FL-53	FL-24	f1-12
JPCA	15% CW	10	----	----	TE-29	----
JPCA	(HFIR type)	10	----	----	TE-30	----
JPCA	(HFIR type)	30	----	----	TE-31	----
JPCA	(HFIR type)	30	----	----	TE-32	----
JPCA	25% CW	10	GL-6	----	GL-1	----
JPCA	25% CW	10	GL-7	----	GL-2	----
JPCA	25% CW	10	GL-8	----	----	----
JPCA	25% CW	20	GL-9	----	----	----
JPCA	25% CW	20	GL-10	----	----	----
JPCA	25% CW	20	GL-11	----	----	----
JPCA	25% CW	30	GL-12	----	GL-3	----
JPCA	25% CW	30	GL-13	----	GL-4	----
JPCA	Aged	10	DLA-6	----	LILA-1	----
JPCA	Aged	10	DLA-7	----	DLA-2	----
JPCA	Aged	10	DLA-8	----	----	----
JPCA	Aged	20	DLA-10	----	----	----
JPCA	Aged	20	DLA-11	----	----	----
JPCA	Aged	20	DLA-12	----	----	----
JPCA	Aged	30	DLA-13	----	DLA-3	----
JPCA	Aged	30	DLA-14	----	DLA-4	----
JPCA	SA	10	CL-3	CL-42	CL-7	c1-19
JPCA	SA	10	CL-4	CL-43	CL-8	c1-20
JPCA	SA	10	CL-5	CL-55	CL-9	c1-21
JPCA	SA	10	----	CL-46	CL-10	c1-22
JPCA	SA	10	----	CL-47	CL-11	c1-23
JPCA	SA	10	----	CL-48	CL-12	CL-24

Table 2.4.6. (continued).

Alloy	Condition	dpa	Specimen identification			
			60°C	200°C	330°C	400°C
JPCA	SA	20	CL-36	CL-49	CL-13	c1-25
JPCA	SA	20	CL-38	CL-50	CL-14	c1-26
JPCA	SA	20	CL-39	CL-51	CL-15	c1-27
JPCA	SA	30	CL-40	CL-52	CL-16	CL-28
JPCA	SA	30	CL-41	CL-53	CL-17	c1-29
JPCA	SA	30	----	CL-54	CL-18	c1-30
316 SS	SA	10	EL-33	EL-43	EL-I	EL-14
316 SS	SA	10	EL-34	EL-44	EL-2	e1-15
316 SS	SA	10	EL-36	EL-46	EL-3	e1-16
316 SS	SA	10	----	EL-47	EL-4	e1-17
316 SS	SA	10	----	EL-48	EL-5	EL-18
316 SS	SA	10	----	EL-49	EL-6	e1-19
316 SS	SA	20	EL-37	EL-50	EL-7	e1-20
316 SS	SA	20	EL-38	EL-51	EL-8	e1-21
316 SS	SA	20	EL-39	EL-52	EL-9	e1-22
316 SS	SA	30	EL-40	EL-53	EL-IO	e1-23
316 SS	SA	30	EL-41	EL-54	EL-11	e1-24
316 SS	SA	30	----	EL-55	EL-12	e1-25
316 SS	SA	30	16	24	24	24
J316	SAR	10	HL-6	HL-8	HL-1	h1-3
J316	SAR	10	HL-7	HL-9	HL-2	h1-4
Dual Phase (K)	SA	10	IL-6	IL-8	IL-I	11-3
	SA	10	IL-7	IL-9	IL-2	11-4
All Martensite Heat Tr.		10	ML-6	----	ML-1	m1-3
All Martensite Heat Tr.		lo	ML-7	----	ML-2	m1-4
J316	SA, TIG (W.J.)	10	ELW-1	ELW-3	----	----
J316	SA, TIG (W.J.)	10	ELW-2	----	----	----
5316	CW, TIG (W.J.)	10	FLW-1	FLW-7	----	----
5316	CW, TIG (W.J.)	10	FLW-6	----	----	----
J316	SA, EB (W.J.)	10	JL-6	JL-8	JL-1	j1-3
J316	SA. EB (W.J.)	10	JL-7	JL-9	JL-2	j1-4
J316	SA, TIG (Depo)	10	D-29	----	9-17	0-23
5316	SA, TIG (Depo)	10	D-30	----	D-19	D-24
J316	CW, TIG (Depo)	10	0-57	----	D-49	D-53
J316	CW, TIG (Depo)	10	D-58	----	D-50	D-54
JPCA	SA, TIG (Depo)	10	CLW-13	CLW-18	CLW-5	c1w-9
JPCA	SA, TIG (Depo)	10	CLW-14	----	CLW-6	CLW-10
JPCA	SA, TIG (Depo)	10	CLW-15	----	----	----
JPCA	SA, TIG (Depo)	10	CLW-16	----	----	----
JPCA	SA, EB (W.J.)	10	KL-6	KL-8	KL-I	k1-3
JPCA	SA, EB (W.J.)	10	KL-7	KL-9	KL-2	KL-4

Table 2.4.7. **JAERI fatigue test matrix** in **MFE-6J and -75 capsules**

	Condition	dpa	Specimen identification			
			60°C	200°C	330°C	400°C
JPCA	15% CW	10	GFB-30	GFB-44	GFB-1	GFB-15
JPCA	15% CW	10	GFB-31	GFB-45	GFB-2	GFB-16
JPCA	15% CW	in	GFB-32	-----	GFB-3	GFB-17
JPCA	15% CW	10	GFB-33	-----	GFB-4	GFB-18
JPCA	15% CW	10	GFB-34	-----	GFB-5	GFB-19
JPCA	15% CW	10	GFB-35	-----	GFB-6	GFB-20
JPCA	15% CW	20	GFE-36	GFB-46	GFB-7	GFB-21
JPCA	15% CW	20	GFB-37	GFE-47	GFB-8	GFB-22
JPCA	15% CW	20	GFE-38	-----	GFB-9	-----
JPCA	15% CW	20	GFB-39	-----	GFB-10	-----
JPCA	15% CW	30	GFB-40	GFB-48	GFB-11	GFB-23
JPCA	15% CW	30	GFB-41	GFB-49	GFB-12	GFB-24
JPCA	15% CW	30	GFB-42	-----	GFB-13	-----
JPCA	15% CW	30	GFB-43	-----	GFB-14	-----
JPCA	15% CW	10	-----	-----	-----	FE-9[a]
JPCA	15% CW	10	-----	-----	-----	FE-17[a]
JPCA	15% CW	10	-----	-----	-----	FE-18[a]
JPCA	155 CW	30	-----	-----	-----	FE-19[a]
JPCA	15% CW	30	-----	-----	-----	FE-31[a]
JPCA	SA	10	GFA-30	GFA-44	GFA-1	GFA-15
JPCA	SA	in	GFA-31	GFA-45	GFA-2	GFA-16
JPCA	SA	10	GFA-32	-----	GFA-3	GFA-17
JPCA	SA	10	GFA-33	-----	GFA-4	GFA-18
JPCA	SA	in	GFA-34	-----	GFA-5	GFA-19
JPCA	SA	10	GFA-35	-----	GFA-6	GFA-20
JPCA	SA	20	GFA-36	GFA-46	GFA-7	GFA-21
JPCA	SA	20	GFA-37	GFA-47	GFA-8	GFA-22
JPCA	SA	20	GFA-38	-----	GFA-9	-----
JPCA	SA	20	GFA-39	-----	GFA-10	-----
JPCA	SA	30	GFA-40	GFA-48	GFA-11	GFA-23
JPCA	SA	30	GFA-41	GFA-49	GFA-12	GFA-24
JPCA	SA	30	GFA-42	-----	GFA-13	-----
JPCA	SA	30	GFA-43	-----	GFA-14	-----
J316	20% CW	10	GFD-30	GFD-44	GFD-1	GFD-15
J316	20% CW	10	GFD-31	GFO-45	GFD-2	GFD-lh
J316	20% CW	10	GFD-32	-----	GFO-3	GFD-17
5316	20% CU	10	GFD-33	-----	GFD-4	GFD-18
J316	20% CW	10	GFD-34	-----	GFD-5	GFD-19
J316	20" CW	in	GFD-35	-----	GFD-6	GFD-20
J316	20% CW	20	GFD-36	GFD-46	GFD-7	GFD-21
J316	20% CW	20	GFD-37	GFD-48	GFD-8	GFD-22
J316	20% CW	20	GFD-38	-----	GFD-9	-----
J316	20% CW	20	GFD-39	-----	GFD-10	-----
J316	20" CW	30	GFD-40	GFD-49	GFD-11	GFD-23
J316	20% CW	30	GFD-41	GFD-50	GFD-12	GFD-24
3316	20% CW	30	GFD-42	-----	GFD-13	-----
3316	20% CW	30	GFD-43	-----	GFD-14	-----
J316	SA	10	GFC-30	GFC-44	GFC-1	GFC-15
J316	SA	10	GFC-31	GFC-45	GFC-2	GFC-16
3316	SA	in	GFC-32	-----	GFC-3	GFC-17
J316	SA	10	GFC-33	-----	GFC-4	GFC-18
J316	SA	10	GFC-34	-----	GFC-5	GFC-19
J316	SA	10	GFC-35	-----	GFC-6	GFC-20
5316	SA	20	GFC-36	GFC-46	GFC-7	GFC-21
J316	SA	20	GFC-37	GFC-47	GFC-8	GFC-22
J316	SA	20	GFC-38	-----	GFC-9	-----
J316	SA	20	GFC-39	-----	GFC-10	-----
J316	SA	30	GFC-40	GFC-48	GFC-11	GFC-23
J316	SA	30	GFD-41	GFC-49	GFC-12	GFC-24
J316	SA	30	GFC-42	-----	GFC-13	-----
J316	SA	30	GFC-43	-----	GFC-14	-----

[a]Hourglass; all others **Grodzinski.**

2.4.4.4 Crack-Growth Specimens

The MFE-6J and -7J capsules contain crack-growth specimens from HEDL and JAERI. The specimen configuration is given in Fig. 2.4.7 and the test matrix is shown in Tables 2.4.8 and 2.4.9. The specimen width shown in Fig. 2.4.7 does not apply for specimens being irradiated at 200°C. As a result of capsule design restraints, the width of these specimens is 10.16 mm. At all other temperatures the specimen width is 12.70 mm as shown.

Table 2.4.8. Test matrix of HEDL crack-growth specimens in MFE-6J capsule

Alloy	Condition	dpa	Specimen identification	
			60°C	200°C
316 SS	20% CW	10	AH-01	AH-17
316 SS	20% CW	10	AH-02	AH-18
316 SS	20% CW	10	AH-03	--
316 SS	20% CW	20	AH-04	AH-19
316 SS	20% CW	20	AH-05	AH-20
316 SS	20% CW	20	AH-08	--
316 SS	20% CW	30	AH-09	AH-24
316 SS	20% CW	30	AH-14	AH-25
316 SS	20% CW	30	AH-15	--
PCA	25% CW	10	AT-01	AT-27
PCA	25% CW	10	AT-05	AT-28
PCA	25% CW	10	AT-07	AT-31
PCA	25% CW	20	AT-15	AT-32
PCA	25% CW	20	AT-16	AT-33
PCA	25% CW	20	AT-17	AT-36
PCA	25% CW	30	AT-19	AT-38
PCA	25% CW	30	AT-20	AT-39
PCA	25% CW	30	AT-24	--
HT-9	Tempered Martensite	30	--	EH-01
		30	--	EH-03
		30	--	EH-09

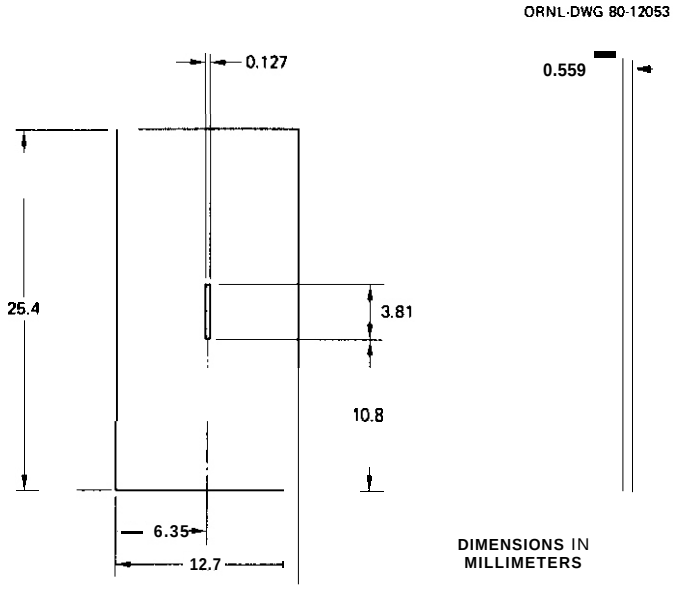

Fig. 2.4.7. Crack-growth specimen. Tabs are welded along the 25.4-mm edge following irradiation.

Table 2.4.9. Description of JAERI crack-growth specimens in MFE-6J and -7J capsules

Alloy	Condition	dpa	Specimen identification			
			60°C	200°C	330°C	400°C
JPCA	15% CW	10	CGE-6	CGD-1	CGB-1	CGE-3
JPCA	15% CW	10	CGE-7	CGD-2	CGB-2	CGB-4
JPCA	15% CW	10	CGE-8	CGD-3	----	----
JPCA	15% CW	10	CGB-9	CGD-4	----	----
JPCA	15% CW	10	CGB-10	CGD-5	----	----
JPCA	15% CW	10	CGE-11	CGD-6	----	----
JPCA	SA	10	CGA-8	CGC-1	CGA-1	CGA-4
JPCA	SA	10	CGA-9	CGC-2	CGA-2	CGA-5
JPCA	SA	10	CGA-10	CGC-3	CGA-3	CGA-6
JPCA	SA	10	CGA-11	CGC-5	----	----
J316	20% CW	10	CGF-6	CGH-1	CGF-1	CGF-3
J316	20% CW	10	CGF-7	CGH-2	CGF-2	CGF-4
J316	20% CW	10	CGF-8	CGH-3	----	----
J316	20% CW	10	CGF-9	CGH-4	----	----
J316	SA	10	CGE-8	CGG-1	CGE-1	CGE-4
J316	SA	10	CGE-9	CGG-2	CGE-2	CGE-5
J316	SA	10	CGE-10	CGG-4	CGE-3	CGE-6
J316	SA	10	CGE-11	CGG-5	----	----

2.4.4.5 TEM Disks

Transmission electron microscopy (TEM) disks are coin-shaped specimens 3 mm in diameter by 0.25-mm thick, which are stacked as tightly as possible into tubular holders with inner diameters of 3.35 to 3.45 mm. These holders were made of type 6061 aluminum for MFE-6J and of type 304 stainless steel for the MFE-7J capsules. For purposes of identification and due to the limits of space availability, TEM tube holders were of several different lengths, shown in Table 2.4.10. As is also shown, disk packets are scheduled for removal at 10-, 20-, and 30-dpa levels. The ORNL TEM test matrix is given in Table 2.4.11 and the HEDL TEM test matrix is given in Tables 2.4.12 and 2.4.13. The JAERI test matrix consists of engineering, alloys (Table 2.4.14) and base research alloys (Table 2.4.15).

Table 2.4.10. Test matrix of TEM disk packets in MFE-6J and -7J capsules

Source	Length (in.)	Holder material	dpa	Specimen identification			
				60°C	200°C	330°C	400°C
ORNL	0.65	Al	10	A	D	--	--
ORNL	0.65	Al	20	B	E	--	--
ORNL	0.65	Al	30	C	F	--	--
ORNL	0.50	Al	10	H	I	--	--
JAERI	1.00	Al	10	J1	J6	--	--
JAERI	1.00	Al	10	J2	J7	--	--
JAERI	1.00	Al	10	J3	J8	--	--
JAERI	1.00	Al	10	--	J9	--	--
JAERI	1.00	Al	10	--	J10	--	--
JAERI	1.00	Al	30	J4	J11	--	--
JAERI	1.00	Al	30	J5	J12	--	--
JAERI	1.00	SS	10	--	--	JP1	JP7
JAERI	1.00	SS	10	--	--	JP2	JPB
JAERI	1.00	SS	10	--	--	JP3	JP9
JAERI	1.00	SS	10	--	--	JP4	JP10
JAERI	1.00	SS	30	--	--	JP5	JP11
JAERI	1.00	SS	30	--	--	JP6	JP12
ORNL	0.75	SS	10	--	--	4	D
ORNL	0.75	SS	20	--	--	B	E
ORNL	0.75	SS	30	--	--	C	F
ORNL	0.75	SS	10	--	--	G	K
ORNL	0.75	SS	10	--	--	H	L
ORNL	0.75	SS	10	--	--	I	M
ORNL	0.75	SS	10	--	--	J	N
ORNL	0.75	SS	10	--	--	--	(Blank)
ORNL	0.50	SS	10	--	--	A	B
HEDL	0.75	SS	10	--	--	LB	LH
HEDL	0.75	SS	10	--	--	LB1	LH2
HEDL	0.75	SS	20	--	--	LE	LK
HEDL	0.75	SS	30	--	--	LF	LL

Table 2.4.11. ORNL TEM matrix for MFE-6J and -7J capsules

Alloy	Condition	Specimen identification in tube											
		MFE						MFE 7J					
		60°C			200°C			330 C			400 C		
		A	B	C	D	E	F	A	B	C	D	E	F
		(10 dpa)	(20 dpa)	(30 dpa)	(10 dpa)	(20 dpa)	(30 dpa)	(10 dpa)	(20 dpa)	(30 dpa)	(10 dpa)	(20 dpa)	(30 dpa)
PCA	25% CW	EC-101	EC-105	EC-108	EC-112	EC-115	EC-118	EC-01	EC-05	EC-09	EC-15	EC-27	EC-31
PCA	25% CW	EC-103	EC-107	EC-110	EC-114	EC-116	EC-119	EC-03	EC-07	EC-14	EC-25	EC-29	EC-34
HT-9	*a*	SA-25	SA-27	SA-29	SA-31	SA-33	SA-35	SA-37	SA-39	SA-41	SA-43	SA-45	SA-47
HT-9	*a*	SA-26	SA-28	SA-30	SA-32	SA-34	SA-36	SA-38	SA-40	SA-42	SA-44	SA-46	SA-48
1B	SA	1B-01	1B-03	1B-05	1B-07	1B-09	1B-11	1B-13	1B-15	1B-17	1B-19	1B-21	1B-23
1B	SA	1B-02	1B-04	1B-06	1B-08	1B-10	1B-12	1B-14	1B-16	1B-18	1B-20	1B-22	1B-24
2B	SA	2B-01	2B-03	2B-05	2B-07	2B-09	2B-11	2B-13	2B-15	2B-17	2B-19	2B-21	2B-23
2B	SA	2B-02	2B-04	2B-06	2B-08	2B-10	2B-12	2B-14	2B-16	2B-18	2B-20	2B-22	2B-24
3B	SA	3B-01	3B-03	3B-05	3B-07	3B-09	3B-11	3B-13	3B-15	3B-17	3B-19	3B-21	3B-23
SA	SA	3B-02	3B-04	3B-06	3B-08	3B-10	3B-12	3B-14	3B-16	3B-18	3B-20	3B-22	3B-24
SA	SA	S1-A9	S2-A2	SA-A4	S2-A6	S2-A8	S3-A1	S3-A4	S3-A6	S3-A8	S4-A0	S4-A2	S4-A4
SA	SA	S2-A0	S2-A3	S2-A5	S2-A7	S2-A9	S3-A3	S3-A5	S3-A7	S3-A9	S4-A1	S4-A3	S4-A5
B1	SA	B1-01	B1-03	B1-05	B1-07	B1-09	B1-11	B1-13	B1-15	B1-17	B1-19	B1-21	B1-23
B1	SA	B1-02	B1-04	B1-06	B1-08	B1-10	B1-12	B1-14	B1-16	B1-18	B1-20	B1-22	B1-24
B2	SA	B2-01	B2-03	B2-05	B2-07	B2-09	B2-11	B2-13	B2-15	B2-17	B2-19	B2-21	B2-23
B2	SA	B2-02	B2-04	B2-06	B2-08	B2-10	B2-12	B2-14	B2-16	B2-18	B2-20	B2-22	B2-24
B3	SA	B3-01	B3-03	B3-05	B3-07	B3-09	B3-11	B3-13	B3-15	B3-17	B3-19	B3-21	B3-23
B3	SA	B3-02	B3-04	B3-06	B3-08	B3-10	B3-12	B3-14	B3-16	B3-18	B3-20	B3-22	B3-24
B5	SA	B5-01	B5-03	B5-05	----	----	----	B5-07	B5-09	B5-11	B5-13	B5-15	B5-17
B5	SA	B5-02	B5-04	B5-06	----	----	----	B5-08	B5-10	B5-12	B5-14	B5-16	B5-18
B10	SA	BA-01	BA-03	BA-05	----	----	----	BA-07	BA-09	BA-11	BA-13	BA-15	BA-17
B10	SA	BA-02	BA-04	BA-06	----	----	----	BA-08	BA-10	BA-12	BA-14	BA-16	BA-18
B11	SA	BB-01	BB-03	BB-05	BB-07	BB-09	BB-11	BB-13	BB-15	BB-17	BB-19	BB-21	BB-23
B11	SA	BB-02	BB-04	BB-06	BB-08	BB-10	BB-12	BB-14	BB-16	BB-18	BB-20	BB-22	BB-24
M1	SA	M1-01	M1-03	M1-05	M1-07	M1-09	M1-11	M1-13	M1-15	M1-17	M1-19	M1-21	M1-23
M1	SA	M1-02	M1-04	M1-06	M1-08	M1-10	M1-12	M1-14	M1-16	M1-18	M1-20	M1-22	M1-24
M3	SA	M3-01	M3-03	M3-05	M3-07	M3-09	M3-11	M3-13	M3-15	M3-17	M3-19	M3-21	M3-23
M3	SA	M3-02	M3-04	M3-06	M3-08	M3-10	M3-12	M3-14	M3-16	M3-18	M3-20	M3-22	M3-24
M4	SA	M4-01	M4-03	M4-05	----	----	----	M4-07	M4-09	M4-11	M4-13	M4-15	M4-17
M4	SA	M4-02	M4-04	M4-06	----	----	----	M4-08	M4-10	M4-12	M4-14	M4-16	M4-18
M6	SA	M6-01	M6-03	M6-05	M6-07	M6-09	M6-11	M6-13	M6-15	M6-17	M6-19	M6-21	M6-23
M6	SA	M6-02	M6-04	M6-06	M6-08	M6-10	M6-12	M6-14	M6-16	M6-18	M6-20	M6-22	M6-24
M9	SA	M9-01	M9-03	M9-05	----	----	----	M9-07	M9-09	M9-11	M9-13	M9-15	M9-17
M9	SA	M9-02	M9-04	M9-06	----	----	----	M9-08	M9-10	M9-12	M9-14	M9-16	M9-18
M11	SA	MA-01	MA-03	MA-05	----	----	----	MA-07	MA-09	MA-11	MA-13	MA-15	MA-17
M11	SA	MA-02	MA-04	MA-06	----	----	----	MA-08	MA-10	MA-12	MA-14	MA-16	MA-18

Table 2.4.11. (continued).

Alloy	Condition	Specimen identification in tube											
		MFE-6J						MFE-7J					
		60°C			200°C			330°C			400°C		
		A	B	C	D	E	F	A	B	C	D	E	F
		(10 dpa)	(20 dpa)	(30 dpa)	(10 dpa)	(20 dpa)	(30 dpa)	(10 dpa)	(20 dpa)	(30 dpa)	(10 dpa)	(20 dpa)	(30 dpa)
C	SA	----	----	----	X1-C0	X1-C3	X1-C5	X1-C7	X1-C9	X2-C1	X2-C3	X2-C5	X2-C8
C	SA	----	----	----	X1-C2	X1-C4	X1-C6	X1-C8	X2-C0	X2-C2	X2-C4	X2-C6	X2-C9
D	SA	----	----	----	X1-D0	X1-D2	X1-D4	X1-D7	X1-D9	X2-D1	X2-D3	X2-D8	X3-D1
D	SA	----	----	----	X1-D1	X1-D3	X1-D6	X1-D8	X2-D0	X2-D2	X2-D5	X2-D9	X3-D2
E	SA	----	----	----	X1-E0	X1-E2	X1-E4	X1-E6	X1-E8	X2-E0	X2-E2	X2-E4	X2-E6
E	SA	----	----	----	X1-E1	X1-E3	X1-E5	X1-E7	X1-E9	X2-E1	X2-E3	X2-E5	X2-E7
H	SA	----	----	----	X1-H0	X1-H2	X1-H5	X1-H7	X2-H2	X2-H5	X2-H7	X2-H0	X3-H2
H	SA	----	----	----	X1-H1	X1-H3	X1-H6	X2-H0	X2-H4	X2-H6	X2-H8	X3-H1	H3-H3
K	SA	----	----	----	----	----	----	X1-K9	X1-K4	X1-K6	X2-K9	X1-K0	X1-K5
K	SA	----	----	----	----	----	----	X2-K7	X3-K1	X1-K3	X1-K7	X2-K3	X3-K4
L	SA	----	----	----	----	----	----	X2-L0	X2-L6	X2-L9	X1-L7	X3-L2	X1-L1
L	SA	----	----	----	----	----	----	X2-L7	X3-L0	X2-L4	X1-L0	X3-L3	X2-L8
M	SA	----	----	----	X1-M0	X1-M2	X1-M4	X1-M7	X1-M9	X2-M1	X2-M3	X2-M6	X2-M8
M	SA	----	----	----	X1-M1	X1-M3	X1-M5	X1-M8	X2-M0	X2-M2	X2-M4	X2-M7	X2-M9
P	SA	----	----	----	X1-P0	X1-P2	X1-P6	X1-P9	X2-P1	X2-P3	X2-P6	X2-P8	X3-P0
P	SA	----	----	----	X1-P1	X1-P3	X1-P8	X2-P0	X2-P2	X2-P5	X2-P7	X2-P9	X3-P1

[a]Tempered martensite.

Table 2.4.12. HEDL TEM matrix for MFE-6J capsule

Alloy	Condition	Specimen identification					
		60°C			200°C		
		A (10 dpa)	B (20 dpa)	C (30 dpa)	D (10 dpa)	E (20 dpa)	F (30 dpa)
E90	SA	T9L4	T9L5	T9L6	T9L7	T9L9	T9MA
E20	SA	UBL4	UBL5	UBL6	UBL7	UBL9	UBMA
E22	SA	UEL4	UEL5	UEL6	UEL7	UEL9	EUMA
E23	SA	UFL4	UFL5	UFL6	UFL7	UFL9	UFMA
R58	SA	UHL4	UHL5	UHL6	UHL7	UHL9	UHMA
E37	SA	UKL4	UKL5	UKL6	UKL7	UKL9	UKMA
GE5	SA	BBL4	BBL5	BBL6	BBL7	BBL9	BBMA
E38	SA	UNL4	UNL5	UNL6	UNL7	UNL9	UNMA

Table 2.4.13. HEOL TEM matrix for MFE-7J capsule

Alloy	Conditiona	Specimen identification in tube							
		330°C				400°C			
		LB (10 dpa)	LB-1 (10 dpa)	LE (20 dpa)	LF (30 dpa)	LH (10 dpa)	LH-2 (10 dpa)	LK (20 dpa)	LL (30 dpa)
E18	SA	LBT7	LBT7	LET7	LFT7	LHT7	LHT7	LKT7	LLT7
E18	SA	LBT7	LBT7	LET7	LFT7	LHT7	LHT7	LKT7	LLT7
E90	SA	LBT9	LBT9	LET9	LFT9	LHT9	LHT9	LKT7	LLT7
E90	SA	LBT9	LBT9	LET9	LFT9	LHT9	LHT9	LKT9	LLT9
E19	SA	LBUA	LBUA	LEUA	LFUA	LHUA	LHUA	LKUA	LLUA
E19	SA	LBUA	LBUA	LEUA	LFUA	LHUA	LHUA	LKUA	LLUA
E20	SA	LBUB	LBUB	LEUB	LFUB	LHUB	LHUB	LKUB	LLUB
E20	SA	LBUB	LBUB	LEUB	LFUB	LHUB	LHUB	LKUB	LLUB
E22	SA	LBUE	LBUE	LEUE	LFUB	LHUE	LHUE	LKUE	LLUE
E22	SA	LBUE	LBUE	LEUE	LFUE	LHUE	LHUE	LKUE	LLUE
E23	SA	LBUF	LBUF	LEUF	LFUF	LHUF	LHUF	LKUF	LLUF
E23	SA	LBUF	LBUF	LEUF	LFUF	LHUF	LHUF	LKUF	LLUF
R58	SA	LBUH	LBUH	LEUH	LFUH	LHUH	LHUH	LKUH	LLUH
R58	SA	LBUH	LBUH	LEUH	LFUH	LHUH	LHUH	LKUH	LLUH
E37	SA	LBUK	LBUK	LEUK	LFUK	LHUK	LHUK	LKUK	LLUK
E37	SA	LBUK	LBUK	LEUK	LFUK	LHUK	LHUK	LKUJ	LLUK
E37	20% CW	LBBH	LBBH	LEBH	LFBH	LHBH	LHBH	LKBH	LLBH
GE29	SA	LBUM	LBUM	LEUM	LFUM	LHUM	LHUM	LKUM	LLUM
GE29	SA	LBUM	LBUM	LEUM	LFUM	LHUM	LHUM	LKUM	LLUM
R41	SA	LBUO	LBUO	LEUO	LFUO	LHUO	LHUO	LKUO	LLUO
E38	SA	LBUN	LBUN	LEUN	LFUN	LHUN	LHUN	LKUN	LLUN
GEIO	SA	LBBP	LBBP	LEBP	LFBP	LHBP	LHBP	LKBP	LLBP
GEIO	SA	LBBP	LBBP	LEBP	LFBP	LHBP	LHBP	LKBP	LLBP
GE5	SA	LBBB	LBBB	LEBB	LFBB	LHBB	LHBB	LKBB	LLBB
GE5	SA	LBBB	LBBB	LEBB	LFBB	LHBB	LHBB	LKBB	LLBB
R72	SA	LBFE	LBFE	LEFE	LFFE	LHFF	LHFF	LKFF	LLFF
GE26	SA	LBUL	LBUL	LEUL	LFUL	LHUL	LHUL	LKUL	LLUL
GE26	SA	LBUL	LBUL	LEUL	LFUL	LHUL	LHUL	LKUL	LLUL
R4B	SA	LBUP	LBUP	LEUP	LFUP	LHUP	LHUP	LKUP	LLUP
316	SA	LBNB	LBNB	LENB	LFNB	LHNB	LHNB	LKNB	LLNB
R73	SA	LBFK	LBFK	LEFK	LFFK	LHFK	LHFK	LKFK	LLFK
R76	SA	LBUR	LBUR	LEUR	LFUR	LHUR	LHUR	LKUR	LLUR
R83	SA	LBUT	LBUT	LEUT	LFUT	LHUT	LHUT	LKUT	LLUT
R67	SA	LBE4	LBE4	LEE4	LFE4	LHE4	LHE4	LKE4	LLE4
R69	SA	LBE9	LBE9	LEE9	LFE9	LHE9	LHE9	LKE9	LLE9
R70	SA	LBFA	LBFA	LEFA	LFFA	LHFA	LHFA	LKFA	LLFA
R71	SA	LBFB	LBFB	LEFB	LFFB	LHFB	LHFB	LKFB	LLFB
R66	SA	LBE3	LBE3	LEE3	LFE3	LHE3	LHE3	LKE3	LLE3
R74	SA	LBFL	LBFL	LEFL	LFFL	LHFL	LHFL	LKFL	LLFL
R87	SA	LBUU	LBUU	LEUU	LFUU	LHUU	LHUU	LKUO	LLUO
R75	SA	LBFM	LBFM	LEFM	LFFM	LHFM	LHFM	LKFM	LLFM
10998	D	LBPZ	LBPZ	LEPZ	LFPZ	LHPZ	LHPZ	LKPZ	LLPZ
HT-9	B	LBRF	LBRF	LERF	LFRF	LHRF	LHRF	LKRF	LLRF
10996	0	LBPV	LBPV	LEPV	LFPV	LHPV	LHPV	LKPV	LLPV
VO-2263	A	LBP4	LBP4	LEP4	LFP4	LHP4	LHP4	LKP4	LLP4
VO-2262	A	LBP3	LBP3	LEP3	LFP3	LHP3	LHP3	LKP3	LLP3
YO-2264	B	LBP6	LBP6	LEP6	LFP6	LHP6	LHP6	LKP6	LLP6
uc-19	A	LBP5	LBP5	LEP5	LFP5	LHP5	LHP5	LKP5	LLP5
VO-2265	C	LBP7	LBP7	LEP7	LFP7	LHP7	LHP7	LKP7	LLP7
YO-2268	C	LBRB	LBRB	LERB	LFRB	LHRB	LHRB	LKRB	LLRB
VO-2267	C	LBRA	LBRA	LERA	LFRA	LHRA	LHRA	LKRA	LLRA
YO-2269	C	LBRE	LBRE	LERE	LFRE	LHRE	LHRE	LKRE	LLRE
E38	SA	LBUN	LBUN	LEUN	LFUN	LHUN	LHUN	LKUN	LLUN
R41	SA	LBUO	LBUO	LEUO	LFUO	LHUO	LHUO	LKUO	LLUO

Table 2.4.13. (continued).

Alloy	Conditiona	Specimen identification in tube							
		330°C				400°C			
		LB (10 dpa)	LB-1 (10 dpa)	LE (20 dpa)	LF (30 dpa)	LH (10 dpa)	LH-2 (10 dpa)	LK (20 dpa)	LL (30 dpa)
R48	SA	LBUP	LBUP	LEUP	LFUP	LHUP	LHUP	LKUP	LLUP
R72	SA	LBFE	LBFE	LEFE	LFFE	LHFE	LHFE	LKFE	LLFE
R73	SA	LBFK	LBFK	LEFK	LFFK	LHFK	LHFK	LKFK	LLFK
R74	SA	LBFL	LBFL	LEFL	LFFL	LHFL	LHFL	LKFL	LLFL
R76	SA	LBUR	LBUR	LEUR	LFUR	LHUR	LHUR	LKUR	LLUR
R66	SA	LBE3	LBE3	LEE3	LFE3	LHE3	LHE3	LKE3	LLE3
R83	SA	LBUT	LBUT	LEUT	LFUT	LHUT	LHUT	LKUT	LLUT
VO-2266	C	LBP9	LBP9	LEP9	LFP9	LHP9	LHP9	LKP9	LLP9
R67	SA	LBE4	LBE4	LEE4	LFE4	LHE4	LHE4	LKE4	LLE4

[a]SA: 1030°C/30 min/AC. A: 900°C/20 h/WQ + 950°C/20 min/WQ + 650°C/2 h/AC. B: 1000°C/20 h/AC + 1100°C/5 min/AC + 700°C/2 h/AC. C: 1000°C/20 h/AC + 1100°C/10 min/AC + 700°C/2 h/AC. D: 1000°C/20 h/AC + 1100°C/30 min/AC + 700°C/2 h/AC.

Table 2.4.14. JAERI engineering alloy TEM matrix in MFE-6J and -7J capsules

Alloy	Condition	Abbrevidted name	Identification of tuber containing alloys			
			60°C	200°C	330°C	400°C
JPCA	SA 1175°C	PS1	J1, J4	J6, J11	J1, J5	J7, J11
JPCA	SA 1100°C	PS2	J1, J4	J6, J11	J1, J5	J7, J11
JPCA	SA 1050°C	PS3	J1, J4	J6, J11	J1, J5	J7, J11
JPCA	PS2 + 10% CW	PC1	J1, J4	J6, J11	J1, J5	J7, J11
JPCA	PS2 + 20% CW	PC3	J1, J4	J6, J11	J1, J5	J7, J11
C	SA 1100°C	CS1	J1, J4	J6, J11	J1, J5	J7, J11
C	CS1 + 20% CW	CC1	J1, J4	J6, J11	J1, J5	J7, J11
K	SA 1050°C	KS1	J1, J4	J6, J11	J1, J5	J7, J11
K	KS1 + 20% CW	KC1	J1, J4	J6, J11	J1, J5	J7, J11
5316	SA 1050°C	SS1	J1, J4	J6, J11	J1, J5	J7, J11
J316	SS1 + 20% CW	SC1	J1, J4	J6, J11	J1, J5	J7, J11
Aged JPCA	PC3 + 2 h at 800°C	PA1	J1, J4	J6, J11	J1, J5	J7, J11
Aged JPCA	PC3 + 8 h at 800°C	PA2	J2, J4	J7, J12	J2, J6	J8, J12
High Ni Alloy I	SA 1100°C	Ist	J2, J4	J7, J12	J2, J6	J8, J12
High Ni Alloy I	Ist + 3000 h at 700°C	Iag	J2, J4	J7, J12	J2, J6	J8, J12
High Ni Alloy Q	SA 1100°C	Qst	J2, J5	J7, J12	J2, J6	J8, J12
High Ni Alloy q	Qst + 3000 h at 700°C	Qag	J2, J5	J7, J12	J2, J6	J8, J12
Ferritic Steel	SA 1050°C + AC	FD1	J2, J5	J7, J12	J2, J6	J8, J12
Ferritic Steel	FD1 + 1 h at 775°C	FD2	J2, J5	J7, J12	J2, J6	J8, J12
HT-9	SA 1050°C + AC + 1 h at 780°C	F03	J2, J5	J7, J12	J2, J6	J8, J12
J316 TIG weld	Matrix	SW1	J5	J8	J3	J9
J316 TIG weld	HAZ	SW2	J5	J8	J3	J9
J316 TIG weld	Bond	SW3	J5	J8	J3	J9
J316 TIG weld	Deposit	SW4	J5	J8	J3	J9
SAR (type 304)	A[a]	SR1	J2, J5	J7, J12	J2, J6	J8, J12
SAR (type 316)	B[a]	SR2	J2, J5	J7, J12	J2, J6	J8, J12
High Mn 1	SA 1050°C	MS1	J3	J9	J4	J10
High Mn 2	SA 1050°C	MS2	J3	J9	J4	J10
SN 1	SA 1050°C	SA1	----	J7, J12	J2, J6	J8, J12
SN 5	SA 1050°C	DP1	J2, J5	J7, J12	J2, J6	J8, J12
Dual phase A	SA 1050°C	DP2	J3	J8	J3	J9
Dual phase B	SA 1050°C	DP3	J3	J8	J3	J9
Dual phase C	SA 1050°C	DP4	J3	J8	J3	J9
Dual phase D	SA 1100°C	DP5	J3	J8	J3	J9
Dual phase E	SA 1050°C	DP6	J3	J9	J3, J4	J9, J10
Dual phase K	SA 1050°C	DP7	J3	----	J4	J10
Dual phase G	SA + 5 h at 1200°C	DP8	J2	J9	J4	J10
Oual phase I	SA + 4 h at 1200°C	DP9	J2	J9	J4	J10
Dual phase J	SA + 1 h at 1200°C	DP10	J3	J9	J4	J10
All martensite	C[a]	AM1	J4	J9	----	J7, J11
Incoloy 800	SA at 1120°C	IN1	J4	J9	----	J7, J11
HP 12 Ni	SA at 1200°C	HP1	J4	J9	----	J7, J11
HP 35 Ni	SA at 1200°C	HP2	J4	J9	----	J7, J11
HP 50 Ni	SA at 1200°C	HP3	J4	J9	----	J8, J11

[a]A: SA — 1080°C + 50% CW + 15 h at 575°C + 5 h at at 650°C + 5 h at 775°C. C: SA — 1050°C + AC + 1 h at 775°C + AC. 8: SA — 1150°C + 50% CW + 15 h

Table 2.4.15. JAERI basic research TEM test matrix in MFE-6J and -7J capsules

Alloy composition	Condition	Abbreviated name	Identification of tubes containing alloy			
			(60°C)	(200°C)	(330°C)	(400°C)
Fe–0.055C–0.53Si–1.88Mn–0.024P–0.009S–15.27Ni–15.80Cr–2.66Mo–0.24Ti–0.0032B–0.0039N	20% CW	UP1	J3	J10	J4	J10
Fe–0.056C–0.74Si–0.20Mn–0.008P–0.006S–1.37Ni–8.86Cr–2.46Mo–0.06Nb–0.0069N	SA 1050°C + 1 h 775°C	UF1	J3	J10	J4	J10
Fe–22Cr-5.5 Ni–3Mo–0.1N–0.02C	SA 1050°C	UI1	J3	J10	J4	J10
Fe–14.5Cr–16Ni–2.5Mo–0.006N–0.003C	SA 1050°C	UI2	J3	J10	J4	J10
Fe–14.5Cr–16Ni–2.5Mo–0.007N–0.054C	SA 1050°C	UI3	J3	J10	J4	J10
FE-14.5Cr–16Ni–2.5Mo–0.076N–0.061C	SA 1050°C	U14	J3	J10	J4	J10
Fe–16Cr–15Ni–2.5Mo–0.008N–0.001C–0.1P	SA 1050°C	U15	J3	J10	J4	J10
Fe–9Cr–1Mo–0.2Zr–0.05Y	SA 1000°C + 1 h 780°C	UY1	J3	J10	J4	J10
Fe–9Cr–1Mo–0.2Zr–0.2V–0.05Y	SA 1000°C + 1 h 780°C	UY2	J3	J10	J4	J10
Fe–9Cr–2.Mo–0.2Zr–0.2V–0.05Y	SA 1000°C + 1 h 780°C	UY3	J3	J10	J4	J10
Fe–9Cr–2Mo–0.2Zr–0.05Y	SA 1000°C t 1 h 780°C	UY4	J3	J10	J4	J10
Fe–7Cr–1.5Mo–0.2Zr-0.2 V–0.05Y	SA 1000°C t 1 h 780 °C	UY5	J3	J10	J4	J10
Fe–15Cr–16Ni	SA 1050°C	UK1	J3	J10	J4	J10
Fe–15Cr–16Ni–0.25Ti	SA 1050°C	UK2	J3	J10	J4	J10
Fe–15Cr–16Ni–0.25Ti–0.06C	SA 1175°C	UK3	J3	J10	J4	J10
Fe–15Cr–16Ni–0.06C	SA 1050°C	UN1	J3	J10	J4	J10
Fe–15Cr–16Ni–0.2Nb–0.06C	SA 1050°C	UN2	J3	J10	J4	J10
Fe–15Cr–16Ni–0.1Nb–0.06C	SA 1050°C	UN3	J3	J10	J4	J10
Fe	SA	UA1	J3	J10	J4	J10
Ni	SA	UA2	J3	J10	J4	J10
cu	SA	UA3	J3	J10	J4	J10
Au	SA	UA4	J3	J10	J4	J10
Al	SA	UA5	J3	J10	J4	J10
Mo	SA	UA6	J3	J10	J4	J10
Nb	SA	UA7	53	J10	J4	J10
Al–0.1 at. % Si	SA	UB1	53	J10	J4	J10
Cu–0.2Ni	SA	UB2	J3	J10	54	J10
Ni–0.2Cu	SA	UB3	J3	J10	J4	J10
A1-O.l at. % Mg	SA	UB4	J3	J10	J4	J10
Al–0.1 at. % Li	SA	UB5	J3	J10	J4	J10
A1-O.l at. % Mn	SA	UB6	J3	J10	J4	J10
V	SA 1000°C	UTI	J3	J10	J4	J10
V–0.2Ti	SA 1000°C	UT2	J3	J10	J4	J10
Fe–31Ni–3Ti	SA 1000°C	UU1	J3	J10	J4	J10

2.4.5 References

1. J. L. Scott et al., "Description of the U.S./Japan Spectral Tailoring Experiment in ORR," pp. 12–19 in *ADIP Semiannu. Prog. Rep. March 31, 1985*, DOE/ER-0045/14, U.S. DOE, Office of Fusion Energy.

2. M. L. Grossbeck and K. R. Thorns, "ORR-MFE-4: A Spectral Tailoring Experiment to Simulate the He/dpa Ratio of a Fusion Reactor in Austenitic Stainless Steel," pp. 10–23 in *ADIP Quart. Prog. Rep. June 30, 1980*, DOE/ER-0045/3, U.S. DOE, Office of Fusion Energy.

3. M. L. Grossbeck, "Irradiation Creep in Path A Alloys Irradiated to 5 dpa in the ORR-MFE-4A Spectral Tailoring Experiment," pp. 38-43 in *ADIP Semiannu. Prog. Rep. sept. 30, 1982*, DOE/ER-0045/9, U.S. DOE, Office of Fusion Energy.

4. E. R. Gilbert and B. A. Chin, "In-Reactor Creep Measurements," *Nucl. Technol.* 52, 273–83 (1981).

5. K. Ehrlich, "Irradiation Creep in Austenitic Stainless Steels," pp. 149–56 in *Mechanical Behavior and Nuclear Applications* of *Stainless Steel at Elevated Temperatures,* The Metals Society, London, 1982.

2.5 ASSEMBLY AND OPERATION OF THE U.S./JAPAN SPECTRAL TAILORING EXPERIMENTS - I. I. Siman-Tov (Oak Ridge National Laboratory)

2.5.1 AOIP Task

ADIP Task I.A.2, Define Test Matrices and Test Procedures.

2.5.2 Objectives

The experiments in the U.S./Japan collaborative testing program for the ORR irradiate austenitic stainless steel candidate alloys for use at first-wall and blanket structural materials in fusion reactors. These alloys will be irradiated with mixed-spectrum neutrons and with spectral tailoring to achieve helium-to-displacement-per-atom (He/dpa) ratios predicted for fusion reactor service.

2.5.3 Summary

MFE-6J and -7J started irradiation in the ORR with cycle 172F on June 28, 1985. The total accumulated power through September 30, 1985 is 72.81 d at 30 MW.

2.5.4 Progress and Status

The details of the U.S./Japan collaborative irradiation program have been described previously.[1-3]

ORR-MFE-6J: Assembly of the capsule and the facility preparation were completed one cycle ahead of schedule. The experiment was installed in the ORR on June 27, 1985, and started irradiation on June 28.

ORR-MFE-7J: This capsule was inserted also on June 27, 1985, three cycles past the original scheduled insertion cycle because of some major difficulties encountered during assembly.

The assembly of the outer and inner tube3 may have caused minor delay in the insertion date; however, a problem with a leak that developed in the very last stage of assembly in the primary bulkhead was the major cause of the delay in the insertion date. As a result of repairing the leak, two thermocouples were lost: TE2 measuring the temperature in the middle of the 330°C region and TE6 at the bottom of the 400°C region. We were granted special permission to operate the capsule with the remaining minute leak in the primary bulkhead. However, some I&C changes had to be incorporated into the facility to satisfy safety requirements for the NaK system. At present no leak is observed in the primary region.

At startup the temperatures stabilized at 299°C in the 330°C region and at 380°C in the 400°C region with a control gas composition of 100% helium. The top region of the first cycle was not heated to 330°C to be able to observe the temperature fluctuations during the cycle due to control rod movements and the effect of the presence of the HSST experiments in the production support facility. In the second cycle (1726) the average temperature of the 330°C region was 329.1°C and 394.5°C in the 400°C region. Observing the temperature gradients in the 330 and 400°C regions, it was noted that there is an overlap of temperatures since in the 330°C region there was practically no gradient, while in the 400°C region there was a gradient of 10°C/cm. It was then decided to change the operating temperature of the 400°C region to an average of 400°C instead of a maximum of 400°C. This change was initiated in cycle 173B starting on September 20, 1985.

The capsule now operates with a maximum temperature of 330°C in the upper region and an average temperature of 400°C in the lower region. The controlling thermocouples are TE3 in the top region (or TE1, whichever reads the maximum temperature in the region) and TE5 in the lower region since it is located in the middle of the region.

2.5.5 References

1. J. A. Conlin and J. W. Woods, "Irradiation Experiments for the U.S./Japan Collaborative Testing in HFIR and ORR," p. 37 in *ADIP Semiannu. Frog. Rep. Mar. 31, 1984,* DOE/ER-0045/12, U.S. DOE, Office of Fusion Energy.

2. J. A. Conlin and J. W. Woods, "Irradiation Experiments for the U.S./Japan Collaborative Testing in HFIR and ORR," pp. 66–67 in *ADIP Semiannu. Frog. Rep. Sept. 30, 1984,* DOE/ER-0045/13, U.S. DOE, Office of Fusion Energy.

3. I. I. Siman-Tov, J. A. Conlin, and J. W. Woods, "Irradiation Experiments for the U.S./Japan Collaborative Testing in HFIR and ORR," p. 6 in *ADIP Semiannu. Frog. Rep. Mar. 31, 1985*, DOE/ER-0045/14, U.S. DOE, Office of Fusion Energy.

2.6 NEUTRONIC8 ANALYSIS IN SUPPORT OF THE U.S. JAPAN SPECTRAL TAILORING CAPSULES — R. A. Lillie (Oak Ridge National Laboratory)

2.6.1 ADIP Task

ADIP Task 1.A.2, Define Test Matrices and Test Procedures.

2.6.2 Objective

The objective of this work is to provide the neutronic design for materials irradiation experiments in the Oak Ridge Research Reactor (ORR). Spectral tailoring to control the fast and thermal fluxes is required to provide the desired displacement and helium production rates in alloys containing nickel.

2.6.3 Summary

The neutron fluxes calculated and measured' for the ORR-MFE-6J dosimetry capsule have been compared. Scale factors obtained from this comparison are being used to scale the neutron fluences obtained from three-dimensional neutronics calculations. As of September 30, 1985, this procedure yields 3.15 at. ppm He (not including 20 at. ppm He from ^{10}B) and 1.22 dpa for type 316 stainless steel in ORR-MFE-6J and 4.44 at. ppm He and 1.71 dpa in ORR-MFE-7J.

2.6.4 Progress and Status

A comparison of the measured and calculated data for the ORR-MFE-6J dosimetry capsule is presented in Table 2.6.1. This capsule was in the ORR from September 6, 1984, to January 20, 1985, and received *82,096* MWh of exposure. The calculated total flux is approximately 16% higher than the measured total flux whereas the calculated thermal flux is only 2% higher than the measured thermal flux. Almost all of the difference in total flux is attributed to the difference in fast flux (i.e., the flux above 0.1 MeV). These differences in calculated and measured fluxes are very similar to the differences obtained in the ORR-MFE-4 experimental irradiations.

Table 2.6.1. Comparison of calculated and measured data for the ORR-MFE-6J dosimetry capsule

	Calculated	Experimental[a]	C/E[b]
Flux (> 0.1 MeV), neutrons/m^2/s	2.40 + 18[c]	2.03 + 18	1.18
Total flux, neutrons/m^2/s	6.93 t 18	5.99 + 18	1.16
Thermal flux, neutrons/m^2/s	2.01 + 18	1.97 + 18	1.02
Nickel, dpa			
Fast	1.84	1.59	1.16
Thermal	0.07	0.10	0.70
Total	1.91	1.69	1.13
Nickel-Helium, at. ppm			
Fast	8.06	7.34	1.10
Thermal	40.9	56.0	0.73
Total	49.0	63.4	0.77
316 stainless steel			
dpa	1.82	1.56	1.17
He, at. ppm	6.98	8.63	0.81
Total fluence, neutrons/m^2/s	6.83 + 25	5.90 + 25	1.16
Thermal fluence, neutrons/m^2/s	1.98 + 25	1.94 t 25	1.02

[a] See ref. 1.

[b] C/E represents the calculated to experimental ratio.

[c] 2.40 t 18 is read as 2.40 × 10^{18}.

The ratio between the calculated and measured dpa level in both the nickel and stainless steel 316 specimens is essentially identical to the ratio of the calculated and measured total fluxes. The ratio between the fast neutron helium productions in nickel is slightly lower than the ratio of fast fluxes, thus indicating the use of a slightly different-helium production *cross* section by the dosimetry evaluator, L. R. Greenwood, of Argonne National Laboratory. The rather drastic difference in thermal neutron helium production levels in nickel (and in the 316 stainless steel) specimens is unexplained at the present time, especially in view of the excellent agreement between the calculated and measured thermal fluxes.

The operating and current calculated data based on the fluence scaling factors obtained from the comparison between the calculated and measured data for ORR-MFE-6J dosimetry capsule are summarized in Table 2.6.2 for the ORR-MFE-6J and -7J experiments. Both experimental capsules went into the ORR on June 28, 1985, and both capsules have been exposed to 52,420 MWh. Also presented for comparison are the unscaled fluences and the helium production and dpa levels obtained with these unscaled fluences. At the present time, the dpa rate based on the scaled total fluences is 6.11 and 7.40 dpa per full power year for the ORR-MFE-6J and -7J experiments, respectively. The greater dpa rate in the ORR-MFE-7J experiment is due to its being in core position C3, whereas the ORR-MFE-6J experiment is in core position C7.

The real-time projections of the helium-to-displacement ratios based on current calculated data as of September 30, 1985, are presented in Figs. 2.6.1 and 2.6.2 for the ORR-MFE-6J and -7J experiments, respectively. As with the ORR-MFE-4A and -4B experiments, the projected dates were obtained assuming an ORR duty factor of 0.86. Real-time projections obtained with both the scaled and unscaled fluences are given.

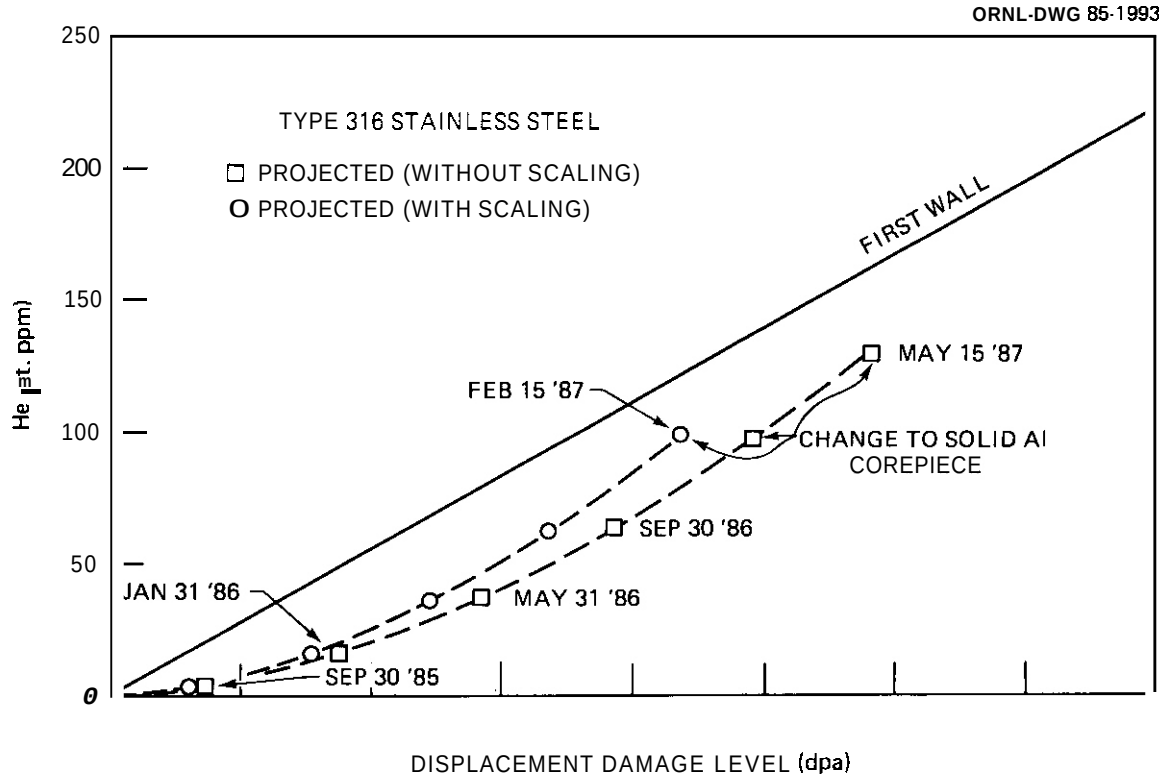

Fig. 2.6.1. Current and projected helium and displacement damage levels in the ORR-MFE-6J experiment.

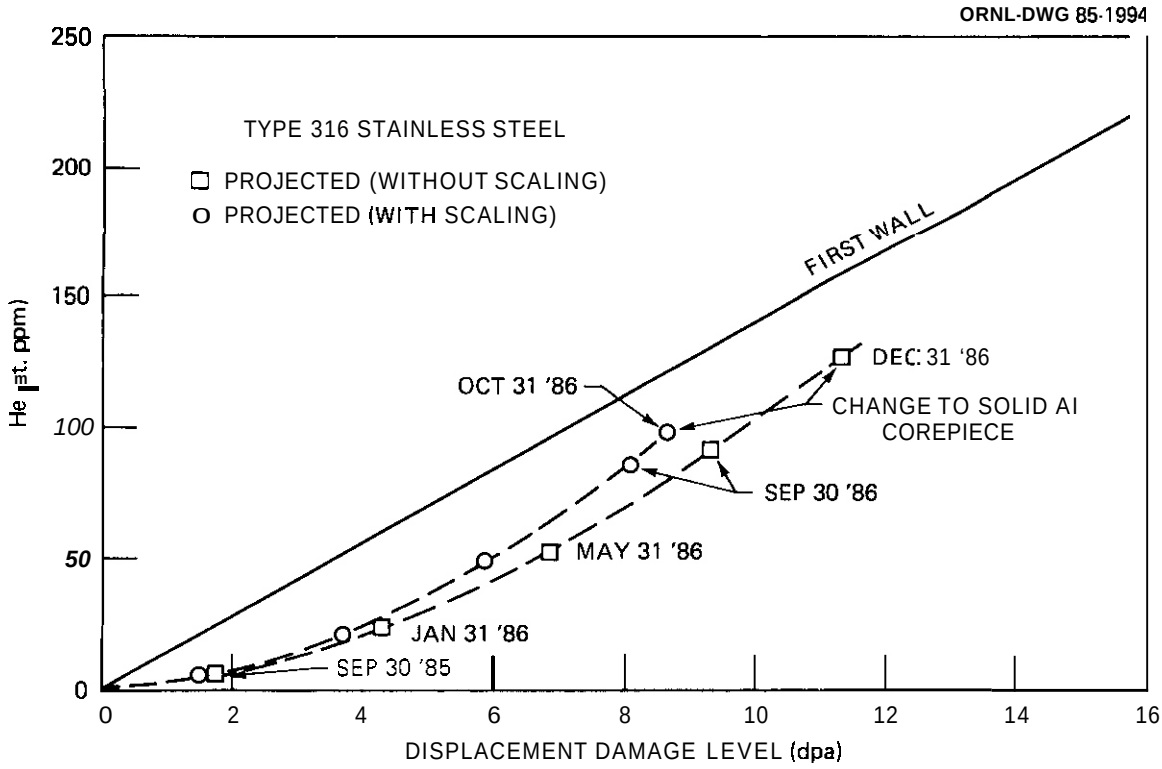

Fig. 2.6.2. Current and projected helium and displacement damage levels in the ORR-MFE-7J experiment.

Because the calculated-to-measured total fluence ratio is much greater than the calculated-to-measured thermal fluence ratio, scaling decreases the dpa rate much more than the helium production rate. Thus, scaling reduces the time to insertion of the solid aluminum core piece.

2.6.5 Future Work

The three-dimensional neutronics calculations that monitor the radiation environment of the ORR-MFE-63 and -73 experiments will continue with each ORR cycle. The scale factors used to scale the calculated fluences will be updated as new experimental data become available. In addition, the rather large discrepancy between the helium production predicted due to the calculated and measured thermal fluences will be resolved.

2.6.6 Reference

1. L. R Greenwood, "Neutron Dosimetry and Damage Calculations for ORR-6J Test, HFIR-RB-Hafnium Test, and HFIR-RB-1 and RB-2 Experiments," Sect. 2.1, this report.

Table 2.6.2. Operating and calculated data for the ORR-MFE-6J and -7J experimental capsules as of September 30, 1985

	ORR-MFE-6J	ORR-MFE-7J
Insertion date	6/28/85	6/28/85
Exposure, MWh	52,419.8	52,419.8
Equivalent full power days[a]	72.8	72.8
Thermal fluence, neutrons/m^2	1.46 + 25[b]	1.76 + 25
	(1.48 + 25)[c]	(1.80 + 25)
Total fluence, neutrons/m^2	5.03 + 25	6.08 + 25
	(5.82 + 25)	(7.04 + 25)
Helium,		
at. ppm[d]	3.15 (3.39)	4.44 (4.82)
dpa[d]	1.22 (1.41)	1.48 (1.71)

[a] Full power for ORR is 30 MW.

[b] 1.46 + 25 is read as 1.48×10^{25}.

[c] Values in parentheses represent unscaled fluences or values calculated using unscaled fluences.

[d] Helium and dpa values are for type 316 stainless steel.

2.7 NEUTRONICS CALCULATIONS IN SUPPORT OF THE ORR-MFE-4A AND -48 SPECTRAL TAILORING EXPERIMENTS — R. A. Lillie (Oak Ridge National Laboratory)

2.7.1 AOIP Task

ADIP Task 1.A.2, Define Test Matrices and Test Procedures.

2.7.2 Objective

The objective of this work is to provide the neutronic design for materials irradiation experiments in the Oak Ridge Research Reactor (ORR). Spectral tailoring to control the fast and thermal fluxes is required to provide the desired displacement and helium production rates in alloys containing nickel.

2.7.3 *Summary*

The final operating and calculated data for the ORR-MFE-4A and -4B experiments have been obtained. The scaled calculated fluences yield 201.9 at. ppm He (not including 2.0 at. ppm He from ^{10}B) and 13.19 dpa for type 316 stainless steel in ORR-MFE-4A and 172.4 at. ppm He and 11.64 dpa in ORR-MFE-4B.

2.7.4 Progress and Status

The final operating and calculated data for the ORR-MFE-4A and -48 experiments are summarized in Tables 2.7.1 and 2.7.2. The calculated data for the Al-H_2O and solid aluminum core pieces are based on the fluence scaling factors given previously.' The calculated data for the hafnium core piece (the same hafnium core piece was used in both experimental capsules) are based on these same scaling factors folded with experimentally measured hafnium-induced fluence reductions also previously reported.2

The ORR-MFE-4A experiment was removed from the ORR on January 20, 1985, and the ORR-MFE-4B experiment was removed on June 10, 1985. The data are presented for each core piece. The final entry in each table indicates the "closeness" of the experimental helium to dpa ratio to that expected in a fusion device first wall. At the time of their removal from the reactor, the helium to dpa ratios were approximately 9.6% and 6.0% higher in the ORR-MFE-4A and -4B experiments, respectively, than those expected in a first wall.

Table 2.7.1. Final operating and calculated data for the ORR-MFE-4A experiment

Core piece	Al-H_2O	Al	Hf	Total
Exposure, MWh	337,332	277,476	160,124	774,932
Full power days[a]	468.5	385.4	222.4	1076.3
Thermal fluence, neutrons/m^2	8.39 + 25b	4.57 + 25	1.64 + 25	1.46 + 26
Total fluence, neutrons/m^2	2.21 + 26	2.20 + 26	1.04 + 26	5.45 + 26
Helium,				
at. ppm[c]	76.7	87.8	37.4	201.9
dpa	5.35	5.35	2.49	13.19
Ratio[d]	1.026	1.175	1.075	1.096

[a]Full power for ORR is 30 MW.

[b]8.39 + 25 is read as 8.39 × 10^{25}.

[c]He values represent the difference in helium values at the end of the current core piece and the previous core piece since helium production is dominated by the cumulative thermal fluence and not by the thermal fluence seen by a particular core piece.

[d]Ratio represents the experimental helium-dpa value divided by the calculated fusion device first wall value of 13.97.

Table 2.1.2. Final operating and calculated data for the ORR-MFE-4B experiment

Core piece	Al-H_2O	Al	Hf	Total
Exposure, MWh	305,355	324,432	87,800	717,587
Full power days[a]	424.1	450.6	122.0	996.6
Thermal fluence, neutrons/m^2	7.30 t 25b	5.02 + 25	9.80 + 24	1.33 + 26
Total fluence, neutrons/m^2	1.86 + 26	2.38 + 26	5.36 + 25	4.78 + 26
Helium,				
at. ppm[c]	59.7	91.4	21.3	172.4
dpa	4.49	5.79	1.36	11.64
Ratio[d]	0.952	1.130	1.121	1.060

[a]Full power for ORR is 30 MW.

[b]7.30 t 25 is read as 7.30 x 10^{25}.

[c]He values represent the difference in helium values at the end of the current core piece and the previous core piece since helium production is dominated by the cumulative thermal fluence and not by the thermal fluence seen by a particular core piece.

[d]Ratio represents the experimental helium-dpa value divided by the calculated fusion device first wall value of 13.97.

2.1.5 Future Work

This completes the neutronics calculations for the ORR-MFE-4A and -48 experiments.

2.7.6 References

1. R. A. Lillie and T. A. Gabriel, "Neutronics Calculations in Support of the ORR-MFE-4 Spectral Tailoring Experiments," pp. 19-20 in *ADIP Semiannu. Prog. Rep., Mar. 31, 1983*, DOE/ER-0045/10, U.S. DOE, Office of Fusion Energy.

2. R. A. Lillie, "Neutronics Calculations in Support of the ORR-MFE-4A and -48 Spectral Tailoring Experiments," pp. 18-19 in *ADIP Semiannu. Prog. Rep., Sept. 30, 1984*, DOE/ER-0045/13, U.S. DOE, Office of Fusion Energy.

2.8 OPERATION OF THE ORR SPECTRAL TAILORING EXPERIMENTS ORR-MFE-4A AND -4B — I. I. Siman-Tov (Oak Ridge National Laboratory)

2.8.1 ADIP Task

ADIP Task I.A.2, Define Test Matrices and Test Procedures.

2.8.2 Objectives

Experiments ORR-MFE-4A and -4B, which irradiate austenitic steel, use neutron spectral tailoring to achieve the same helium-to-displacement-per-atom (He/dpa) ratios as predicted for fusion reactor first-wall service. Experiment ORR-MFE-4A contains mainly type 316 stainless steel, and Path A Prime Candidate Alloy (PCA) at irradiation temperatures of 330 and 400°C. Experiment URR-MFE-4B contains similar materials at irradiation temperatures of 500 and 600°C.

2.8.3 Summary

Both ORR-MFE-4A and -4B have been capped and are cooling down in the ORR pool awaiting removal and postirradiation examination.

The specimens contained in the ORR-MFE-4B experiment have operated for a total of 996.64 d at 30 MW reactor power with temperatures of 500 and 600°C.'

2.8.4 Progress and Status

The details of the Oak Ridge Research Reactor (ORR) spectral tailoring experiments have been documented previously.[1-10]

The ORR-MFE-4B experiment started operating with a hafnium sleeve on February 3, 1985, and was removed from the core on June 26, 1985. The total irradiation time was 996.34 d at 30 MW; of this time, it spent (a) a total of 424.10 d at 30 MW with the hollow core piece, (b) a total of 450.30 d at 30 MW with the aluminum core piece, and (c) a total of 121.94 d at 30 MW with the hafnium sleeve core piece.

2.8.5 References

1. K. R. Thorns and M. L. Grossbeck, "Operation of the ORR Spectral Tailoring Experiment ORR-MFE-4A," pp. 20–24 in *ADIP Quart. Prog. Rep. Sept. 30, 1980,* DOE/ER-0045/4, U.S. DOE, Office of Fusion Energy.

2. K. R. Thorns, "Operation of the ORR Spectral Tailoring Experiment ORR-MFE-4A," pp. 18—21 in *ADIP Quart. Prog. Rep. Mar. 31, 1981,* DOE/ER-0045/6, U.S. DOE, Office of Fusion Energy.

3. I. T. Dudley, "Operation of the ORR Spectral Tailoring Experiments ORR-MFE-4A and ORR-MFE-4B," pp. 24-29 in *ADIP Semiannu. Prog. Rep. Sept. 30, 1981,* DOE/ER-0045/7, U.S. DOE, Office of Fusion Energy.

4. I. T. Dudley and J. A. Conlin, "Operation of the ORR Spectral Tailoring Experiments ORR-MFE-4A and MFE-4B," pp. IC—I2 in *ADIP Semiannu. Prog. Rep. Mar. 31, 1982,* DOE/ER-0045/8, U.S. DOE, Office of Fusion Energy.

5. J. A. Conlin, I. T. Dudley, and E. M. Lees, "Operation of the ORR Spectral Tailoring Experiments URR-MFE-4A and ORR-MFE-4B," pp. 17—20 in *ADIP Semiannu. Prog. Rep. Sept. 30, 1982,* DOE/ER-0045/9, U.S. DOE, Office of Fusion Energy.

6. J. A. Conlin, I. T. Dudley, and E. M. Lees, "Operation of the ORR Spectral Tailoring Experiments ORR-MFE-4A and ORR-MFE-4B," pp. 21—22 in *ADIP Semiannu. Prog. Rep. Mar. 31, 1983,* DOE/ER-0045/10, U.S. DOE, Office of Fusion Energy.

7. J. A. Conlin, I. T. Dudley, and E. M. Lees, "Operation of the ORR Spectral Tailoring Experiments ORR-MFE-4A and ORR-MFE-4B," pp. 40-41 in *ADIP Semiannu. Prog. Rep. Sept. 30, 1983,* DOE/ER-0045/11, U.S. DOE, Office of Fusion Energy.

8. J. A. Conlin and J. W. Woods, "Irradiation Experiments for the U.S./Japan Collaborative Testing in HFIR and ORR," p. 31 in *ADIP Semiannu. Prog. Rep. Mar. 31, 1984,* DOE/ER-0045/12, U.S. DOE, Office of Fusion Energy.

9. J. A. Conlin and J. W. Woods, "Irradiation Experiments for the U.S./Japan Collaborative Testing in HFIR and ORR," pp. 66–67 in *ADIP Semiannu. Prog. Rep. Sept. 30, 1984,* DOE/ER-0045/13, U.S. DOE, Office of Fusion Energy.

10. I. I. Siman-Tov, J. A. Conlin, and I. T. Dudley, "Operation of the ORR Spectral Tailoring Experiments ORR-MFE-4A and ORR-MFE-4B," p. 5 in *ADIP Semiannu. Prog. Rep. Mar. 31, 1985,* DOE/ER-0045/14, U.S. DOE, Office of Fusion Energy.

3.1 SWELLING OF Fe-Cr-Mn ALLOYS IN FFTF AT 420 TO 600°C - F. A. Garner and H. R. Brager (Hanford Engineering Development Laboratory)

3.1.1 ADIP Tasks

ADIP Task 1.C.2. Microstructure and Swelling of Austenitic Alloys.

3.1.2 Objective

The object of this effort is to determine those factors which control the swelling of alloy systems which have the potential for reduced activation.

3.1.3 Summary

Three binary Fe-Mn and six Fe-Mn-Cr ternary alloys have been irradiated in FFTF at temperatures of 420, 500 and 600°C to exposures ranging from 9-14 dpa. In contrast to the behavior of Fe-Cr-Ni alloys irradiated under comparable conditions there is essentially no dependence of void swelling on chromium or manganese content, and there also appears to be no dependence on irradiation temperature. Like Fe-Cr-Ni alloys, however, Fe-Cr-Mn and Fe-Mn alloys do swell at ~1%/dpa after the transient regime.

While density change data indicate an apparent weak dependence of swelling on manganese level, microscopy shows that radiation-induced second phases that form may be responsible for a densification of the matrix. This densification approaches 2.2% at 35% manganese.

3.1.4 Progress and Status

3.1.4.1 Introduction

In previous reports[1,2] it was shown that the swelling of simple Fe-Mn binary and Fe-Mn-Cr ternary alloys in FFTF-MOTA at 520°C and ~14 dpa is remarkably insensitive to the chromium level and only weakly dependent on the manganese level as shown in Figure 1a. Figure 1b shows that this behavior is quite different from that of Fe-Cr-Ni alloys which are strongly sensitive to both chromium and nickel for comparable irradiation conditions.

Additional immersion density data are now becoming available for this irradiation series. The portion of the data matrix that is now complete leads us to revise somewhat our earlier conception of the parametric dependence of swelling in the Fe-Cr-Mn system.

3.1.4.2 New Data

Figure 2 shows that the swelling data of one alloy, Fe-5Cr-15Mn, does not fit the behavior typical of the other previously reported alloys irradiated at 520°C and 14 dpa. At 600°C and 14 dpa essentially the same swelling is observed for this alloy, however, which leads us to speculate that irradiation above 500°C has caused some relatively temperature-independent phase evolution for this alloy that is different from that of the others. Figure 3 shows that, with the exception of Fe-5Cr-15Mn, all other alloys exhibit after irradiation at 600°C and 14 dpa essentially *the* same swelling as observed at 520°C and 14 *dpa*. The scatter at 600°C is somewhat larger, however. This implies that there is little or no dependence of swelling on temperature in the range 520-600°C. It is desired to determine whether the independence of temperature extends as low as 420°C but unfortunately the data at 420°C exist only at 9 dpa. as is also shown in Figure 3. Note that at 420°C most alloys not only densify but that rather large densifications are exhibited at the higher manganese levels.

At this point we can borrow from our experience on Fe-Cr-Ni alloys and remember that at low temperatures there is usually no temperature dependence of swelling and thus we can often plot the data ignoring the temperature.[3,4] Note in Figure 4 that we can draw lines between (420°C, 9 dpa) data and (520°C, 14 dpa) data for each alloy and that each line exhibits a slope of ~1%/dpa. This apparent swelling rate is identical to that observed for all other austenitic alloys in the post-transient regime.[3] The densification shown in Figures 3 and 4 tends to imply that much of the previously observed composition dependence of post-irradiation density change is a reflection of a process other than void swelling. Therefore the composition dependence of swelling in the Fe-Cr-Mn system appears to be even less than previously reported.[1]

3.1.4.3 Microstructural Development

Examination of these alloys by electron microscopy is now in progress. Two alloys irradiated at 520°C have been examined. These are Fe-10Cr-30Mn and Fe-10Cr-20Mn. Both contained large voids (~100 nm) and comparable dislocation densities (13×10^{10} cm^{-2}). There were two distinct differences in microstructure, however. First, the *20%* manganese alloy had a moderate density (~3×10^{13} cm^{-3}) of large (200-500 nm) and sometimes elongated precipitates which are as yet unidentified. Similar precipitates existed at much lower densities in the 30% manganese alloy. Second, the 20% manganese alloy contained a higher density of voids, ~2×10^{14} cm^{-3} as compared to ~5×10^{13} cm^{-3} for the 30% manganese alloy. This difference in void density was the major cause of the difference in local swelling (8% vs. 3%) of the two alloys.

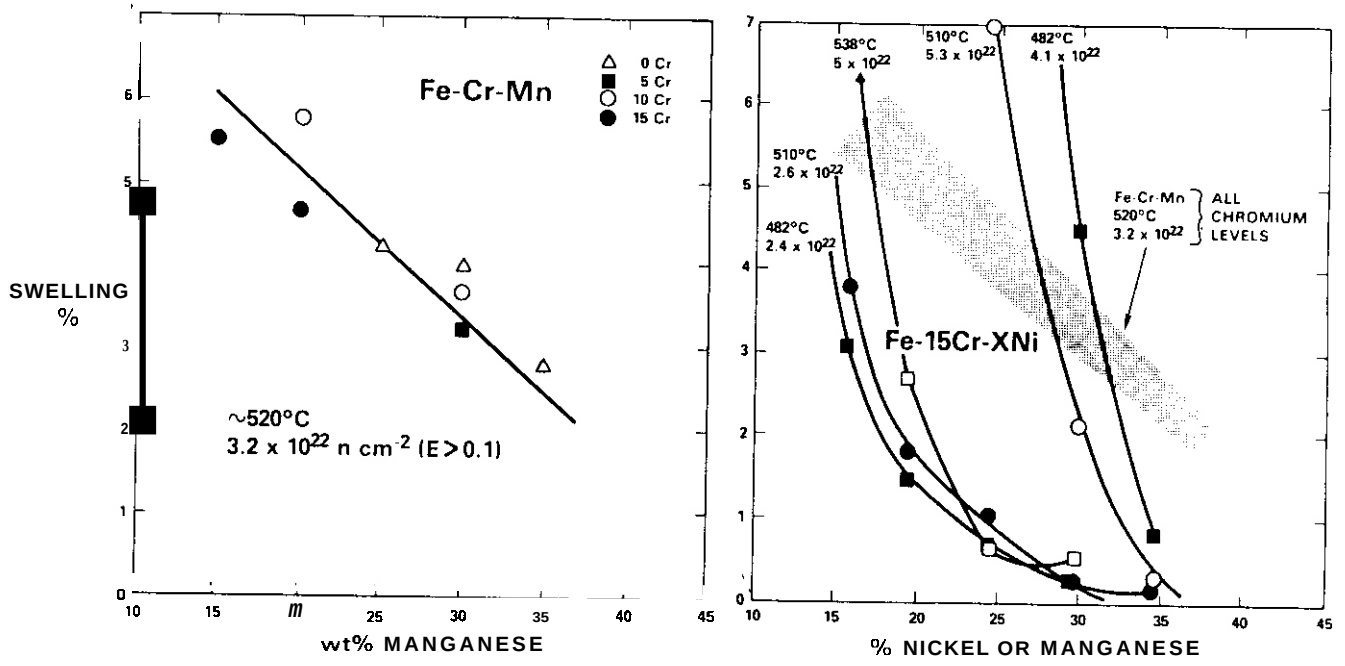

FIGURE 1. Comparison between neutron-induced swelling in Fe-Cr-Mn and Fe-Cr-Ni alloys.(1)

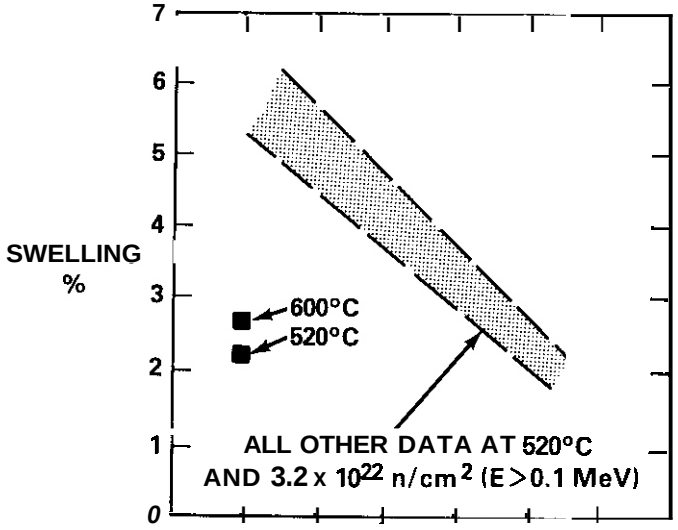

FIGURE 2. Comparison of additional data on swelling of Fe-5Cr-15Mn at 14 dpa and the trend of previously published data for other Fe-Cr-Mn alloys at 520°C and 14 dpa.(2)

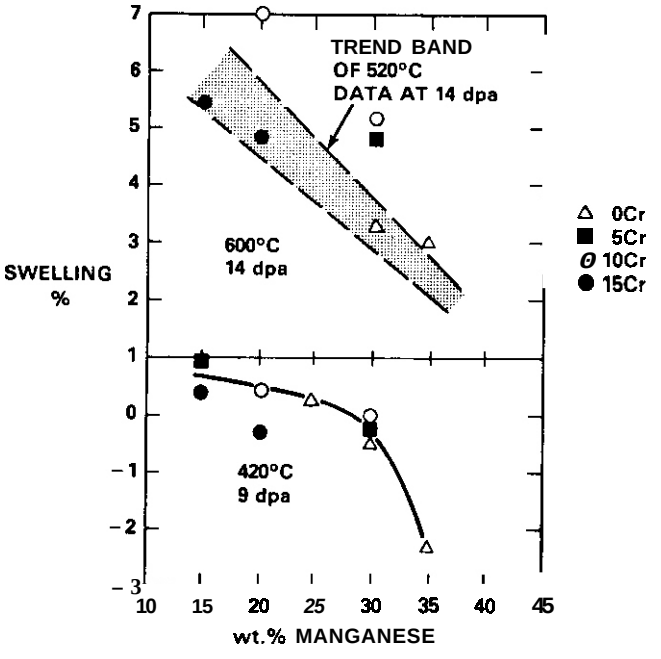

FIGURE 3. New data showing swelling of Fe-Cr-Mn alloys at 420°C and 600°C. Some alloys densify at 420°C.

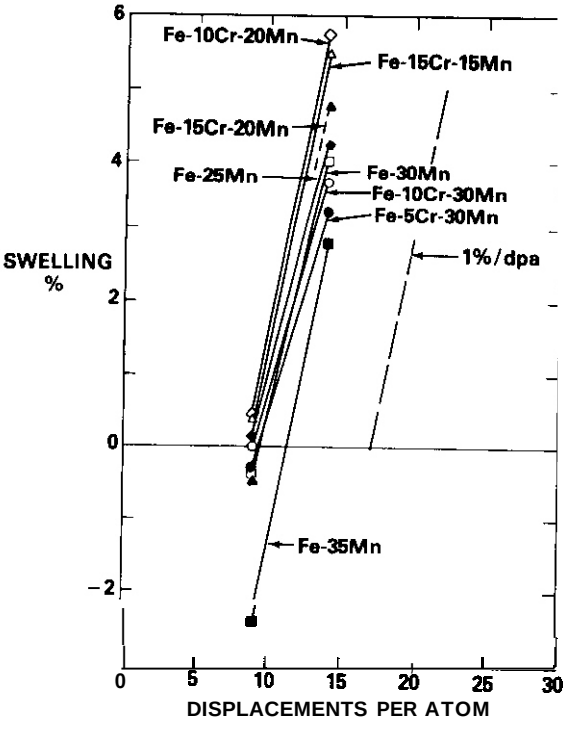

FIGURE 4. Plot of Fe-Cr-Mn swelling data assuming independence of swelling on temperature between temperatures of 420 and 520°C.

3.1.5 Discussion

The alloys irradiated in this experiment were selected to explore the possibility that a correlation exists between anomalous Invar properties and swelling resistance.[5] Since the Fe-Cr-Mn system also exhibits Invar behavior in the range around 35% Mn[6-8] it was thought that there might be some advantage to developing low activation austenitic alloys which contain manganese levels of this magnitude.

Just as radiation-induced spinodal-like decomposition is a consequence of the same metastability that produces anomalous properties in the Fe-Cr-Ni Invar regime, it is suggested that spinodaling also occurs in the Fe-Cr-Mn Invar regime. In order to quickly and almost completely destroy the compositional and temperature dependence of swelling, however, spinodal decomposition in the Fe-Cr-Mn system must occur faster than it does in the Fe-Cr-Ni system. The densification of 2.2% observed in Fe-35Mn is much larger than the 0.9% that occurs in the Fe-Ni-Cr system.[9] This implies a much larger driving force in the Fe-Cr-Mn system. Figure 5 indeed shows that below 35% manganese the rate of change with manganese content of pre-irradiation density of Fe-Cr-Mn alloys is very large. If the density again rises steeply above 35% manganese, spinodal decomposition could indeed lead to a very substantial densification and a large driving force. It appears, however. that there is another phase separation process occurring at lower manganese levels. More microscopy data are required to determine the nature of the swelling-phase stability relationship in this alloy system.

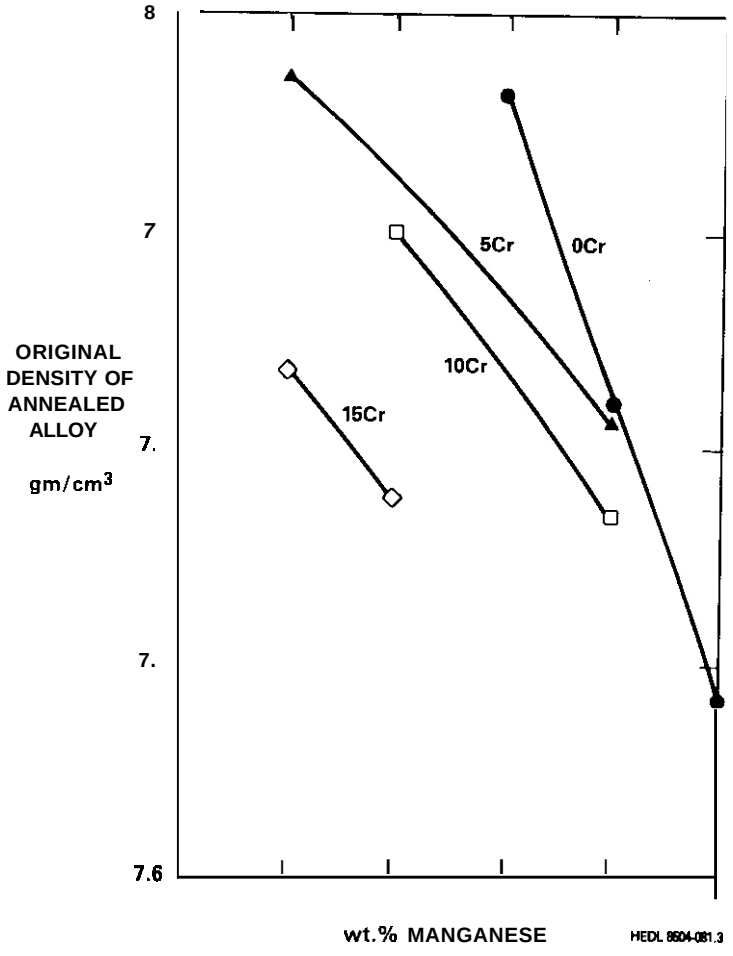

FIGURE 5. Dependence of pre-irradiation density on composition for annealed Fe-Cr-Mn alloys.

3.1.6 Conclusions

There does not appear to be any large advantage to be gained at higher (>20%) manganese contents in terms of the intrinsic swelling resistance of simple Fe-Cr-Mn alloys. However, this conclusion may not apply to the solute-modified Fe-Cr-Mn alloys which have not yet been examined. If radiation-induced precipitation or spinodal-like decomposition is causing both a large densification and the destruction of the swelling resistance, then the study of the differences between Fe-Cr-Mn and Fe-Cr-Ni Invar alloys may lead to clues as to how to suppress the spinodal-like process and extend the incubation period of swelling. Therefore examination of the Fe-Cr-Mn Invar alloys will continue despite the initially unsuccessful application of the Invar-swelling resistance correlation to the simple Fe-Cr-Mn system.

3.1.7 References

1. H. R. Brager and F. A. Garner, "Swelling of Fe-Cr-Mn Ternary Alloys in FFTF," ADIP Semi-annual Progress Report, DOE/ER-0045/13, September 1984, 81-82.
2. F. A. Garner and H. R. Brager "Neutron-Induced Swelling of Fe-Cr-Mn Ternary Alloys," DAFS Quarterly Progress Report, DOE/ER-0046/19, May 1985, pp. 41-45.
3. F. A. Garner, J. Nucl. Mater., 122 & 123 (1984) 459-471.
4. F. A. Garner, "Application of High Fluence Fast Reactor Data to Fusion-Relevant Materials Problems," J. Nucl. Mater., 133 & 134 (1985) 113-118.
5. H. R. Brager and F. A. Garner, "Fundamental Alloy Studies," DAFS Quarterly Progress Report DOE/ER-0046/17, May 1984, 93-101.
6. Y. Endoh, Y. Noda and M. Iizumi, J. Phys. Soc. Japan, 50, No. 2 (1981) 469-475.
7. O. G. Sokolov and A. I. Mel'ker, Soviet Physics-Doklady, 9, No. 1 (1965) 1019-1021.
8. O. A. Khomenko and I. F. Khil'kevich, Met. Term. Obra. Met., 6 (1982) 42-44.
9. H. R. Brager and F. A. Garner, "Swelling of Fe-Ni-Cr Ternary Alloys at High Exposure," DAFS Quarterly Progress Report DOE/ER-0046/16, Feb. 1984, 38-45.

3.1.8 Future Work

Density change and microscopy data will continue to be accumulated on both simple and solute-modified Fe-Cr-Mn alloys at higher fluence. Microscopy on specimens irradiated to 16 dpa will also continue.

3.2 PHASE STABILITY DURING ANNEALING AND AGING IN LOW-ACTIVATION Fe-Cr-Mn AUSTENITIC STAINLESS STEELS — P. J. Maziasz and R. L. Klueh (Oak Ridge National Laboratory)

3.2.1 ADIP Task

ADIP tasks I.A.5, Perform Fabrication Analysis, and I.C.l, Microstructural Stability.

3.2.2 Objective

Manganese-stabilized austenitic stainless steels are being developed to replace nickel-stabilized austenitic stainless steels for fusion reactor application because their radioactivity decays more quickly after shutdown. Phase stability is being studied after solution annealing (1050 to 1275°C) and after lower temperature aging as a function of alloy composition to find suitable base compositions from which to develop more complex, radiation-resistant alloys, similar to the austenitic prime candidate alloy (PCA).

3.2.3 *Summary*

The first group of laboratory heats of low-activation, manganese-stabilized austenitic steels were aged for 168 h at 800°C, following solution annealing and cold working, to explore their relative precipitation responses. Delta (δ) ferrite, which was present in many alloys after solution annealing, was absent in the cold-worked materials after aging. These aged alloys recovered and/or recrystallized, and the matrix became completely austenitic, with varying amounts of σ phase and $M_{23}C_6$ (τ) precipitates. Only the 15Cr-19Mn-0.4C alloy had finely distributed τ carbide particles without any evidence of σ phase. Both the σ and τ phases contained substantial amounts of manganese, whereas in nickel-stabilized steels, these phases would reject nickel.

3.2.4 Progress and Status

Details of purpose, strategy, and preparation of the first ten manganese-stabilized austenitic stainless steel alloys have been reported.[1] The emphasis in this work is on the phase stability and precipitation behavior of the cold-worked alloys at temperatures below the solution-annealing range (1050–1275°C). Chromium, manganese, and carbon compositional variations for these steels, labeled PCMA-0 through -9, are given in Table 3.2.1. PCMA-3 was dropped from this investigation due to fabrication difficulties. The alloys were solution annealed for 1 h at 1150°C and then cold worked 30% to provide maximum precipitation kinetics and sensitivity to intermetallic phase formation prior to aging for 168 h at 800°C. Microstructure and phase changes were evaluated via optical microscopy, via ferromagnetic behavior using a "Ferritescope," and via analytical electron microscopy using JEM 100CX and 2000FX and Philips EM400 instruments. Tentative phase identifications for various alloys are given in Table 3.2.2, and the results of ferromagnetism measurements are listed in Table 3.2.3.

Table 3.2.1. Chemical composition of button heats melted for fast induced-radioactivity decay (FIRD) alloy-development program

Alloy	Chemical compositiona (wt %)									
	C	Mn	Si	Ni	Cr	Mo	V	Nb	Cu	N
PCMA-0	0.069	13.4	0.04	0.01	15.0	0.01	0.01	(0.01	0.03	0.001
-1	0.014	14.2	0.02	0.01	14.8	0.01	0.01	<0.01	0.03	0.001
-2	0.056	17.1	0.04	0.01	15.2	0.01	<0.01	(0.01	0.03	0.001
-3	0.089	13.9	0.02	0.01	10.0	0.01	(0.01	(0.01	0.03	0.002
-4	0.093	18.9	0.02	0.01	9.9	(0.01	<0.01	(0.01	0.02	0.002
-5	0.18	13.9	0.02	0.01	15.3	0.01	(0.01	(0.01	0.04	0.002
-6	0.18	14.3	0.02	0.01	16.0	0.01	<0.01	(0.01	0.03	0.003
-7	0.38	19.1	0.02	0.01	14.8	0.01	<0.01	(0.01	0.05	0.005
-8	0.13	17.7	0.02	<0.01	20.1	0.01	(0.01	<0.01	0.03	0.003
-9	0.26	17.6	0.03	0.01	20.2	0.01	(0.01	(0.01	0.03	0.006

[a]Balance iron.

Table 3.2.2. Tentative identification of microstructural constituents of aged Fe-Mn-Cr-C steels

Alloy	Phases	
	1150°C/1 h (SA)[a]	SA + 30% CW + 800°C/166h[b]
PCMA-0	γ + δ	Not determined
-1	γ + δ	γ + σ
-2	γ + δ	γ + σ + $M_{23}C_6$
-3	γ + δ	Not determined
-4	γ + M	γ + $M_{23}C_6$ + σ
-5	γ + δ + M	Not determined
-6	γ + δ + P	γ + σ + $M_{23}C_6$
-7	γ	γ + $M_{23}C_6$
-8	γ + δ + P	Not determined
-9	γ + δ + P	γ + $M_{23}C_6$ + σ

[a] γ = austenite, δ = δ ferrite, M = martensite, P = precipitate. Evaluated from optical metallography.

[b] Evaluated from transmission electron microscopy.

Table 3.2.3. Ferrite numbera as a measurement of the extent of ferromagnetism

Alloy	Ferrite numberb		
	1150°C/1 h	Cold worked	800°C/168 h
PCA-0	30+	30+	0.5
-1	30+	30+	6.8
-2	30+	30+	0.2
-3	4.0	30+	
-4	0.2	11.0	0.2
-5	5.8	30+	0.5
-6	6.3	5.5	0.2
-7	0	0.5	0.2
-8	30+	30+	0.2
-9	19.0	6.0	0

[a] Measurements made with a Ferritescope.

[b] Maximum number measured with a Ferritescope is 30.

Alloys PCMA-0 through -4 generally contained less carbon and chromium than the other heats of steel. Upon annealing, either some 6-ferrite or ε-martensite (hcp) formed with the austenite, as seen in Fig. 3.2.1. Alloys PCMA-0 through -2 showed maximum measurable ferromagnetic behavior, which is attributed to the presence of the δ-ferrite in the annealed condition, and hence showed little additional change with further cold working (Table 3.2.3). However, alloy PCMA-4 did become more magnetic after cold working, presumably due to formation of the α′-martensite (bct). Alloys PCMA-5 through -9 generally had more carbon and/or chromium and, after annealing, contained 6 ferrite and probably some carbide precipitates together with austenite, but with no evidence of martensite (see Fig. 3.2.2). Of this latter group, only PCMA-5 appeared to form a' martensite upon cold working, to increase its ferromagnetism. Alloy PCMA-7 was entirely austenitic after solution annealing as well as after cold working (see Fig. 3.2.3 and Table 3.2.3).

Aging of the 30%-CW materials produced refined substructures and/or precipitation of carbides and intermetallics, with no evidence of the prior 6-ferrite or martensite, as shown metallographically in Figs. 3.2.1 through 3.2.3. With the exception of PCMA-1, all alloys showed little or no ferromagnetic behavior. Alloy PCMA-1, with only 0.05 wt % C, may have retained a small amount of δ-ferrite in some regions. Transmission electron microscopy (TEM) showed that new small recrystallized grains and stacking faults, as well as coarse σ-phase particles, were responsible for most of the refined substructures shown in the aged specimens in Figs. 3.1.1 through 3.2.3. TEM analysis was performed on alloys PCMA-1, -2. -4, -6. -7, and -9. and phase identification from TEM/AEM observations is found in Table 3.2.2.

With regard to grain boundaries and substructure, alloys PCMA-1, -2, and -4 recrystallized completely into a new assembly of small, dislocation-free grains. This can be seen metallographically in Fig. 3.2.1 and by TEM in Fig. 3.2.4. Alloys PCMA-5 through -9 retain similar grain sizes after aging compared to their as-solution-treated conditions. as seen metallographically in Fia. 3.2.1. TEM of these samples showed large extended faults within large grains and higher concentrations of-dislocation-networks within the subregions. PCMA-6 contained a mixture of dislocated and dislocation-free regions, whereas PCMA-7 and -9 contained a higher dislocation content and finer fault structures.

Next, considering precipitation, alloy PCMA-I (the lowest carbon content — 0.014 wt %) contained austenite and σ-phase, whereas alloy PCMA-7 (the highest carbon content — 0.38 wt %) contained austenite and $M_{23}C_6$ (τ). All other alloys contained mixtures of σ-phase and $M_{23}C_6$; alloys PCMA-2 and -9 appeared to have the highest volume fractions of precipitate, judging from both metallography and TEM. Increased chromium content tended to promote σ-phase formation, but the $\sigma/M_{23}C_6$ ratio seemed most sensitive to carbon variation. Microstructurally, a-phase particles formed at grain boundaries or along faulted bands and ranged in size from <1 to 4 to 5 μm in diameter. These particles were largest in alloys PCMA-0 through -2. A representative σ-phase particle and convergent beam electron diffraction (CBED) pattern characteristic of the (001) zone axis pattern (ZAP) are shown in Fig. 3.2.5. The $M_{23}C_6$ carbide particles were smaller. generally 1 to 2 μm or less in diameter. They were sparsely distributed or clustered in most alloys except for PCMA-7 and -9, in which they were distributed more uniformly. Only PCMA-7 had fine carbide precipitation (particles were ~23 nm in diameter), as shown in Fig. 3.2.6 with a CBED of the $(001)_\tau$ ZAP for identification.

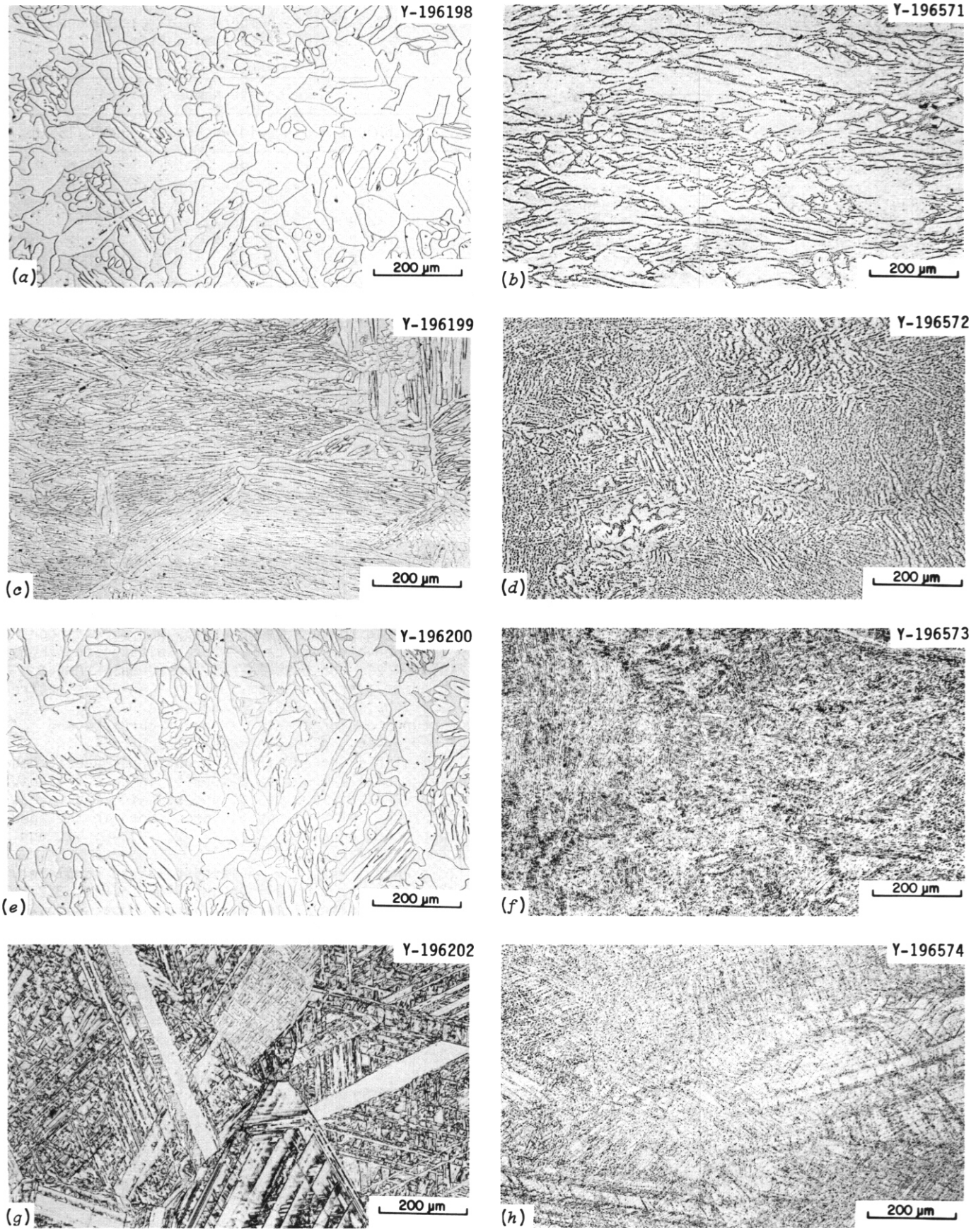

Fig. 3.2.1. Metallography illustrating the effects of 30%-cold working (CW) and aging for 168 h at 800°C relative to the as-solution-annealed (SA) (1 h at 1150°C) structure for alloys PCMA-0, -1, -2, and -4.

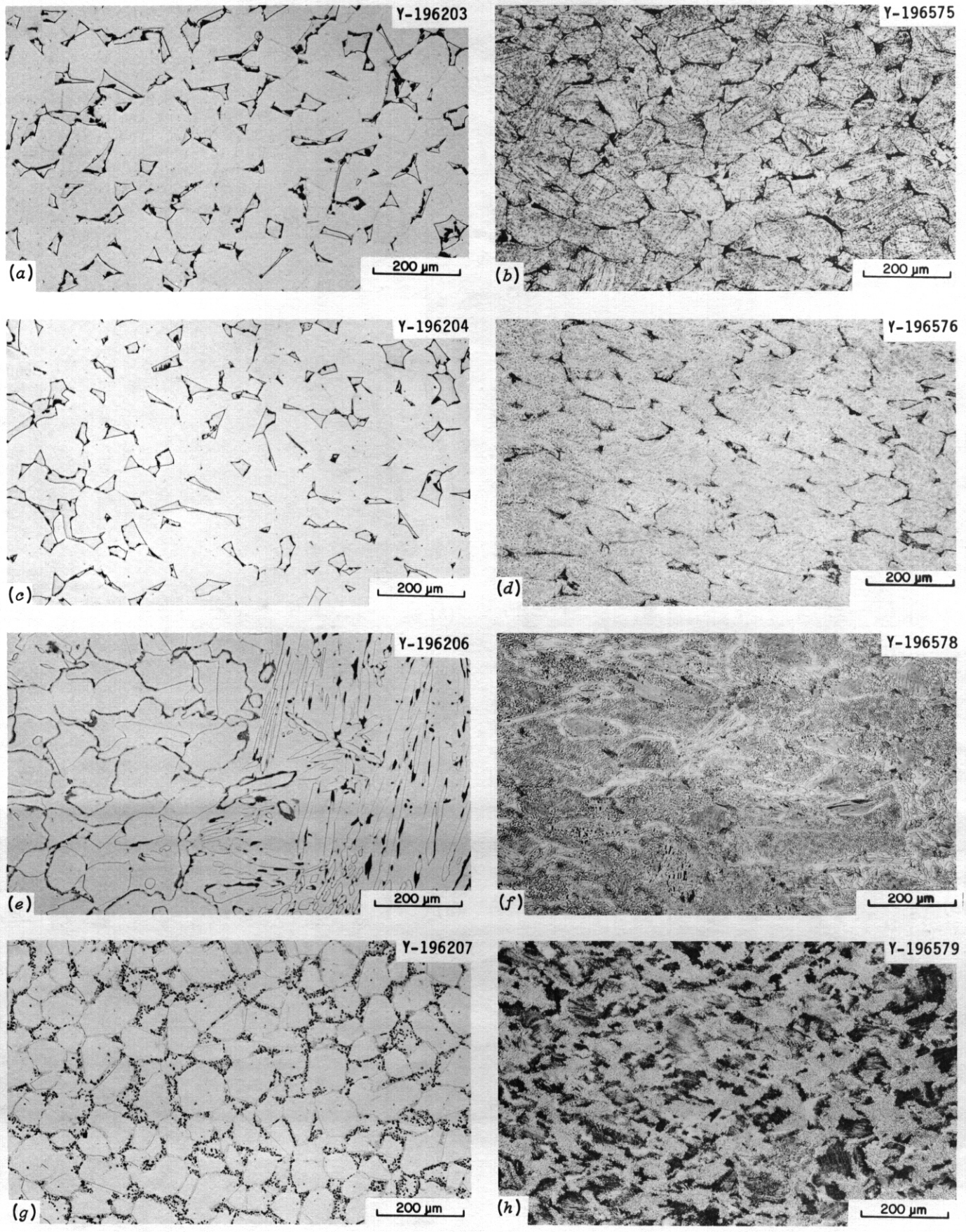

Fig. 3.2.2. Metallography illustrating the effects of 30%-cold working (CW) and aging for 168 h at 800°C relative to the as-solution-annealed (SA) (1 h at 1150°C) structure for alloys PCMA-5, -6, -8, and -9.

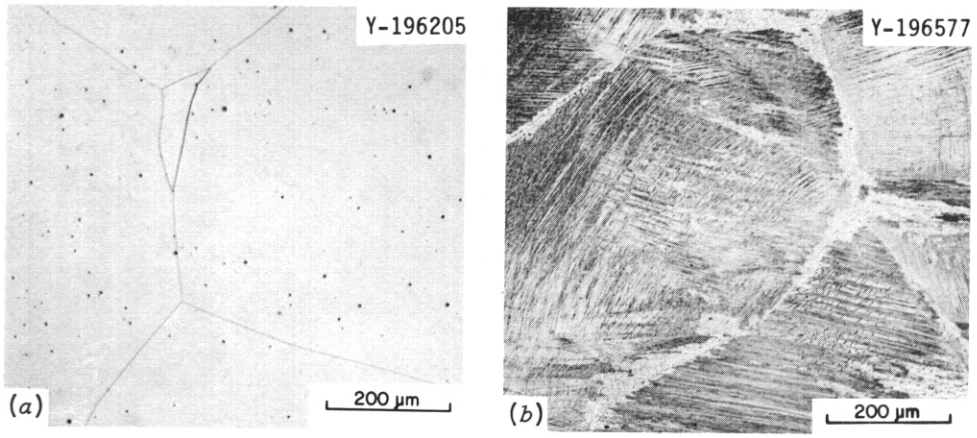

Fig. 3.2.3. Metallography illustrating the effects of 30%-cold working (CW) and aging for 168 h at 800°C relative to the as-solution-annealed (SA, 1 h at 1150°C) structure for alloy PCMA-7.

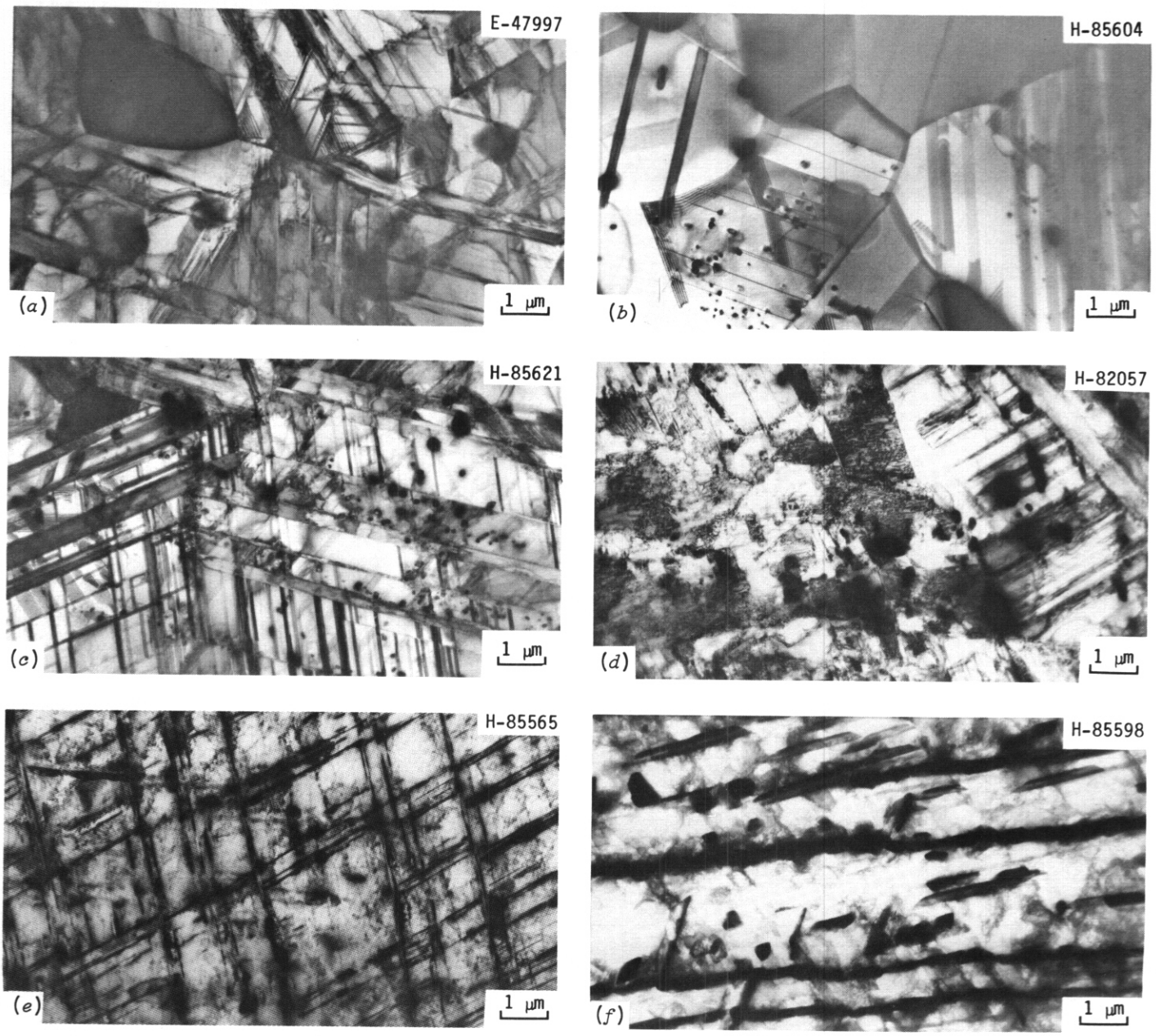

Fig. 3.2.4. Microstructures of alloys (*a*) PCMA-1, (*b*) PCMA-2, (*c*) PCMA-4, (*d*) PCMA-6, (*e*) PCMA-7, and (*f*) PCMA-9 after aging for 168 h at 800°C in the 30%-CW condition.

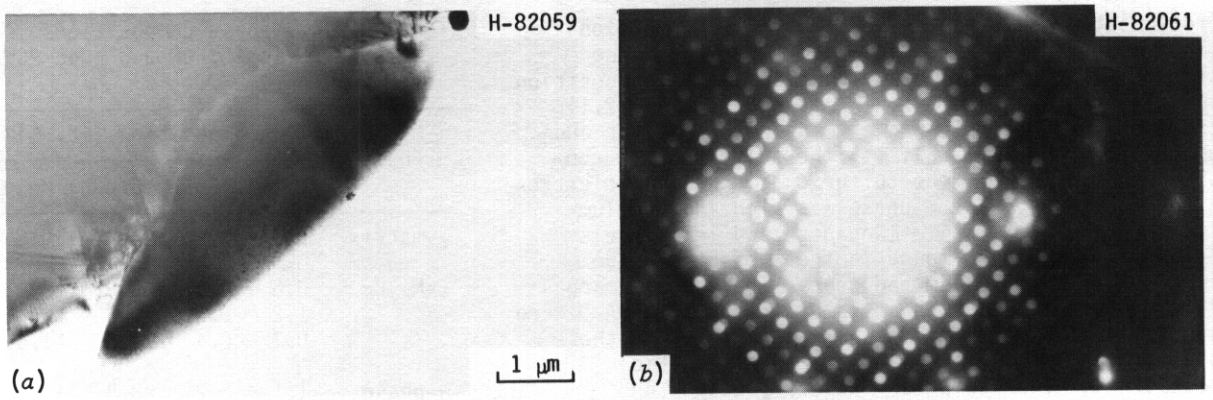

Fig. 3.2.5. (*a*) TEM of a σ-phase particle in 30%-CW PCMA-6 formed during aging at 800°C for 168 h and (*b*) characteristic CBED of the $(001)_\sigma$ ZAP for identification.

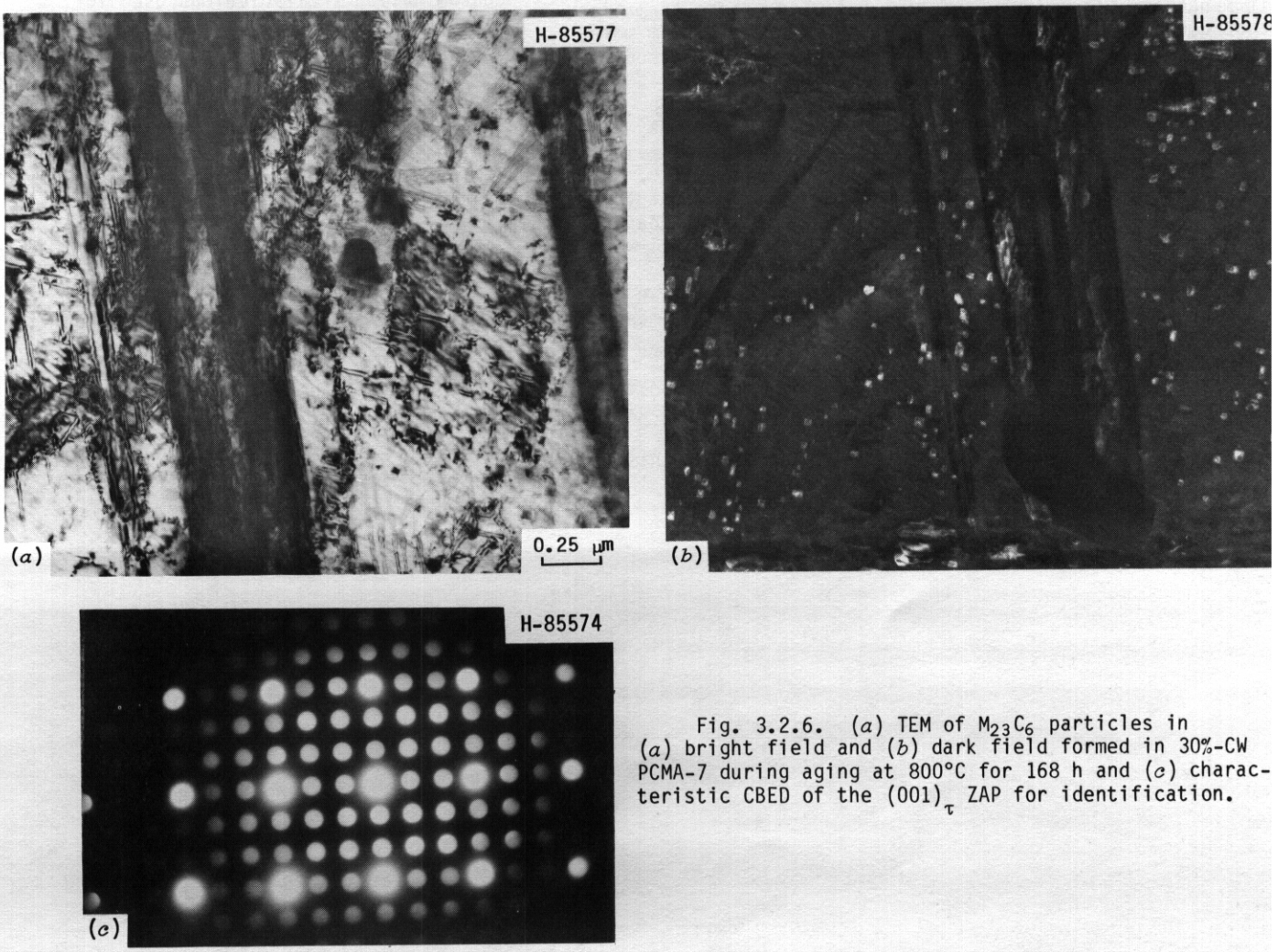

Fig. 3.2.6. (*a*) TEM of $M_{23}C_6$ particles in (*a*) bright field and (*b*) dark field formed in 30%-CW PCMA-7 during aging at 800°C for 168 h and (*c*) characteristic CBED of the $(001)_\tau$ ZAP for identification.

Precipitate phase and austenite matrix compositions were measured by in-foil XEDS for aged PCMA-9, and the results are given in Table 3.2.4. The austenite composition was close to that measured by bulk methods (Table 3.2.1), but XEDS indicated slightly higher manganese. Sulfur and calcium showed up in the analysis; the sulfur may be contamination remaining from the sulfuric acid used to electropolish the specimens. The a-phase was rich in chromium relative to the matrix, while manganese and iron levels remained similar to those found in the austenite. The $M_{23}C_6$ was richer in chromium and poorer in iron and manganese than the matrix. The phase compositions in PCMA-9 were remarkably similar in chromium and iron contents to those same phases found in a nickel-stabilized austenitic stainless Steel, like the PCA.[2] However, both σ and $M_{23}C_6$ phases would reject nickel relative to the austenitic matrix in nickel-stabilized steels, whereas manganese was present to nearlv the matrix concentration with little rejection or enrichment in the PCMA steel. The nickel rejection by a-phase may be one factor favoring its suppression with increasing austenite nickel concentration. If manganese plays even a neutral role in a-phase formation, that could partially explain why the PCMA steels seem more prone to a-phase formation, despite their higher carbon contents, than normal nickel-stabilized steels.

Table 3.2.4. Phase compositions measured via XEOS in 30%-CW and aged PCMA-9

Phase	Composition (at. %)[a,b]				
	S	Ca	Cr	Mn	Fe
γ-matrix	2.3	0.2	20.4	19.5	57.7
τ-$M_{23}C_6$	0.6	0.4	55.8	15.3	27.7
	1.2	0.4	70.9	12.4	15.1
	0.7	0.4	72.6	11.6	14.6
o-phase	1.1	0.2	28.8	18.7	51.2

[a] Normalized composition for elements heavier than aluminum, phases measured in-foil.

[b] At least sulfur may come from contamination from solutions used for electropolishing (H_2SO_4).

With regard to guidance for future alloy development, PCMA-7 appears attractive, due to its fine $M_{23}C_6$ carbide precipitation formed during aging at 800°C as well as its entirely austenitic structure after solution annealing. A second generation of PCMA alloys, -10 through -14, have been melted in the compositional range of 10 to 16 at. % Cr, 20% Mn, and 0.1 to 0.2% C.[3] Although welding considerations tend to put a limit on carbon contents, the present aging results suggest that higher carbon contents are beneficial for producing finer carbide distributions and retarding a-phase formation.

3.2.5 References

1. R. L. Klueh and P. J. Maziasz, "The Development of Austenitic Steels for Fast Induced-Radioactivity Decay," pp. 69–75 in *ADIP Semiannu. Prog. Rep. Sept. 30, 1984,* DOE/ER-0045/13, U.S. DOE, Office of Fusion Energy.

2. P. J. Maziasz and S. Jitsukawa, "Minor Compositional Variations of the Austenitic PCA to Explore MC Formation and Stability Characteristics for Improved Radiation Resistance," pp. 37-48 in *ADIP* Semiannu. *Prog. Rep. Mar. 31, 1985,* DOE/ER-0045/14.

3. R. L. Klueh and P. J. Maziasz, Sect. 3.5, this report.

3.3 MICROSTRUCTURE OF TYPE 316 STEEL IRRADIATED TO 30 dpa AT 300°C IN HFIR — S. Hamada, M. P. Tanaka (Japan Atomic Energy Research Institute, assigned to ORNL) and P. J. Maziasz (Oak Ridge National Laboratory)

3.3.1 ADIP Task

I.C.2 Microstructures and swelling in austenitic alloys.

3.3.2 Objective

The objective of this research is to evaluate the change of microstructures in Type 316 stainless steel irradiated in HFIR at lower temperatures.

3.3.3 Summary

Solution-annealed (SA) and 20%-cold-worked (20% CW) type 316 stainless steels were irradiated at 300°C in HFIR to 33.0 dpa and 2116 at. ppm He. Many fine (1.5–4.5 nm in diameter) bubbles were observed uniformly in the matrix; the bubble concentration was ~3 × 10^{23} bubbles/m^3 with average diameters of about 2.0 nm in both specimens. Both bubble volume swellings were about 0.3%. Dense tangles of dislocation networks and Frank loops were also observed in both materials. Size and concentration of Frank loops were about 10.3 nm and 1.4 × 10^{22} loops/m^3, respectively. The results of the present work were compared to previous data on cavities.

3.3.4 Progress and Status

3.3.4.1 Experimental

The chemical composition appears in Table 3.3.1. After disks (3 mm in diameter) were punched from the cold-rolled 0.27-mm-thick sheet, they were solution annealed for 30 min at 1050°C. However, to produce 20% CW material, the steel (0.34-mm in thickness) was annealed for 30 min at 1050°C prior to the final 20% reduction by cold rolling and then disks were punched from the sheet. Both front and back surfaces of the disk were lightly mechanically polished to 0.25-mm-thick sheet so as not to have strain prior to irradiation. The disks were irradiated in the JP-1 capsule of HFIR at 300°C to 33.0 dpa (2116 at. ppm He). After irradiation, disks were electropolished in a twin-jet Tenupol unit and examined with a JEM 2000FX high-resolution electron microscope operating at 200 kV. Cavity and loop size distributions were measured using a Zeiss particle size analyzer.

Table 3.3.1. Chemical composition of J316 stainless steel

Element	Composition[a] (wt %)	Element	Composition[a] (wt %)
Cr	16.75	Si	0.61
Ni	13.52	P	0.028
Mo	2.46	S	0.003
Mn	1.80	N	
C	0.058	B	
Ti	0.005	Co	<0.01

[a]Balance iron.

3.3.4.2 Results

Small cavities were observed in the microstructures of both SA and 20% CW specimens. Figure 3.3.1 shows cavities in both SA and 20% CW material. In both cases, cavities were quite uniformly dispersed throughout the matrix and cavities along the grain boundary were similar in size to matrix cavities (Fig. 3.3.2). Average diameter, number density, and cavity volume swelling are given in Table 3.3.2. Cavities range from 1.5 to 4.5 nm in diameter in both specimens. The average diameter was slightly larger in SA than in 20% CW, but by contrast, number density was slightly larger in 20% CW material. The 20% CW structure results in a higher dislocation network concentration of 3 to 5 × 10^{15} m/m^3 compared to solution-annealed type 316 stainless steel.[1] These dislocation networks do not recover much during irradiation at 300°C in HFIR. Dislocations play an important role as nucleation sites of helium bubbles, consistent with the cavity microstructural differences between 20% CW and SA material, but cavity volume swelling was about 0.3% in both materials.

Helium production in this 316 stainless steel irradiated to 33.0 dpa in HFIR was calculated to be 2116 at. ppm. If all observed cavities are treated as equilibrium bubbles, the helium concentration required in SA and 20% CW material was calculated at 1632 and 1561 at. ppm He, respectively. The cavities could be overpressured, but because helium can also be trapped in unresolved vacancy clusters or released by the specimen surface and surface energies used for the calculations are uncertain, the observed cavities may also be equilibrium helium bubbles; certainly they are not voids.

For comparison with present work, cavity data for 316 stainless steel of U.S. irradiated in HFIR are given in Table 3.3.3. In 20% CW (DO-heat) 316 stainless steel irradiated at 325 to 350°C to 8.4 dpa (390 at. ppm) in HFIR, very large voids (12 nm in diameter) were observed and void swelling was large (0.46%), in spite of lower fluence than this work. However, differences in dislocation concentration, particularly loop evolution, may explain such heat-to-heat differences in void formation in 316 stainless steels.

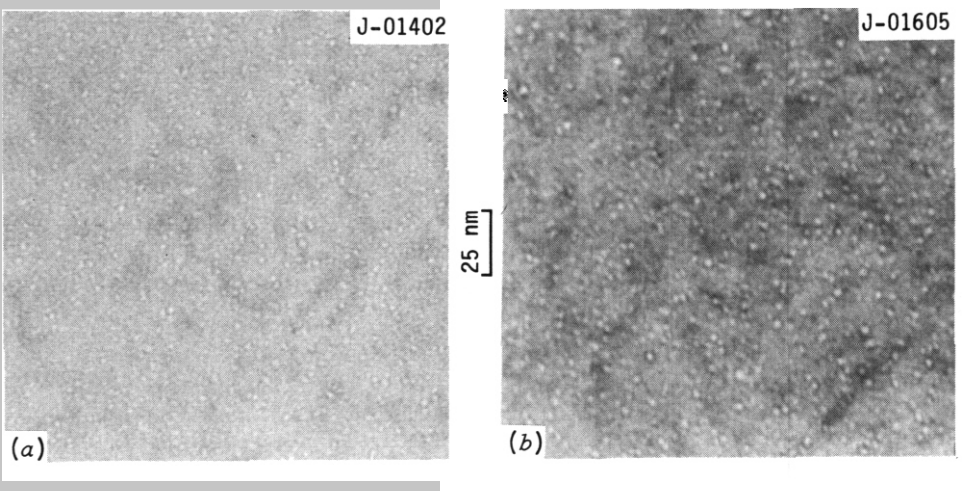

Fig. 3.3.1. Cavities in SA and 20% CW 316 irradiated at 300°C to 33.0 dpa and 2116 at. ppm He in HFIR. *(a)* SA and *(b)* 20% CW.

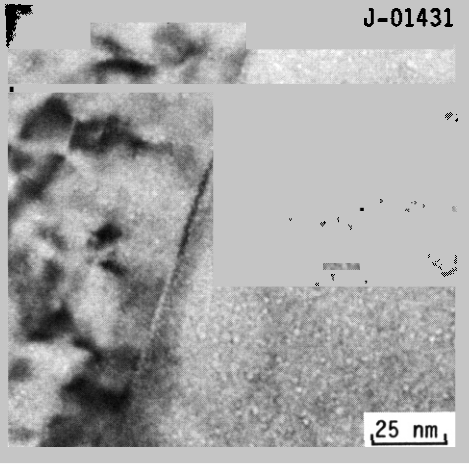

Fig. 3.3.2. Grain boundary cavities in SA 316 irradiated at 300°C to 33.0 dpa and 2116 at. ppm He in HFIR.

Table 3.3.2. Cavity data for type 316 stainless steel irradiated in HFIR

Specimen	Irradiation conditions			Cavity data			
	Displacement damage (dpa)	Temperature (°C)	Helium content (at. ppm)	Type	Average diameter (nm)	Number density (cavities/m^3)	Cavity volume fraction (%)
SA	33.0	300	2116	Bubble	2.7	3.0×10^{23}	0.29
20% CW	33.0	300	2116	Bubble	2.5	3.5×10^{23}	0.28

In 20% CW (N-lot) 316 stainless steel irradiated at 300°C to 10 dpa (375 at. ppm He) in HFIR, previous experiments showed that cavities were not detectable.[3] However, in 20% (N-lot) 316 stainless steel irradiated at 300°C to 44 dpa (2613 at. ppm He) in HFIR, small cavities were found" similar to those in this work. Further, recent work using the 2000FX suggests that small cavities may be resolvable in N-lot 316 irradiated at 300°C to ~10 dpa in HFIR.[5]

The dislocation structure of both SA and 20% CW stainless steel consisted of a heavy concentration of networks and Frank loops (Fig. 3.3.3). Frank faulted loops were imaged separately from the network, using high-resolution dark field with <111> kinematical satellite streaks around g_{200} type matrix reflections.[6] Figure 3.3.4 shows Frank faulted loops imaged by the above reflection condition. Dislocation parameters measured from these pictures are given in Table 3.3.4. The size of Frank faulted loops was similar in both specimens, but the concentration of loops was slightly larger in 20% CW compared to the SA material.

Table 3.3.3. Cavity data for U.S. heats of type 316 stainless steel irradiated in HFIR

Specimen	Irradiation conditions			Cavity data				Reference
	Displacement damage (dpa)	Temperature (°C)	Helium content (at. ppm)	Type	Average diameter (nm)	Number density (cavities/m^3)	Cavity volume fraction (%)	
SA (DO-heat)	5.3	325–350	180			none observed		4
20% CW (DO-heat)	8.4	325–350	390	Voids	12	4×10^{21}	0.46	2
20% CW (N-lot)	10	300	375			none observed		3
20% CW (N-lot)	44	300	2613	Bubbles	2.3	1.6×10^{23}	0.11	4

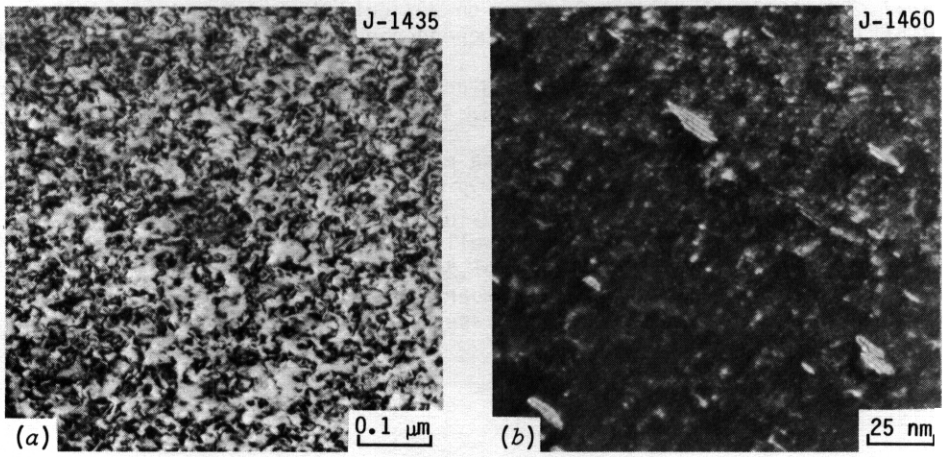

Fig. 3.3.3. Dislocation microstructures of SA 316 irradiated at 300°C to 33.0 dpa and 2216 at. ppn He in HFIR. (*a*) Dislocation network and (*b*) Frank loops.

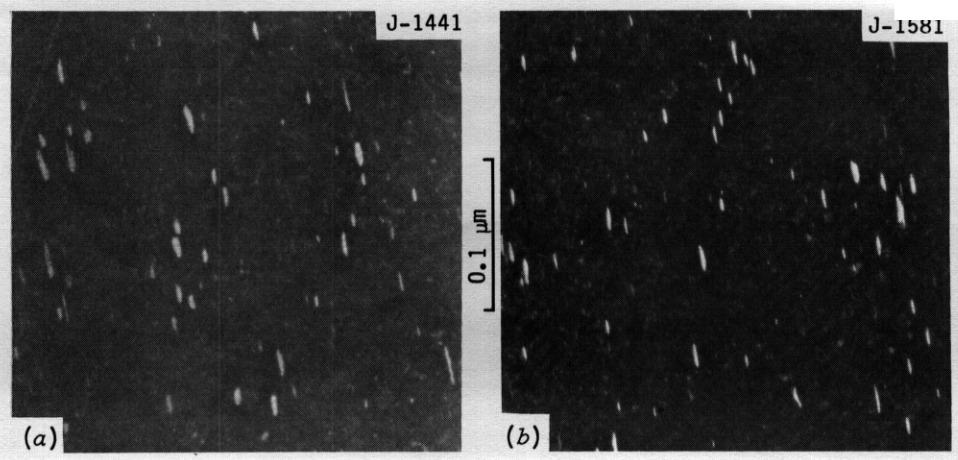

Fig. 3.3.4. Frank loop component of dislocation microstructure of SA and 20% CW 316 irradiated at 300°C to 33.0 dpa and 2116 at. ppm He in HFIR. (*a*) SA and (*b*) 20% CW.

3.3.5 Conclusions

Cavities were observed in both solution-annealed and 20%-cold worked type 316 stainless steels irradiated at 300°C in HFIR to 33.0 dpa and 2116 at. ppm He. A dense population of fine cavities (~2.5 nm in diameter) was uniformly observed throughout the matrix (~3 × 10^{23} cavities/m^3). Cavity fraction swelling was 0.3% in both materials.

Dislocation structures of both network and Frank faulted loops were found. Averaae diameter and number densitv of Frank loops were ~10.3 nm and ~1.4 × 10^{22} loops/m^3.

Table 3.3.4. Frank faulted loop parameters for type 316 stainless steel irradiated in HFIR

Specimen	Average diameter (nm)	Number density (loops/m^3)
SA	10.3	1.3 × 10^{22}
20% CW	10.4	1.5 × 10^{22}

3.3.6 Future Work

Microstructures produced in type 316 stainless steels including DO-heat and N-lot 316 irradiated at 300°C in HFIR will be observed using high-resolution electron microscopy and the behavior of cavities, dislocations, and precipitates under lower temperature irradiation in HFIR will be correlated in type 316 stainless steel.

3.3.7 References

1. P. J. Maziasz, "Microstructural Development on 20%-Cold-Worked Type 316 and 316 + Ti Stainless Steels Irradiated in HFIR: Temperature and Fluence Deoendence of the Dislocation Component," pp. 54–97 in *ADIP Semiann. Rog. Rep. Sept. 30, 1981,* DOE/ER-0045/7, U.S. DOE, Office of Fusion Energy.
2. P. J. Maziasz and M. L. Grossbeck, "Swelling and Microstructure of HFIR-Irradiated 20%-Cold-Worked Types 316 Stainless Steel and 316 + 0.23 wt % Ti," pp. 43-59 in *ADIP Semiann. Prog. Rep. Dec. 31, 1980,* DOE/ER-0045/5, U.S. DOE, Office of Fusion Energy.
3. P. J. Maziasz and D. N. Braski, "Swelling and Microstructural Development in Path A PCA and Type 316 Stainless Steel Irradiated in HFIR to About 22 dpa," pp. 44–62 in *ADIP Semiannu. moa. Rep. Sept. 30, 1982,* DOE/ER-0045/9, U.S. DOE, Office of Fusion Energy.
4. P. J. Maziasz and D. N. Braski, "Improved Swelling Resistance for PCA Austenitic Stainless Steel under HFIR Irradiation Through Microstructural Control," *J. Nucl. Mater.* 1226123. 311–316 (1984).
5. P. J. Maziasz, private communication, September 1985.
6. P. R. Okamoto and S. D. Harkness, "Stress-Biased Loop Nucleation in Irradiated Type 316 Stainless Steel," *J. Nucl. Mater.* 48, 204–206 (1973).

3.4 MICROSTRUCTURAL DEVELOPMENT IN THE AUSTENITIC PCAs IRRADIATED IN HFIR TO 34.0 dpa 300°C — M. P. Tanaka and S. Hamada (Japan Atomic Energy Research Institute, assigned to ORNL) and P. J. Maziasz (Oak Ridge Natio

3.4.1 ADIP Task

ADIP Task I.C.1, Microstructur

3.4.2 Objective

The objective of this work is to determine the microstructural response of JPCA to 34.0 dpa neutron irradiation at 300°C in the High Flux Isotope Reactor (HFIR), and to compare the results with those obtained on U.S. PCA.

3.4.3 Summary

Microstructural observations on JPCA specimens in the solution annealed (SA) and 10 and 20%-cold-worked (CW) conditions indicated that all specimens developed high concentrations of small helium bubbles. In addition, 20%-CW JPCA developed a high concentration of radiation-induced MC precipitates in the matrix. The comparison with U.S. PCA will be given in the next report.

3.4.4 Progress and Status

This work is a part of the U.S./Japan collaborative program to investigate the irradiation response of U.S. and Japanese structural alloys to high levels of atomic displacement and helium content in order to evaluate their use for first wall and blanket structural applications in future fusion reactors.[1] The details and experimental plan for the series of experiments from JP-1 to -8 have also been presented elsewhere.[2,3] This report describes the microstructural development in JPCA during irradiation at 300°C to a neutron fluence producing 34.0 dpa and 2501 at. ppm He.

3.4.4.1 Experimental Procedure

Sheets of 7.5-mm-thick JPCA, whose composition is given in Table 3.4.1, were annealed at 1100°C in air for 1 h. After a surface layer 1 mm thick was ground off each surface, the sheets were reduced to the appropriate thicknesses by alternate cold rolling and vacuum annealing. After a final solution anneal for 1 h at 1100°C, part of the material was cold rolled 10 and 20%. The final thickness of all plates was 0.254 mm. Then disks of 3-mm diameter were punched out from the sheets. The disks were irradiated at 300°C for 16 cycles (= 8000 h) to 33,644 MWd to produce 34.0 dpa and a helium content of 2501 at. ppm. Disks for transmission electron microscopy (TEM) were thinned with an automatic dual-jet Tenupol thinning unit in a hot cell and examined via standard methods using JEM 100CX and 2000FX electron microscopes.

Table 3.4.1. Composition of JPCA

Element	Composition (wt %)	Element	Composition (wt %)
C	0.06	Cr	14.22
Si	0.50	Mo	2.28
Mn	1.77	Ti	0.24
P	0.027	B	0.0031
S	0.005	N	0.0039
Ni	15.60	Fe	Bal

3.4.4.2 Microstructural Development

Quantitative data on dislocation loops, cavities, and swelling are given in Table 3.4.2. Figure 3.4.1 compares the cavity microstructure observed in SA, 10, and 20% CW JPCA. A high concentration of fine cavities (~3 nm in diameter) ($2 \times 10^{23}/m^3$) can be observed in all specimens, resulting in 0.2 to 0.3% swelling of each specimen. The size distribution of the cavity microstructure is shown in Fig. 3.4.2. The sharp peak in the size distribution suggests that the high population of fine cavities is most likely helium bubbles. The ratio of helium concentration for materials calculated from cavity microstructure to that produced by transmutations are listed in Table 3.4.2. The high ratio also suggests that most of the cavities are helium bubbles.

Table 3.4.2. Dislocation loop and cavity microstructural data for JPCA irradiated in HFIR to 34.0 dpa at 300°C

Specimen	Loops		Cavity			
	Diameter (nm)	Density (m^{-3})	nm	Density (m^{-3})	ΔV/V (%)	R[a]
SA	11.5	1.2×10^{22}	2.9	1.9×10^{23}	0.23	0.6
10% CW	10.	1.6×10^{22}	3.0	2.1×10^{23}	0.31	0.8
20% CW	10.6	2.5×10^{22}	2.6	2.3×10^{23}	0.21	0.5

[a]Ratio of calculated helium concentration for specimens from cavity microstructure to that calculated for transmutation.

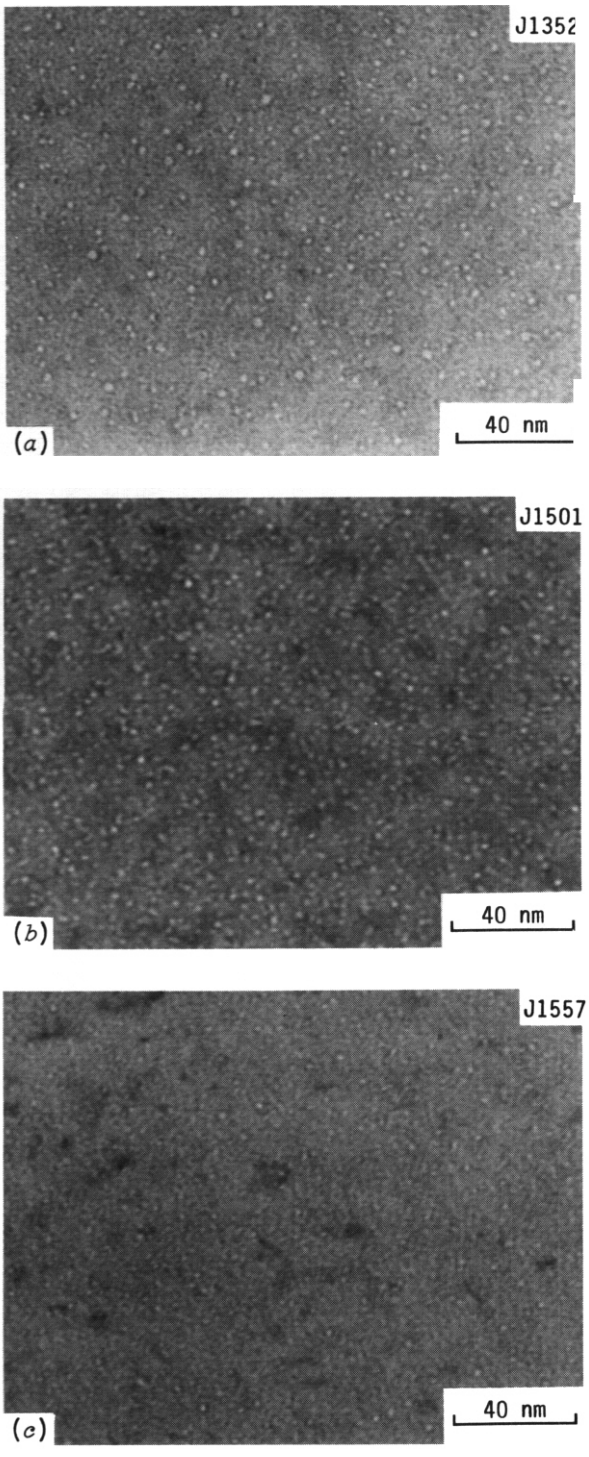

Fig. 3.4.1. Cavity microstructure of (a) JPCA-SA, (6) JPCA-10% CW and (c) JPCA 20% CW after irradiation in HFIR to 34.0 dpa at 300°C.

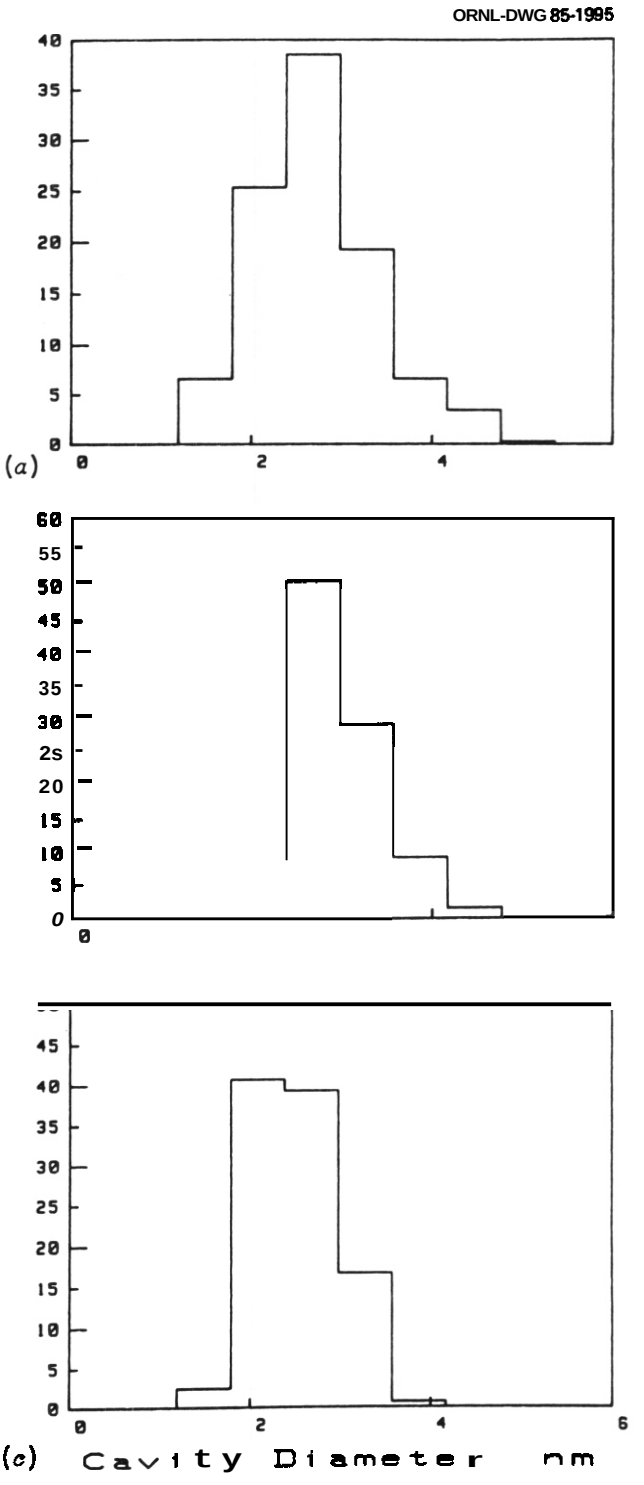

Fig. 3.4.2. Cavity size distribution of (a) JPCA-SA., (b) JPCA-10% CW. and (c) JPCA-20% CW after irradiation in HFIR to-34.0 dpa at 300°C.

Figure 3.4.3 shows Frank faulted loop image separately from the dislocation network, using dark field with <111> kinematical satellite streaks around g_{200} type matrix reflections observed in SA, 10- and 20% CW JPCA. The size distribution of the loop microstructure is shown in Fig. 3.4.4. No big difference can be observed among the examined specimens. However, the average loop size decreases and loop concentration increases in the CW JPCAs compared to SA JPCA.

Figure 3.4.5 shows the radiation produced precipitation in 20%-CW JPCA. The spacing of Moiré fringes of the particles is 1.0 nm, and the direction of the fringes is perpendicular to <200> reflections of the matrix indicating that these particles are MC-type precipitates which have a cube-on-cube relationship with the matrix. It is not certain yet whether or not irradiated SA and 10%-CW JPCA contain MC particles.

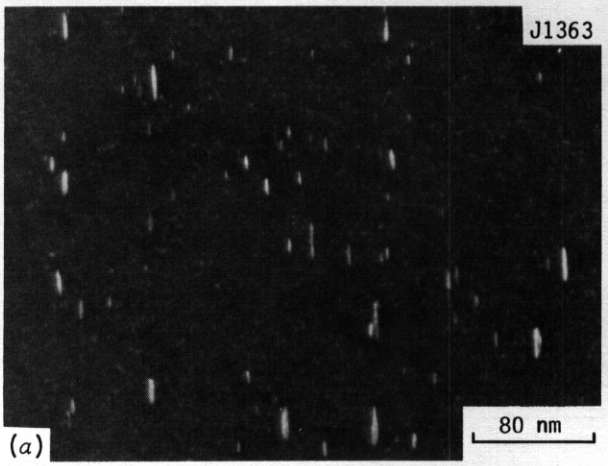

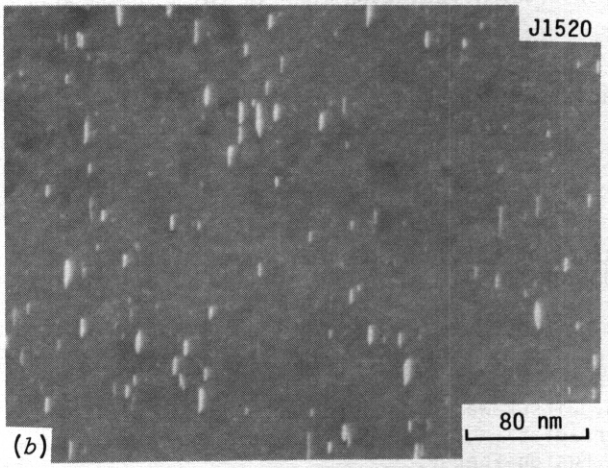

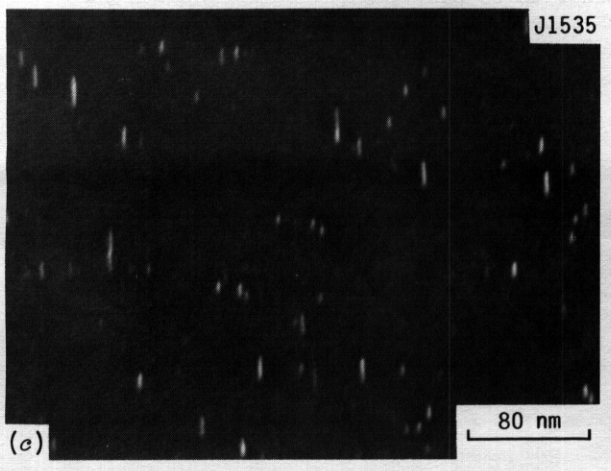

Fig. 3.4.3. Loop microstructure of (*a*) JPCA-SA, (*b*) JPCA-10% CW, and (*c*) JPCA 20% CW after irradiation in HFIR to 34.0 dpa at 300°C.

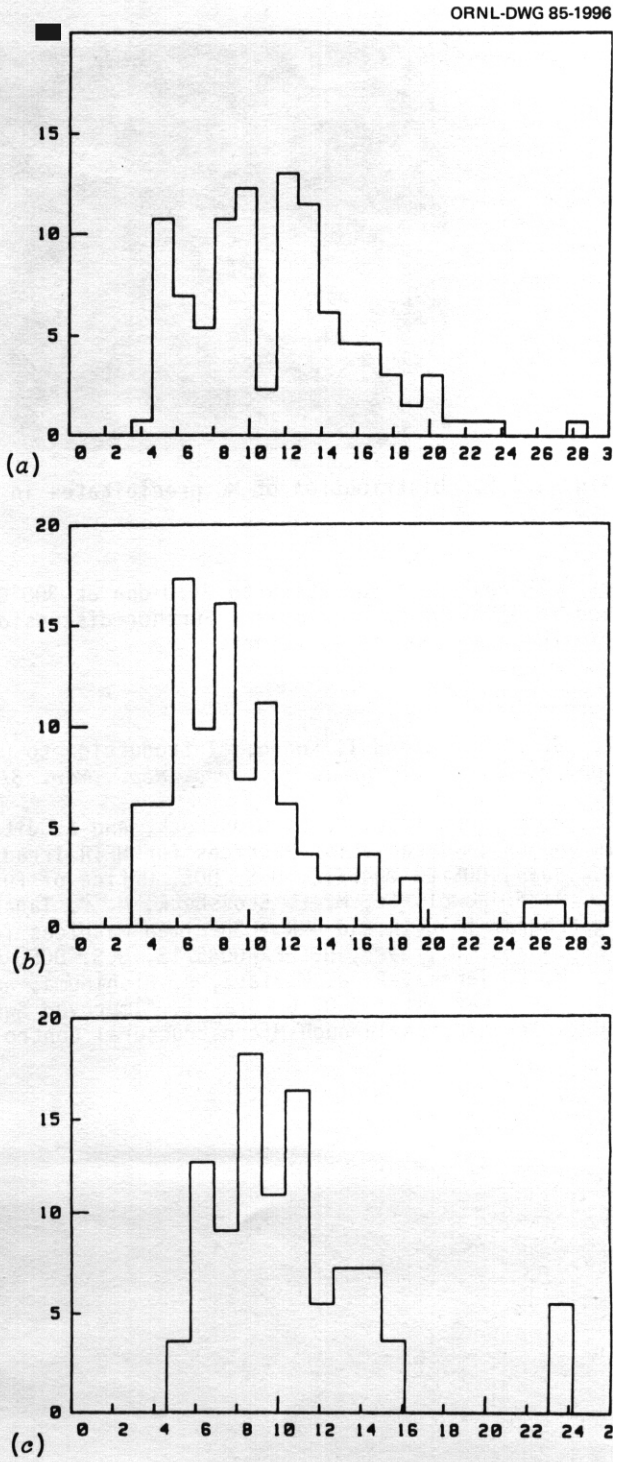

Fig. 3.4.4. Loop size distribution of (*a*) JPCA-SA, (*b*) JPCA-10% CW, and (*c*) JPCA-20% CW after irradiation in HFIR to 34.0 dpa at 300°C.

U.S. PCA with identical metallurgical conditions also show a similar microstructure with a high po tion of fine cavities after the HFIR irradiation to 10 (ref. 4) and 44 (ref. 5) dpa at 300°C. In addit a similar loop structure is observed in U.S. PCAs with identical irradiations conditions. However, a m quantitative analysis is needed to make a direct comparison with JPCA-microstructural data.

In summary, the comprehensive microstructural data of JPCA in the SA, 10- and 20%-CW conditions reveals that all of the specimens examined in this series clearly show a high concentration of fine hel

51568

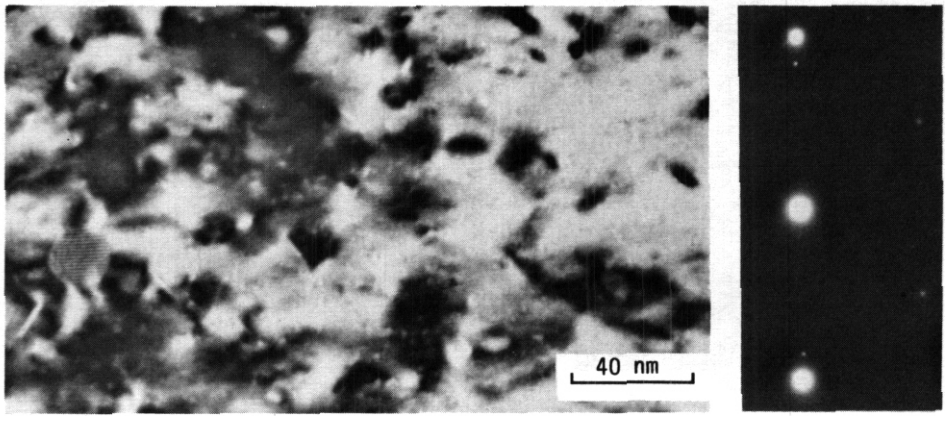

Fig. 3.4.5. Distribution of MC precipitates in JPCA-20% CW after irradiation in HFIR to 34.0 dpa at 300°C.

bubbles HFIR neutron irradiation to 34.0 dpa at 300°C. And radiation produced precipitation of MC is observed in JPCA-20% CW specimens. Further discussions and more detailed comparison with U.S. PCA will be given in the next semiannual report.

3.4.5 References

1. J. L. Scott and T. Kondo, "Introduction to U.S./Japan Collaborative Testing Program in HFIR and ORR," pp. 3 M 6 in *ADIP Semiannu. Prog. Rep., Mar. 31, 1984,* DOE/ER-0045/12, U.S. DOE, Office of Fusion Energy.

2. A. F. Rowcliffe, M. L. Grossbeck, and S. Jitsukawa, "The U.S./Japan Collaborative Testing Program in HFIR and ORR: Irradiation Matrices for HFIR Irradiation," pp. 38-43 in *ADIP Semiannu. Prog. Rep. Mar. 31,* 1984, DOE/ER-0045/12, U.S. DOE, Office of Fusion Energy.

3. A. F. Rowcliffe, M. L. Grossbeck, M. P. Tanaka, and S. Jitsukawa, "The U.S./Japan Collaborative Testing Program in HFIR and ORR: Specimen Matrices for HFIR Irradiation," pp. 61-62 in *ADIP Semiannu. Prog. Rep. Sept. 30, 1984,* DOE/ER-0045/13, U.S. DOE, Office of Fusion Energy.

4. M. P. Tanaka, P. J. Maziasz, A. Hishinuma, and S. Hamada. to be published.

5. P. J. Maziasz and D. N. Braski, "Improved Swelling Resistance for PCA Austenitic Stainless Steel Under HFIR Irradiation Through Microstructural Control," *J. Nucl. Muter.* 122&123, 311316 (1984).

3.5 THE DEVELOPMENT OF AUSTENITIC STAINLESS STEELS FOR FAST INDUCED-RADIOACTIVITY DECAY — R. L. Klueh and P. J. Maziasz (Oak Ridge National Laboratory)

3.5.1 ADIP Task

ADIP tasks I.A.5, Perform Fabrication Analysis, and I.C.1, Microstructural Stability.

3.5.2 Objectives

During the operation of a fusion reactor, the structural material of the first wall and blanket structure will become highly radioactive from activation by the fusion neutrons. Disposal of this material after the service lifetime will be a difficult radioactive waste-management problem. One way to minimize the disposal problem is to use structural materials in which radioactive isotopes induced by irradiation decay quickly to levels that allow simplified disposal techniques. We are assessing the feasibility of developing such austenitic stainless steels.

3.5.3 Summary

Based on the microstructural observations on ten heats of Fe-Mn-Cr-C steels, five more small laboratory heats were obtained. After various heat treatments, optical and transmission-electron microscopy studies and magnetic measurements were used to assess the microstructural constituents present.

3.5.4 Progress and Status

3.5.4.1 Introduction

During the operation of a fusion reactor, the various elements of the alloys that are proposed for the first wall and blanket structure undergo transmutation reactions when irradiated by high-energy neutrons. After the service lifetime of the reactor, these radioactive components must be properly disposed of. The complexity of this waste disposal procedure depends on the time required for the induced radioactivity to decay to levels that no longer pose a threat to people and the environment. The more rapid the decay, the simpler is the disposal task.

We have proposed an alloy-development program for fast induced-radioactivity decay (FIRD) versions of present conventional first-wall and blanket structural candidate alloys.[1] For the austenitic alloys, manganese was proposed as a replacement for nickel, although it was recognized[1] that this may be difficult, because manganese is not as strong an austenite stabilizer as nickel. Hence, it is not possible to simply replace nickel with equal amounts of manganese. It was proposed that an effort be made to determine stable Fe-Cr-Mn-C compositions that are austenitic and that could then be further alloyed to obtain the strength and irradiation-resistant properties required for a fusion reactor structural material.[1]

We previously reported on the microstructure of ten heats of Fe-Mn-Cr-C steels with compositions of 15 or 20% Mn, 10, 15, or 20% Cr, and 0.05, 0.1, 0.2, or 0.4% C.[2] Those alloys were selected on the basis of the Schaeffler diagram.[3] The results indicated that either the boundaries of the Schaeffler diagram need to be modified or the multiplying factor for manganese (taken as 0.5) needs to be changed. This latter approach has been suggested by several investigators.[4-6] Regardless of the best approach to explain the discrepancy with the Schaeffler diagram, the investigation of the ten heats of steel provided insight into possible austenitic-base compositions. Five additional button heats were obtained to verify those observations. Ir

3.5.4.2 Exp

Five 600-g button heats were melted and cast with goal compositions of 20% Mn for all heats. Three heats were to have 0.1% C and 10, 12, and 14% Cr. Two heats with 0.2% C were to have 12 and 16% Cr. The actual compositions are given in Table 3.5.1.

Table 3.5.1. Chemical compositions of button heats melted for fast induced-radioactivity decay (FIRD) alloy-development program

Alloy	Chemical composition,[a] wt %									
	C	Mn	Cr	Si	Ni	Mo	V	Nb	Cu	N
PCMA-10	0.081	19.92	9.97	0.04	0.01	0.01	0.01	0.01	0.02	0.005
-11	0.084	19.99	11.94	0.03	0.01	0.01	0.01	0.01	0.02	0.009
-12	0.18	20.04	11.95	0.02	0.01	0.01	0.01	0.01	0.02	0.008
-13	0.088	19.14	14.01	0.03	0.01	0.01	0.01	0.01	0.04	0.013
-14	0.17	19.85	15.89	0.05	0.01	0.01	0.01	0.01	0.02	0.0012

[a]Balance iron.

The alloys were cast into an ingot of rectangular cross section of 12.7 by 25.4 mm by 152 mn. The ingots were hot rolled at 1050°C to a 6.4-mm thickness, after which they were homogenized 5 h at 1200°C. Each steel was cold rolled to 0.76- and 0.25-mm sheet. The reductions from the 6.4-mm bar were made by successively reducing the cross section 50% and then annealing 1 h at 1150°C. The final sheet was 20% cold worked.

Specimens were examined by optical metallography after the homogenization treatment (5 h at 1200°C), after cold working to 0.76 mn, after the cold-worked sheet was annealed for 1 h at 1150°C and for 8 and 24 h at 1050°C, and after the cold-worked sheet was aged 168 h at 800°C. After each of these treatments, magnetic measurements were made with a "Ferritescope" to obtain a qualitative measure of the ferromagnetic properties of each alloy. Specimens were examined by transmission-electron microscopy after annealing 1 h at 1150°C. Analytical electron microscopy (AEM) was performed on specimens annealed 1 h at 1150°C on a JEM 2000FX microscope equipped with a Tracor-Northern dectector and computer analyzer, using a beryllium soecimen holder to minimize the x-ray background during x-ray energy dispersive spectroscopy (XEDS) analysis.

3.5.4.3 Results and Discussion

A summary of the microstructures observed by optical microscopy is given in Table 3.5.2. Except for the relative amount of a given phase or constituent present, the microstructures after 5 h at 1200°C and 8 and 24 h at 1050°C were generally similar to those observed after 1 h at 1150°C; the microstructure of the specimens annealed at 1150°C will be discussed later. Microstructures of the cold-worked steels annealed 168 h at 800°C were considerably different, primarily in the large amount of precipitate that formed at the lower temperature. Because of the complicated precipitate structure of the aged cold-worked steels, no phases are given in Table 3.5.2. However, for the other heat treatments, δ-ferrite (δ), austenite (γ), and martensite (M) were identified as constituents (Table 3.5.2). No precipitate phases are listed in Table 3.5.2 beyond stating that a precipitate (P) was observed, meaning that a large amount of a precipitate ohase for phases) was obvious. Possible precipitate phases'inciude carbides, Laves phase, sigma phase, and chi phase. The precipitate phases will be discussed in more detail after TEM studies have been completed.

Table 3.5.2. Tentative identification[a] of microstructural constituents of Fe-Mn-Cr-C steels

Alloy	Constituents[b]		
	1200°C/5 h	1150°C/1 h	1050°C/8 h
PCMA-10	γ + M	γ + M	γ + M
-11	γ + M	γ + M	γ + M
-12	γ + P	γ	γ
-13	γ + δ	γ + δ	γ + δ
-14	γ + δ	γ + δ	γ + δ

[a] Identified by optical microscopy.

[b] γ = austenite, 6 = 6 ferrite, M = martensite, and P = precipitate.

The magnetic measurements are aualitative and meant to indicate the presence of magnetic constituents (6-ferrite or α′-martensite) in the 'microstructure. Results from the Ferritescope measurements are given in Table 3.5.3. The Ferritescope is routinely used to mangetically determine the amount of 6-ferrite present in austenitic stainless steel weld metals where austenite and ferrite are the primary constituents present. A "ferrite number" is determined. This number is approximately equal to the percent of 6-ferrite in the austenitic weld metal for low ferrite contents. A maximum Ferritescope reading of 30 is possible, and several of the first ten alloys had such readings.2 No maximum readings were obtained for PCMA-10 to -14 (Table 3.5.3). The ferrite numbers of Table 3.5.3 are used here to indicate qualitatively the amount of magnetic constituent present.

Table 3.5.3. Ferrite numbera as a measurement of the extent of ferromagnetism of an alloy

Alloy	Ferrite numberb					
	Cold worked	1200°C/ 5 h	1150°C/ 1 h	1050°C/ 8 h	1050°C/ 24 h	800°C/ 168 h
PCMA-10	3	0	0.4	0.2	0.1	0
-11	5	0	0.6	0.6	0	0
-12	2	0	0.4	0.2	0	0
-13	9	7.5	16	6.2	8	0
-14	5	2	20	18	17	0

[a] Measurements made by a Ferritescope.

[b] Maximum number measured with a Ferritescope is 30.

There appear to be similarities in the microstructures of the two low-chromium, low-carbon alloys (PCMA-10 and -11). The steel with 10% Cr–0.1% C (PCMA-10) contains considerable amounts of an acicular-appearing constituent [Fig. 3.5.1(*a*)], which was initially assumed to be E-martensite. because the magnetic readings for the annealed steel were extremely low. The 12% Cr–0.1% C steel (PCMA-11) has a finer structure than the 10% Cr steel. With optical microscopy it was not possible to determine if the microstructure contained martensite or a high density of annealing twins [Fig. 3.5.1(*b*)], although it was assumed to be martensite (Table 3.5.2).

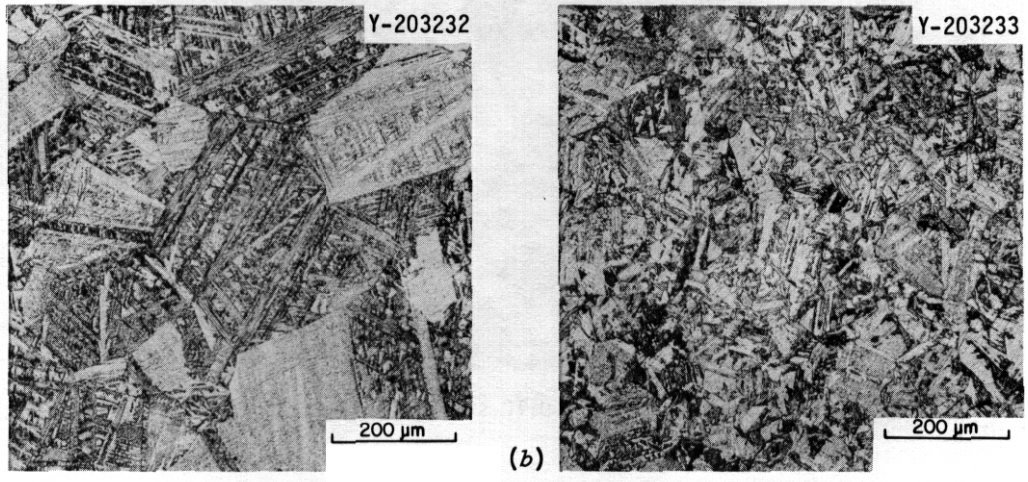

Fig. 3.5.1. Microstructure of *(a)* Fe–20Mn–10Cr–0.1C (PCMA-IO) and *(b)* Fe–20Mn–12Cr–0.1C (PCMA-11) steels solution annealed 1 h at 1150°C.

The 10- and 12%-Cr steels with 0.1% C annealed 1 h at 1150°C were examined by TEM. It appears that the steel with 10% Cr contains a high density of stacking faults (Fig. 3.5.2), but the steel with 12% Cr contains ε-martensite (Fig. 3.5.3). If this is true, it would be contrary to predictions obtained from the Schaeffler diagram.3 The TEM observations do indicate that the steels are basically austenite, which was the reason for choosing these compositions.2 It also reinforces the observation that the Schaeffler diagram based on the equation for the nickel equivalent with a multiplying factor for manganese of 0.5 is not applicable for these high-manganese steels. Based on the Schaeffler diagram, we would have expected to find martensite in the low-chromium steel and then disappear with an increase in chromium. More TEM will be required to understand the present observations.

The 12Cr–0.2%C steel (PCMA-12) solution annealed 1 h at 1150°C was entirely austenitic. Optical microscopy showed the steel to have a propensity for twin formation [Fig. 3.5.4(*a*)]; electron microscopy revealed a matrix devoid of other phases, stacking faults, or dislocations [Fig. 3.5.4(*b*)].

The two high-chromium steels (PCMA-13 and -14) contained 6-ferrite (Fig, 3.5.5). Based on the optical microscopy and the magnetic measurements, the nominally 16% Cr–0.2% C steel (PCMA-14) contained the most δ-ferrite. Figure 3.5.6 shows a TEM micrograph of a δ-ferrite particle in an austenite matrix. Note the high dislocation density in the 6-ferrite compared to the austenite. These dislocations could be either the result of transformation stresses or of differential contractions of the phases during cooling. When the cold-worked steels were aged 168 h at 800°C and then etched for sigma phase, the phase was observed, especially for the steel with 16% Cr, where it was obvious that the sigma phase had formed in what had previously been 6-ferrite (Fig. 3.5.7).

The compositions of the 6-ferrite particles and the austenite grains of PCMA-14 were analyzed by REM (Table 3.5.4). For the iron, chromium, and manganese. the primary components, only the chromium showed a significant partitioning between the ferrite and austenite (Fig. 3.5.8), with the concentration greater in the δ-ferrite. The manganese and iron concentrations were essentially the same in the two phases. These observations on manganese differ from observations for nickel in nickel-chromium austenitic stainless steels.[7] For type 308 stainless steel, which nominally contains 20.5% Cr, 10.5% Ni, Vitek and David[8] found that nickel was strongly partitioned to the austenite, chromium to the 6-ferrite. In the annealed condition, the concentrations of the nickel in austenite and ferrite were 10.2 and 4.8%, respectively; the chromium concentrations in austenite and ferrite were 21.9 and 31.8%, respectively. The difference in partitioning behavior of manganese and nickel between austenite and ferrite suggests at least different solubilities of these elements in the δ-ferrite. These results may also add insight into the difficulties with expressing the effects of manganese in terms of the simple nickel and chromium equivalent equations used in conjunction with the Schaeffler diagram.

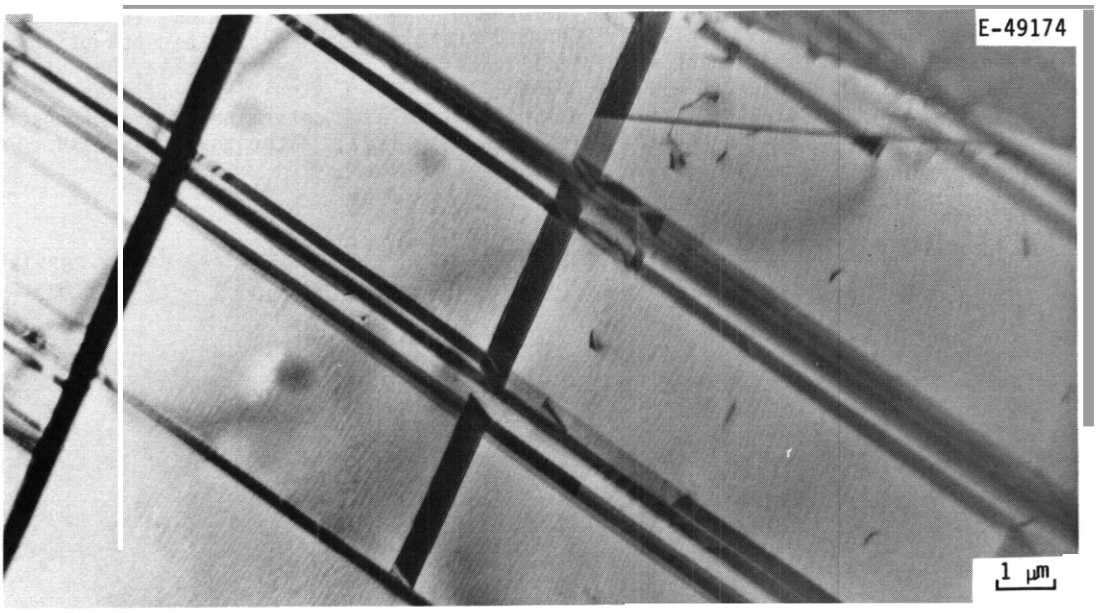

Fig. 3.5.2. Microstructure of Fe–20Mn–10Cr–0.1C steel showing the austenite matrix with a high density of stacking faults.

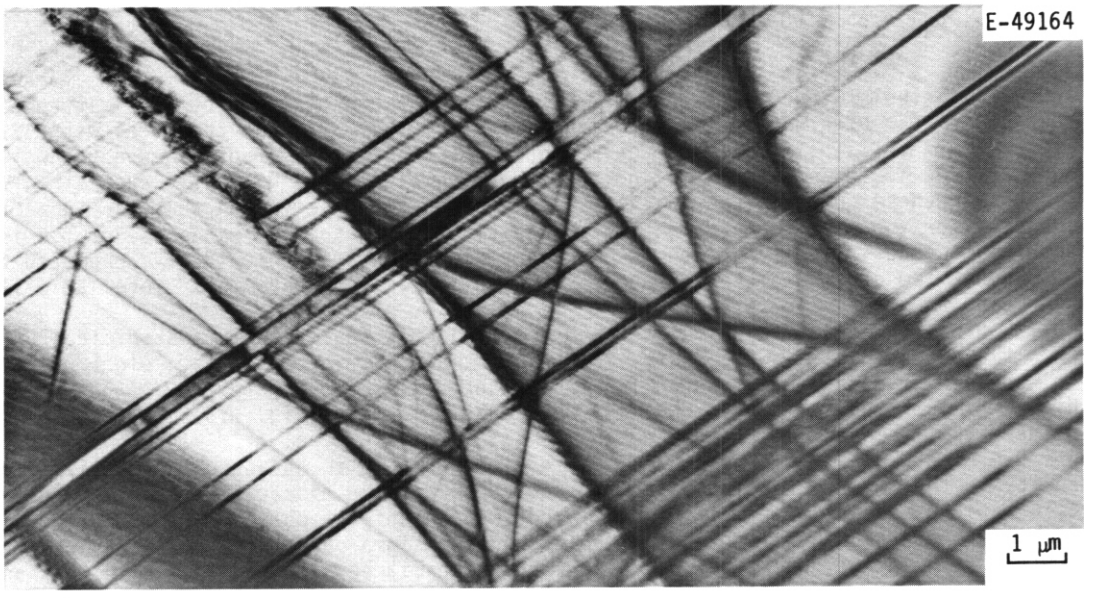

Fig. 3.5.3. Microstructure of Fe–20Mn–12Cr–0.1C steel solution annealed 1 h at 1150°C showing the austenite matrix with martensite needles.

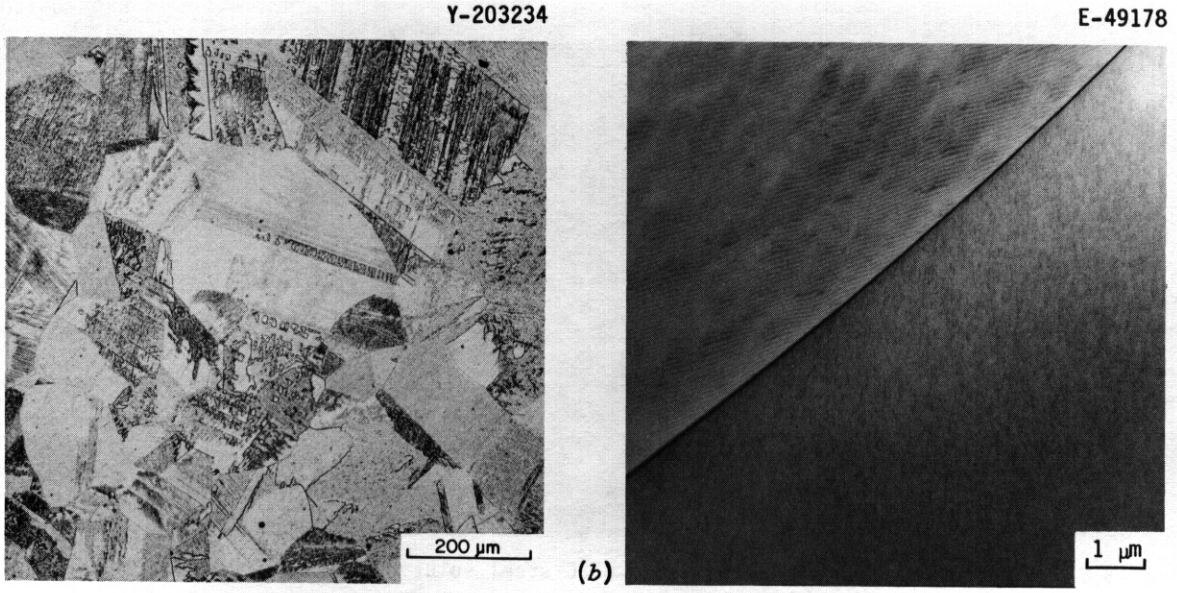

Fig. 3.5.4. Microstructure of Fe–20Mn–12Cr–0.2C steel (PCMA-12) solution annealed 1 h at 1150°C as observed by (*a*) optical and (*b*) electron microscopy.

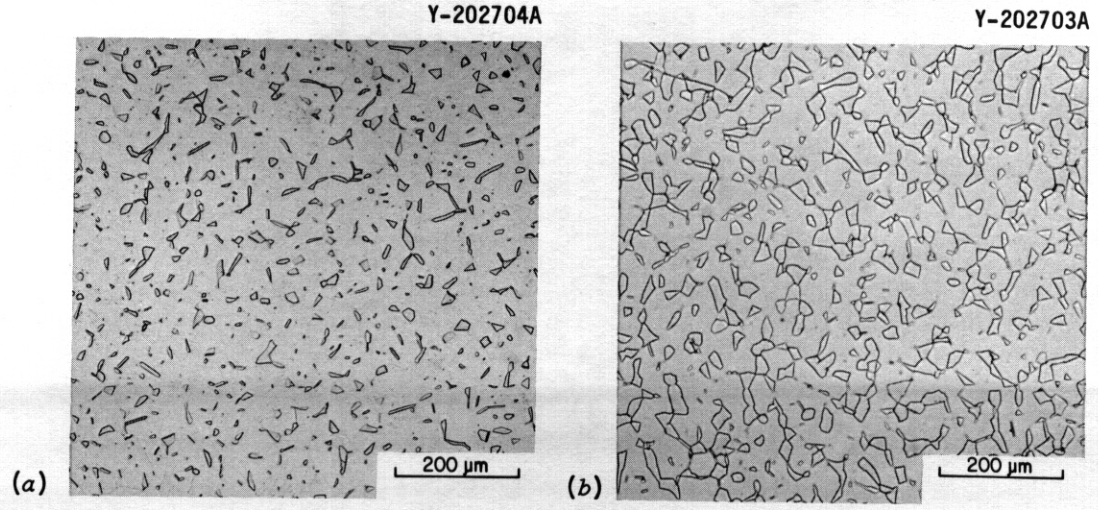

Fig. 3.5.5. Microstructure of (*a*) Fe–20Mn–14Cr–0.1C (PCMA-13) and (*b*) Fe–20Mn–16Cr–0.2C (PCMA-14) steels solution annealed 1 h at 1150°C.

J-1408

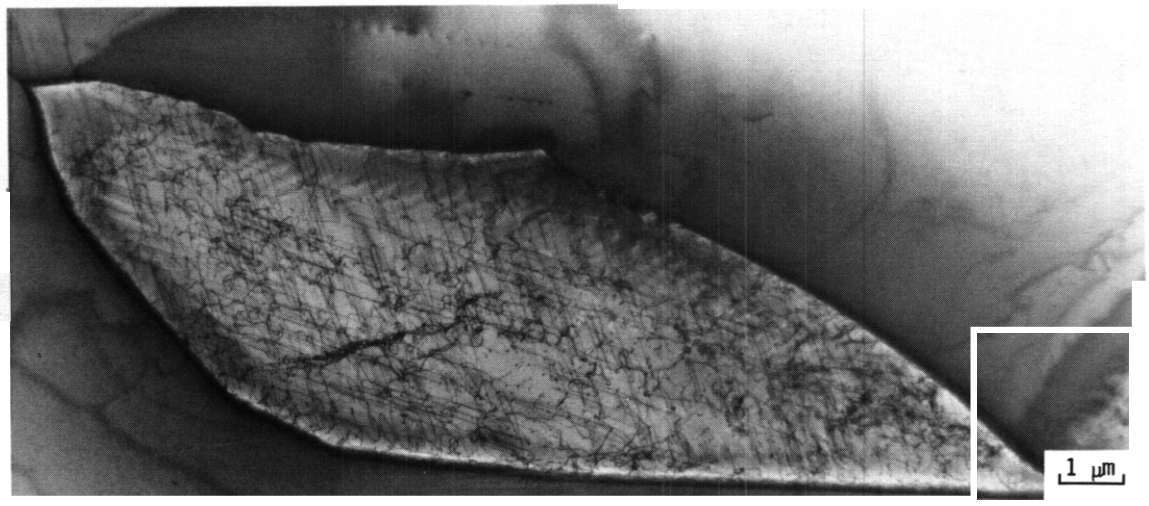

Fig. 3.5.6. Microstructure of Fe–20Mn–16Cr–0.2C steel solution annealed 1 h at 1150°C. showing a δ-ferrite grain in the austenite matrix.

Y-203239

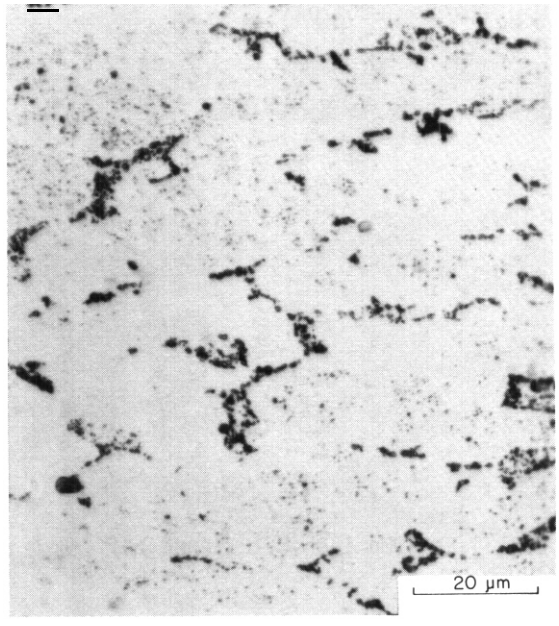

Fig. 3.5.7. Microstructure of Fe–20Mn–16Cr–0.2C steel cold worked, then aged 168 h at 800°C. Specimen was etched with Maurakami's reagent. The dark phase that formed in the regions that were previously δ-ferrite is identified by this etching technique as sigma phase.

3.5.5 *Summary*

The results of the microstructural observations on 15 button melts of Fe-Mn-Cr-C steels have revealed interesting characteristics of these high-manganese alloys. Further work is required to understand the effect of composition on the stacking fault and martensite formation and the interpretation of the effectiveness of manganese as an austenite stabilizer. The major objective of this work was the determination of base compositions that could be further alloyed for radiation resistance and strength. We feel that we have reached the point where such a base composition can be selected. During the next reporting period, base compositions will be selected, and alloys will be prepared with alloying elements added for strength and radiation resistance.

3.5.6 References

1. R. L. Klueh and E. E. Bloom, "The Development of Austenitic Steels for Fast Induced-Radioactivity Decay for Fusion Reactor Applications," pp. 73–85 in ***Optimizing Materials for Nuclear Applications.*** The Metallurgical Society of AIME, Warrendale, PA, 1985.
2. R. L. Klueh and P. J. Maziasr, "The Development of Austenitic Steels for Fast Induced-Radioactivity Decay," pp. 69–75 in *ADIP* ***Semiannu.*** *Prog. Rep.* ***Sept. 30, 1984,*** DOE/ER-0045/13, U.S. DOE, Office of Fusion Energy.
3. H. Schneider, "Investment Casting of High Hot-Strength 12-Percent Chrome Steel," *Foundry* ***Trade J.*** 108, 563–564 (1960).
4. E. R. Szumachowski and O. J. Kotecki, "Manganese Effect on Stainless Steel Weld Metal Ferrite." *Welding J.* 63. 156s–161s (1984).
5. F. C. Hull, "Delta Ferrite and Martensite Formation in Stainless Steels," *Welding J.* **52,** 193s–203s (1973).
6. R. H. Espy, "Weldability of Nitrogen-Strensthened Stainless Steels." *Welding J.* **61,** 149s–156s (1982).
7. J. M. Vitek and S. A. David. "Analytical Electron Microscopy Evaluation of Laser Welded 308 Stainless Steel," pp. 169–175 in ***Scanning Electron*** *Microscopy/1981/I*, SEM, Inc., AMF O'Hare, Chicago, 1981.

Table 3.5.4. XEOS phase compositional measurements in Fe–20Mn–16Cr–0.2C steel (PCMA-14), solution annealed 1 h at 1150°C

Composition,[a] at. %[a,b]								
Si	P	Ti	V	Cr	Mn	Fe	Ni	Mo
γ-austenite matrix								
0.7	1.0	0.1	0.3	17.9	21.5	58.4	0.0	0.1
0.7	1.0	0.1	0.1	17.8	20.6	59.6	0.0	0.05
δ-ferrite particles								
0.0	0.0	0.0	0.0	23.2	20.0	56.4	0.0	0.1
0.1	0.0	0.0	0.2	23.1	19.5	57.0	0.0	0.1
0.0	0.0	0.2	0.2	23.1	19.4	56.8	0.0	0.1

[a]Metallic elements with 2 greater than Al.

[b]Each line of compositional numbers represents one individual measurement.

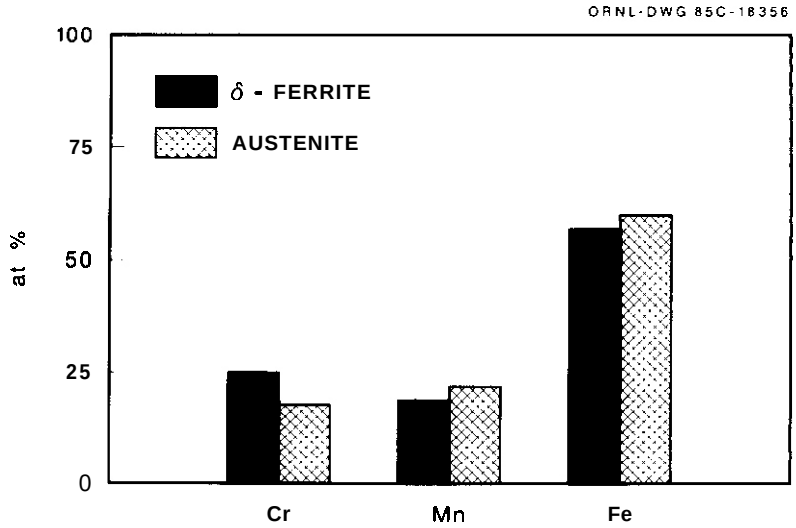

Fig. 3.5.8. Chemical composition of chromium, magnesium, and iron in δ-ferrite and austenite phases as determined by XEOS on the Fe–20Mn–16Cr–0.2C steel solution annealed 1 h at 1150°C.

4. HIGHER STRENGTH Fe-Ni-Cr ALLOYS

5.1 EFFECT OF THERMAL-MECHANICAL TREATMENT AND IMPURITY LEVEL ON THE YIELD STRENGTH AND MICRUSTKUCTUKE OF V-15Cr-5Ti ALLOY - B. A. Loomis and B. J. Kestel (Argonne National Laboratory)

5.1.1 ADIP Task

ADIP Task I.A.I. Define Material Property Requirements and Make Structural Life Predictions.

5.1.2 Objective

The objective of this work is to provide guidance on the applicability of alloys for structural components in a magnetic fusion reactor.

5.1.3 *Summary*

The yield stress, total elongation, and hardness for V-15Cr-5Ti alloys with a range of O, N, and C concentration and annealing treatment are presented in this report. The experimental results suggest that these mechanical properties are not determined solely by the O, N, and C concentration.

5.1.4 Progress and Status

5.1.4.1 Introduction

Observations of the microstructure in ion-irradiated V-15Cr-5Ti specimens by transmission electron microscopy have shown that irradiation-induced dimensional change due to voids or gas-filled cavities in a V-15Cr-5Ti structural material will not be a major concern during the lifetime of a reactor. However, these observations suggest that the ductility of the alloy may be decreased substantially by the presence of a high density of irfadiation-produced, disc-like precipitates in the vicinity of grain boundaries and intrinsic precipitates.

The ductility of the irradiated alloy may be improved with a suitable pre-irradiation heat treatment and a maximum concentration of O, N, and C impurity in the alloy. In this report the yield stress, ductility, and hardness are presented for unirradiated V-15Cr-5Ti alloys with a range of O, N, and C concentration and heat treatment.

5.1.4.2 Materials and Procedure

The V-15Cr-5Ti alloys (Table 5.1.1) were obtained from the Fusion Materials Inventory (ORNL) and the ANL materials inventory. Experime tal data from an earlier study on a relatively pure V-15Cr-5Ti alloy are also presented for comparison.[1] Sheet tensile specimens with a nominal thickness of 0.4 mm and a guage length and width of 7.6 mm and 1.5 mm, respectively, were machined from the as-rolled material.

Table 5.1.1 Impurity concentrations in V-15Cr-5Ti alloys

V-15Cr-5Ti Source*	Concentration (wppm)		
	C	N	O
FPP CAM 834-6	320	460	310
FPP CAM 835-4	170	520	230
ANL AM 114	195	16	205
ANL AM 274	230	138	810
TID-4500[2]	130	90	100

*The V-15Cr-5Ti alloys contained approximately 15 w/o Cr and 5 w/o Ti.

The tensile specimens (wrapped in tantalum foil) were annealed in quartz tubes containing high-purity argon for one hour at either *950,* 1050, 1125, or 1200°C and quenched in the capsules in water. The annealed specimen surfaces were subsequently polished to a 0.3-μm finish. Load versus elongation curves for the tensile specimens were obtained at ambient room temperature using a strain rate of 1.1 x 10^{-3} s^{-1}.

5.1.4.3 Results

Alloy microstructure - The microstructures for the annealed specimens are shown in Figs. 5.1.1 and 5.1.2. It can be noted in Fig. 5.1.1 that precipitates were uniformly distributed in the matrix of the CAM 835-4 (Fig. 5.1.1b) and ANL AM 274 (Fig. 5.1.1d) alloys which was not the case for the CAM 834-6 (Fig. 5.1.1a) and ANL AM 114 (Fig. 5.1.1c) alloys. The TEM microstructures (Fig. 5.1.2) showed that the grain boundaries in these alloys were relatively free of precipitates irregardless of the O, N, and C concentration in the alloy. The average grain diameters in the recrystallized allays after the one-hour

anneal at 1125 and 1200°C are listed in Table 5.1.2. Since the fabrication history for these alloys could not be documented, the grain diameters in Table 5.1.2 may not be directly related to the different O, N, C concentrations in the alloys. Nevertheless, the higher purity materials had the largest grain diameter.

Table 5.1.2 Average grain diameter in recrystallized V-15Cr-5Ti alloys.

Alloy	Average Grain Diameter(mm)	
	1125°C	1200°C
FPP CAM 834-6	0.024	0.020
FPP CAM 835-4	0.008	0.007
ANL AM 114	0.030	0.030
ANL AM 274	0.013	0.012
TID-4500	0.04-0.08	0.08

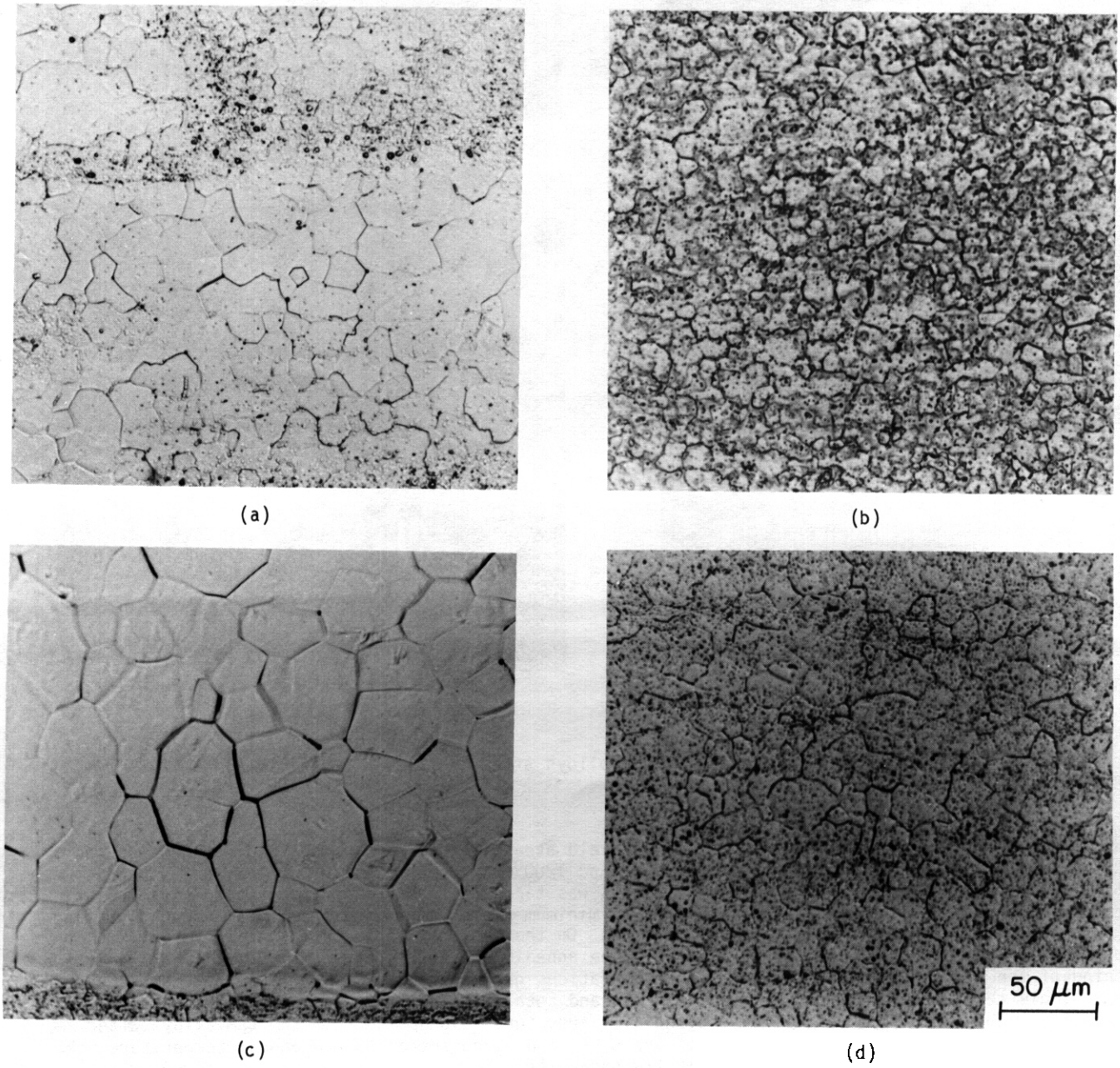

Fig. 5.1.1. Microstructure for V-15Cr-5Ti alloys after the 1125°C anneal : (a) CAM 834-6, (b) CAM 835-4, (c) ANL AM 114, (d) ANL AM 274.

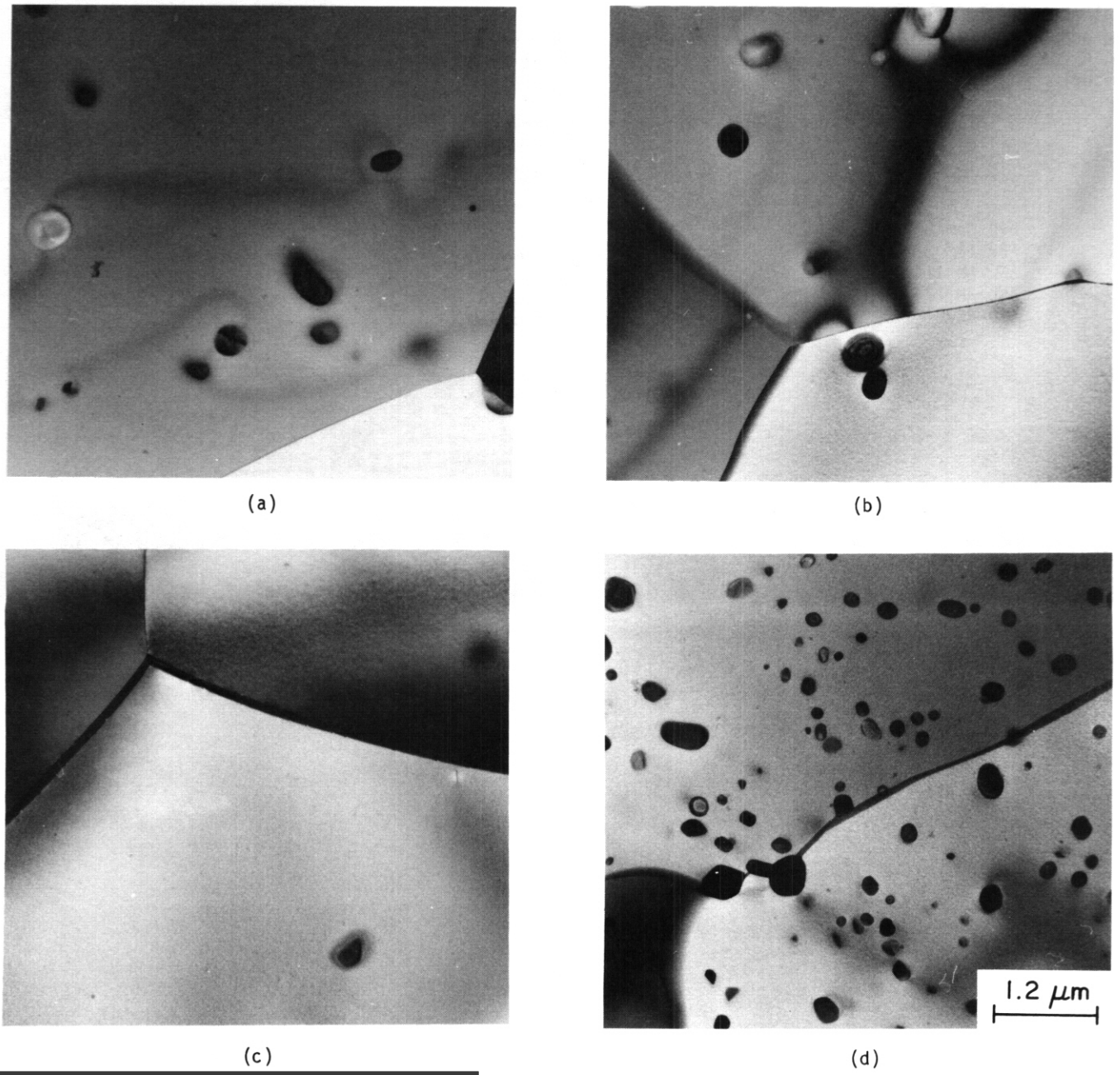

Fig. 5.1.2. TEM microstructure for V-15Cr-5Ti alloys after the 1125°C anneal: (a) CAM 834-6, (b) CAM 835-4, (c) ANL AM 114, (d) ANL AM 274.

Yield stress, total elongation. and hardness - The yield stress, total elongation, and hardness of the V-15Cr-5Ti alloys after anneals at 950, 1050, 1125, and 1200°C are shown in Figs. 5.1.3, 5.1.4, and 5.1.5, respectively. The yield stress for the alloys was taken as the stress at the upper yield point. These results showed that the V-15Cr-5Ti alloy had a minimum yield stress, maximum total elongation, and minimum hardness after the one-hour anneal at 1125°C. On the basis of these data, the recrystallization temperature for the V-15Cr-5Ti alloy was ~1125°C. The anneals at 1200°C resulted in significant solution hardening of the alloy for total O, N, and C concentrations greater than ~300 wppm. There did not appear to be a simple relationship between the yield stress and total elongation and the impurity concentration in the alloy. The ANL alloys exhibited substantially less total elongation than the CAM alloys after anneals at 1125°C and 1200°C. Irregardless of the O, N, and C concentration and anneal temperature, the fracture mode for the alloys was predominantly transgranular.

AES, XEDS, and SAM analyses - The V-15Cr-5Ti alloys have been examined for constituent distribution in the microstructure by use of auger electron spectroscopy (AES), x-ray energy dispersive spectroscopy

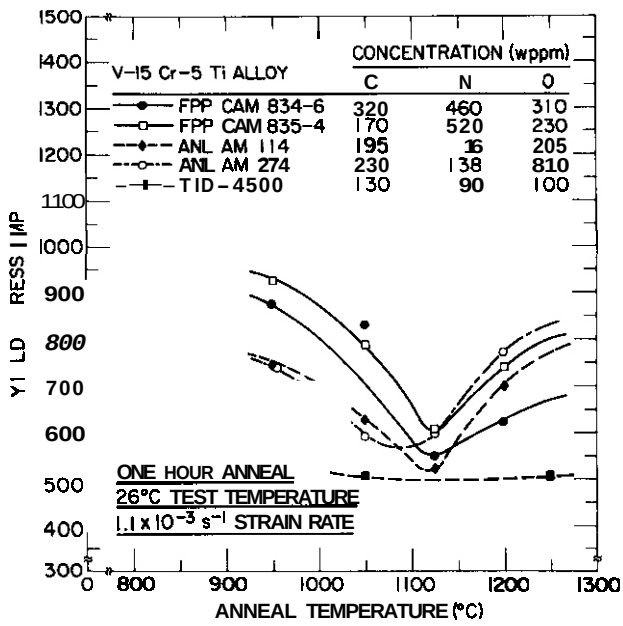

Fig. 5.1.3. Yield stress of V-15Cr-5Ti alloys.

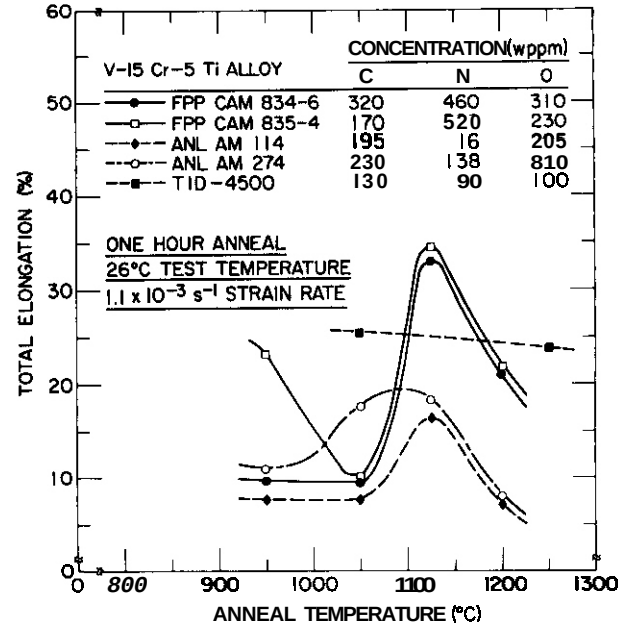

Fig. 5.1.4. Total elongation of V-15Cr-5Ti alloys.

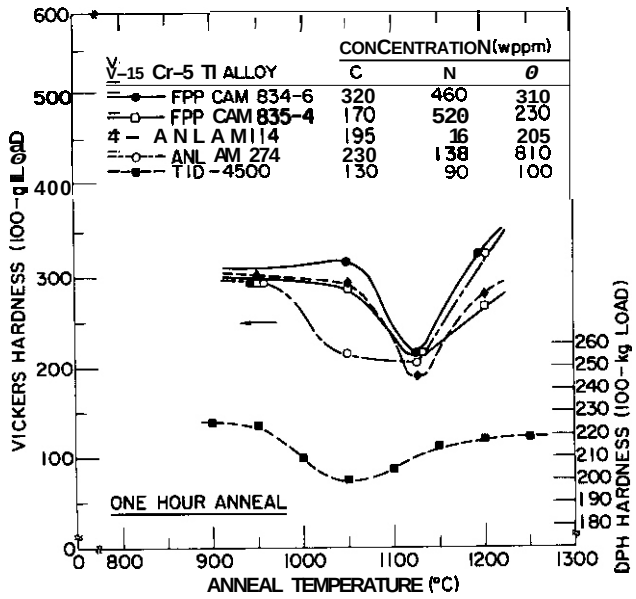

Fig. 5.1.5. Hardness of V-15Cr-5Ti alloys.

(XEDS), and scanning auger microprobe *(SAM)* techniques. These analyses are incomplete at the present time, but some general aspects on constituent distribution have emerged from these initial analyses. The AES analyses have shown significant concentrations of Mg, Si, and S in the near-surface layer (~10 nm) of the specimens annealed at 1125°C. The concentrations of these impurities were not strongly dependent on the alloy. The XEDS analyses have shown a depletion of Cr and Ti concentration in the vicinity of grain boundaries in the annealed alloys. In the case of ion-irradiated (50 dpa) V-15Cr-5Ti alloys, the XEUS analyses have shown significant enrichment of the Cr and Ti concentration in the vicinity of grain boundaries. Also, the AES analyses on ion-irradiated alloys have shown significant Cr enrichment in the near-surface layers. The lineal SAM analyses suggested that the Cr and Ti concentration in the annealed alloys had a quasi-periodic (~0.1 mm) variation. These variations were more evident for the ANL alloys.

5.1.4.4 Discussion of results

The experimental results obtained in this study have shown that the ductility of the V-15Cr-5Ti alloy can be increased by limiting the heat treatment temperature for the alloy to ~1125°C. An unexpected result from this study was the absence of an obvious relationship between the impurity concentration and the yield stress and total elongation for the alloy. Because of the substantial difference between the total elongation for the CAM alloys and tne ANL alloys, there must have been an additional factor that was important for determining the total elongation. Uifferent fabrication schedules for the CAM alloys and the ANL alloys may have contributed to their different response to tensile deformation.

5.1.4.5 Conclusions

1. The recrystallization temperature for the rolled V-15Cr-5Ti alloy was ~1125°C.
2. The mechanical properties of the V-15Cr-5Ti alloy were not determined solely by the O, N, and C impurity concentration.
3. The fabrication schedule for the V-15Cr-5Ti alloy will likely have a major impact on *the* mechanical properties *of* this alloy.

5.1.4.6 References

1. B. A. Loomis and D. L. Smith, "Solute Segregation and Void Formation in Ion-Irradiated Vanadium-Base Alloys", pp. 85-90 in *Alloy Development for Irradiation Performance,* Semiannual Progress Report September 30, 1984, DOE/ER-0045/13, U. S. Department of Energy, Office of Fusion Eneryy.
2. J. C. La Vake and C. T. Wang, "Vanadium Purification", CEND-3742-356, UC-25, Metals, Ceramics, and Materials, TID-4500, 54th Edition, November, 1969.

5.2 THE EFFECT OF COLD WORK ON THE OUCTILITY OF V-15Cr-5Ti IMPLANTED WITH HELIUM — D. N. Braski (Oak Ridge National Laboratory)

5.2.1 AOIP Task

ADIP Task I.B.15, Tensile Properties of Reactive and Refractory Alloys.

5.2.2 Objective

The goal of this research is to investigate the effects of displacement damage and helium generation on the properties of vanadium alloys.

5.2.3 *Summary*

Cold working the V-15Cr-5Ti alloy eliminated embrittlement, due to 282 at. ppm of ^3He, by creating a microstructure in which the grain boundaries were broken up and the helium was distributed rather uniformly on the dense dislocation networks.

5.2.4 Progress and Status

5.2.4.1 Introduction

Disks and tensile specimens of V-15Cr-5Ti, in both the annealed and cold-worked conditions, were implanted with helium using the tritium trick technique. The resulting helium bubble distributions and their effect on the subsequent tensile properties of the alloy were studied.

5.2.4.2 Experimental

The material used in this experiment was from the Westinghouse heat CAM-834-3 and contains, by weight percent, 14.5 Cr, 6.2 Ti, 0.032 C, 0.031 O, 0.046 N, balance V. The 3-mm-diam disks were punched from 0.25-mm-thick sheet (50% cold worked) and the SS-3 tensile specimens' were machined from 0.86-mm-thick sheet (50% cold worked). Following fabrication, a portion of both disks and tensile specimens were annealed for 1 h at 1200°C to produce the annealed condition. The helium was implanted to two different levels using the tritium trick.2 A ^3He level of 90 at. ppm was produced by using injection and pump-out temperatures of 600°C while 282 at. ppm was produced using temperatures of 400°C. The helium analyses were performed by Dr. B. M. Oliver of Rockwell International Corporation, Canoga Park, CA. The tensile specimens were tested under a vacuum of less than 10^{-4} Pa, at 420, 520, and 600°C, using a strain rate of 1.1×10^{-3} s^{-1}. Fracture surfaces were examined by scanning electron microscopy (SEM) and microstructures by transmission electron microsopy (TEM).

5.2.4.3 Results and Discussion

The results of the tensile tests for the annealed and cold-worked V-15Cr-5Ti specimens are listed in Tables 5.2.1 and 5.2.2, respectively. Since the implanted helium affected the ductility of annealed V-15Cr-5Ti quite significantly, values of total elongation at the three temperatures were plotted as function of helium level as shown in Fig. 5.2.1. The values for the cold-worked material are also shown for comparison. As shown previously,[3] a helium level of approximately 300 at. ppm in annealed specimens will lower the total elongation to a very low value. A number of data points from that previous experiment (data at 14. 80, and 300 at. ppm) have been plotted along with the present data and are seen to be consistent. For the annealed material, there appears to be a threshold between 100 and 300 at. ppm He where the implanted gas begins to markedly affect its tensile ductility. In contrast to the results for the annealed specimens, the cold-worked ones were much less sensitive to helium, at least within the range of levels used in the present experiment. The cold-worked material, without helium, exhibited the relatively low values of total elongation that

Table 5.2.1. Tensile properties of annealed V–15Cr–5Ti with different levels of implanted helium

Test temperature (°C)	Helium level (at. ppm)	Strength, MPa		Elongation, %	
		Yield	Ultimate tensile	Uniform	Total
420	0	370	504	15.2	24.3
420	90	451	619	12.6	21.6
420	90	438	617	13.6	22.8
420	282	358	371	0	0
420	282	345	352	0	0
520	0	334	513	13.5	23.3
520	90	416	623	13.2	20.6
520	90	404	611	13.0	20.5
520	282	329	343	0	0
520	282	324	331	0	0
600	0	317	557	12.6	20.5
600	90	399	638	11.8	20.0
600	90	403	635	11.2	19.0
600	282	340	425	0	2.6
600	282	331	390	0	1.4

normally accompany large increases in yield strength. The ductilities were actually increased by implanting 90 at. ppm He. The improvement was probably due to the recovery of the cold-worked microstructure which could have occurred during the tritium trick procedure. Further additions of implanted helium had little effect on the ductility of cold-worked specimens. The reason why the cold-worked microstructure was able to successfully accommodate the helium will be clear after viewing the transmission electron micrographs presented later in this report.

After testing at all three temperatures, the fracture surfaces of both the annealed and cold-worked specimens containing 90 at. ppm He were characteristic of ductile failure. At 282 at. ppm, the annealed specimens tested at all three temperatures failed intergranularly, as illustrated by a representative micrograph taken from a specimen tested at 420°C [Fig.5.2.2(*a*)]. All of the cold-worked specimens tested at the higher helium level failed by ductile shear, as shown in Fig.5.2.2(*b*). Therefore, cold working successfully changed the mode of failure in-the V-15Cr-5Ti alloy from brittle to ductile. Tests are currently being evaluated to determine how much helium can be accommodated in the cold-worked alloy before it too becomes embrittled.

The microstructure of the annealed V-15Cr-5Ti with 282 at. ppm He tensile testing, is shown in Fig. 5.2.3. It was found to contain a large number of small, approximately 100-A-diam loops in the grain matrices as shown in Fig. 5.2.3(*a*). Narrow denuded regions adjacent to the grain boundaries were observed. Although it was not possible to resolve here, previous examinations of ^{3}He-implanted V-15Cr-5Ti specimens have shown that either a helium bubble or cluster of small bubbles resides at the center of each loop. The highly pressurized matrix bubbles apparently punch out the loops during the tritium trick procedure. In addition to these "assumed" matrix bubbles, a dense network of small coalesced bubbles were observed in the grain boundaries [Fig.5.2.3(*b*)]. The coalescense of the helium bubbles (see micrograph inset) was so advanced that it nearly formed a continuous film of helium in the grain boundaries. There is little doubt that this grain boundary bubble distribution caused the brittle intergranualar failure of the annealed V-15Cr-5Ti specimens at the higher helium level. On the other hand, the cold-worked specimens containing the same amount of helium had a relatively uniform distribution of small bubbles trapped on the dense dislocation networks (Fig. 5.2.4). In this cold-worked microstructure, grain boundaries from the original cast material were broken up and could not be observed by TEM. Therefore, it appears that cold-working is a useful technique for enhancing helium accommodation in V-15Cr-5Ti and should be studied further. Although helium accommodation plays an important role in the overall performance of an alloy under neutron irradiation, irradiation hardening, creep, swelling, etc., must also be considered.

Table 5.2.2. Tensile properties of cold-worked V-15Cr-5Ti with different levels of implanted helium

Test temperature (°C)	Helium level (at. ppm)	Strength, MPa		Elongation, %	
		Yield	Ultimate tensile	Uniform	Total
420	0	994	1057	1.2	4.3
420	0	1042	1077	1.0	4.0
420	90	800	881	6.0	10.3
420	90	808	881	6.0	11.2
420	282	852	900	6.1	10.2
420	282	848	901	6.2	10.9
520	0	994	1033	1.0	3.7
520	0	998	1050	0.7	33
520	90	800	888	4.8	7.8
520	90	787	893	6.3	10.4
520	282	815	896	3.8	6.6
520	282	829	899	5.7	10.4
600	0	1011	1038	0.7	1.7
600	0	1008	1037	0.7	1.7
600	90	779	900	5.2	6.7
600	90	806	903	4.7	6.9
600	282	832	928	3.5	5.6
600	282	808	908	3.6	5.7

5.2.5 Conclusions

(1) Annealed V-15Cr-5Ti tensile specimens, implanted with 3He via the tritium trick, were ductile at a helium level of 90 at. ppm but failed intergranularly at level of 282 at. ppm. The brittle failure was caused by a thin film of helium that formed in the grain boundaries.

(2) Cold-working eliminated the embrittlement at the higher helium level by breaking up the grain boundaries and by providing a dense dislocation network to trap the helium.

5.2.6 References

1. O. N. Braski, "Vanadium Alloy Irradiation Test Matrix in FFTF," pp. 63-65 in *ADIP Semiannu. Prog. Rep., Sept. 30, 1984,* DOE/ER-0045/13, U.S. DOE, Office of Fusion Energy.

2. O. N. Braski and D. W. Ramey, "Helium Doping of a Vanadium Alloy by a Modified Tritium Trick," pp. 72-74 in *ADIP Semiannu. Prog. Rep. Mar. 31, 1984,* DOE/ER-0045/12, U.S. DOE, Office of Fusion Energy.

3. D. N. Braski, "The Effect of Helium on the Tensile Properties of Several Vanadium Alloys," pp. 95-98 in *ADIP Semiannu. Prog. Rep., Sept. 30, 1984,* DOE/ER-0045/13, U.S. DOE, Office of Fusion Energy.

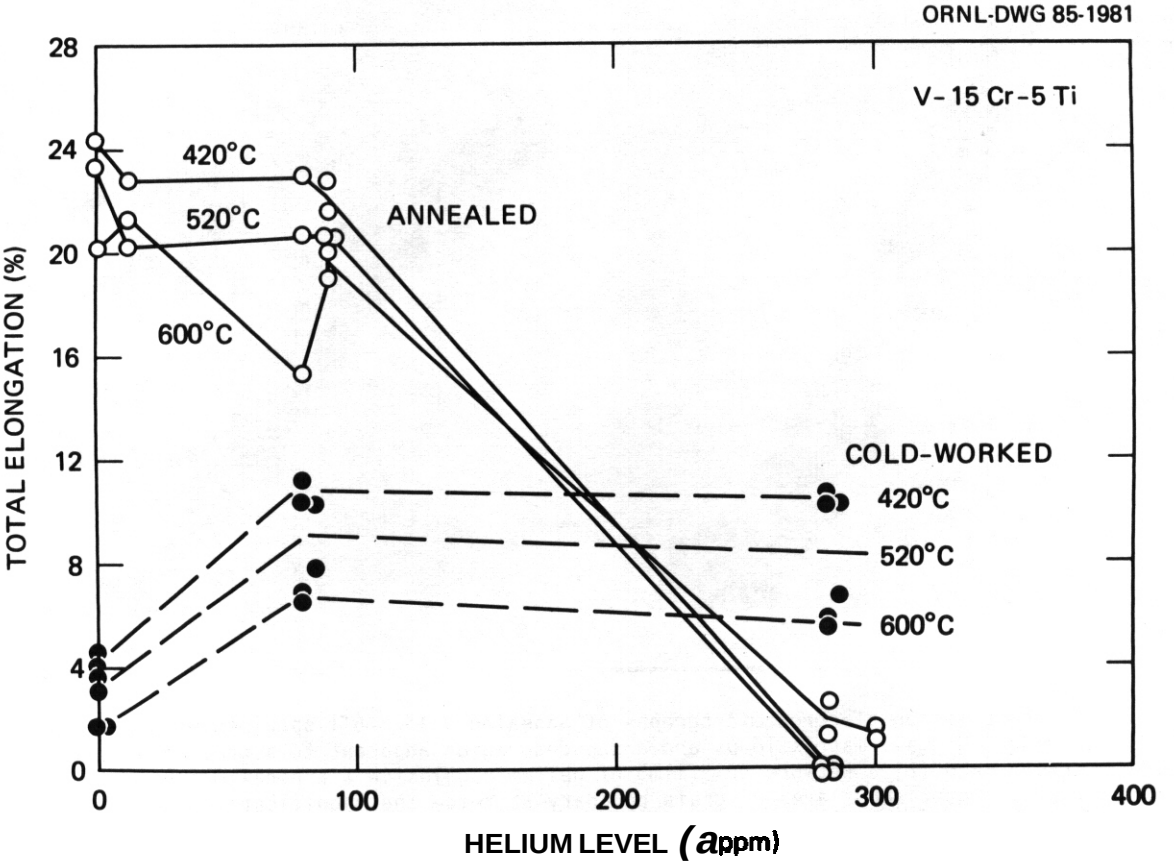

Fig. 5.2.1. The effect of implanted helium on the total elongation of annealed and cold-worked V–15Cr–5Ti tensile specimens tested at elevated temperature.

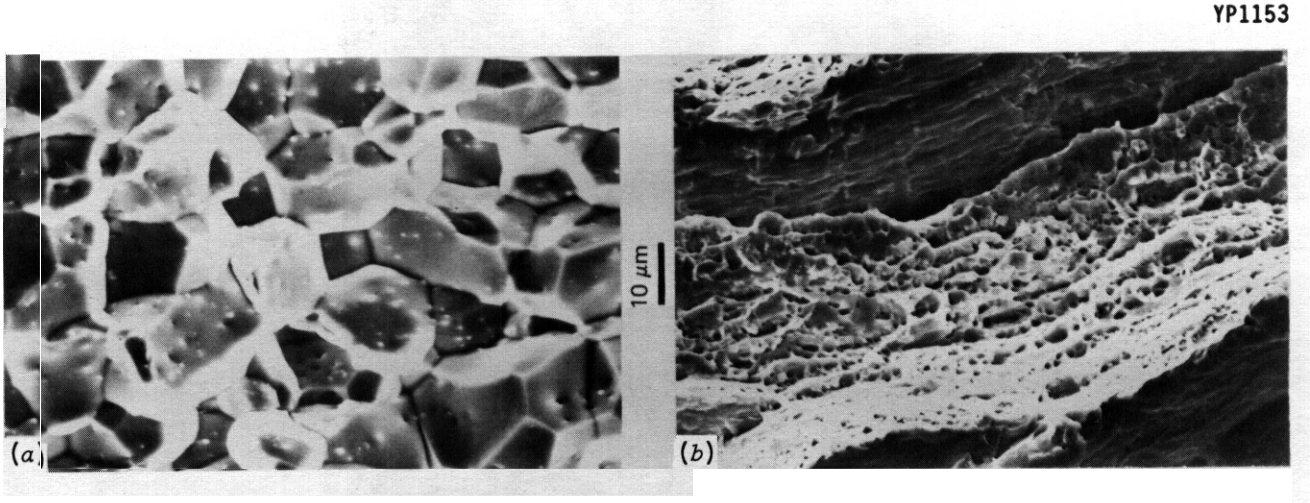

Fig. 5.2.2. Scanning electron micrographs of fracture surfaces of helium-implanted V–15Cr–5Ti tensile specimens in the (a) annealed and (b) cold-worked condition.

YP1154

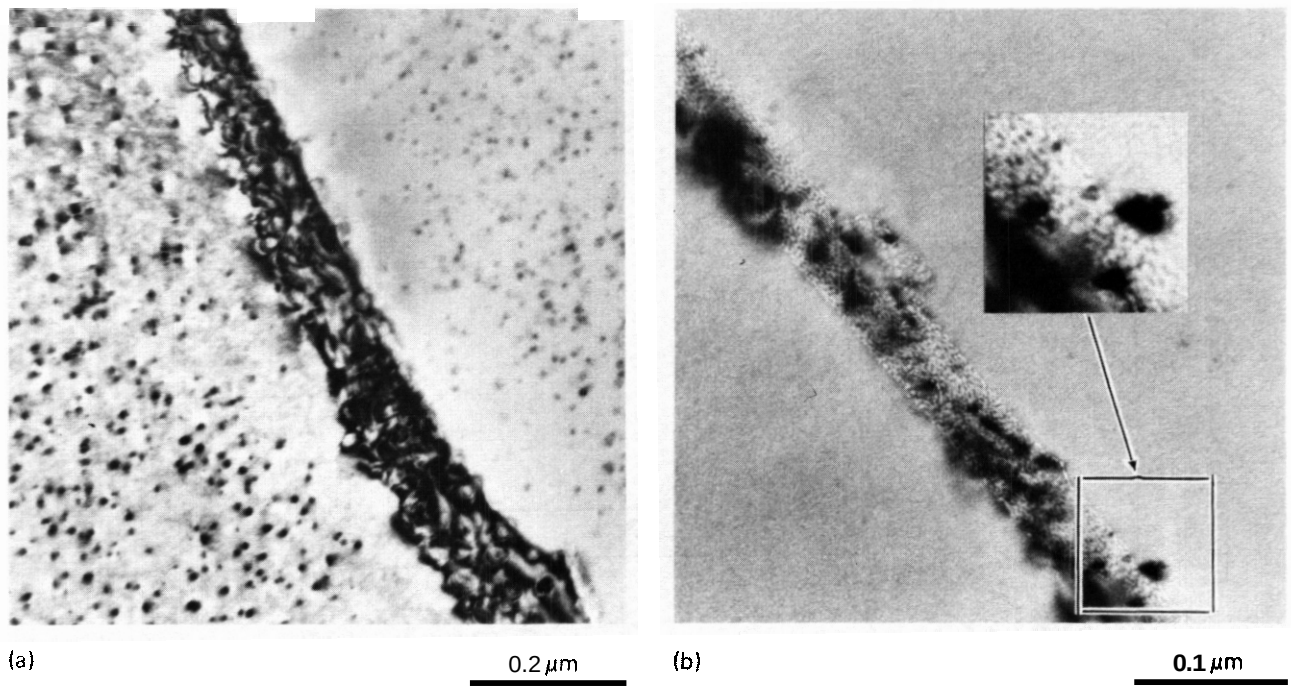

Fig. 5.2.3. Transmission electron micrographs of annealed V–15Cr–5Ti specimen with 282 at. ppm of implanted ^{3}He showing *(a)* small matrix loops and a denuded region adjacent to a grain boundary (using diffraction contrast), and *(b)* a network or "film" of helium bubbles in a typical grain boundary (using absorption contrast). Inset shows area of grain boundary at twice the magnification.

H–85530

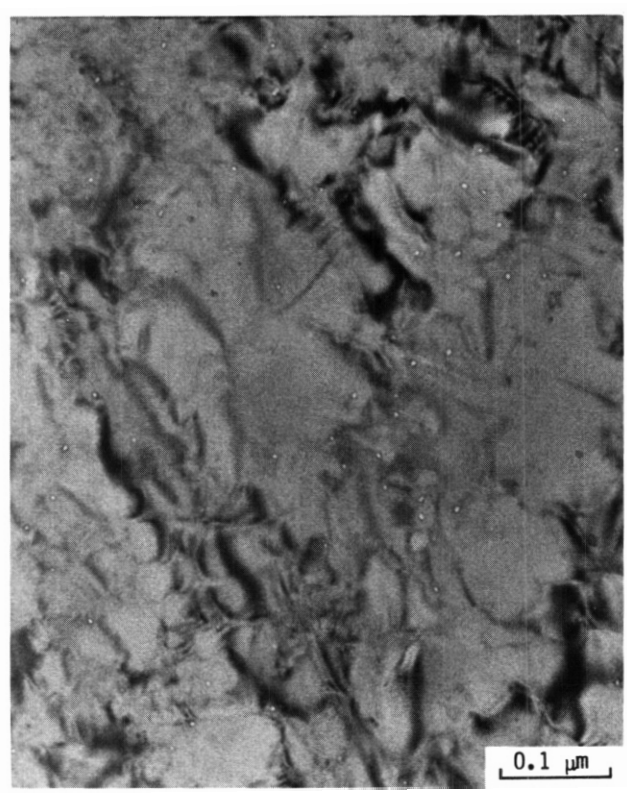

Fig. 5.2.4. Transmission electron micrograph of cold-worked V–15Cr–5Ti specimen with 282 at. ppm of implanted ^{3}He showing absence of grain boundaries and rather uniform distribution of small helium bubbles trapped on the dislocation network.

5.3 PREPARATION AND FABRICATION OF VANADIUM BASE ALLOYS -- H. R. Thresh (Argonne National Laboratory)

5.3.1 ADIP Task

I.D.l Materials Stockpile for MFE Programs (Path C).

5.3.2 Objective

Previous efforts have established a stockpile to provide sufficient quantities of vanadium and niobium Path C Scoping Alloys to evaluate the potential of these materials for fusion reactor applications. Depletion of the vanadium alloys has reached the level where additional inventory must be produced to maintain further work in the scoping studies. The immediate objective embraces the preparation of 50 lbs of the ternary alloy V-15%Cr-5%Ti in flat stock form to rebuild refractory alloy inventory.

5.3.3 Summary

Planning and procurement activities have been initiated to replenish the inventory of vanadium ternary alloy for Path C Scaping Studies. Appropriate quantities of pure vanadium, chromium and titanium have been acquired and a fabrication approach adopted where emphasis has been placed on the control of the interstitial elements O, N, H and C to a minimum level. Delivery of this alloy will begin late February FY 1986.

5.3.4 Progress and Status

During the current period the necessary pure metals were procured for the formulation of 50 lbs of V-15%Cr-5%Ti. In particular, the question of vanadium supply was resolved by the purchase of a 275 lb forged ingot from Teledyne Wah Chang. This material, shown in Figure 5.3.1, possesses a very good chemistry level with total interstitials of O, N, H and C at the 300 ppm level. The vanadium chemistry is recorded in Table 5.3.1 where total impurities classify the ingot purity as 99.9 wt% base metal.

Past evaluation efforts an the fabrication of this ternary alloy were never matured to the point where mechanical properties data would be related to the level of interstitial elements contained in a given alloy. The goal of the current fabrication work is to contaip the interstitial content to a minimum level providing a chemistry reference point. Previous work has shown that control over chromium homogeneity can be achieved by synthesizing from the particulate form of each metal constituent. In the current work, this approach will not be used to avoid the risk of interstitial pick up if the ingot vanadium is machined to turnings ok chips. Plans call for the slicing of the appropriate amount of vanadium ingot into 1" thick portions prior to cold rolling to a thickness where the final starting size can be obtained by a shearing operation. A series of small cylindrical ingots will be formulated by an arc melting operation allowing the preparation of a consumable electrode by TIG welding a series of the primary ingots under a protective atmosphere. Consumable arc melting will provide input material for a hot extrusion step, prior to final reduction. At this time, vanadium ingot partitioning and cold rolling are underway to provide stock for arc-melting initiation.

Table 5.3.1. Vanadium Ingot Chemistry

Element	Content (wt%)
si	0.0465
P	<0.0030
S	<0.(1020
Fe	<0.(3100
Al	0.(3185
Mo	<0.(3020
B	0.0004
U	<0.0002
O	0.(3200
N	0.(3041
C	0.(3070
H	<0.(3005

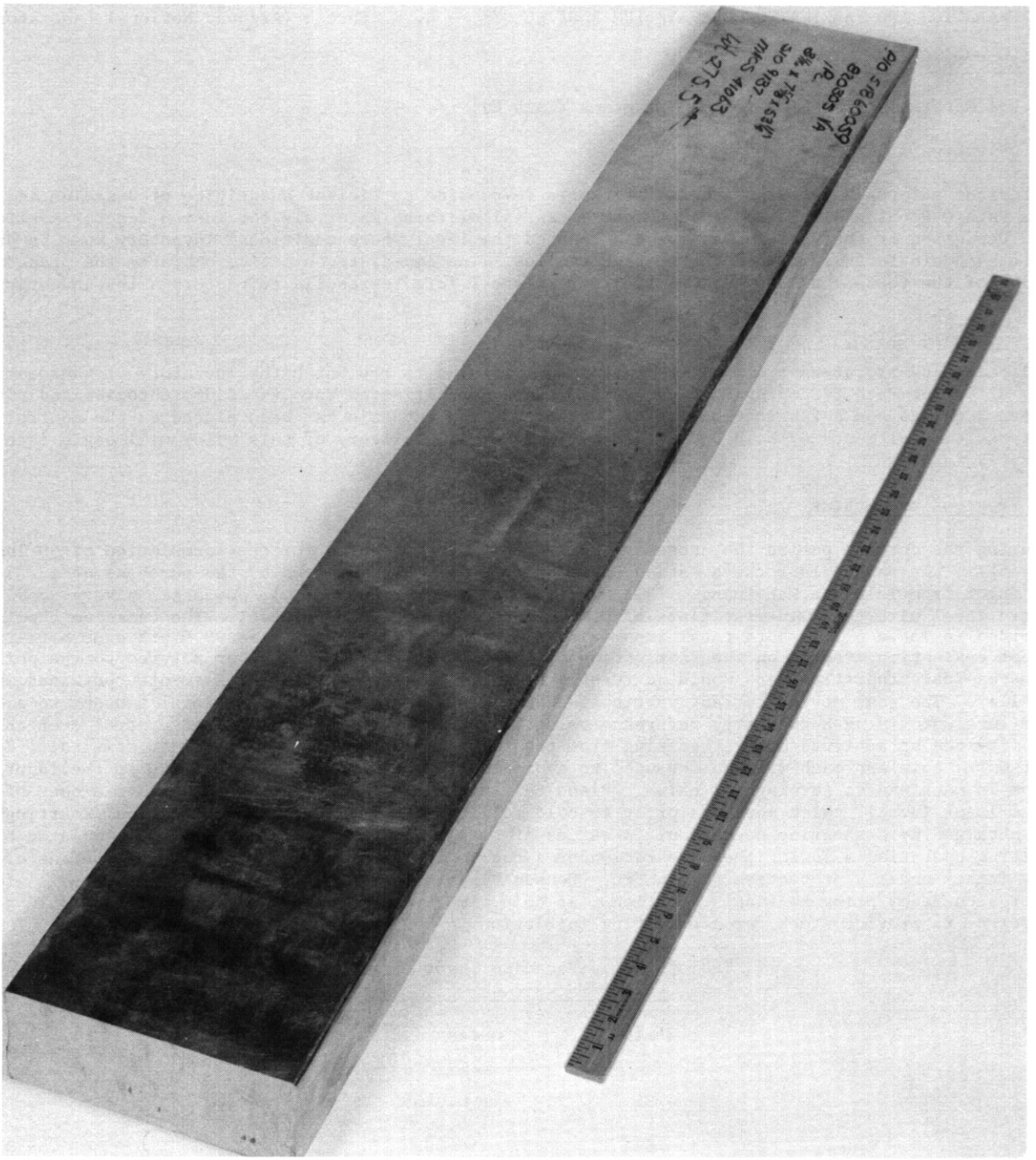

Fig. 5.3.1. High Purity Vanadium Ingot for Ternary Alloy Preparation.

5.3.5 References

1. W. C. Kramer, W. R. Burt, F. J. Karasek, J. E. Flinn and R. M. Mayfield, "Vanadium Alloy Screening Studies of V-15 w/o Ti - 7.5 w/o Cr Tubing for Nuclear Fuel Cladding," Argonne National Laboratory Report ANL-7206, Aug. 1966.

6. INNOVATIVE MATERIAL CONCEPTS

7.1 THE EFFECTS OF INCREASED HELIUM GENERATION ON MICROSTRUCTURE AND SWELLING OF NICKEL-DOPED 9Cr-1MoVNb and 12Cr-1MoVW STEELS IRRADIATED IN HFIR — P. J. Maziasz, R. L. Klueh, and J. M. Vitek (Oak Ridge National Laboratory)

7.1.1 AOIP Task

ADIP Tasks are not defined for Path E, ferritic steels in the 1978 Program Plan.

7.1.2 Objective

Ferritic 9Cr-1MoVNb and 12Cr-1MoVW steels have been doped with up to 2 wt. % Ni to increase helium production during HFIR irradiation. The goals of this work are to examine the microstructural evolution of bubbles and voids in response to increased helium concentrations, as well as to study the precipitation behavior during irradiation via analytical electron microscopy (AEM).

7.1.3 *Summary*

Voids formed in undoped and Ni-doped 12Cr-1MoVW at 400 and 500°C in HFIR at 36 to 39 dpa, but not at 300 or 600°C; results were similar for 9Cr-1MoVNb steels. Increased helium caused more void formation in the 9Cr-1MoVNb steel than it did in 12Cr-1MoVW steels, particularly at 400°C. At 300 to 500°C, the 9 Cr steels also experienced more dissolution of as-tempered precipitates and coarsening of the lath/subboundary structures than did the 12 Cr steels. In the 12 Cr steels, voids formed mostly in the coarsest subgrain regions of the material. Irradiation of 9Cr-1MoVNb - 2Ni at 400°C caused compositional modification of fine V-rich MC and produced new precipitation of compositionally modified $M_{23}C_6$ (τ) together with a fine matrix M_6C (η) phase which was Si, Cr, and Ni-rich. Identical η precipitation was found in 12Cr-1MoVW - 2Ni at 400°C, but similar fine particles were mainly Si and Cr-rich in the undoped 12 Cr steel. Finally, HFIR irradiation produced large, globular chi (χ) phase particles in all Ni-doped steels at 500°C; large voids formed exclusively within these χ-phase particles.

7.1.4 Progress and Status

7.1.4.1 Introduction

Small amounts of nickel have been added to 9Cr-1MoVNb and 12Cr-1MoVW ferritic steels as an innovative method to increase helium production during mixed-spectrum reactor irradiations (i.e., HFIR) for fusion-relevant microstructure and mechanical properties studies.[1] Void swelling resistance has been demonstrated in various fast breeder reactor (FBR) irradiated ferritic steels for fluences up to 120 dpa.[2-4] However, little or no helium is generated during fast reactor irradiation. Even the small levels of nickel present in undoped 9 Cr and 12 Cr steels produce enough helium to stimulate some void formation during HFIR irradiation at 400°C (refs. 5–7). Previous work has demonstrated that increased helium generation due to doping with 2% Ni further increased void formation for 9Cr-1MoVNb irradiated in HFIR at 400°C, and extended the void formation regime to 500°C after 36 to 39 dpa.[8] The purpose of this work is to continue the investigations of Ni-doping effects on 12Cr-1MoVW steels and to begin detailed analysis of the precipitation behavior during HFIR irradiation in both the 9 Cr and 12 Cr steels.

7.1.4.2 Experimental

The compositions of heats of 9Cr-1MoVNb with 0.1% and 2% Ni, and of 12Cr-1MoVW with 0.4, 1% and 2% Ni are given in Table 7.1.1. The various normalization and tempering heat treatment conditions are listed in Table 7.1.2. Note that the undoped steels contain small amounts of Ni, with the 12Cr-1MoVW having more than the 9Cr-1MoVNb (0.4 wt % compared to 0.1%, respectively). The 2% Ni doped 9 Cr and 12 Cr alloys were tempered at lower temperatures than their respective undoped alloys, but the 12Cr-1MoVW - 1Ni was tempered the same as the undoped 12 Cr steel.

Alloys were irradiated side by side in HFIR CTRs-30 through -32 in the form of standard 3-mm-diam transmission electron microscopy (TEM) disks punched from 0.254-mm-thick sheet stock. This work examines only the highest fluence disks from HFIR-CTR-30. Irradiation conditions are given in Table 7.1.3. Irradiation temperatures ranged from 300 to 600°C and have been verified by analysis of temperature monitors.[9] Displacement damage and helium generation were calculated by L. R. Greenwood based on dosimetry performed for this experiment,[10] including dpa due to nickel recoils.

Specimens were thinned remotely in an automatic Tenupol twin-jet polishing unit and examined on a JEM 100C TEM, equipped with a special objective lens polepiece designed to lower the magnetic field at the specimen. Standard techniques were used for imaging cavities, dislocations, and precipitates.

Extraction replicas were also produced from selected specimens in a special shielded, hands-on facility. Nevertheless, specimens were highly radioactive and difficult to handle. Specimens were prepared for extraction by polishing, lightly etching and then coating them with a carbon film. Precipitates were extracted from the matrix electrolytically using 10% HCl in methanol at a current of 50 mA at room temperature, and then the carbon films were washed in ethanol, removed in distilled water and suspended on beryllium grids. Precipitates were studied by means of analytical electron microscopy (AEM), using either a Philips EM400 microscope equipped with a field emission gun (FEG) for very high electron intensity at small probe sizes and an EDAX detector and computer, or a JEM 2000FX microscope with an LaB_6 gun and Tracor-Northern detector and computer.

Table 7.1.1. Compositions of 9Cr-1MoVNb and 12Cr-1MoVW heats of steel with and without nickel doping

Alloy designation	Heat number	Concentration,[a] (wt %)										
		Cr	Mo	Ni	Mn	C	Si	V	Nb	Ti	W	N
9Cr-1MoVNb	(XA 3590)	8.6	1.0	0.1	0.36	0.09	0.08	0.21	0.063	0.002	0.01	0.05
9Cr-1MoVNb - 2% Ni	(XA 3591)	8.6	1.0	2.2	0.36	0.064	0.08	0.22	0.066	0.002	0.01	0.05
12Cr-1MoVW	(XAA 3587)	12	0.9	0.4	0.5	0.2	0.18	0.27	0.018	0.003	0.54	0.02
12Cr-1MoVW - 1%Ni	(XAA 3588)	12.0	1.0	1.1	0.5	0.2	0.13	0.31	0.015	0.003	0.53	0.02
12Cr-1MoVW - 2% Ni	(XAA 3589)	11.7	1.0	2.3	0.5	0.2	0.14	0.31	0.015	0.003	0.54	0.02

[a]Balance iron.

Table 7.1.2. Normalizing and tempering conditions for various steels

Alloy	Normalization	Tempering
9Cr-1MoVNb	0.5 h at 1040°C	1 h at 760°C
9Cr-1MoVNb - 2% Ni	0.5 h at 1040°C	5 h at 700°C
12Cr-1MoVW	0.5 h at 1050°C	2.5 h at 780°C
12Cr-1MoVW - 1%Ni	0.5 h at 1050°C	2.5 h at 780°C
12Cr-1MoVW - 2% Ni	0.5 h at 1050°C	5 h at 700°C

7.1.4.3 Results

Cavity Microstructure. The 9Cr-1MoVNb steel showed void formation only after HFIR irradiation at 400°C to ~37 dpa and ~30 at. ppm He [Fig. 7.1.1(*a*) and (*b*)], whereas more helium generation (~400–420 at. ppm) caused increased void formation at 400°C and extended it to 500°C in 9Cr-1MoVNb - 2Ni [Fig. 7.1.1(*c*) and (*d*)]. Many fine bubbles were also found at all temperatures in the 9Cr-1MoVNb - 2Ni, but voids were not found at either 300 or 600°C. The 12Cr-1MoVW steel also showed void formation at 400°C in HFIR [Fig. 7.2.1(*a*)], similar or slightly more than found in the 9Cr-1MoVNb. Unlike the 9 Cr steel at 500°C, some large (20–40 nm in diam) voids formed very non-uniformly in the undoped 12 Cr steel after ~38 dpa [Fig. 7.1.3(*a*)]; these voids were nonuniformly distributed spacially, being found only in the largest subgrains. Void formation and swelling appeared to increase with increased helium generation (and increased nickel) at 500°C,

Table 7.1.3. Damage parameters for 9Cr-1MoVNb and 12Cr-1MoVW, with and without nickel, irradiated in HFIR-CTR-30

Alloy designation	Irradiation temperature (°C)	Displacement damage[a] (dpa)	Helium content[b] (at. ppm He)
9Cr-1MoVNb	300	36.5	30.5
	400	36.5	30.5
	500	38.5	32.2
	600	38.5	32.2
9Cr-1MoVNb - 2Ni	300	37.2	402.5
	400	37.2	402.5
	500	39.2	424.0
	600	39.2	424.0
12Cr-1MoVW	300	36.4	85.3
	400	36.4	85.3
	500	38.2	89.6
	600	38.2	89.6
12Cr-1MoVW - 1Ni	300	36.7	212.4
	400	36.7	212.4
	500	38.5	223.0
	600	38.5	223.0
12Cr-1MoVW - 2Ni	300	37.1	429.0
	400	37.1	429.0
	500	39.0	450.0
	600	39.0	450.0

[a]Displacement damage calculated from dosimetry measurements performed by L. R. Greenwood ("Fission Reactor Dosimetry – HFIR-CTR-30, -36, -46," pp. 22–26 in *ADIP Semiannu.* Prog. *Rept. Mar. 31, 1985*, DOE/ER-0045/14). The effect of nickel recoils is included.

[b]Helium generation calculated from dosimetry measurements performed by L. R. Greenwood, ("Fission Reactor Dosimetry – HFIR-CTR-30, -36, -46," Sect. 2.6, this report).

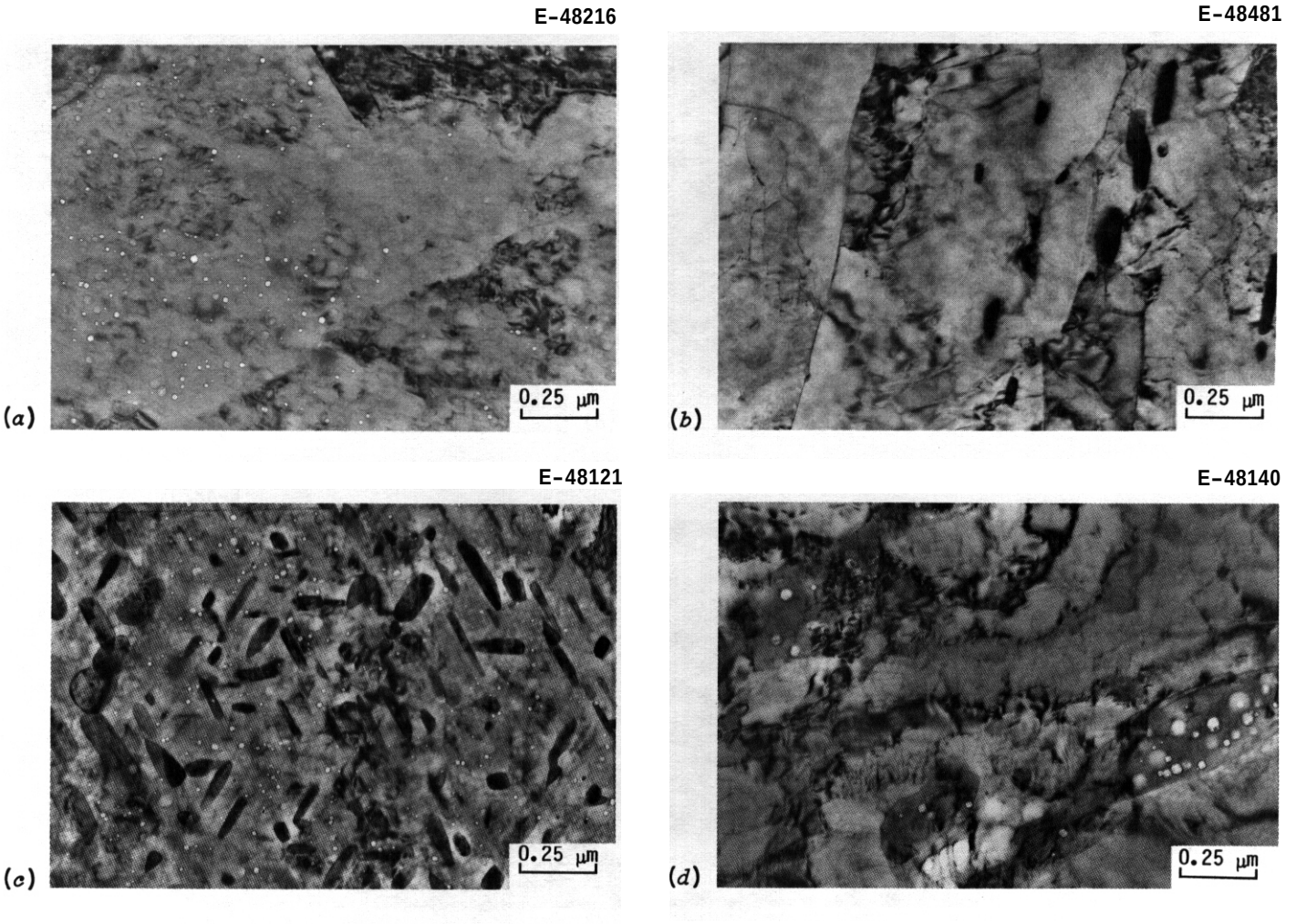

Fig. 7.1.1. A comparison of (a) and (*b*) 9Cr-1MoVNb (–30 at. ppm. He) and (c) and (d) 9Cr-1MoVNb - 2Ni (–400 at. ppm He) irradiated in HFIR at 400 and 500°C, respectively, to –37 to 39 dpa. Both cases show that helium increases void formation.

but not at 400°C in the Ni-doped 12Cr-1MoVW steels (Figs. 7.1.2 and 7.1.3). At 400°C, void size appeared refined (15–25 nm as compared to 7–19 nm in diam) as void formation became spacially more uniform with increased helium in the 12Cr-1MoVW - 1Ni, whereas in 12Cr-1MoVW - 2Ni, void formation appeared patchy and similar to the undoped steel. The 12Cr-1MoVW - 2Ni, however, also had a finer as-tempered lath-subgrain/precipitate structure than the undoped steel, due to a lower tempering temperature, and there seemed to be fewer voids in regions with the finest lath-boundary structure [Fig. 7.1.2(*c*)].

Fine dispersions of bubbles were observed in all of the Ni-doped steels after irradiation at 600°C in HFIR. As shown in Fig. 7.1.4, bubbles were distributed along cell or lath boundaries or along intra-cell dislocations, and there was little difference between 9Cr-1MoVNb - 2Ni and 12Cr-1MoVW - 2Ni.

At 400°C, most voids occurred in the matrix, without any particular precipitate association. At 500°C, large voids (50–77 nm in diam) in the Ni-doped 9 Cr or 12 Cr steels were found exclusively inside large, globular chi (χ) phase particles. A few such particles were also observed in the Ni-doped steels at 400°C [see 7.1.2(*b*)].

In summary, while the 9Cr-1MoVNb had similar or slightly less void swelling than 12Cr-1MoVW at 400 and 500°C, increased helium generation in the Ni-doped steels seemed to cause more swelling in the 9Cr-1MoVNb steel. Swelling appears to be in the 0.2 to 0.4% range or less in all cases at 36 to 39 dpa.

Subgrain Boundary/Precipitate Microstructure. Figure 7.1.5 shows the martensite lath boundary and carbide precipitate structures produced by tempering for 2.5 h at 780°C in the 12Cr-1MoVW steel prior to irradiation. The intracell dislocation network concentration produced during HFIR irradiation at 400°C was considerably higher than the as-tempered concentration, but only slightly higher after irradiation at 500°C. Dislocation concentration after irradiation was similar in 9 Cr and 12 Cr steels, and there was little effect of Ni doping. In any given steel, however, the dislocation networks were more concentrated in the largest cells of the subgrain structure.

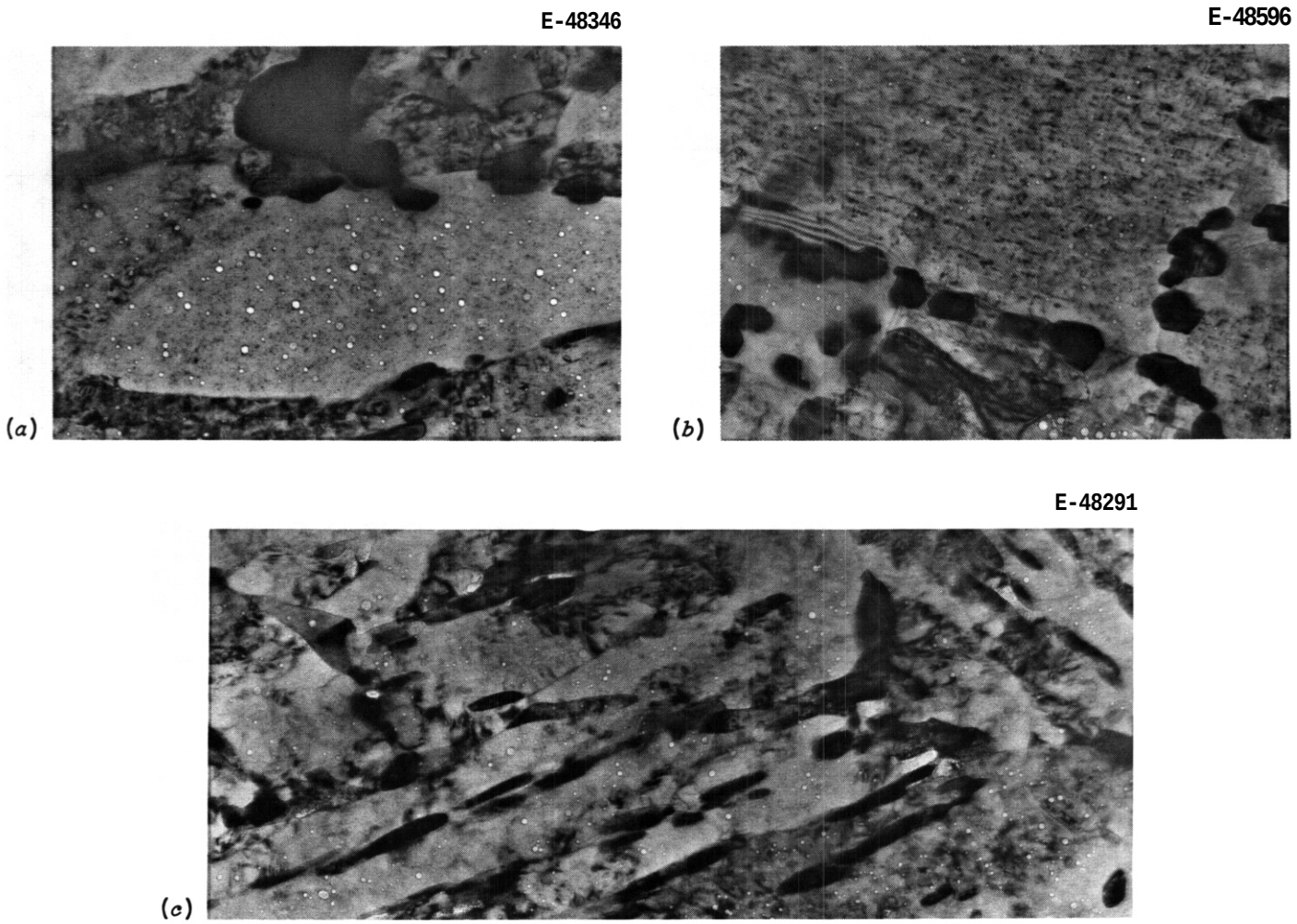

Fig. 7.1.2. A comparison of 12Cr-1MoVW steel irradiated in HFIR at 400°C to ~36 to 39 dpa with (a) 0.4 wt % Ni (85 at. ppm He), (b) 1.1% Ni (212 at. ppm He) and (c) 2.3% Ni (429 at. ppm He). Void formation does not show a clear increase with increased helium content, and swelling may actually decrease.

HFIR irradiation at 300 to 500°C caused considerable coarsening of the lath/subgrain structure in doped and undoped 9Cr-1MoVNb, coincident with some apparent dissolution of the as-tempered carbide precipitate structure. The coarser subgrain structure can be seen by comparing the as-tempered structure with that produced by HFIR irradiation at 400°C in 9Cr-1MoVNb - 2Ni, shown in-foil and on extraction replicas in Fig. 7.1.6. There appear to be less of the as-tempered precipitation in the undoped 9Cr-1MoVNb after irradiation at 400°C, but copious additional $M_{23}C_6$ (τ) formed during irradiation within the large subgrains and along boundaries in the Ni-doped steel. At 500°C, large globular χ phase particles appeared to replace the as-tempered precipitation along boundaries in the 9Cr-1MoVNb - 2Ni [compare Fig. 7.1.1(b) and (d)]. However, at 600°C, both undoped and Ni-doped 9 Cr steels showed little or no effect of irradiation on the as-tempered subgrain and precipitate structure.

By contrast, the as-tempered structure of the 12Cr-1MoVW steels, which contained much more $M_{23}C_6$ carbide precipitate relative to the 9 Cr steels, remained relatively stable during HFIR irradiation at 300 to 500°C to 36 to 39 dpa. An exception, however, was the undoped 12Cr-1MoVW at 500°C. As shown from a lower magnification comparison of Ni doped and undoped 12 Cr steels irradiated at 400 and 500°C in Fig. 7.1.7, carbide precipitate size and spatial distributions had coarsened noticeably while subgrains were larger and more polygonal in the undoped 12 Cr steel at 500°C. Voids were often found in the largest subgrains after irradiation at 500°C.

With regard to fine precipitation, HFIR irradiation at 400°C produced fine M_6C (η) precipitation in all steels but the 9Cr-1MoVNb; at 500°C, M_6C was found only in the 12Cr-1MoVW steel. These particles are shown in Fig. 7.1.8 for 12Cr-1MoVW irradiated at 400°C and can be in Fig. 7.1.6(d) seen on the replica of 9Cr-1MoVNb - 2Ni irradiated at 400°C. Identification was based on the compositional analysis and preliminary diffraction analysis. The fine η-phase particles were uniformly distributed throughout the matrix and along subgrain boundaries at 400°C, but were found only in the largest subgrain regions (often together with voids) at 500°C. Finally, the as-tempered MC carbides appeared to coarsen in all steels during irradiation at 300 to 500°C.

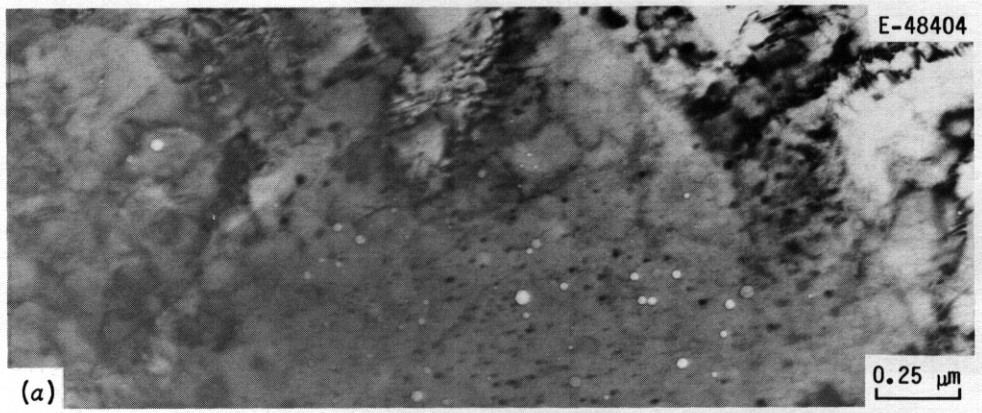

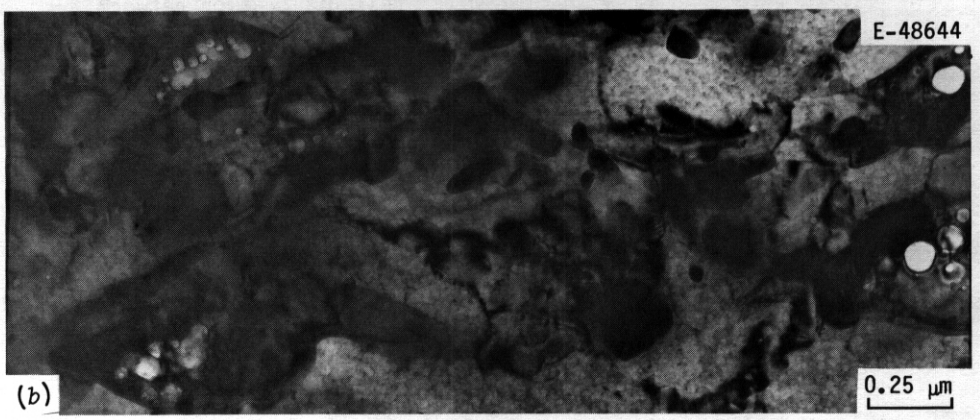

Fig. 7.1.3. A comparison of 12Cr-1MoVW steel irradiated in HFIR at 500°C to ~38 dpa with (*a*) 0.4 wt % Ni (85 at. ppm He) and (*b*) 1.1% Ni (212 at. ppm He). Void formation increases with increased helium content, but large voids occur only within larger χ phase particles in the 1.1% Ni steel.

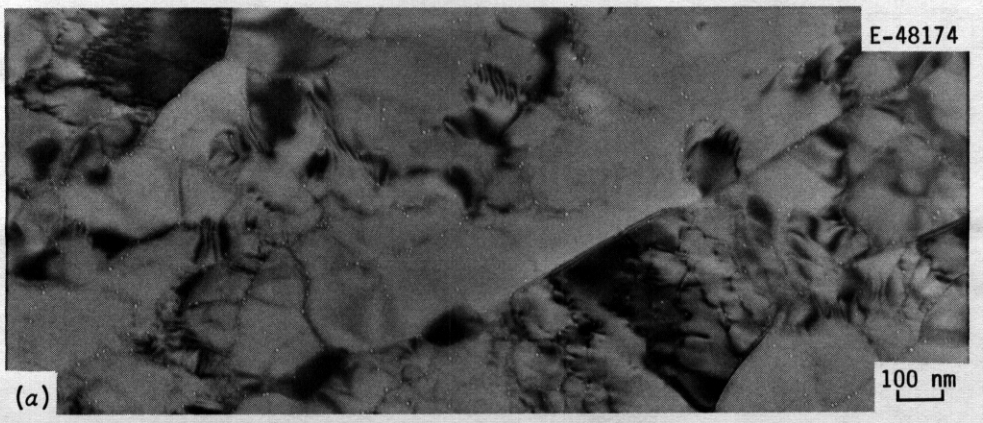

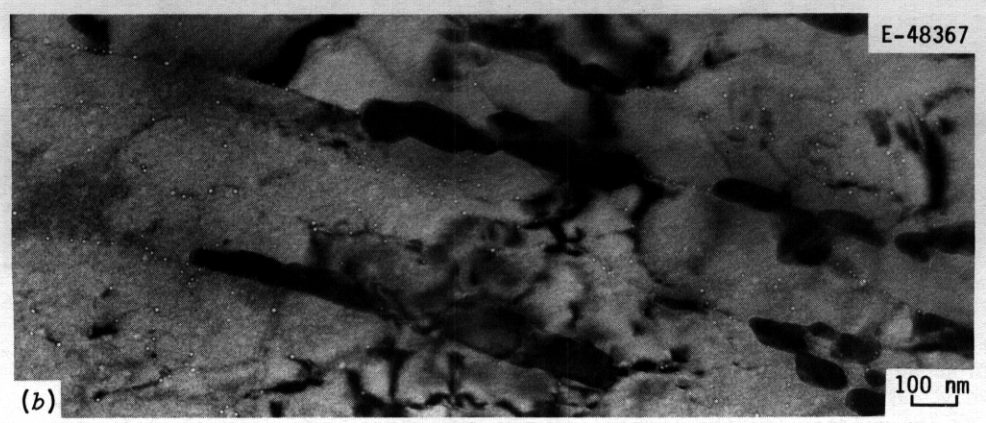

Fig. 7.1.4. A comparison of (*a*) 9Cr-1MoVNb - 2Ni and (*b*) 12Cr-1MoVW - 2Ni irradiated in HFIR at 600°C to ~39 dpa and 420 to 450 at. ppm He. Many fine bubbles are observed in both, with no evidence of voids.

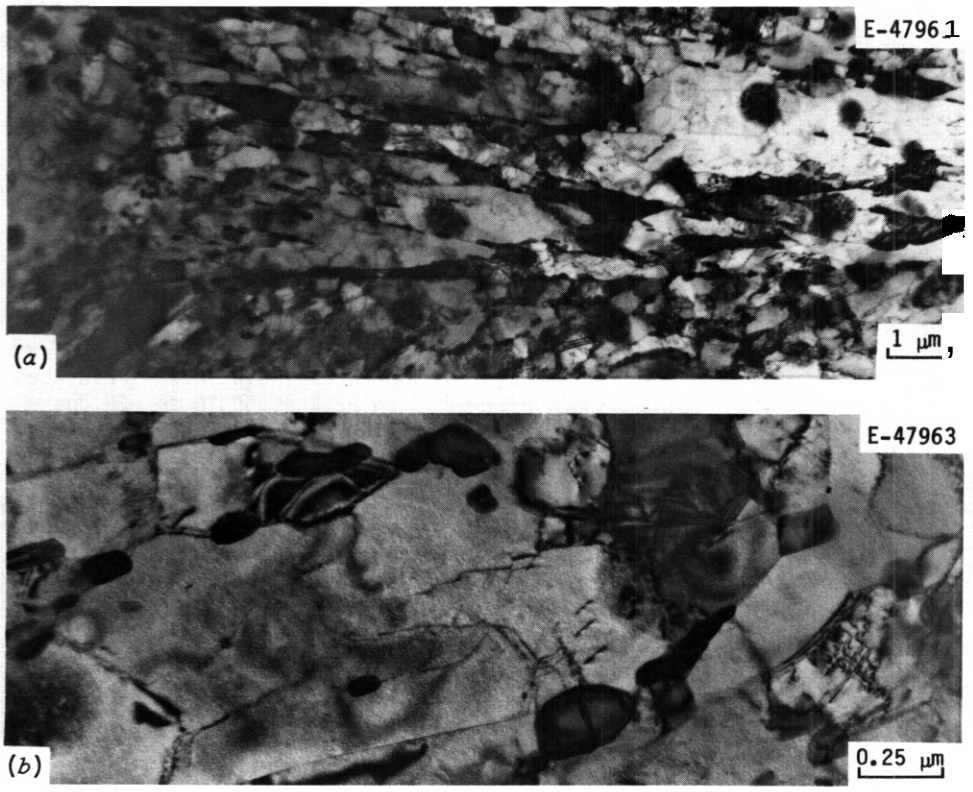

Fig. 7.1.5. The as-tempered (2.5 h at 780°C) microstructure of 12Cr-1MoVW shown (a) at low magnification to illustrate the subboundary structure from prior martensite laths and (b) at higher magnification to show the low intracell dislocation network concentration and some of the carbide precipitates produced during tempering along the subgrain structure.

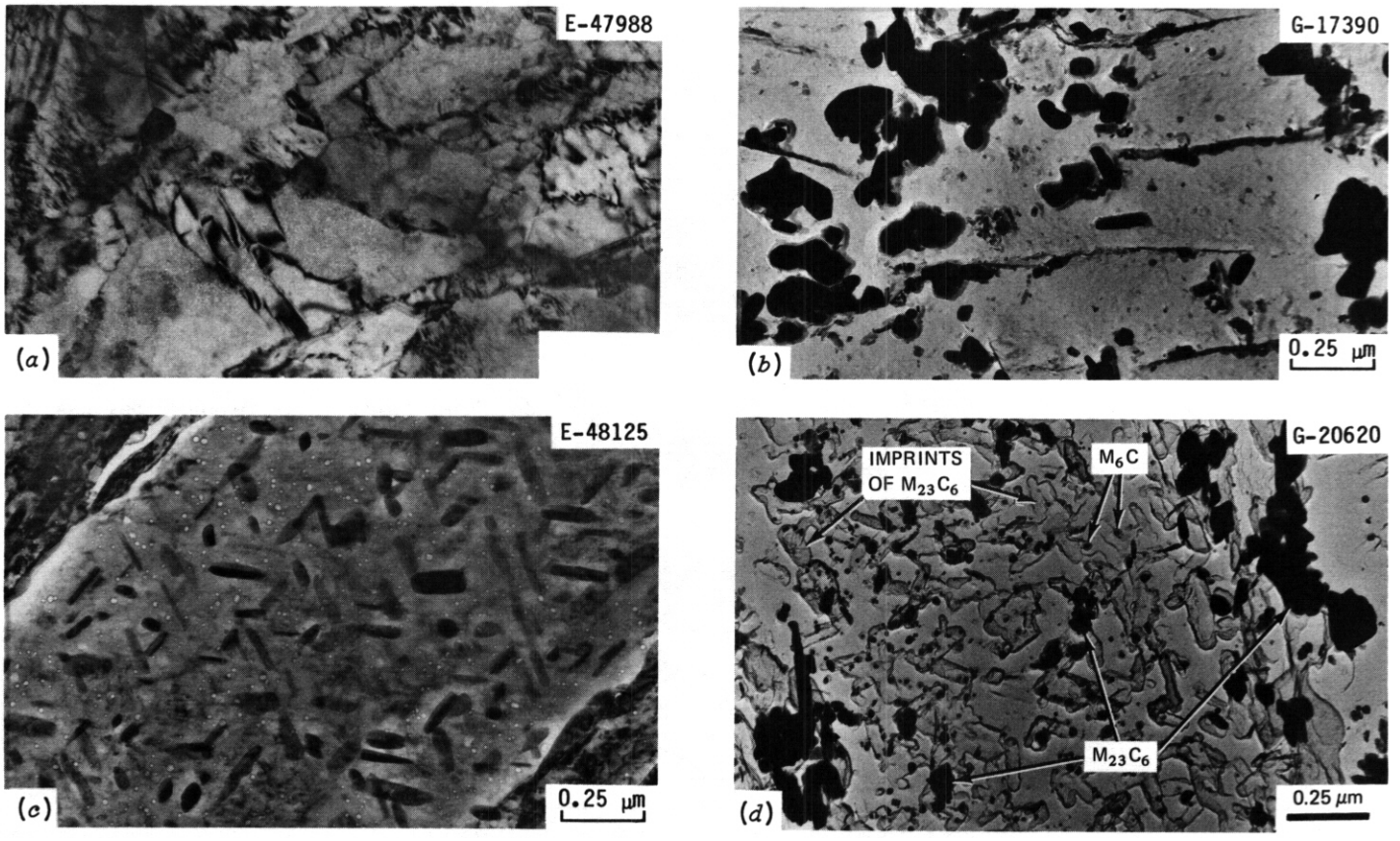

Fig. 7.1.6. A comparison of precipitate and subgrain structures in 9Cr-1MoVNb - 2Ni in (a) and (b) the as-tempered (5 h at 700°C) condition and (c) and (d) after HFIR irradiation at 400°C to ~31 dpa, in-foil and on extraction replicas, respectively. Irradiation has definitely produced a coarser subgrain structure with many more $M_{23}C_6$ particles within grains relative to the tempered structure. Fine background particles in (d) are M_6C (η).

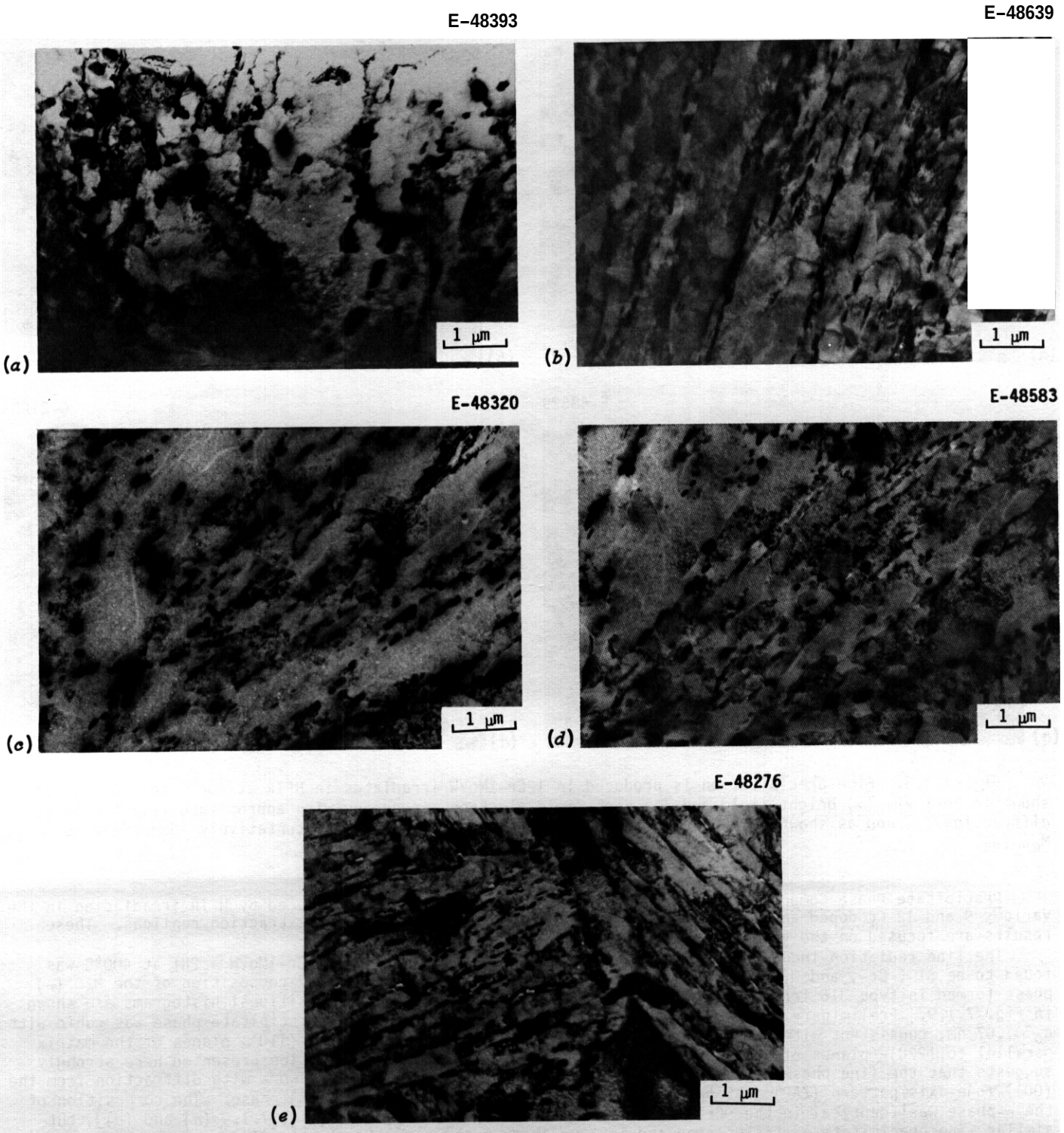

Fig. 7.1.7. A comparison of the subgrain structure at low magnification in 12Cr-1MoVW irradiated to 36 to 39 dpa at 500°C with (*a*) 0.4 wt % Ni (~90 at. ppm He) and (*b*) 1.1% Ni (~220 at. ppm He) and at 400°C with (*c*) 0.4% Ni, (*d*) 1.1% Ni and (*e*) 2.3% Ni (450 at. ppm He). Only the undoped steel irradiated at 500°C shows considerable coarsening of the subgrain and precipitate structures.

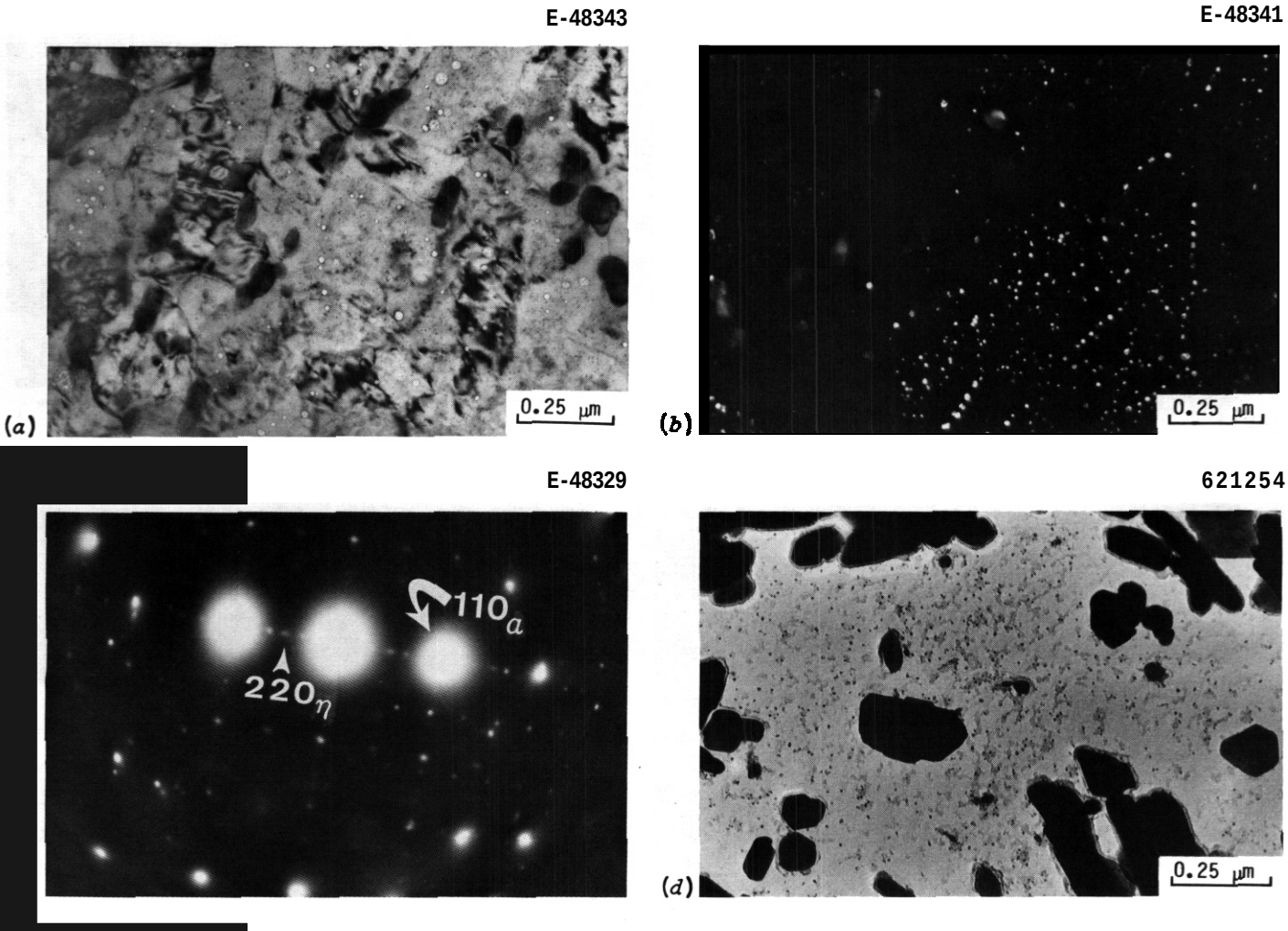

Fig. 1.1.0. Fine precipitation is produced in 12Cr-1MoVW irradiates in HFIR at 400°C to ~36 dpa. as shown in-foil via (*a*) bright-field and (*b*) dark-field electron microscopy with appropriate selected area diffraction (c) and as shown on an extraction replica in (d). This phase is tentatively identified as M_6C (η).

Precipitate Phase Composition. A systematic study of precipitation produced by HFIR irradiation in the various 9 and 12 Cr doped and undoped steels is being conducted using AEM on extraction replicas. These results are focused on the void formation regime of 400 to 500°C.

The fine radiation-induced precipitate formed in 9Cr-1MoVNb - 2Ni and 12Cr-1MoVW - 2Ni at 400°C was found to be Si-, Cr-, and Ni-rich, similar to the characteristic "fingerprint" composition of the M_6C (η) phase formed in type 316 irradiated in HFIR at similar temperatures.[11] Compositional histograms are shown in Fig. 7.1.9. Preliminary electron diffraction results indicated that the precipitate phase was cubic with a_0 ~1.07 nm, consistent with M_6C (η) phase. An orientation relationship with $(110)_\alpha$ planes of the matrix parallel to $(220)_\eta$ planes of the precipitate was found. Although the information presented here strongly suggests that the fine phase produced in the Ni-doped steels is η phase, more work with diffraction from the (001) zone-axis pattern (ZAP) must be done to prove the identity of the M_6C (η) phase. The composition of the η-phase was identical in the 9Cr-1MoVNb - 2Ni and the 12Cr-1MoVW - 2Ni [Fig. 7.1.9 (a) and (*c*)], but similar fine precipitate particles produced in 12Cr-1MoVW were unusually rich in Si and contained no Ni. While more work is needed, the diffraction evidence again suggests that this precipitate is η-phase.

The abundant $M_{23}C_6$ that reprecipitated within subgrains during HFIR irradiation of 9Cr-1MoVNb - 2Ni at 400°C (see Fig. 7.1.6) was compositionally modified relative to the $M_{23}C_6$ (τ) particles present in the original as-tempered structure.[12] Compositional histograms of the $M_{23}C_6$ (τ) are shown in Fig. 7.1.10(*a*) and (*b*). Some larger particles of $M_{23}C_6$ (τ) found along boundaries in the HFIR irradiated 9Cr-1MoVNb - 2Ni had the same composition as those found after tempering, thereby suggesting that the new particles with different compositions were peculiar to the irradiation. The $M_{23}C_6$ (τ) produced during irradiation had somewhat less Cr and Mo and measurably more Si, V, and Nb. and a little more Ni. By contrast, $M_{23}C_6$ (τ) found after HFIR irradiation at 400°C in the undoped 9 Cr alloy and in the doped and undoped 12 Cr alloys did not show these changes, but retained identical microstructure and phase composition to the as-tempered carbides.

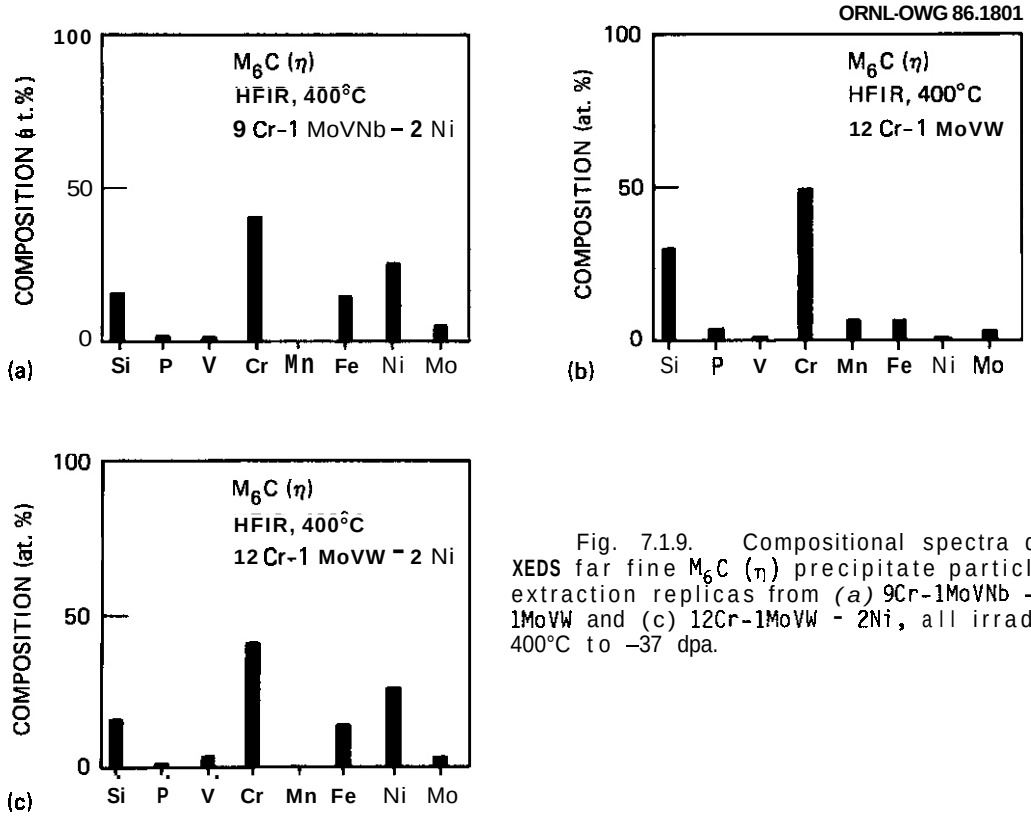

Fig. 7.1.9. Compositional spectra determined via XEDS far fine M_6C (η) precipitate particles analyzed on extraction replicas from *(a)* 9Cr-1MoVNb - 2Ni, *(b)* 12Cr-1MoVW and (c) 12Cr-1MoVW - 2Ni, all irradiated in HFIR at 400°C to –37 dpa.

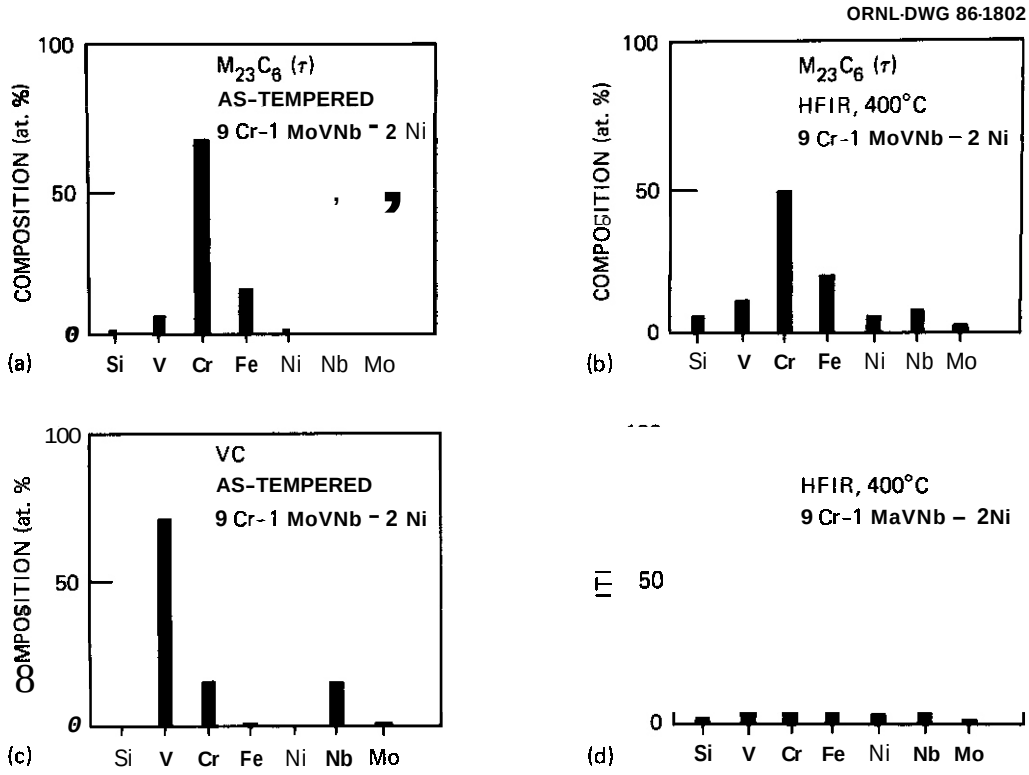

Fig. 7.1.10. Compositional spectra determined via XEDS for *(a)* and *(b)* V-rich MC and *(c)* and *(d)* $M_{23}C_6$ (τ) phase particles analyzed on extraction replicas from 9Cr-1MoVNb - 2Ni in both the as tempered condition *(a,c)* as well as after HFIR irradiation at 400°C to –37 dpa *(b,d)*. Compositions of both phases are modified during irradiation.

The V-rich MC carbides showed compositional modification that was similar in all steels (Ni-doped as well as undoped) irradiated at 400 to 500°C. Compositional histograms of the MC phase in 9Cr-1MoVNb - 2Ni are shown in Fig. 7.1.10(c) and (d). Coincident with microstructural coarsening, the V-rich MC particles became uniformly much richer in Cr at the expense of V, and no particles were found with the composition of the as-tempered VC carbides. The compositional change was similar for the 9 Cr and 12 Cr steels and similar for large and small MC particles. No NbC particles, of the type found after tempering,[13] were found after HFIR irradiation. Very fine needles of VC produced during aging of 9Cr-1MoVNb at 482 to 530°C for 25,000 h were slightly richer in Cr than the as-tempered carbides,[13] but nowhere near to the degree to which the MC carbides were modified during HFIR irradiation. These compositional modifications therefore appear to be an unusual effect of the irradiation rather than an enhanced thermal effect.

7.1.4.4 Discussion

The results on void formation at higher helium generation rates in the nickel-doped steels are consistent with previous results by others which suggested that the increase in helium generation in undoped 9 Cr and 12 Cr steels between ERR-I1 and HFIR irradiation increases void formation.[5-7] More helium definitely produces more voids in the 9Cr-1MoVNb steel at 400 and 500°C, but not necessarily in the 12Cr-1MoVW steel. Details of the microstructural/microcompositional data indicate that the results in the Ni-doped steels are normal effects of helium rather than strange effects caused by the increased alloy nickel content.

Although the microstructural results suggest that helium bubbles are necessary for void nucleation (consistent with the critical cavity radius approach to void nucleation), they also suggest a very strong effect of the subgrain boundary structure, and possibly some effects of precipitation, on void formation. A fine, stable lath and subboundary structure seems to be one source of the void swelling resistance often attributed to the ferritic steels. Indeed, instability and coarsening of this subgrain structure appear to be important to assist void formation. The boundary substructure stability in turn appears related to the stability of the as-tempered precipitate structure under irradiation. At 500°C, void formation appears to depend on the formation of either the irradiation induced fine M_6C (η) or coarse χ phases.

With regard to phase formation and stability under irradiation, Gelles and Thomas' found manganese-rich G-phase in HT-9 (12 Cr-1MoVW steel) irradiated in EBR-II at 400°C, but not in 9Cr-1MoNb steel. They found no M_6C (η), but their data did show MC that was both V-rich and Cr-rich when produced under irradiation in the modified 9Cr-1Mo alloy. Stoter and Little[14] found M_6C (η), compositionally very similar to ours, as well as χ phase in various 12 Cr steels irradiated in the Dounreay Fast Reactor (DFR). They also found σ, Laves and α', which we did not find; they found no G-phase. Both sets of researchers found rods of a Cr-rich M_2X-type phase, but our work is still incomplete with regard to this phase. The compositional modification of $M_{23}C_6$ (τ) and the production of a Si, Cr-rich η phase under irradiation appear to be new results, in our work, as are data on the compositional modifications of the V-rich MC phase.

7.1.5 Conclusions

(1) Nickel doping increased helium generation in 9Cr-1MoVNb and 12Cr-1MoVW steels irradiated in HFIR and enhanced fine bubble nucleation at 300 to 600°C after 36 to 39 dpa.

(2) Voids were not found in either doped or undoped 9 Cr and 12 Cr steels at 300 or 600°C, but voids formed to varying degrees at 400 and 500°C. Void formation and swelling increased with increased helium generation in 9Cr-1MoVNb - 2Ni at 400 and 500°C and in 12Cr-1MoVW - 1Ni at 500°C. However, void formation and swelling at 400°C did not clearly increase with helium in the 12Cr-1MoVW steels.

(3) The 9Cr-1MoVNb showed similar or slightly better void-swelling resistance than 12Cr-1MoVW steel at 400 to 500°C, but that trend appeared reversed with higher helium generation in the Ni-doped steels.

(4) The as-tempered subgrain structure in 9Cr-1MoVNb coarsened during irradiation at 300 to 500°C, in doped and undoped steels. Subgrain coarsening coincides with instability of the as-tempered precipitate structure. By comparison, the as-tempered subgrain and precipitate structures were more stable in the 12Cr-1MoVW steels, except at 500°C in the undoped steel. Particularly in the 12 Cr steels irradiated at 500°C, most voids formed in the coarsest subgrains.

(5) At 400 and 500°C, void formation was often accompanied by irradiation-produced precipitation. At 400°C in 9Cr-1MoVNb - 2Ni and in doped and undoped 12Cr-1MoVW steels, void formation coincided with fine precipitation of a phase tentatively identified as M_6C (η). At 500°C in 12Cr-1MoVW, M_6C was found only in those regions containing voids. Very large voids were found exclusively inside large, globular chi (χ) phase particles in the Ni-doped 9 Cr and 12 Cr steels at 500°C.

(6) XEDS on extraction replicas identified the fine irradiation-induced matrix precipitate as M_6C (η) from the Si-, Cr-, and Ni-rich characteristic spectra in 9Cr-1MoVNb - 2Ni and 12Cr-1MoVW - 2Ni at 400°C. Morphology and diffraction suggest that the Si and Cr-rich phase found in 12Cr-1MoVW was also η, but more work is needed.

(7) The $M_{23}C_6$ (τ) and V-rich MC phases were compositionally modified during irradiation at 400°C in 9Cr-1MoVNb - 2Ni. After irradiation the MC contained significantly less V and more Cr, whereas the τ phase had somewhat less Cr and Mo, but measurably more Si, V, Ni, and Nb.

7.1.6 Future Work

Future work will include quantification of the cavity microstructural results qualitatively presented here, as well as continued AEM study and identification of the precipitation in these steels. Further work will also extend microstructural and precipitation studies of samples of these same Ni-doped and undoped 9Cr-1MoVNb and 12Cr-1MoVW steels irradiated in FFTF at 400°C to similar fluences.

7.1.1 References

1. R. L. Klueh, J. M. Vitek, and M. L. Grossbeck, "Nickel-Doped Ferritic (Martensitic) Steels for Fusion Reactor Irradiation Studies: Tempering Behavior and Unirradiated and Irradiated Tensile Properties," pp. 648–64 in ***Effects of Radiation on Materials: Eleventh Conference,*** eds., H. R. Brager and J. S. Perrin, ASTM STP 762, American Society for Testing and Materials, 1982.

2. D. S. Gelles and L. E. Thomas, "Effects of Neutron Irradiation on Microstructure in Experimental and Commercial Ferritic Alloys," p. 559 in ***Proceedings of Topical Conference on Ferritic Alloys for Use in Nuclear Energy Technologies,*** ed. J. W. Davis and D. J. Michel (The Metallurgical Society of AIME), Warrendale, PA, 1984.

3. D. S. Gelles, "Swelling in Several Commercial Allovs Irradiated to Very High Neutron Fluence," ***J Nucl. Mater.*** **122&123** (1984) 207–213.

4. K. Anderko, "Zur Eignung Warmfester Vergitungsstahle mit 9 bis 12% Chrom fiir Komponenten in Kern Schneller Reaktoren – ein Uberblick," ***J. Nucl. Mater.*** **95**(1980) 31-43.

5. J. M. Vitek and R. L. Klueh, "Microstructure of HFIR-Irradiated 12Cr-1MoVW Ferritic Steel," pp. 551–58 in *Proc. Topical Conf. Ferritic Allous for Use in Nuclear Energy Systems*, eds. J. W. Davis and D. J. Michel, The Metallurgical Society of AIME; Warrendale, PA, 1984.

6. J. M. Vitek and R. L. Klueh, "Microstructure of 9Cr-1MoVNb Steel Irradiated to 36 dpa at Elevated Temperatures in HFIR," ***J. Nucl. Mater.*** **122&123** 254 (1984).

7. D. S. Gelles, "Microstructural Comparison of HT-9 Irradiated in HFIR and EBR-II," pp. 129–136 in ***ADIP Semiann. Frog. Rep. March 31, 1985,*** DOE/ER-0045/14, U. S. DOE, Office of Fusion Energy.

8. P. J. Maziasz, R. L. Klueh, and J. M. Vitek, "Some Effects of Increased Helium Generation Microstructure and Swelling of Nickel-Doped 9Cr-1MoVNb Steel Irradiated in HFIR," pp. 81-86 in ***ADIP Semiann. Prog. Rep. March 31, 1985,*** DOE/ER-0045/14, U. S. DOE, Office of Fusion Energy.

9. M. L. Grossbeck, J. W. Woods, and G. A. Potter, "Experiments HFIR-CTR-30, -31, and -32 for Irradiation of Transmission Electron Microscopy Disk Specimens," pp. 36-44 in ***ADIP Quart.*** *Frog.* ***Rep. Sept. 30,*** *1980*, DOE/ER-0045/4, U. S. DOE, Office of Fusion Energy.

10. L. R. Greenwood, "Fission Reactor Dosimetry – HFIR-CTR-30, -36, -46," pp. 22–26 in ***ADIP*** **Semiann. *Prog. Rep. March 31, 1985,*** DOE/ER-0045/14, U. S. DOE, Office of Fusion Energy.

11. P. J. Maziasz, "Effects of Helium Content on Microstructural Development in Type 316 Stainless Steel Under Neutron Irradiation," ORNL-6121, November 1985.

12. P. J. Maziasz and R. L. Klueh, "Microstructural/Microcompositional Analysis of Normalized-and-Tempered 9Cr-1MoVNb and 12Cr-1MoVW Steels Doped with 2% Nickel," pp. 74–80 in ***ADIP Semiann. Prog. Rep. March 31, 1985,*** DOE/ER-0045/14, U. S. DOE, Office of Fusion Energy.

13. P. J. Maziasz and V. K. Sikka, "The Effects of 25,000 h Aging at 480 to 700°C on Precipitation and Microstructural Stability in Several Heats of Tempered 9Cr-1MoVNb Steel," Sect. ***1.2*** in this report.

14. L. P. Stoter and E. A. Little, "Microstructural Evolution and Phase Stability in Fast Reactor Irradiated 12% Cr Martensitic Stainless Steel," pp. 369–378 in *Conf. Roc. Advances in the Physical Metallurgy* ***and Applications of Steels,*** The Metals Society, London, 1981.

7.2 THE EFFECTS OF 25,000 h AGING AT 480 TO 700°C ON PRECIPITATION AND MICROSTRUCTURAL STABILITY IN SEVERAL HEATS OF TEMPERED 9Cr-1MoVNb STEEL

— P. J. Maziasz and V. K. Sikka
(Oak Ridge National Laboratory)

7.2.1 AOIP Task

ADIP Tasks are not defined for Path E, Ferritic Steels, in the 1978 Program Plan.

7.2.2 Objectives

This investigation was undertaken on two heats of 9Cr-1MoVNb aged for up to 25,000 h. This material was made available by the Breeder Reactor Structural Materials Program to study the phase/microstructure response during thermal aging. These data will also provide a base line for fusion program studies of precipitation formed in reactor-irradiated 9Cr-1MoVNb.

7.2.3 *Summary*

Two heats of tempered 9Cr-1MoVNb, with silicon variation as their main difference, were aged for up to 25,000 h at 482 to 704°C. The as-tempered grain and subboundary structure remained stable after 25,000 at 593°C and below, but then recovered and coarsened at 650°C and above. The as-tempered precipitate structure of $M_{23}C_6$ and MC particles remains stable upon aging at 650°C and below, but then coarsened somewhat after 25,000 h at 704°C. A considerable amount of Laves phase forms at 482 to 593°C after 25,000 h, with much more occurring in the higher silicon heat of steel. Neither heat had Laves after 10,000 h at 650°C, and Laves forms only in the higher silicon heat of steel after 25,000 h. An intracell precipitate of very fine VC needles was found in both heats of steel after aging at 482 to 593°C. The overall precipitate composition reflects the dominance of the chromium-rich $M_{23}C_6$ phase, but the molybdenum content also increased as the fraction of Laves phase increased. Compositionally, the various phases were not very sensitive to temperature, time, or particle size, except for minor sensitivities of VC to size at 538°C, and of $M_{23}C_6$ and VC *to* temperature at 704°C.

7.2.4 Progress and Status

7.2.4.1 Introduction

There have been short-term (2.5–6 h) aging studies of normalized 9Cr-1MoVNb at 400 to 780°C,[1] and longer term (–20,000 h) aging studies of 9Cr-1Mo at 500 to 550°C,[2] but no long-term studies of the niobium- or vanadium-modified 9Cr-1Mo over a wide temperature range. Samples had become available from studies by the Liquid Metal Fast Breeder Reactor (LMFBR) Materials and Structure Program of DOE to investigate the effects of long-term aging (up to 25,000 h) at 480 to 700°C on mechanical properties. The 9Cr-1MoVNb steel is also one of the candidate ferritic (Path E) alloy being considered for application as the first wall of a fusion reactor. This work was therefore initiated to examine the microstructural stability of the 9Cr-1MoVNb after aging. These data are important to the fusion materials program because, when correlated with the mechanical properties, they can provide mechanistic insight into the properties changes. Furthermore, the thermal aging data provides a base line aqainst which to compare precipitate evolution in these same steels under neutron irradiation to judge whether the phenomena are enhanced thermal or radiation-induced processes.[3,4]

7.2.4.2 Experimental

Various bulk tensile, creep, and Charpy-impact specimens were machined from two heats of 9Cr-1MoVNb steel, whose compositions are listed in Table 7.2.1. The major difference between the two heats was their silicon content. The specimens were aged in the normalized and tempered (1 h at 760°C) condition, stress-free, at temperatures ranging from 482 to 704°C for times of 10,000 and 25,000 h.

After aging, several transmission electron microscopy (TEM) disks (3-mm diam by 0.254-mm thick) were cut from the shoulders of tensile specimens. From a larger shoulder slice, bulk preci itation was extracted electrolytically and the residue weighed to determine the precipitate weight fraction.! From one of the TEM disks, precipitates were again electrolytically extracted onto a carbon replica, which was suspended on either a copper or beryllium grid.6 Remaining disks were thinned via electropolishing for TEM. Quantitative x-ray energy dispersive spectroscopy (XEDS) was performed on the extraction replicas using JEM 2000FX and Philips EM400 analytical electron microscopes (AEMs); the latter was equipped with a field-emission gun, which provided the very fine, high-brightness electron probe that made analysis of very small (<10 nm in diameter) precipitate particles possible. Thin-foil microscopy was performed on a JEM 100C TEM equipped with a special objective lens pole-piece designed to minimize the ferromagnetic effect of the specimens on the electron beam.

Table 7.2.1. Compositions of commercial heats of 9Cr-1MoVNb investigated

Heat designation	Alloy compositiona (wt %)										
	Cr	Mo	V	Nb	Mn	Si	C	Cu	W	P	N
30176	8.6	0.9	0.21	0.072	0.37	0.11	0.081	0.04	<0.01	0.01	0.055
30394	8.6	1.0	0.20	0.073	0.46	0.4	0.084	0.04	0.05	0.01	0.053

[a]Balance Fe.

7.2.4.3 **Results**

Microstructure — subboundary and dislocation structure

Specimen designations and aging conditions, as well as precipitation fractions and phases, are listed in Table 7.2.2. The TEM microstructures from thin-foil specimens of the low silicon heat (30176) of 9Cr-1MoVNb are shown at lower and higher magnifications in the as-tempered condition and after aging for 25,000 h at 540 to 700°C in Fig. 7.2.1.

Relative to the as-tempered starting material, the subboundary structure within the prior austenite grains remains fairly constant after aging for 25,000 h at up to 593°C. At 650°C. however, some of the cell structure coarsened slightly as the elongated former martensite laths become polygonal. At 704°C, the subgrains were noticeably larger, as seen in Fia. 721. At hiaher magnification; the intracell dislocation density after aging at 538 and 593°C was hiaher than found in the as-tempered stricture, particularly at 538°C. However, at both 650 and 704°C. recovery produced many fairly dislocation-free subgrains. Boundary and dislocation structures showed little effect of time, comparing aging for 10,000 to 25,000 h at 538 and 650°C in heat 30176, and little or no heat-to-heat variation.

Table 7.2.2. Specimen treatment conditions and general precipitation data

Specimen designation	Aging conditions		Bulk precipitate extraction (wt %)	Phases observed on extraction replicas via XEDP
	Time (h)	Temperature (°C)		
		Heat 30176 (0.1 wt % Si)		
T-20	As-tempered (1 h at 760°C)		1.713	$M_{23}C_6$ + VC + NbC
24047	25,000	482	2.087	$M_{23}C_6$ + Laves + VC t NbC t Cr_2X(?)
T-214	10,000	538	2.027	$M_{23}C_6$ t Laves t VC
T-344	25,000	538	2.358	$M_{23}C_6$ + Laves t VC + some fine Fe-Cr phase
T-362	**25.000**	**593**	***2.247***	$M_{23}C_6$ + Laves + VC + NbC
T-246	10,000	650	1.748	$M_{23}C_6$ t VC t NbC
T-378	25,000	650	1.810	$M_{23}C_6$ + VC + NbC
T-394	25,000	704	1.786	$M_{23}C_6$ t VC + NbC
		Heat 30394 (0.4 wt % Si)		
T-19	As-tempered		1.833	$M_{23}C_6$ t VC t NbC
23985	25,000	482	3.137	$M_{23}C_6$ t Laves + VC t NbC
T-616	25,000	538	3.183	$M_{23}C_6$ t Laves t VC t some fine Fe-Cr phase
T-313	10,000	650	1.802	$M_{23}C_6$ t VC + NbC
T-584	25,000	650	2.729	$M_{23}C_6$ + Laves + VC + NbC

[a]Phase identified from individual particle analysis and characteristic spectra, relative phase fraction determined from broad-beam XEDS of many particles. Order represents decreasing phase fraction.

Precipitation — microstructural information

The weight fractions of precipitation for both heats of 9Cr-1MoVNb are plotted as a function of aging temperature in Fig. 7.2.2(*a*). The precipitate microstructures can be seen on carbon extraction replicas from the low silicon heat (30176) of 9Cr-1MoVNb at higher and lower magnifications after aging for 25,000 h at 482 to 704°C in Fig. 7.2.3.

The amount of precipitation in heat 30176 of 9Cr-1MoVNb increased measurably after 25,000 h aoino at 482 to 593°C, but showed little change at 650 and 704°C relative to as-tempered amount of precipitate in the structure [Fig. 7.2.2(*a*)]. Maximum precipitation occurred at 538°C, and the weight

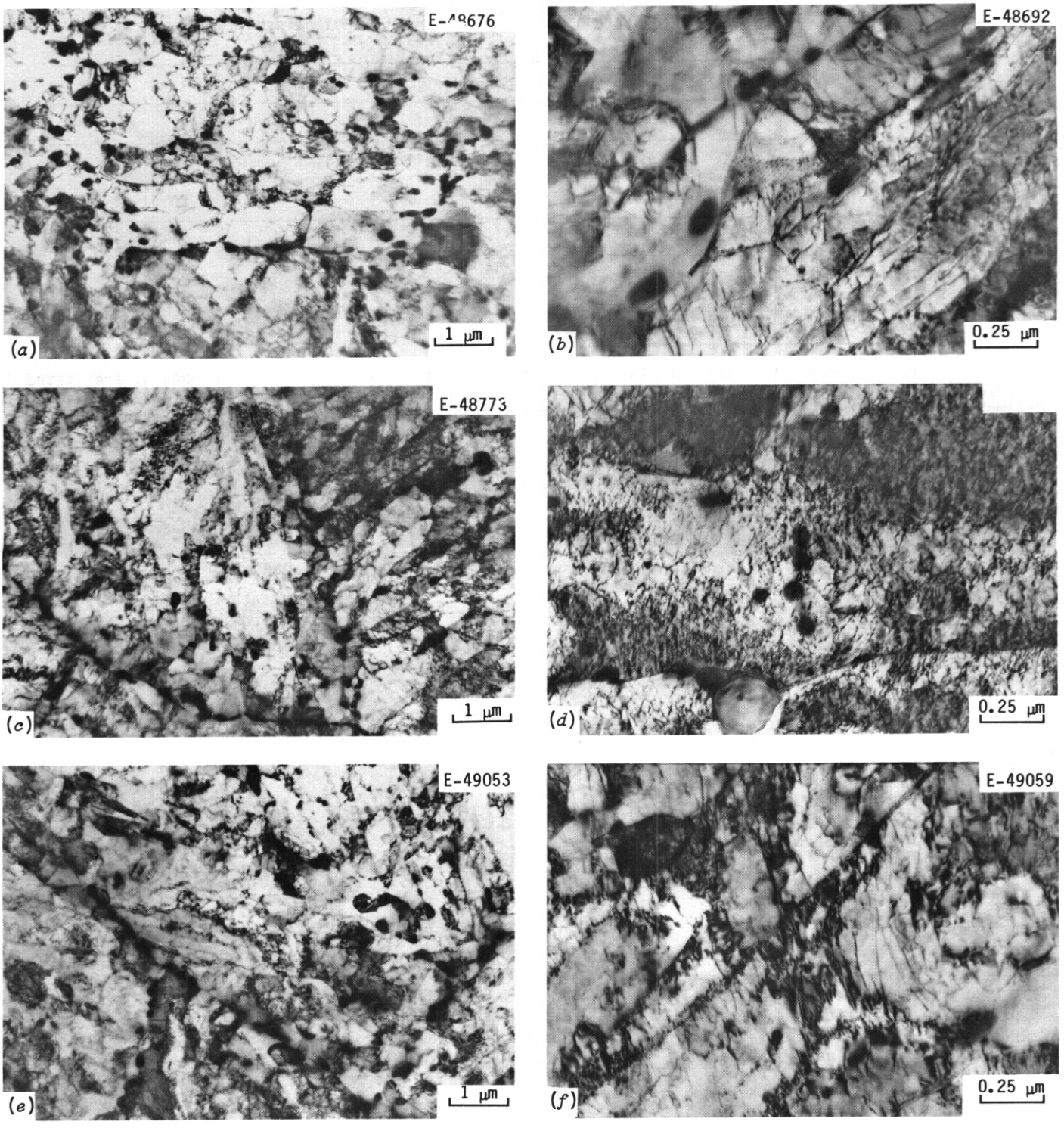

Fig. 7.2.1. The microstructure of heat 30176 of 9Cr-1MoVNb steel (a,b) as-tempered (1 h at 760°C) and after aging for 25,000 h at (c,d) 538°C, (e,f) 593°C, (g,h) 650°C, and (i,j) 704°C. Low magnification shows the overall subboundary structure and higher magnification shows the intracell dislocation structure; both pictures are included for each sample, as indicated. (Figure continued.)

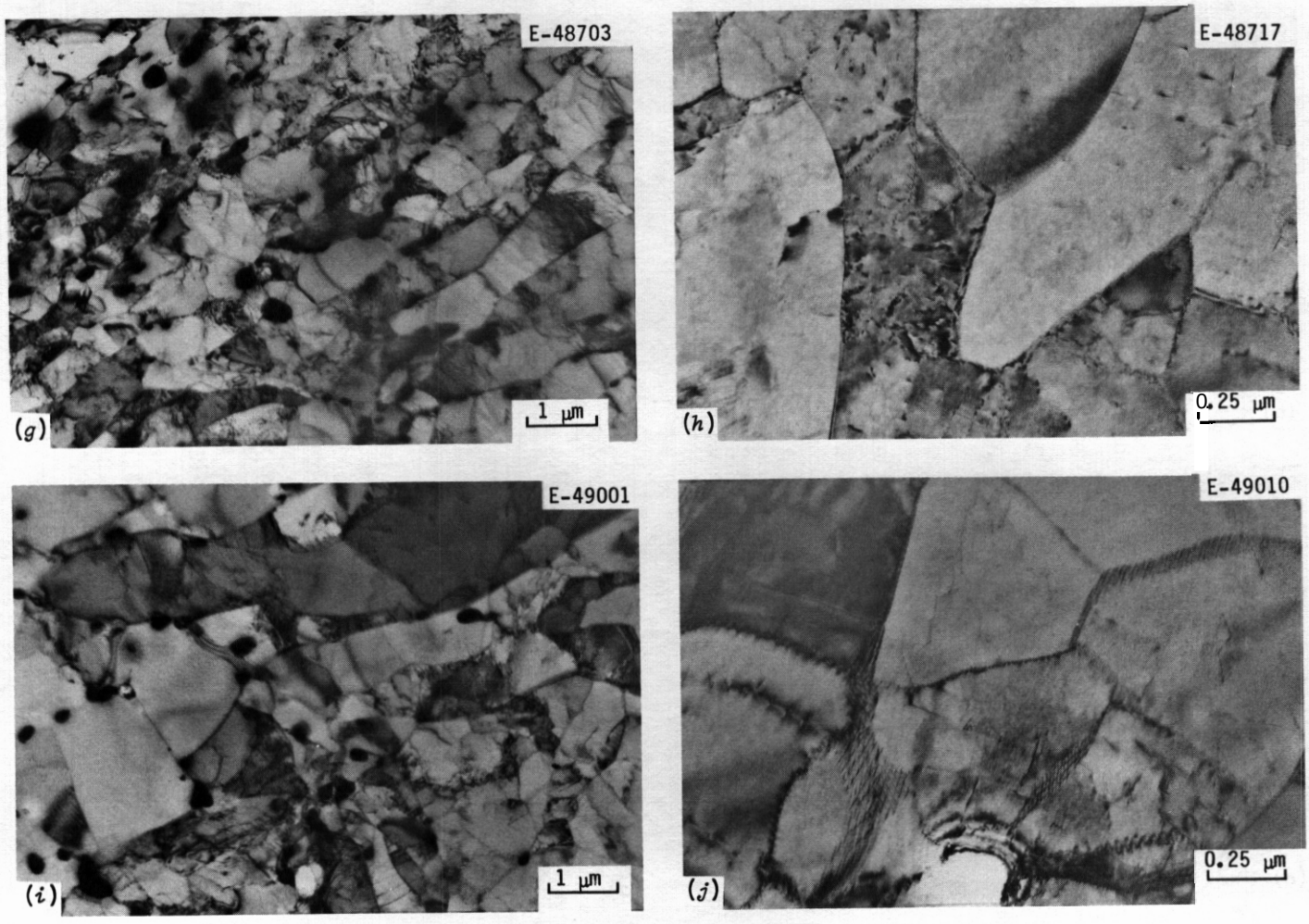

Fig. 7.2.1. (continued).

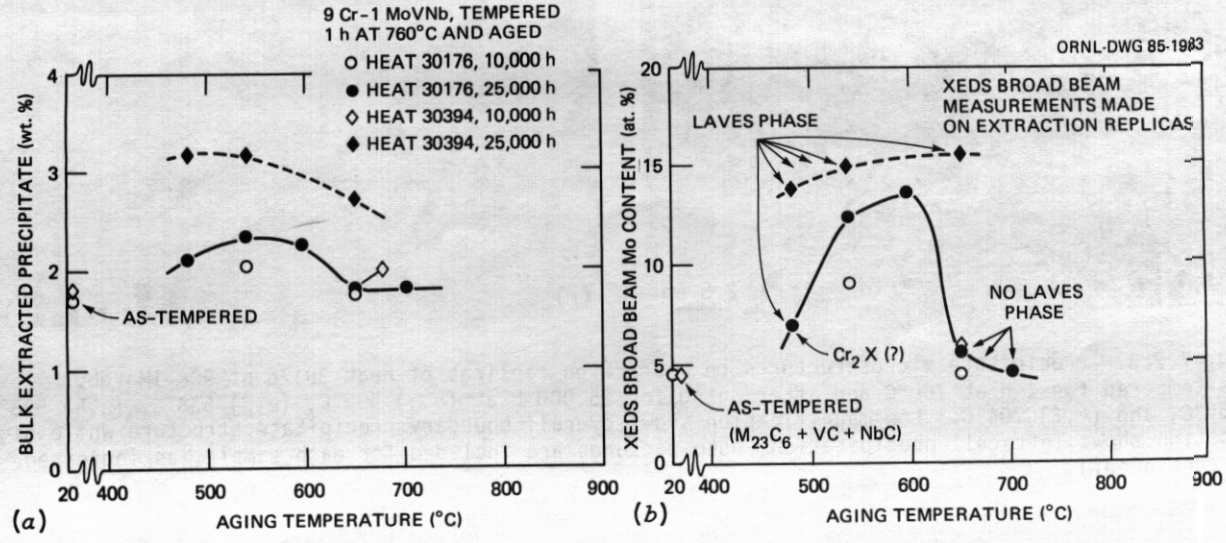

Fig. 7.2.2. (*a*) Bulk residue weight extraction of precipitate and (*b*) XEDS broad-beam measurement of molybdenum content of the overall precipitate extracted on carbon-film replica for 9Cr-1MoVNb aged from 10,000 to 25,000 h at 482 to 704°C. Increased molybdenum above the level found in the as-tempered material indicates the presence of Laves phase.

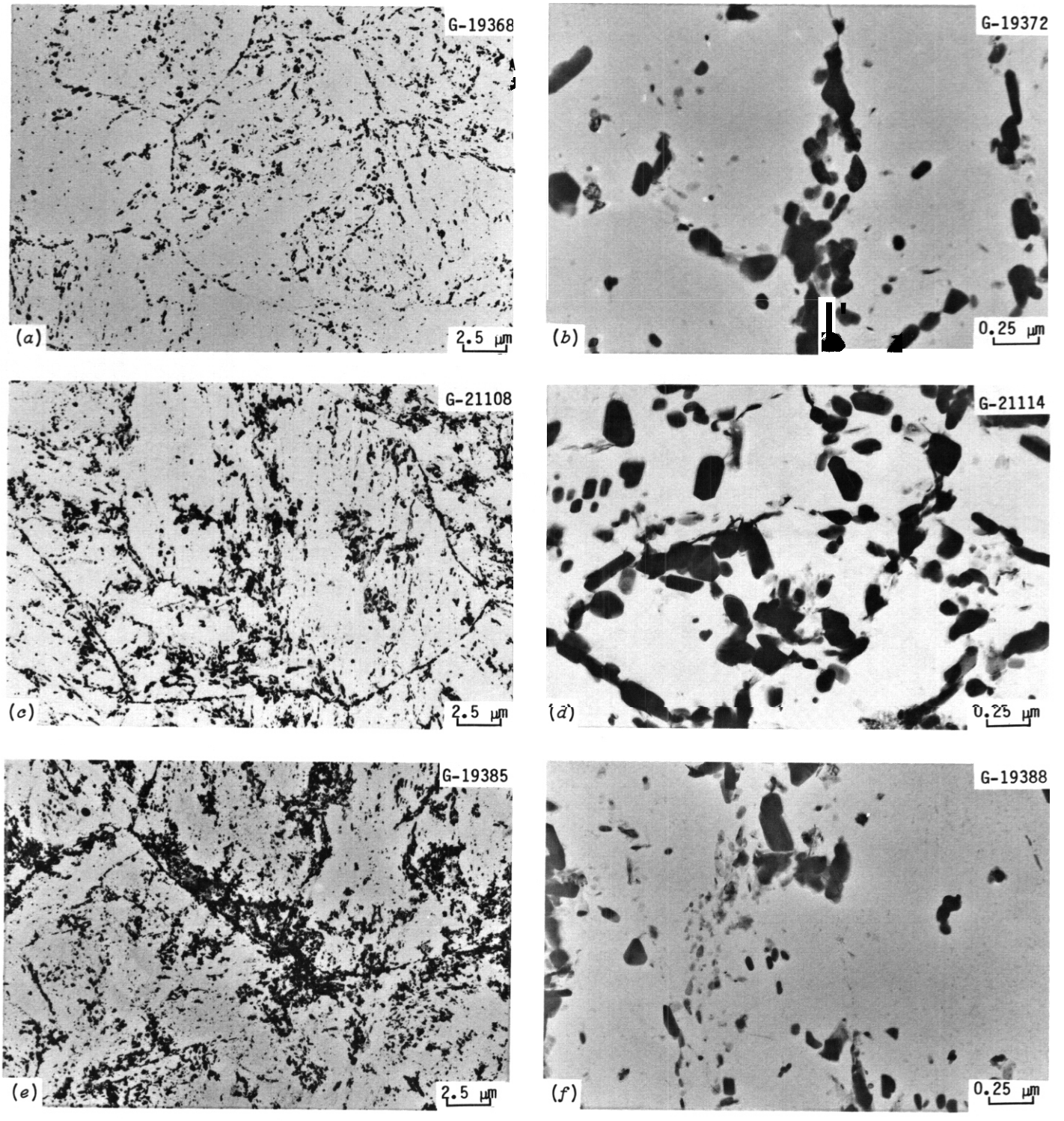

Fig. 7.2.3. Precipitate microstructures on extraction replicas of heat 30176 of 9Cr-1MoVNb. (*a*,*b*) As-tempered for 1 h at 760°C and after aging for 25,000 h at (*c*,*d*) 482°C, (*e*,*f*) 538°C, (*g*,*h*) 593°C, (*i*,*j*) 650°C, and (*k*,*l*) 704°C. Low magnification shows overall boundary precipitate structure while higher magnification shows intracell precipitation; both pictures are included for each sample, as indicated. (Figure continued.)

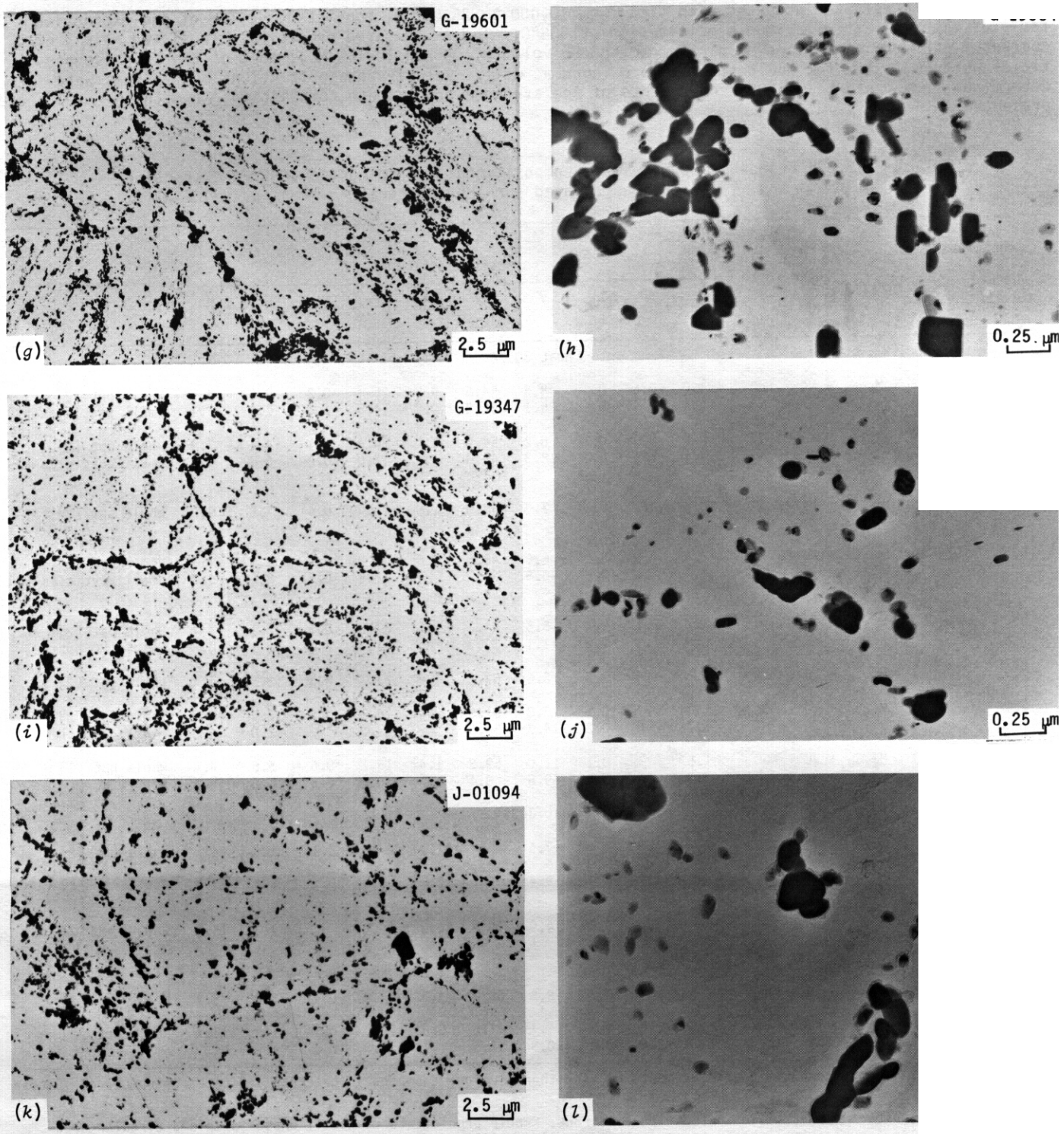

Fig. 7.2.3. (continued).

fraction of precipitate increased with time from 10,000 to 25.000 h; consistently, TEM of the extraction replicas also indicated maximum precipitation at 538°C. The as-tempered precipitate consisted mainly of coarser $M_{23}C_6$ with some finer MC particles (~85–90 vol % $M_{23}C_6$ and 1045% MC); most of the MC phase particles were VC, but a few NbC particles were found as well. Relative phase fractions on replicas were determined from broad-beam XEDS measurements of the averaged precipitate composition,[7] and these results are presented in Table 7.2.3.

Table 7.2.3. Broad-beam precipitate compositional averaging via XEDS in extraction replicas of aged 9Cr-1MoVNb steel

Tempera-	Ti		Composition[a] (at. %)										Comments[b]
Heat 30176													
As-tempered		$M_{23}C_6$ + VC + NbC	4.0	0.5	0.1	8.3	54.5	0.2	25	0.2	3.0	4.5	Whole ppt [2]
			11.2	0.4	0.1	26.1	36.8	0.2	14.5	0.1	7.8	3.1	Small particles [2]
482	25,000	$M_{23}C_6$ + Laves + VC + NbC + Cr_2X(?)	0.5	0.9	0.1	8.2	54.2	0.1	24.8	0.1	4.1	7.0	Whole ppt [2]
			1.1	1.1	0.1	18.3	49.3		17.0	0.2	6.8	6.2	Small particles [1]
538	10.000	$M_{23}C_6$ t Laves + VC	2.7	2.3	0.1	7.0	48.0	1.5	27.4	0.4	1.8	9.0	Whole ppt [2]
538	25.000	$M_{23}C_6$ + Laves + VC + fine Fe-Cr phase	2.4	1.3	0.1	6.6	45.6	0.6	29.3	0.1	1.8	12.3	Whole ppt [2]
			4.7	2.1	0.5	46.5	24.7		12.2	0.5	3.0	6.2	Small particles [2]
593	25.000	$M_{23}C_6$ + Laves t VC + NbC	3.7	2.1	0.1	5.5	44.7	0.5	27.5	0.1	2.1	13.7	Whole ppt [2]
			3.8	1.3	0.2	71.1	13.3		1.3		8.1	0.8	Matrix MC ppt [2]
650	10.000	$M_{23}C_6$ + VC + NbC	4.5	1.4	0.2	66	63.2	1.2	17.0	0.3	2.3	4.4	Whole ppt [2]
650	25.000	$M_{23}C_6$ + VC + NbC	4.3	0.7	0.1	8.8	61.5	0.4	16.1	0.2	2.9	5.3	Whole ppt [2]
			5.7	0.6	0.2	14.7	56.5		14.8		2.8	4.8	Small particles [2]
704	25,000	$M_{23}C_6$ + VC + NbC	1.5		0.1	11.0	59.2	1.4	16.2	0.6	56	4.4	Whole ppt [3]
			2.3		0.8	69.8	8.4		0.8	0.6	16.8	0.4	Matrix MC [2]
Heat 30394													
As-tempered		$M_{23}C_6$ + VC + NbC	2.8	1.3		7.5	56.4	1.3	24.5	0.1	1.3	4.5	Whole ppt [2]
482	25,000	$M_{23}C_6$ + Laves + VC + NbC	3.8	1.2	0.1	9.4	39.6	0.6	27.4	0.2	3.9	13.8	Yhole ppt [2]
538	25,000	$M_{23}C_6$ + Laves + VC + NbC t some fine Fe-Cr phase	5.6	2.0	0.1	4.9	39.5	0.8	30.8		1.3	15.0	mole ppt [2]
650	10,000	$M_{23}C_6$ + VC + NbC	1.3	1.6	0.2	8.5	59.7	1.3	17.9	0.4	3.8	5.4	Whole ppt [2]
650	25.000	$M_{23}C_6$ + Laves t VC + NbC	5.5	1.6	0.1	4.7	41.6	0.6	28.9	0.1	1.3	15.7	Whole ppt [2]
			10.5	1.6	0.1	60.9	18.9		2.5	0.1	4.4	1.1	Small MC ppt [1]

[a]Normalized, averaged composition for elements heavier than aluminum (numbers in brackets indicate the number of spectra analyzed.).

[b]Comments describe the areas illuminated with electrons. Whole precipitate means all phases within a circular area 15 μm in diameter or larger. Small broad-beams included small particles within grains or lath boundaries 1 to 3 μm in diameter.

Broad-beam XEDS analysis (molybdenum content) as well as conventional TEM indicated that increased precipitation at 482 to 593°C was due to Laves formation at those conditions. Much more Laves phase formed at 482 to 593°C in the higher silicon heat (30394) of 9Cr-1MoVNb. This can easily be seen from the weight fractions in Fig. 7.2.2(*a*), the broad-beam molybdenum concentration in Fig. 7.2.2(*b*), and via TEM of replicas of material aged at 538°C in Fig. 7.2.4(*a*) and (*b*). Laves phase particles formed between the carbides which were formed along subgrain boundaries in both heats of steel during tempering. In heat 30394, the Laves particles were larger and engulfed the carbides to form large, globular particle clusters [see Fig. 7.2.4(*c*) and (*d*)]. Some subgrain boundaries at 538°C also had thin layers of Laves growing almost continuously along the boundaries, as shown via bright- and dark-field TEM in Fig. 7.2.5. Laves particles were much coarser at 593°C. The amount of Laves phase increased with time in both heats of steel at 538°C. Laves phase was not found in either heat of steel at 650°C after aging for 10,000 h, but then was found only in the high silicon heat (30394) after 25,000 h.

In addition to coarse precipitation, fine matrix VC precipitates were found in both heats of steel at 482 to 593°C after 25,000 h, but not at 650°C or above. Figure 7.2.6 shows these fine particles from two areas at high magnification on a replica to show their morphological variation in heat 30176 of 9Cr-1MoVN aged for 25,000 h at 538°C. Most often, they appeared as needles, as shown in Fig. 7.2.6(*b*), but occasionally they also appeared as thin platelets or equiaxed particles. Thin-foil TEM on the same sample in Fig. 7.2.6(*c*), (*d*), and (*f*) shows that these needles were distributed uniformly along dislocations within the laths or cells. On a larger scale, this fine precipitation was heterogeneous because many groups of cells would have it while some would not. It was more heterogeneous at 593°C than at lower temperatures. A few fine particles of an unknown Fe-Cr phase were found mixed among the fine VC only in heat 30176 after 25,000 h at 538°C. However, many larger rods of a chromium- and vanadium-rich phase were also only found in heat 30176 after 25,000 h at 482°C; they were tentatively identified as an M_2X phase because of their similarity to that phase found by others.[2,8,9]

The as-tempered precipitate structures appeared to remain stable, while the above-mentioned precipitation superimposed upon it during aging at 482 to 593°C. At 650°C, aging caused little change compared to the as-tempered structure [Fig. 7.2.3(*b*) and (*i*)]. There may, however, have been a little more VC precipitation due to particle growth in heat 30176 after aging for 25,000 h, judging from an increased vanadium signal in the broad-beam measurements (see Table 7.2.3). At 704°C, however, particles of both the $M_{23}C_6$ and the MC phases definitely coarsened, and there appeared to be a moderate increase in the MC relative to the $M_{23}C_6$ phase fraction as well. Figure 7.2.3 shows the obvious coarsening at low magnification [cf. (*a*) and (*k*)]; at higher magnification, there are less small MC particles and more particles that are larger after aging at 704°C than found in the as-tempered structure [cf. (*b*) and (*l*)]. The broad-beam measurements in Table 7.2.3 show the definite increases in vanadium and niobium contents of overall precipitates, which indicates a larger relative fraction of both VC and the mixed vanadium- and niobium-rich MC.

Precipitation — microcompositional information

The various phases were compositionally distinct, and easily identified by characteristic "fingerprint" spectra, as shown in Fig. 7.2.7. Averaged compositions for $M_{23}C_6$ and Laves phases as well as MC and other fine phase particles are given in Tables 7.2.4 through 7.2.6, respectively. Most of the phases were very rich in chromium and/or vanadium and niobium. Only the Fe-Cr phase and Laves phase showed appreciable in contents, and only Laves phase showed substantial enrichments of phosphorus, silicon, and molybdenum.

Laves was the only phase to show any systematic compositional sensitivity to heat chemistry of the steel; the silicon content of Laves phase was significantly higher in the higher silicon heat of steel (30394) after aging at 538 to 593°C for 25,000 h (Table 7.2.5). None of the phases showed any measurable compositional change with time at temperatures of 650°C or below. Phase compositions were not sensitive to aging temperature below 650°C. However, at 650 to 704°C, the $M_{23}C_6$ phase became progressively richer in chromium content at the expense of iron as aging temperature increased for both heats of steel after 25,000 h (Table 7.2.4). At 704°C, the MC phase composition also changed relative to the as-tempered or lower temperature aging conditions, as the VC particles became richer in niobium at the expense of chromium (Table 7.2.6). In addition, there were more mixed vanadium- and niobium-rich MC particles at 704°C, as opposed to the either vanadium- or niobium-rich particles found at lower temperatures.

Finally, VC was the only phase to show any compositional sensitivity to particle size. At 482 to 538°C, the very tiny VC needles had more chromium and less vanadium than did larger VC particles (Table 7.2.6).

7.2.5 Discussion

This discussion will be limited only to an overall perspective of the various microstructural/microcompositional changes relative to one another and of results in this work relative to work done by others.

The various microstructural/microcompositional changes correlate with each other in a reasonable manner. The overall subgrain boundary structure remains stable as long as the as-tempered precipitate structure remains stable. The as-tempered carbide precipitate structure only becomes unstable at the temperatures above those at which there is no longer additional phase precipitation during aging. Only under these conditions does the subgrain structure recover into larger, more equiaxed cells, suggesting that th

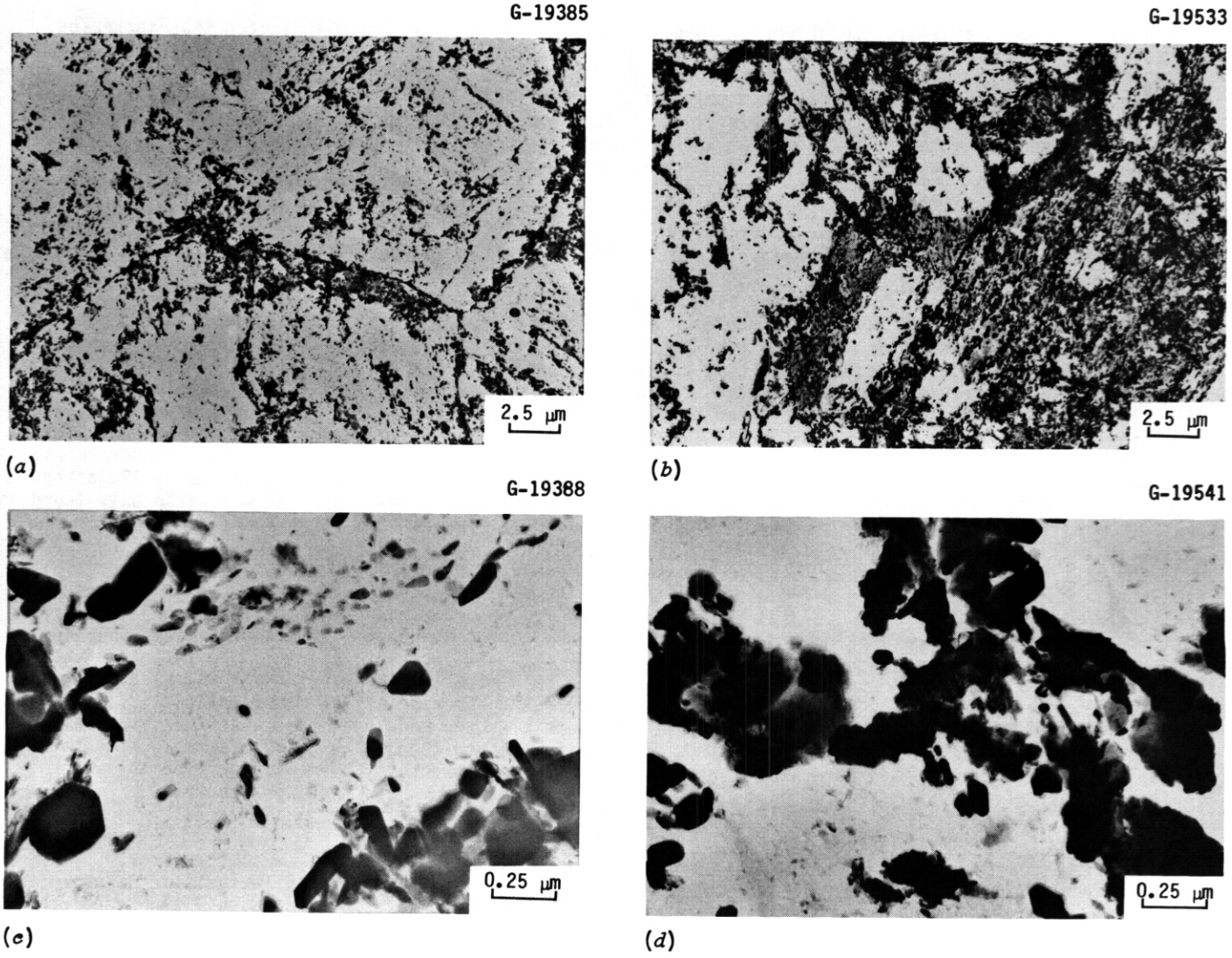

Fig. 7.2.4. Replica microstructures show the heat-to-heat variation in Laves precipitation in 9Cr-1Mo-Nb aged 25,000 h at 538°C. (*a*,*c*) heat 30176, 0.1 wt % Si and (*b*,*d*) heat 30394, 0.4 wt % Si.

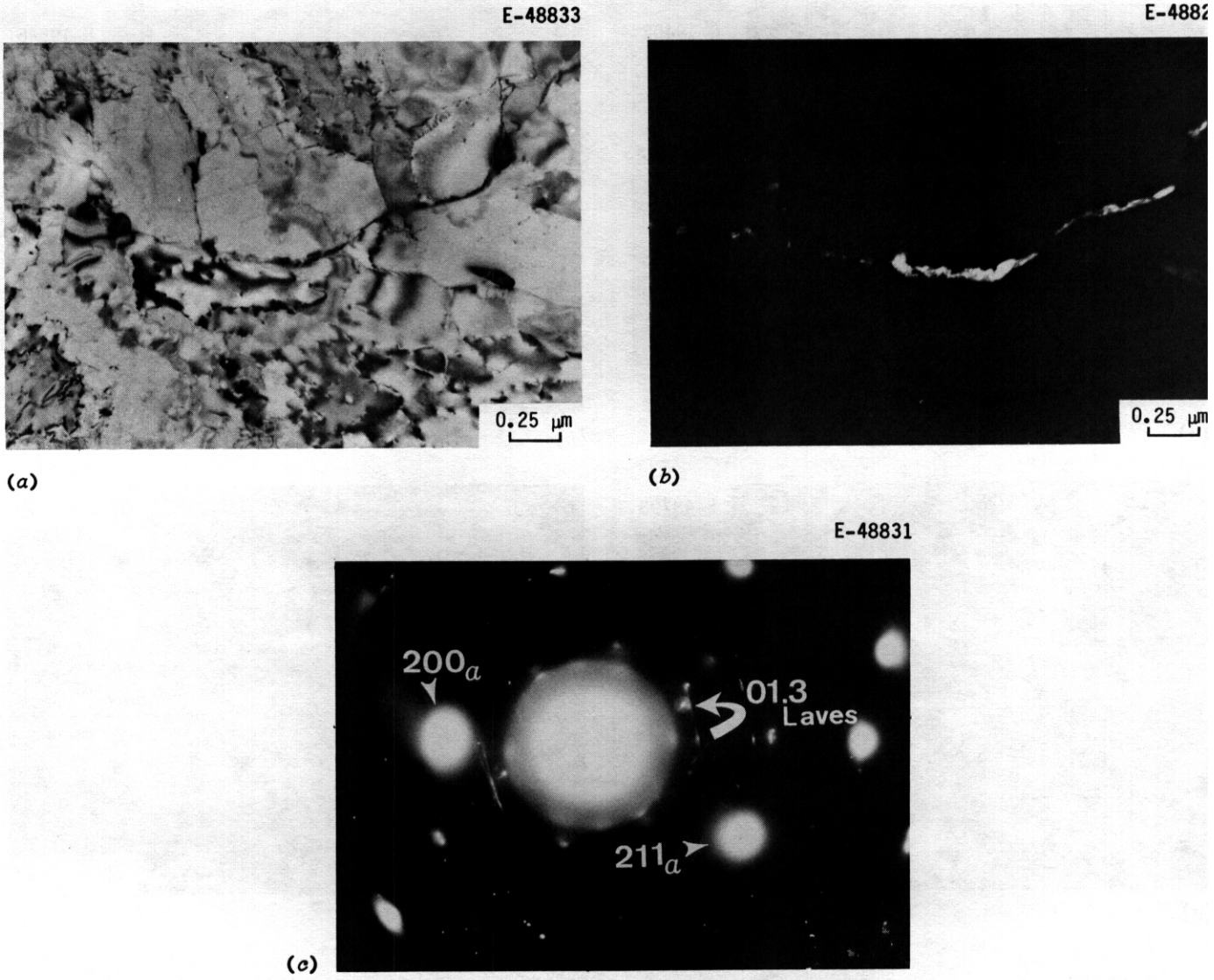

Fig. 7.2.5. Laves phase precipitation along grain boundaries in heat 30394 of 9Cr-1MoVNb aged for 25,000 h at 538°C. (*a*) Bright field, (*b*) precipitate dark field, and (*c*) selected area diffraction showin aperture placement for (*b*).

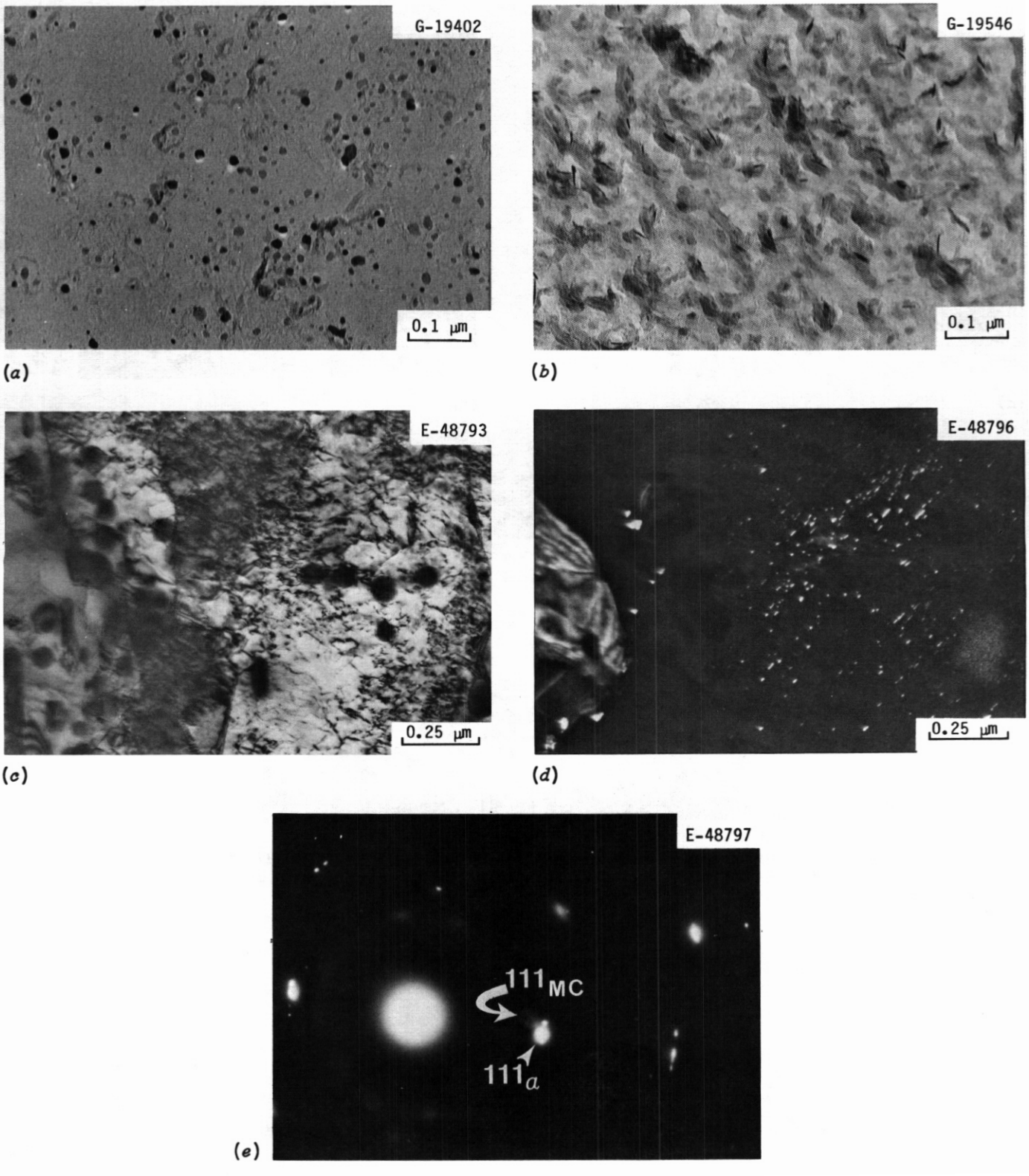

Fig. 7.26. Fine VC precipitate particles formed in both heats of 9Cr-1MoVNb aged for 25,000 h at 538°C. (a) Equiaxed particles (heat 30176) and (b) needle-shaped particles (heat 30394), both on extraction replicas. In-foil TEM shows (c) bright field, (d) precipitate dark field. and (e) selected area diffraction of fine needle particles formed in heat 30176 [arrow in (E) indicates objective aperture].

precipitate particles restrain boundary migration. Increased intracellular dislocation concentrations coincide both with the increased precipitation due to Laves phase formation as well as the fine VC formation along the dislocations. Finally, compositional changes of the as-tempered phase only occurs at the highest aging temperatures, when mirostructural coarsening is caused by the dissolution of smaller particles in order to form or grow larger ones.

These results on microstructure and precipitation are generally consistent with observations by others on related steels, but these results are new for long-term aging of these specific 9Cr-1MoVNb alloys (also termed modified 9Cr-1Mo). Laves phase has been found by Titchmarsh et al.[2] in an unmodified 9Cr-1Mo steel aged for 20,000 h at 500 to 550°C. They also observed a similar morphological distribution of the Laves phase along substructure boundaries and note consistent phorphorus enrichment, not observed in other phases. Our microstructural/microcompositional observations in vanadium- and niobium-rich variants of the MC phase are generally consistent with those of others in variously modified 9–12 Cr steels.[1,8] Stoter and Little[8] also observed fine VC needles, but in an as-tempered 12Cr-Mo-V steel, not after low-temperature aging. Our observations on the $M_{23}C_6$ phase are also similar to others;[1,2,8] indeed, Stoter and Little observed coupled microstructural coarsening and compositional evolution of that phase toward higher chromium concentration in 12Cr-Mo-V aged at 600°C. Finally, others have observed the formation of a Cr_2X or Cr_2N phase in tempered 9Cr-1Mo (ref. 2) or modified 12-Cr alloys;[8,9] however, they do not find that phase forming at lower aging temperatures and do not find the vanadium enrichment that we find. Our observations of Laves formed below 500°C, of coupled microstructural/microcompositional evolution of the MC phase at 704°C, and of the fine VC needles formed at 482 to 593°C appear to be new data for aged 9Cr-1MoVNb steel.

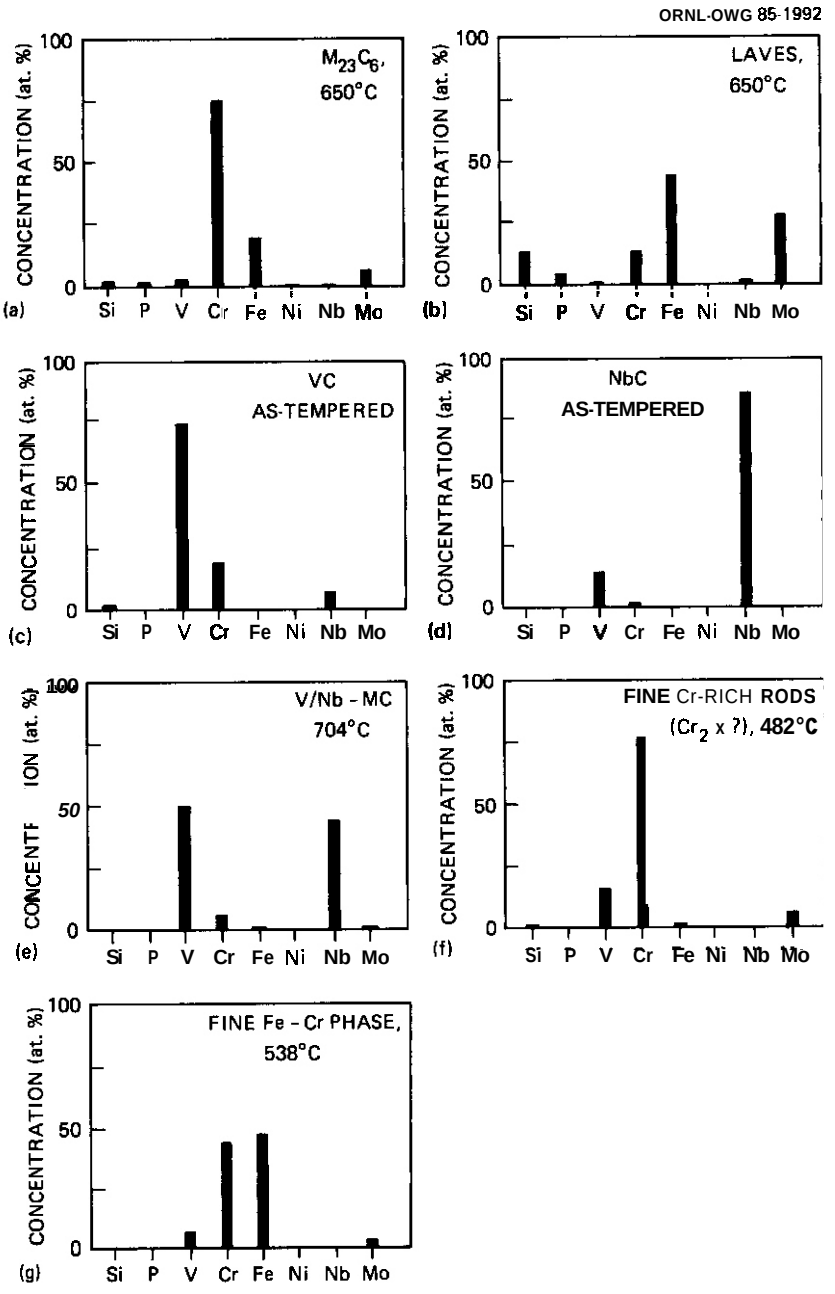

Fig. 7.2.7. Compositional spectra of various phases found in tempered or tempered and aged 9Cr-1MoVNb via XEDS analysis on extraction replicas. *(a)* $M_{23}C_6$ formed at 650°C, *(b)* Laves phase formed at 650°C, *(c)* VC, and *(d)* NbC, both formed during tempering, (e) mixed vanadium- and niobium-rich MC, formed at 704°C, *(f)* fine chromium-rich phase, tentatively identified as Cr_2X, formed at 482°C, and *(g)* fine Fe-Cr phase found at 538°C.

Table 7.2.4. XEOS composition of the $M_{23}C_6$ phase extracted on replicas from aged 9Cr-1MoVNb steel

Aging conditions		Comments[a]	Composition[b] (at. %)									
Temperature (°C)	Time (h)		Si	P	Ti	V	Cr	Mn	Fe	Ni	Nb	Mo
						Heat 30176						
As-tempered		Large [4]	0.8			1.8	62.1	0.3	29.2	0.1	0.2	5.4
		Small [1]	0.8	0.6	0.1	0.7	62.0	0.4	29.8	0.2		5.5
482	25,000	Large [2]		0.4	0.1	0.9	63.6		29.3	0.2	0.2	5.5
		Small [1]	1.3	0.8		0.9	65.1		26.0	0.1		5.9
538	10,000	Large [2]	0.3	0.6	0.1	1.1	64.2	1.3	27.5	0.2	0.1	4.5
538	25,000	Large [4]	0.6	0.6		1.0	63.4	0.4	28.2	0.1	0.1	5.6
		Small [4]	1.7	0.7	0.1	1.3	62.2		27.7	0.1	0.1	6.1
593	25,000	Large [2]	1.1	0.8	0.1	1.1	67.5	0.2	23.1	0.1		5.9
650	10,000	Large [2]	0.8	0.8	0.1	1.2	70.5	1.7	19.3	0.1	0.3	5.2
650	25,000	Large [6]	0.7	0.6		2.5	71.2	0.3	18.3	0.1	0.4	6.1
704	25,000	Large [2]	0.2			1.4	71.0	1.4	20.0	0.3	0.8	4.9
						Heat 30394						
As-tempered		Large [2]	1.3	1.1		1.3	62.7	1.6	27.4		0.1	4.5
538	25,000	Large [2]	1.6	1.0		2.5	61.8	0.5	26.3	0.1	0.1	6.2
		Small [1]		1.0		1.0	68.4	0.6	23.5		0.1	5.7
650	10,000	Large [2]	1.3	0.9	0.1	1.2	67.4	1.7	20.6	0.1	0.4	5.2
650	25,000	Large [2]	1.2	0.3	0.3	0.5	71.5	0.4	20.0	0.1		5.7

[a]Large particles are usually greater than 200 nm in size; small ones are less than 50 nm in size (numbers in brackets indicate the number of individual particle spectra analyzed).

[b]Normalized, averaged composition for elements heavier than aluminum.

Table 7.2.5. XEDS composition of the Laves phase extracted on replicas from aged 9Cr-1MoVNb steel

Aaing conditions		Comments[a]	Composition[b] (at. %)									
Temperature (°C)	Time (h)		Si	P	Ti	V	Cr	Mn	Fe	Ni	Nb	Mo
						Heat 30176						
482	25,000	Large [2]	2.4	4.6	0.1	0.1	17.8	1.0	39.0	0.3	0.2	34.5
538	10,000	Larger31	7.6	5.2	0.1	0.4	12.8	1.4	43.4	0.4	0.3	28.3
538	25,000	Large [3]	7.1	2.8	0.2	0.6	13.2	0.9	43.0	0.2	0.3	31.8
593	25,000	Large [2]	8.2	3.4	0.2	0.1	9.6	0.6	45.1	0.2	0.3	32.3
						Heat 30394						
538	25,000	Large [3]	13.4	3.6		2.2	13.5	0.8	38.3	0.1	0.5	27.0
650	25,000	Large [4]	11.5	3.2	0.1	0.3	12.8	0.6	42.6	0.7	0.7	28.1

[a]Large particles are usually greater than 200 nm in size (numbers in brackets indicate the number of individual particle spectra analyzed).

[b]Normalized, averaged composition for elements heavier than aluminum.

Table 7.2.6. XEOS compositions of MC and other fine phase particles extracted on replicas from aged 9Cr-1MoVNb steel

Aging conditions		Phases and comments[a]	Composition[b] (at. %)									
Temperature (°C)	Time (h)		Si	P	Ti	V	Cr	Mn	Fe	Ni	Nb	Mo
						Heat 30176						
As-tempered		Small VC [5]	1.4	0.1	0.1	74.0	16.9		0.5		6.3	0.6
		Larger NbC [1]				12.2	2.2		0.4		84.7	0.5
		Small NbC [2]				15.3	3.3		0.5		80.2	0.6
482	25,000	g.b.[c] VC [3]	0.5	0.8	0.1	65.8	19.3		3.6		7.1	2.7
		Larger matrix VC [1]	1.2	0.6		68.2	16.1		4.6	0.1	8.7	0.7
		Very fine VC [3]	5.4	1.5	0.2	59.0	23.6		2.8	0.1	3.9	3.5
		Larger matrix NbC [1]		5.9		16.4	3.4	0.1	0.6	0.1	72.5	0.8
		Larger matrix MC [1]		3.0	0.3	51.6	12.8		1.1	0.1	26.9	4.2
		Small Cr-rich rods $[Cr_2X(?)]$ [4]	1.0	0.3	0.1	15.0	75.6		2.1	0.1	0.4	5.4
538	10,000	Small VC [5]	0.5	0.5	0.2	68.0	20.8		2.3	4.6	3.7	3.6
538	25,000	Larger VC C41		0.6	0.1	68.4	22.4		3.1	0.1	4.3	1.0
		Very fine VC [1]	8.1	0.2		52.5	23.1		9.3	0.1	2.7	4.0
		Fine Fe-Cr [3]	0.6	0.3		5.3	43.0		48.4	0.1	0.1	2.2
593	25,000	Larger VC [2]	3.3	0.8	0.2	72.0	12.5	0.1	0.7		9.8	0.6
		Small VC [1]	3.6	1.0	0.2	73.8	14.1	0.1	0.5	0.1	5.8	0.8
		Larger NbC [1]	1.8	1.5	0.3	14.8	3.0	0.2	0.6	0.1	77.6	0.3
650	10,000	Small VC [3]	2.5	0.8		75.8	14.6		0.3		5.1	0.8
650	25,000	Larger VC [5]	1.3	1.1	0.1	67.2	16.2		1.3		12.1	0.7
		Small VC [9]	2.8	0.8	0.1	75.1	13.5		0.6		6.6	0.6
		Small NbC [2]		6.5	0.1	14.0	2.7		0.4		75.6	0.7
704	25,000	Larger VC [2]	1.1		0.7	66.4	6.6		0.7	0.5	23.6	0.2
		Small VC [41]	0.5		0.7	70.7	12.1		0.9	0.6	14.0	0.6
		Larger MC [3]	1.7		0.5	48.5	5.5		0.5	0.7	42.3	0.3
		Small MC [3]	1.8		0.4	49.2	5.2		0.5	0.6	41.8	0.6
		Larger NbC [1]	3.6		0.4	8.1	1.7		0.6	0.9	84.0	0.4
						Heat 30394						
As-tempered		Small VC [1]	1.2	2.1	0.9	75.3	14.2		0.1		5.6	0.7
		Small NbC [1]	6.4	2.0		15.2	3.0		0.5		71.6	1.4
538	25,000	Small VC [6]		1.0		77.6	15.3				5.5	0.3
650	10,000	Larger VC [2]	1.4	2.8	0.1	71.2	8.9		0.4		14.4	0.9
		Small VC [2]	3.1	3.4	0.1	64.2	10.0		0.7	0.1	16.5	1.9
650	25,000	Small VC [5]	3.2	1.8	0.1	70.3	15.0	0.1	0.9		7.5	0.9

[a] Larger particles are greater than ~50 to 60 nm in size, small particles are less than ~30 to 40 nm in size, and very fine particles are usually rods, ~5-nm-thick, 40- to 100-nm long (numbers in brackets indicate the number of individual particle spectra analyzed).

[b] Normalized, averaged composition for elements heavier than aluminum.

[c] g.b. = grain boundary.

7.2.6 Conclusions

1. The grain and subboundary structure of 9Cr-1MoVNb remains stable during long-term aging at up to 593°C, but does begin to recover and coarsen at 650°C and above. Dislocation density within cells increased with aging at 538 and 593°C, but then recovered at 650°C and above relative to the as-tempered dislocation structure.

2. The as-tempered carbide structure ($M_{23}C_6$ + MC) remained stable during aging at 650°C and below, but coarsened at 704°C.

3. New precipitates formed during aging at temperatures below 650°C and super-imposed upon the as-tempered precipitate structure. Laves phase formed in both heats of steel at 482 to 593°C and was maximum at ~538°C after 25,000 h. Much more Laves formed in the higher silicon heat of steel. Laves, however, only formed after 25,000 h at 650°C in the higher silicon (30394) heat of steel.

4. A high concentration of very fine, intracellular precipitates occurred along the dislocation network at 482 to 593°C. Most of these were needles of VC, but a few particles of an unidentified Fe-Cr phase were also found in heat 30176 at 538°C after 25,000 h. A small amount of slightly coarser chromium-rich rods, believed to be an M_2X type phase, were also found in heat 30176 after 25,000 h at 482°C.

5. The various phases were compositionally quite distinct. They generally contained Cr, V, or Nb as their major characteristic constituent, except for the Fe-Cr and Laves phases. Only Laves phase contained substantial enrichments of P, Si, and Mo; Laves phase contained more silicon when formed in the higher silicon heat of steel (30394). Only $M_{23}C_6$ and VC showed composition sensitivity to temperature; at 704°C, $M_{23}C_6$ became richer in chromium at the expense of iron and VC became richer in niobium at the expense of chromium. At 482 to 538°C, the VC phase composition was size sensitive; tiny VC needles had more chromium and less vanadium than did larger particles.

7.2.7 References

1. J. M. Vitek and R. L. Klueh, "Precipitation Reactions During the Heat Treatment of Ferritic Steels," *Met. Trans.* **14A**, 1047–1055 (1983).

2. J. M. Titchmarsh, M. Wall, and B. C. Edwards, "Comparison of Thin-Foil and Carbon Extraction Replicas for the Identification of Particles in 9Cr-1Mo Steels," pp. 247–251 in *Analytical Electron Microscopy — 1984*, eds., D. B. Williams and D. C. Joy, San Francisco Press, Inc., San Francisco, CA, 1984.

3. P. J. Maziasz, R. L. Klueh, and J. M. Vitek, "Some Effects of Increased Helium Generation on Microstructure and Sweiling of Nickel-Doped 9Cr-1MoNb Steel Irradiated in HFIR," pp. 81–86 in *ADIP Semiannu. Prog. Rep., Mar. 31*, 1985, DOE/ER-0045/14, U.S. DOE, Office of Fusion Energy.

4. P. J. Maziasz and R. L. Klueh, Sect. 7.1, this report.

5. W. H. Smith, "Electrolytic Extractions of Precipitates from Steel Alloys," pp. 168-169 in *Proc. 43rd Annual EMSA Meeting*, ed., G. W. Bailey, San Francisco Press, Inc., San Francisco, CA, 1985.

6. E. A. Kenik and P. J. Maziasz, "Application of Extraction Replicas and Analytical Electron Microscopy to Precipitate Phase Studies," pp. 231–234 in *Analytical Electron Microscopy — 1384*, eds., D. B. Williams and D. C. Joy, San Francisco Press, Inc., San Francisco, CA, 1984.

7. P. J. Maziasz and G. R. Odette, "Wide Area Beam Averaged AEM of Precipitate Particles Extracted on Replicas from Type 316 Stainless Steel," pp. 198–199 in *Proc. 41st Annual Meeting of EMSA*, ed., G. W. Bailey, San Francisco Press, Inc., San Francisco, CA, 1983.

8. L. P. Stoter and E. A. Little, "Microstructural Evolution and Phase Stability in Fast Reactor Irradiated 12%Cr Martensitic Stainless Steel," pp. 369–378 in *Conf. Proc. Advances in the Physical Metallurgy and Applications of Steels*, The Metals Society, London, 1981.

9. J. J. Kiu, G. L. Kulcinski, and R. A. Dodd, "The Influence of Thermal Annealing on the Microstructural Evolution in HT-9 Ferritic Steel," pp. 56–67 in *DAFS Quart. Prog. Rept. May 1385*, DOE/ER-0046/21.

7.3 THE OEVELOPMENT OF FERRITIC STEELS FOR FAST INOUCEO-RADIOACTIVITY DECAY — R. L. Klueh, (Oak Ridge National Laboratory)

7.3.1 ADIP Task

ADIP Task I.A.5, Perform Fabrication Analysis, and I.C.l, Microstructural Stability.

7.3.2 Objectives

During the operation of a fusion reactor, the structural material of the first wall and blanket structure will become highly radioactive from activation by the high-energy fusion neutrons. A difficult radioactive waste problem will be involved in the disposal of this material after service. One way to minimize the disposal problem is the use of structural materials in which the induced radioactivity decays rather quickly to levels that allow for simplified disposal techniques. We are exploring the development of ferritic steels to meet this objective.

7.3.3 Summary

Normalizing and tempering studies were continued on eight heats of normalized chromium-tungsten steel that contained variations in the composition of chromium, tungsten, vanadium, and tantalum. Hardness measurements, tensile tests, and optical metallographic observations were used to determine alloying effects on tempering resistance. The results were compared to results for analogous chromium-molybdenum steels.

7.3.4 Progress and Status

7.3.4.1 Introduction

We have continued the studies to characterize eight heats of ferritic steels designed for fast induced-radioactivity decay (FIRO).[1] These steels were patterned on the chromium-molybdenum steels that are of interest for fusion-reactor applications — namely, 2 1/4 Cr-1Mo, 9Cr-1MoVNb, and 12Cr-1MoVW steels. The major changes from the chromium-molybdenum steels involve the replacement of molybdenum with tungsten, the use of vanadium in the 2 1/4% Cr steels, and the replacement of niobium in the 9% Cr steel with tantalum. (Although tantalum can be used in a FIRD steel, the decay of its transmutation products immediately after irradiation in a fast- or mixed-spectrum reactor makes such a steel difficult to study. Therefore, few, if any, irradiated studies will be performed on steels containing tantalum.) The composition of the eight steels is given in Table 7.3.1.

Table 7.3.1. Chemical composition of fast induced-radioactivity decay (FIRD) ferritic steels

Alloy	Chemical composition,[a] (wt %)						
	Cr	W	V	Ta	C	Mn	Si
2 1/4 CrV	2.36		0.25		0.11	0.40	0.17
2 1/4 Cr-1WV	2.30	0.93	0.25		0.10	0.34	0.13
2 1/4 Cr-2W	2.48	1.99	0.009		0.11	0.39	0.15
2 1/4 Cr-2WV	2.42	*1.98*	0.24		0.11	0.42	0.20
5 Cr-2WV	5.00	2.07	0.25		0.13	0.47	0.25
9 Cr-2WV	8.73	2.09	0.24		0.12	0.51	0.25
9 Cr-2WVT[a]	8.72	2.09	0.23	0.075	0.10	0.43	0.23
12 Cr-2WV	11.49	2.12	0.23		0.10	0.46	0.24

[a] P = 0.014–0.016, S = 0.005-0.006, Ni < 0.01, Mo < 0.01, Nb < 0.01, Ti < *0.01*, Co = 0.005–0.008, Cu = 0.02–0.03, Al = 0.02–0.03, B < 0.001, bal Fe.

We previously reported on the tempering characteristics of the Cr-W steels.[2] In the present work, three tasks were completed. The first involved further heat-treating studies on the original eight heats (Table 7.3.1). In the earlier studies, we found that the 12Cr-2WV steel was not 100% martensite, as desired, but contained ~26% 6-ferrite.[2] To determine how a FIRD austenitic steel with 12% Cr might be obtained, three 12Cr-2WV steels were produced, two with different amounts of the austenite-stabilizing element manganese, and one with additional carbon — also an austenitizing element. Finally, tensile properties were determined for the original eight heats of steel.

7.3.4.2 Experimental Procedure

For the heat-treatment studies, pieces of plate and sheet were normalized and then tempered at various temperatures. The steelmaking definition of a normalized steel is one that is austenitized and then air cooled. In the present studies, the "normalization treatment" consisted of austenitization in a helium atmosphere furnace, after which the steel was pulled from the furnace and cooled in flowing helium. Hardness measurements were made on the heat-treated specimens, and pieces of the specimens were used for metallography.

To determine how the 6-ferrite can be eliminated from the 12-Cr steel, three button heats were made by remelting some of the 12Cr-2WV steels. Additions of ~2.5% Mn, 5% Mn, and 0.1% C were made. The compositions of the three new steels along with the composition of the 12Cr-2WV steel to which the additions were made are given in Table 7.3.2.

Tensile tests were made on SS-1 specimens taken from 0.76-mm-thick sheet of the eight heats given in Table 7.3.1. The SS-1 tensile specimens have a reduced gage section 20.3 mm long by 1.52 mm wide by 0.76 mm thick. All specimens were machined with gage lengths parallel to the rolling direction. Tensile tests were made in vacuum on a 44-kN-capacity Instron universal testing machine at a crosshead speed of 8.5 μm/s, which results in a nominal strain rate of 4.2×10^{-4}/s.

Table 7.3.2. Chemical composition of hiah-carbon and high-manganese 12Cr-2WV steel;

Alloy	Chemical compositiona (wt %)					
	Cr	W	V	C	Mn	Si
12Cr-2WV[b]	11.49	2.12	0.23	0.10	0.46	0.24
12Cr-2WV-2.8Mn	11.23	1.79	0.21	0.08	2.76	0.23
12Cr-2WV-5.6Mn	10.86	1.97	0.21	0.08	5.57	0.20
12Cr-2WV-0.2C	11.52	1.83	0.22	0.17	0.40	0.20

[a] P = 0.014–0.016, S = 0.005–0.006, Ni < 0.01, Mo < 0.01, Nb < 0.01, Ti < 0.01, Co = 0.005–0.008, Cu = 0.02–0.03, B < 0.001, bal Fe.

[b] Base composition.

7.3.4.3 Results and Discussion

Heat-treatment studies

For the previous tempering studies,[2] all of the steels except the 2 1/4 Cr-2W were austenitized 0.5 h at 1050°C; the 2 1/4 Cr-2W was austenitized 0.5 h at 900°C. The higher temperature was chosen for the other seven steels because they contained vanadium, which is expected to be present in carbide precipitates. The higher temperature was used to ensure that the carbides were completely dissolved during austenitization.

To determine the optimum austenitiration temperature, a series of 0.76-mm-thick specimens was normalized by annealing 0.5 h at 900, 950, 1000, and 1050°C and then cooling in flowing helium. The results are displayed in Fig. 7.3.1.

The hardnesses of the 2 1/4 CrV and 2 1/4 Cr-1WV increased with temperature and reached similar maximum hardnesses. Maximum hardness for the 2 1/4 CrV occurred at 1000°C and that for the 2 1/4 Cr-1WV occurred at 1050°C. The 9Cr-2W steel reached a maximum hardness after annealing at 950 and 1000°C with a decrease occurring when annealed at 1050°C. Such a hardness decrease could be caused by the increased austenite grain size that would be expected for such a high annealing temperature for a steel without a strong carbide former (e.g., vanadium). The 2 1/4 Cr-2WV steel reached the highest hardness of the 2 1/4% Cr steels. A hardness peak was reached with the 1000°C anneal, although there was little difference between 1000 and 1050°C.

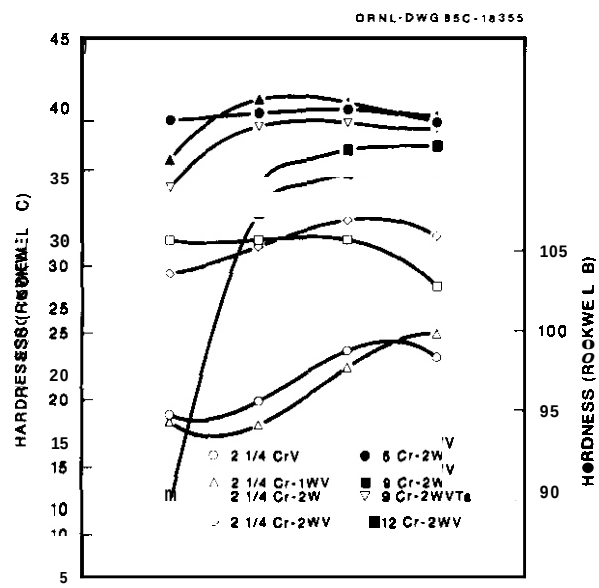

From these results it appears that the tungsten plays an important role in the hardening as the steels with 2% W were considerably harder than the steels with 0 and 1% W. The vanadium had a slight effect on the normalized hardness.

The higher chromium steels fall into two groups: the 5-Cr and 9-Cr steels in one group, the 12-Cr steel in the other. The first group of steels shows a maximum

After that heat treatment, the 2.8% Mn and 5.6% Mn steels contained ~10% and <1% δ-ferrite, respectively. The steel with 0.2% C contained ~5% δ-ferrite in its microstructure. These values compared to the 26% in the base 12Cr-2WV steel.

Although these results indicate that a FIRD martensitic alloy based on 12Cr-2WV steel might be possible, the addition of manganese to the 12Cr-2WV steel to reduce δ-ferrite formation is undesirable if lithium is to be used as the coolant for the first wall of a fusion reactor, the manganese concentration should be minimized, since manganese is highly soluble in lithium. It may therefore be appropriate to use the 0.2% C plus whatever manganese is required to retard δ-ferrite formation (probably about 1.5% in the presence of 0.2% C).

To determine the heat-treatment characteristics of the modified 12Cr-2WV steels, pieces of 0.76-mm-thick sheet were normalized (0.5 h at 1050°C) and then tempered for 2 h at 600, 650, 700, 750, and 780°C. The results are shown in Fig. 7.3.2 along with the results previously obtained for the 12Cr-2WV steel.2 The two steels with manganese added reflect the effect of manganese on raising the Ac_1 temperature. The hardness minimum occurs when the steel is heated above the Ac_1 temperature during tempering. Under these conditions, austenite forms, and when the specimen is cooled from the tempering temperature, martensite forms. The untempered martensite in the microstructure causes the increased hardness with increased tempering temperature. With 5.6% Mn, the Ac_1 temperature is between 650 and 700°C and with 2.8% Mn it is between 750 and 780°C (Fig. 7.3.2). Thus, the high-manganese steel would have to be tempered below 700°C to avoid a microstructure that contained untempered martensite.

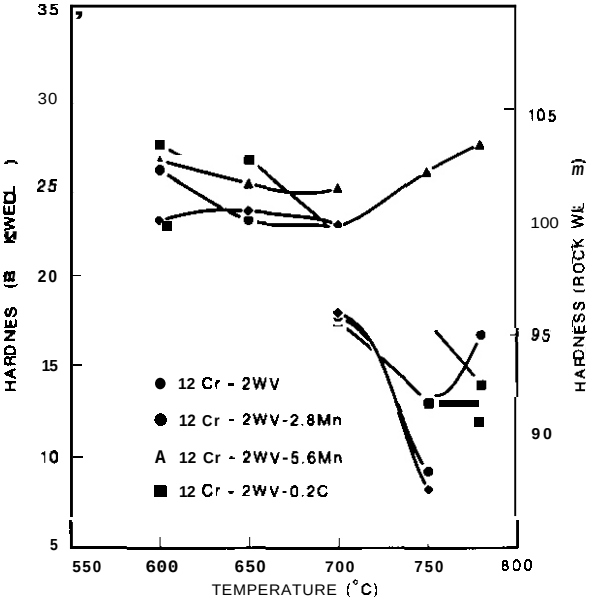

Fig. 7.3.2. Rockwell hardness plotted against tempering temperature for the 12Cr-2WV (0.1% C, 0.4% Mn) steel and three steels obtained from this composition by adjusting the manganese and carbon content. Steel specimens were tempered 2 h at the indicated temperatures.

The tempering results show that the steel with 0.2% C has the highest hardness at the low tempering temperatures (Fig. 7.3.2). If the steels were all tempered at temperatures where the manganese-containing steels do not form untempered martensite when cooled, the 0.2% C steel would probably show the best tempering resistance. However, when the 0.2% C steel is compared to the base composition (0.1% C) for the highest tempering temperature, there is only a slight difference in hardness, indicating similar tempering resistance under these conditions. This indicates that despite the presence of 26% δ-ferrite in the base composition (compared to ~5% in the 0.2% C steel), similar strengths might be expected after long service times.

The good tempering resistance of the 12Cr-2WV steel was pointed out previously.2 This steel with 26% δ-ferrite had hardness values after long tempering times or high tempering temperatures similar to the values for the all-martensitic steels with 5 and 9% Cr. Thus, it appears that it might be possible to consider a duplex steel for a fusion reactor first wall. Because of their better welding characteristics, the Japanese fusion program is considering 9Cr-2Mo duplex steels as first-wall candidates. One problem with

such steels is that the presence of δ-ferrite increases the ductile-brittle transition temperature (DBTT). It remains to be seen how high the DBTT for the 12Cr-2WV duplex steel is and how much it is subsequently raised by irradiation.

Tensile behavior of Cr-W steels

The tensile behavior was determined for the original eight heats of steel (Table 7.3.1). All but the 2 1/4 Cr-2W steel were austenitized 0.5 h at 1050°C prior to cooling in helium. The 2 1/4 Cr-2W was austenitized 0.5 h at 900°C. The 2 1/4 CrV, 2 1/4 Cr-1WV, and 2 1/4 Cr-2W steels were tempered 1 h at 700°C. The other five heats were tempered 0.5 h at 750°C. These tempering treatments were chosen by referring to the treatments for the analogous Cr-Mo steels that are being studied in the fusion program.

The results for the Cr-W steels are given in Tables 7.3.3 and 7.3.4. Figure 7.3.3 shows the yield stress (YS) and ultimate tensile strength (UTS) and Fig. 7.3.4 shows the uniform and total elongation for all eight heats. In comparing the results, it should be recalled that the 2 1/4 Cr steels form bainite when normalized and the 5- and 9-Cr steels form martensite. The 12-Cr steel contains ~26% δ-ferrite, the balance martensite.

Table 7.3.3. Tensile properties of normalized-and-tempered low-chromium Cr-W steels

Test temperature (°C)	Strength (MPa)		Elongation (%)	
	Yield	Ultimate	Uniform	Total
	2 1/4 CrV			
22	674	733	4.4	7.6
200	639	698	3.6	6.4
300	621	697	3.1	6.0
400	619	677	3.0	5.8
500	599	658	2.6	5.6
600	520	539	1.1	4.9
	2 1/4 Cr-1WV			
22	727	163	4.3	6.3
200	731	195	4.3	7.3
300	694	755	3.3	5.8
400	660	731	3.5	6.3
500	659	726	2.9	5.9
600	588	620	1.5	5.1
	2 1/4 Cr-2W			
22	594	668	6.1	9.5
200	588	654	5.9	9.3
300	573	628	5.3	8.0
400	526	631	4.8	7.8
500	509	635	5.5	8.6
600	501	576	3.6	7.6
	2 1/4 Cr-2WV			
22	649	719	6.3	10.0
200	625	692	5.8	9.1
300	620	698	5.0	7.9
400	583	671	4.9	8.0
500	571	674	4.6	8.0
600	528	588	2.8	6.4

Table 7.3.4. Tensile properties of normalized-and-tempered high-chromium Cr-W steels

Test temperature (°C)	Strength (MPa)		Elongation (%)	
	Yield	Ultimate	Uniform	Total
	5Cr-2WV			
22	577	703	6.0	9.9
200	551	664	4.9	8.8
300	524	635	4.5	8.1
400	517	611	3.8	7.0
500	484	583	3.4	6.3
600	440	497	2.5	7.3
	9Cr-2WV			
22	591	725	5.5	9.0
200	573	699	4.4	7.8
300	675	675	4.1	7.4
400	540	621	3.3	6.1
500	531	626	2.4	5.1
600	463	530	2.1	6.0
	9Cr-2WVTa			
22	645	774	3.3	7.9
200	611	127	3.8	6.9
300	606	709	3.4	6.5
400	585	682	2.9	5.9
500	538	615	2.1	4.6
600	489	526	1.6	5.9
	12Cr-2WV			
22	606	757	5.8	9.0
200	589	724	5.0	8.3
300	557	688	4.3	7.4
400	524	646	3.6	6.4
500	506	601	2.6	5.1
600	427	488	2.5	6.1

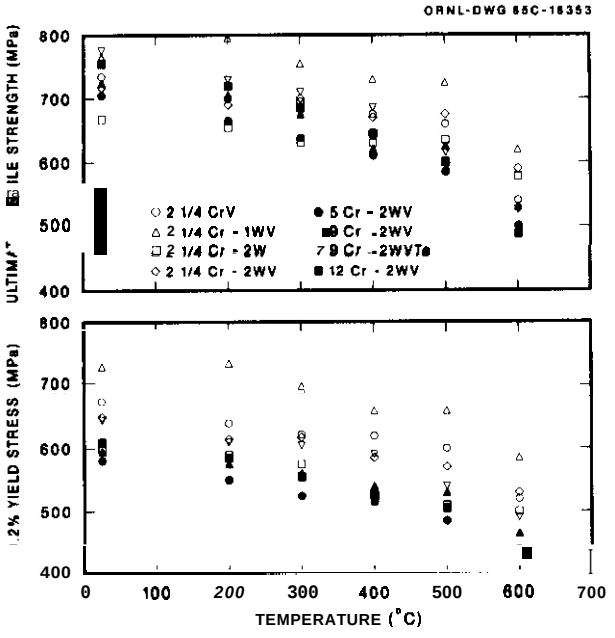

Fig. 7.3.3. The 0.2% yield stress and ultimate tensile strength plotted against test temperature for eight experimental heats of normalized-and-tempered Cr-W steels.

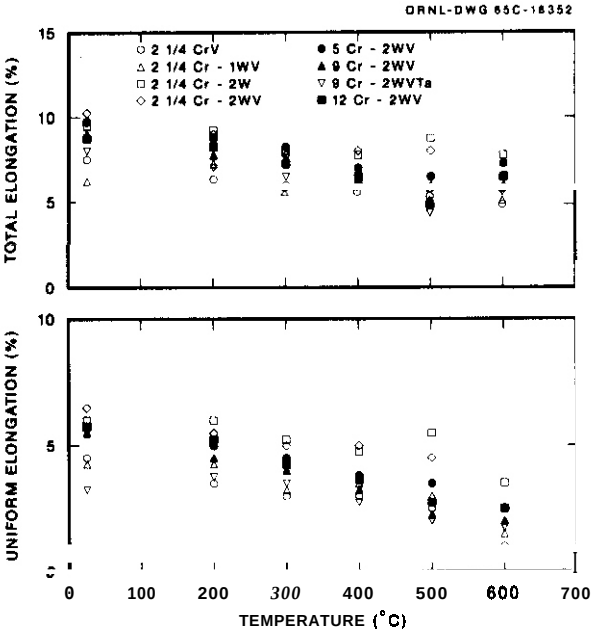

Fig. 7.3.4. The uniform and total elongation plotted against test temperature for eight experimental heats of normalized-and-tempered Cr-W steels.

The results indicate that the tempering temperature affects the YS behavior, because with the exception of the 2 1/4 Cr-2W steel, the steels given the 700°C temper are the strongest. This despite the fact that the 2 1/4 Cr steels are tempered bainite and the high-chromium steels are tempered martensite. To better evaluate the effect of tempering temperature, the results have been replotted in Figs. 7.3.5 through 7.3.8. Figures 7.3.5 and 7.3.6 show the results for the 2 1/4 Cr steels (Table 7.3.3) (tempered bainite microstructures); the results for the high-chromium steels (Table 7.3.4) (tempered martensite) are shown in Figs. 7.3.7 and 7.3.8. The data for the 2 1/4 Cr-2WV steel, which was tempered at 750°C, are shown in all four figures.

An examination of the strengths of the 2 1/4-Cr steels (Fig. 7.3.5) shows the strengthening effects of both vanadium and tungsten: The 2 1/4 Cr-2W steel is weakest, indicating the effect of vanadium; the 2 1/4 Cr-1WV steel is stronger than the 2 1/4CrV steel, which shows the effect of tungsten. Although the 2 1/4 Cr-2WV steel was tempered at 750°C, as the test temperature increased, the relative strength of this steel increased, which may be another indication of the effect of tungsten. There were no large differences in ductility for any of the 2 1/4 Cr steels (Fig. 7.3.6).

When the strengths of the steels tempered at 750°C are compared (Fig. 7.3.7), the 2 1/4 Cr-2WV steel had the highest YS. The 9Cr-2WVTa steel had a comparable YS at the lowest test temperatures. The UTS of the 9Cr-2WVTa is highest at the lowest test temperatures, but at 500 and 600°C, the 2 1/4 Cr-2WV steel has the highest value. The 5-Cr steel generally had the lowest YS and UTS, even though this steel showed the highest peak hardness in tempering studies.2 In those studies, the 5-Cr steel also had a tempering resistance similar to the 2 1/4 Cr-2WV and the 9-Cr and 12-Cr steels.[2] The tensile behavior of the 12Cr-2WV steel, which contained 26% δ-ferrite, was slightly better than the 5Cr-2WV steel at the lowest test temperatures and approached the strength of this steel at 500 and 600°C (Fig. 7.3.7). There was no large difference in the ductility of any of these steels (Fig. 7.3.8).

Tensile specimens of the Cr-W steels are being thermally aged at 400, 500, and 600°C. For comparison, 2 1/4 Cr-1Mo, 9Cr-1MoVNb, and 12Cr-1MoVW steel specimens are also being aged. The 2 1/4 Cr-1Mo steel was normalized and tempered similar to the 2 1/4 Cr-2W steel: 0.5 h at 900°C, gas cool, 1 h at 700°C, gas cool. The 9Cr-1MoVNb and 12Cr-1MoVW steels were heat treated like the Cr-W steels other than 2 1/4 Cr-2W: 0.5 h at 1050°C, gas cool; 1 h at 750°C, gas cool. The Cr-Mo steel controls for the aging tests were tested at 400, 500, and 600°C (the aging temperatures), and in Fig. 7.3.9 the strengths of the 9Cr-1MoVNb and 12-Cr-1MoVW steels are compared with the Cr-W steels heat treated similarly. The strengths of the two Cr-Mo steels fall on the high side of the range of strengths of the Cr-W steels. The results indicate that several of the Cr-W steels have elevated-temperature YS and UTS values comparable to the Cr-Mo steels.

When the 2 1/4 Cr-1Mo steel was compared with the 2 1/4 Cr-2W steels with similar heat treatments (Fig. 7.3.10), the YS for the 2 1/4 Cr-1Mo steel was slightly above that for the 2 1/4 Cr-2W, but below the strengths for the steels containing vanadium. However, the UTS of the 2 1/4 Cr-1Mo fell just below that for the 2 1/4 Cr-1WV, which had the highest UTS of the steels tempered at 700°C. It is expected that if the 2 1/4 Cr-2WV steel was tempered at 700°C, the strength would exceed that of the other 2 1/4 Cr steels.

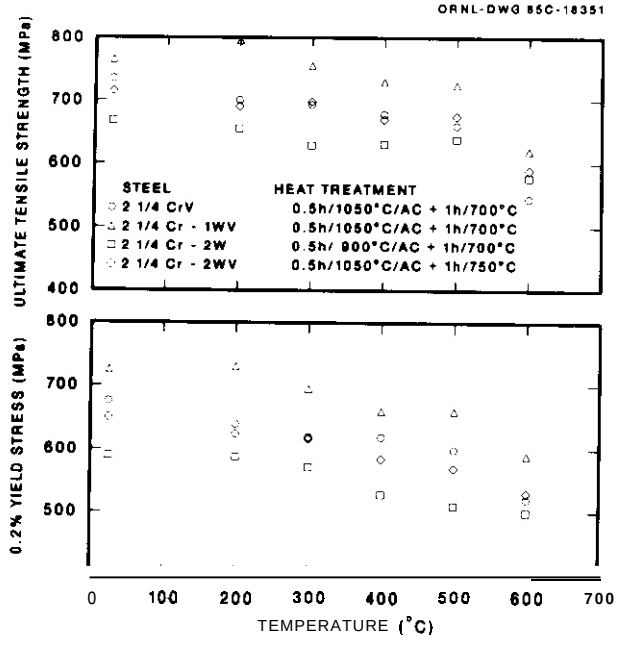

Fig. *7.3.5.* The 0.2% yield stress and ultimate tensile strength plotted against test temperature for the 2 1/4% Cr, Cr-W steels.

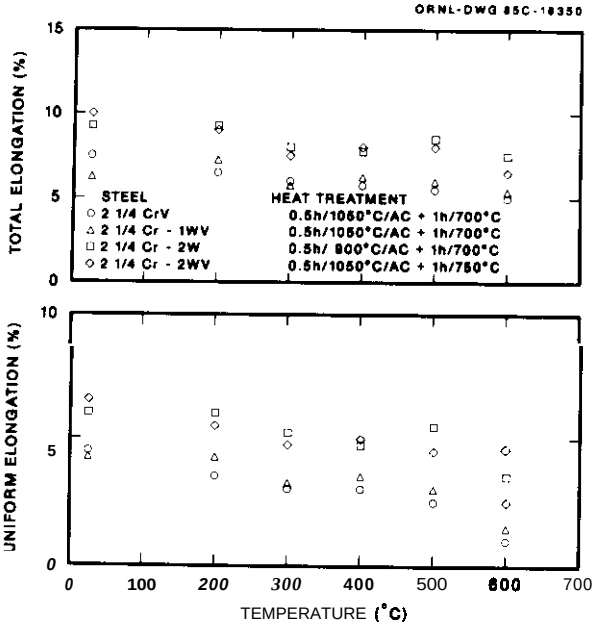

Fig. *7.3.6.* The uniform and total elongation plotted against test temperature for the 2 1/4% Cr, Cr-W steels.

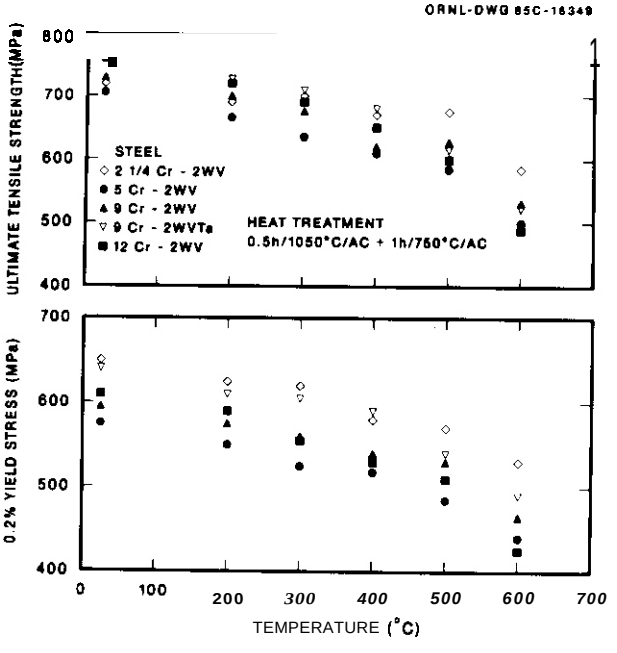

Fig. *1.3.1.* The 0.2% yield stress and ultimate tensile strength plotted against test temperature for the high-chromium, Cr-W steels and the 2 1/4 Cr-2WV steels given similar normalizing-and-tempering treatments.

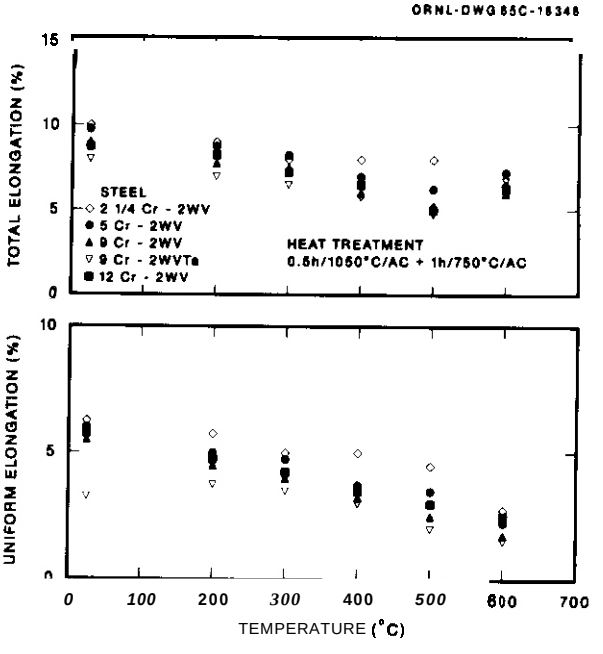

Fig. 7.3.8. The uniform and total elongation plotted against test temperature for the high-chromium, Cr-W steels and the 2 1/4 Cr-2WV steel given similar normalizing-and-tempering treatments.

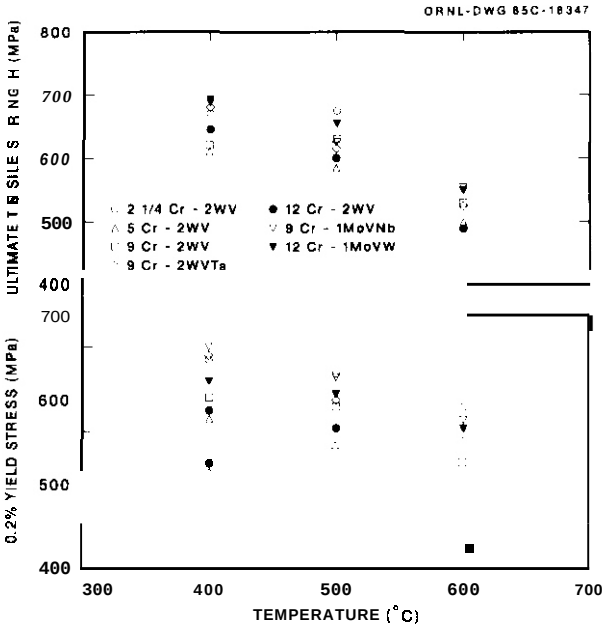

Fig. 7.3.9. The 0.2% yield stress and ultimate tensile strength at 400, 500, and 600°C for the high-chromium, Cr-W steels compared to the strengths for 9Cr-1MoVNb and 12Cr-1MoVW steels.

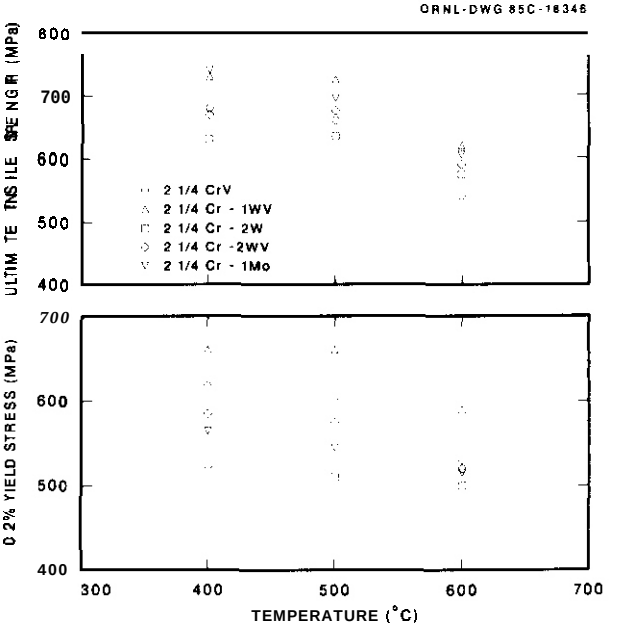

Fig. 7.3.10. The 0.2% yield stress and ultimate tensile strength at 400, 500, and 600°C for the Cr-W steels containing 2 1/4% Cr compared to the strength of 2 1/4 Cr-1Mo steel.

7.3.4 References

1. R. L. Klueh and E. E. Bloom, "The Oevelopment of Ferritic Steels for Fast Induced-Radioactivity Decay for Fusion Reactor Applications," *Nucl. Eng. Design/Fusion* **2**, 383–389 (1985).

2. R. L. Klueh and J. M. Vitek, "The Oevelopment of Ferritic Steels," pp. 141-145 in ***ADIP Semiannu. Prog. Rep., Sept. 30, 1984,*** DOE/ER-0045/13, **U.S.** DOE, Office of Fusion Energy.

3. R. **L.** Klueh, J. M. Vitek, and M. L. Grossbeck, "Nickel-Doped Ferritic (Martensitic) Steels for Fusion Reactor Irradiation Studies: Tempering Behavior and Unirradiated and Irradiated Tensile Properties," pp. 648–664 in ***Effects of Radiation on Materials: Eleventh Conference,*** ASTM STP 782, H. R. Brager and J. S. Perrin, eds., American Society for Testing and Materials, Philadelphia, 1982.

7.4 MICROSTRUCTURAL EXAMINATION OF LOW-ACTIVATION FERRITIC ALLOYS IRRADIATED TO 45 dpa — D. S. Gelles (Westinghouse Hanford Company)

No contribution.

7.5 CHANGE OF CHARPY IMPACT FRACTURE BEHAVIOR OF PRECRACKED FERRITIC SPECIMENS DUE TO THERMAL AGING IN SODIUM - W. L. Hu (Westinghouse Hanford Company)

7.5.1 AOIP Task

The Office of Fusion Energy/Department of Energy has established the need to determine the fracture toughness of candidate fusion program ferritic alloys (Path E).

7.5.2 Objective

The objective of this work is to evaluate the effect of sodium aging on the shift of the ductile-to-brittle transition temperature (DBTT) and the reduction of the upper shelf energy (USE) for precracked ferritic Charpy specimens.

7.5.3 Summary

A series of tests were conducted to evaluate the effect of sodium on the impact fracture behavior of precracked Charpy specimens made of HT-9 weldment. One set of samples was precracked prior to sodium aging and the other set was precracked after aging in sodium. Both set of specimens exhibited the same OETT. Samples precracked prior to sodium exposure, however, showed a 40% reduction in the upper shelf energy (USE) as compared to the set precracked after aging. The results suggest that the fracture toughness of the material may be reduced if an existing crack was soaked in sodium at elevated temperature for a period of time.

7.5.4 Progress and Status

7.5.4.1 Introduction

Charpy impact test results for precracked specimens made of ferritic stainless steel alloys in various thermal mechanical treatments were previously documented.[1-3] Most of the specimens were precracked prior to irradiation. Therefore, some concern was raised whether the in-reactor sodium environment would affect test results. This work is an attempt to evaluate the sodium effect on the Charpy impact fracture behavior of precracked Charpy specimens.

7.5.4.2 Experimental Procedure

Two sets of seven specimens were prepared for this experiment. The specimens were ½-size Charpy specimens made from a weldment of HT-9 ferritic stainless steel. One set of specimens was precracked to an a/w approximately equal to 0.5. All fourteen specimens were then encapsuled in a 304 stainless steel tube with 1" OD and 0.035" wall. The capsule was filled with sodium under argon atmosphere and then sealed with a weld. A double jacket was made for the capsule to assure leak proof operation during the thermal aging. The specimen capsule was then heated in a furnace to 400°C and kept at that temperature continuously for 2200 hours. Specimens removed from the capsule after aging were immersed in methyl alcohol to dissolve all the sodium. The second set of specimens was also precracked to an a/w equal to 0.5. Both sets of specimens were impact tested. The specimens were gas heated or cooled to the test temperature while specimen temperature was monitored by thermocouples welded on the specimen. Impact results were collected by a digital oscilloscope and the data were processed with the help of an on-line computer.

7.5.4.3 Results and Oiscussion

The test results are tabulated in Table 7.5.1 and the fracture energy was plotted against the test temperature in Fig. 7.5.1. Also included in Fig. 7.5.1 are the previous results of irradiated HT-9 weldment samples. Those specimens were irradiated in EBR-II in a sodium environment at 390°C for approximately 2000 hours. Test results for the irradiated specimens[1] are listed in Table 7.5.2 for comparison.

The results show no significant difference in the ductile-to-brittle transition temperature for specimens precracked before and after the sodium aging. Samples precracked prior to sodium exposure, however, exhibited a 40% reduction in the upper shelf energy (USE) as compared to the set of specimens precracked after aging. The reduced USE is approximately the same as the USE shown for the irradiated specimens. The maximum load during the impact, an index closely related to the failure initiation, was almost doubled for the specimens precracked after sodium aging. The data suggest that previously obtained USE data on the irradiated ferritic stainless steel, being soaked in the sodium after the precracking, represent a conservative measurement. On the other hand, should a liquid metal be chosen as the coolant for the first wall of fusion reactors, the effect of sodium aging may drastically reduce the fracture toughness of the material.

Comparing the results of specimens precracked before sodium aging and the irradiated specimens shows the maximum load during the impact is higher in the case of irradiated specimens. This fact accompanied by the upshift of transition temperature indicates that the stress state ahead of the precrack is shifting towards a plane strain case in going from unirradiated specimens to irradiated specimens. Irradiation hardening is the dominant mechanism for this change.

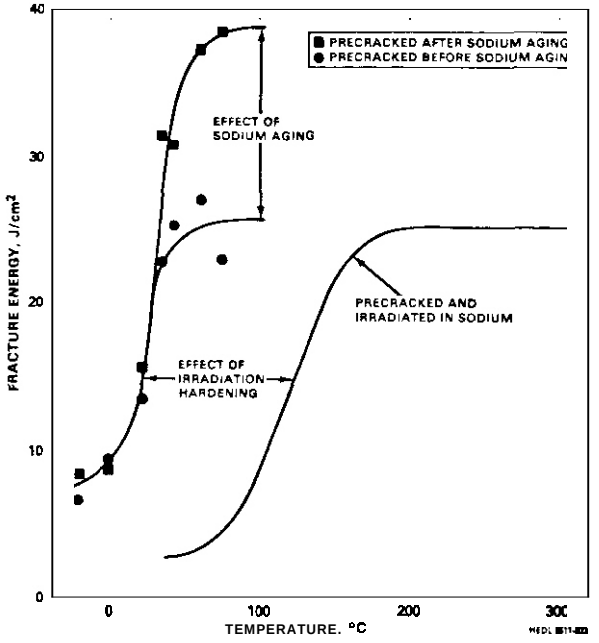

Fig. 7.5.1. Change of charpy impact behavior of orecracked ferritic soecimens due to thermal aging in sodium.

The microstructure and the micro-fracture mechanisms due to the sodium aging are yet to be studied. Since the major effect of sodium aging appears to be on the failure initiation, the investigation should be concentrated on evaluation of the immediate vicinity of the crack tip. Furthermore, a similar study on the fracture toughness of the alloy system *is* highly recommended.

7.5.5 Conclusion

Based on the observations presented in this study, it is concluded that:

1. Sodium aging does not affect the ductile-to-brittle transition temperature.
2. The reduction of upper shelf energy for the irradiated specimens studied in previous reports[1,3] was mainly caused by the sodium aging.
3. Irradiation hardening promotes the plane strain stress state ahead the crack tip and hence increases the transition temperature.

Table 7.5.1. Charpy impact test result of HT-9 weld metal precracked before and after thermal aging in sodium

Specimen I.D.	Tested at (°C)	Fracture Energy (Joules)	Maximum Load (Kilo-Newtons)	Normalized Fracture Energy (J/cm²)
		Precracked Before Sodium Aging		
TI44	75	2.9529	1.2028	23.006
TI53	60	3.3705	1.4578	26.995
TI38	42	3.3087	1.5529	25.290
TI26	35	3.0652	1.4045	22.755
TI25	22	1.7588	1.2977	13.444
TI45	0	1.2122	1.2858	9.320
TI31	-20	0.8696	0.9945	6.592
		Precracked After Sodium Aging		
TI36	75	5.8084	2.4311	38.800
TI40	60	5.6963	2.5768	37.416
TI49	42	4.6325	2.5700	30.814
TI61	34	4.6657	2.7694	31.515
TI39	22	2.3121	2.0086	15.445
TI51	0	1.2919	2.1094	8.638
TI54	-20	1.2800	2.0223	8.550

Table 7.5.2.[1] Previous charpy impact test result on irradiated HT-9 weld metal

Specimen I.D.	Tested at (°C)	Fracture Energy (Joules)	Maximum Load (Kilo-Newtons]	Normalized Fracture Energy (J/cm²)
		HT-9 Weld Metal Irradiated in EBR-II at 390°C to 13 dpa		
TI59	450	2.06	2.10	22.1
TI58	250	2.11	2.13	21.3
TI32	200	2.57	2.00	26.5
TI30	180	2.66	2.46	27.6
TI27	132	1.68	1.92	17.5
TI48	100	0.90	1.93	9.0

7.5.6 Future Work

Fractographic examinations of selected specimens in this study should be conducted with the emphasis on the immediate vicinity of the crack tip. A parallel experiment on the fracture toughness of this alloy system may be valuable to assess the sodium aging effect on the failure initiation.

7.5.7 References

1. W. L. Hu, "Miniature Charpy Impact Test Results for Irradiated Ferritic Alloys", pp. 255-272 in Alloy Development for Irradiation Performance Semiannual Progress Report for Period Ending September 30, 1985, DOE-ER-0045/13, Oak Ridge National Laboratory, Oak Ridge, TN.

2. W. L. Hu and D. S. Gelles. "Miniature Charov Imoact Test Results for the Irradiated Ferritic Alloys HT-9 and Modified 9Cr-1Mo", pp. 631-646 in Proceedings of Topical Conference on Ferritic Alloys for Use in Nuclear Energy Technologies, Snowbird, UT, June 19-23, 1983.

3. W. L. Hu. "Charpy Imoact Test Results of Ferritic Alloys at Fluence to 6 x 10^{22} n/cm^2", p. 106 in Alloy Development for Irradiation Performance Semiannual Progress Report for Period Ending September 30, 1985, DOE-ER-0045/13, Oak Ridge National Laboratory, Oak Ridge, TN.

7.6 THE THERMAL HISTORY OF HEAT-AFFECTED ZONES IN HT-9 WELDMENTS — J. R. Foulds (GA Technologies)

No contribution.

7.7 CORRELATION OF HOT-MICROHARDNESS WITH ELEVATED-TEMPERATURE TENSILE PROPERTIES OF LOW ACTIVATION FERRITIC STEEL - Chen-Yih Hsu (GA Technologies Inc.)

7.7.1 ADIP Task

The Department of Energy (DOE), Office of Fusion Energy (OFE), has cited the need to investigate ferritic alloys under the ADIP program task. Ferritic Steel Development (Path E).

7.7.2 Objective

The objective of this effort is to determine the viability of using the Vickers microhardness technique to monitor the elevated temperature hardeness of the 9Cr-2.5W-0.3V-0.15C ferritic steel and to establish a hot hardness-tensile properties correlationship for predicting the tensile properties of low activation ferritic steel at elevated temperaturer, and also to provide a baseline data for future comparison with irradiated specimens.

7.7.3 Summary

Hot microhardness and elevated temperature tensile tests have been performed on 9Cr-2.5W-0.3V-0.15C (GA3X) low activation ferritic steel at temperatures Prom 20°C to 650°C. The uniform elongation of the tensile test correlated well with the ductility parameter, $P=(h_1+h_2)/2r$, where h_1 and h_2 are the peak heights of the plastically flowed metal adjacent to the indentation and 2r is the distance between the peaks. The hot-microhardness test showed a sensitive response to the eoftening and changes in ductility of the GA3X steel. The preliminary results indicate that the hot-microhardness test accompanied with ductility parameter measurements also can be used as a means to monitor the Strain-hardening characteristics of metals. The ultimate tensile strength and 0.2 percent yield strength of this low activation ferritic steel correlated well with hot microhardness measurements at temperatures up to 400°C using Cahoon's expressions $\sigma_{uts}= (H/2.9)(n/0.217)^n$ and $a_{ys}= (H/3)(0.1)^n$, respectively, where H is the diamond pyramid hardness and n is the strain hardening exponent. At temperature? above 400°C, a more rapid and somewhat disproportionate decrease in microhardness was observed and the tensile strengths were underestimated by these two expressions by up to 20-30%. Fractographic examination of the tensile tested specimens showed an apparent change of dimple morphology from an equiaxed (tensile) dimple to an appearance of mixed equiaxed (tensile)- elongated (shear) dimple at temperatures above 400°C. The main reason for the underestimation of tensile strengths at such high temperatures ($\geq 0.4\ T_m$) is probably attributed to the involvement of creep deformation and may be improved by selecting a proper loading condition.

7.7.4 Progress and Status

7.7.4.1. Introduction

Hardness indentations have been interpreted by both elasticity and plasticity models and hardness values have been correlated empirically with the elastic constants, yield stress, ultimate tensile strength. and work hardening in various metals and austenitic stainless steels (Refs. 1-7). Thus, microhardness appears to be an attractive means for estimating other mechanical properties Of material. Hot microhardness test can be a valuable tool in elevated-temperature materials research and development. The correlation of hot hardness data with short time tensile and with the long time stress-rupture properties of metals and alloys can result in a eignificant saving in both time and cost of generating preliminary elevated temperature engineering data.

The general relationship between the diamond pyramid hardness (H) and the ultimate tensile strength (σ_{uts}) of a given material may be given as:

$$H = C\ \sigma_{uts} \qquad (1)$$

where C is called the constraint factor for the hardness test. The existing theory for indentation hardness considers the materials indented to behave in a rigid-plastic manner and lead? to a constraint factor value of C=2.57. This model ingores the elastic stress field as pointed out by Shaw and DeSalvo (Refs.2 and 3). A new approach to plasticity has been presented in which the

material is assumed to be a plastic-elastic manner (Ref.3). The constraint factor based on the plastic-elastic model is round to be equal to 3.0, which is in excellent agreement with the result? of many experiments where the material doe? not work harden and the indentor is relatively blunt (i.e. Vickers or Knoop).

Tabor (Ref.4) and Cahoon (Ref.5) proposed complex relationships between the tensile strength? and the hardness in which the ?train hardening exponent is explicitly considered. It has been demonstrated that the ultimate tensile strength and yield strength (0.2% offset) can he obtained Prom microhardness measurement? using Cahoon's expressions (Refs.5 and 6):

$$\sigma_{uts} = (H/2.9)\ (n/0.217)^{n} \qquad (2)$$

$$\sigma_{ys} = (H/3)\ (0.1)^{n} \qquad (3)$$

where n is the strain hardening exponent in the classical strain hardening relationship:

$$\sigma = K\ \varepsilon^{n} \qquad (4)$$

where K is the flow stress (σ) at a strain (ε) of unity. The etrain hardening exponent can be obtained directly from an analysis of the atrepa-strain diagram of a uniaxial tensile or compression test. The strain hardening exponent is generally equated to the uniform elongation (ε_u). The uniform elongation can be expressed as (Ref.8):

$$\varepsilon_U = m/P^{a} \qquad (5)$$

where m and a are materials constants and P, the ductility parameter is given by:

$$P = \frac{h_1 + h_2}{2r} \qquad (6)$$

where h_1 and h_2 are the height? of the plastically deformed metal adjacent to the indentation and 2r is the distance between the peaks. Equation (5) suggests that the uniform elongation increases with a decrease in the ductility parameter.

Correlation between microhardness, tensile propertie? and Charpy Y-notched impact properties on irradiated ferritic steel ha? been examined at ambient temperature (Ref.9). However, the correlation between microhardness and tensile propertiea of ferritic steel at elevated temperatures is still lacking. The Present investigation was initiated with an attempt to correlate the hot microhardness measurements and tensile propertie? for low activation ferritic steel at temperature? from 20°C to 650°C, which may allow estimates of elevated-temperature strengths and ductility to be made using only a small amount of test material and may also provide a baseline data for future comparison with irradiated specimen?.

7.1.4.2 Experimental procedures

One 7 kg(15lb) ingot of experimental heat has been melted and cast in a GCA vacuum induction melting furnace. The nominal composition is presented in Table 7.7.1 along with the actual chemistries analyzed. The ingot wa? homogenized at 1100°C for 24 hrs and then hot rolled to a plate of 0.88cm(0.35in) in thicknerr followed by air cooling. The 0.88cm thick plate was further hot rolled at 700°C to a thickness of 0.15cm and air cooled. The flat plate was heat treated (1000°C/1hr, quenched +700°C/1hr, air cooled) to obtain a fully martensitic structure with a optimum strength for further mechanical testing.

Table 7.7.1. The Nominal and Chemical Compositions of the Low Activation Ferritic Steel

Heat #		C	Cr	W	V	Ti	Mn	S
GA3X	Range	0.16 / 0.17	7.4 / 7.6	1.9 / 2.0	0.014 / 0.016	-	0.002	0.005
	Nominal	0.15	9.0	2.5	0.3	-	-	-

Tensile specimens were fabricated parallel to the major rolling direction with a gage section 1.0mm x 3.18mm x 25.4mm (0.04 in thick by 0.125 in wide by 1.0 in long), as indicated in Figure 7.7.1. The thickness of the tensile specimen is more than 20 times the prior austenitic grain size (ASTM 8-9). The total length of the tensile specimen was 68.95mm (2.75 in) and the width of the shoulder region was 14.3mm (0.563 in). The flat tensile Ppecimene were tested in an Instron tensile testlng machine equipped with a resistance heating furnace. The surface of tensile specimens were dipped with a toluene pretreat coating solution to avoid significant corrosion during the tensile test. The cross head speed was 0.5mm/min (0.02in/min) and the strain rate was about $3.5 \times 10^{-4}\ s^{-1}$. The strain hardening exponent was obtained by log-log plot of the true stress and true plastic strain.

The samples for hot microhardness test (0.5mm X 6.5mm X 20mm) were prepared and polished from the heat treated specimen. The volume of material required for the hot-hardness specimen was only 10 percent of that required for one tensile specimen. Hot hardness tests were conducted at the University of Cincinnati. The general test procedure and a description of the hot hardness test equipment are detailed in reference 10. The hot microhardness furnace atmosphere was high purity argon gas. The diamond pyramid hardness was determined on a Vickers hardness tester using a load of 500g. The average value:, were taken from three indentations made at each temperature. The standard deviation of the microhardness measurements was within ±2%. For the evaluation of ductility, a profilometer with a diamond stylus was used to measure the pile-up of metal adjacent to the indentation.

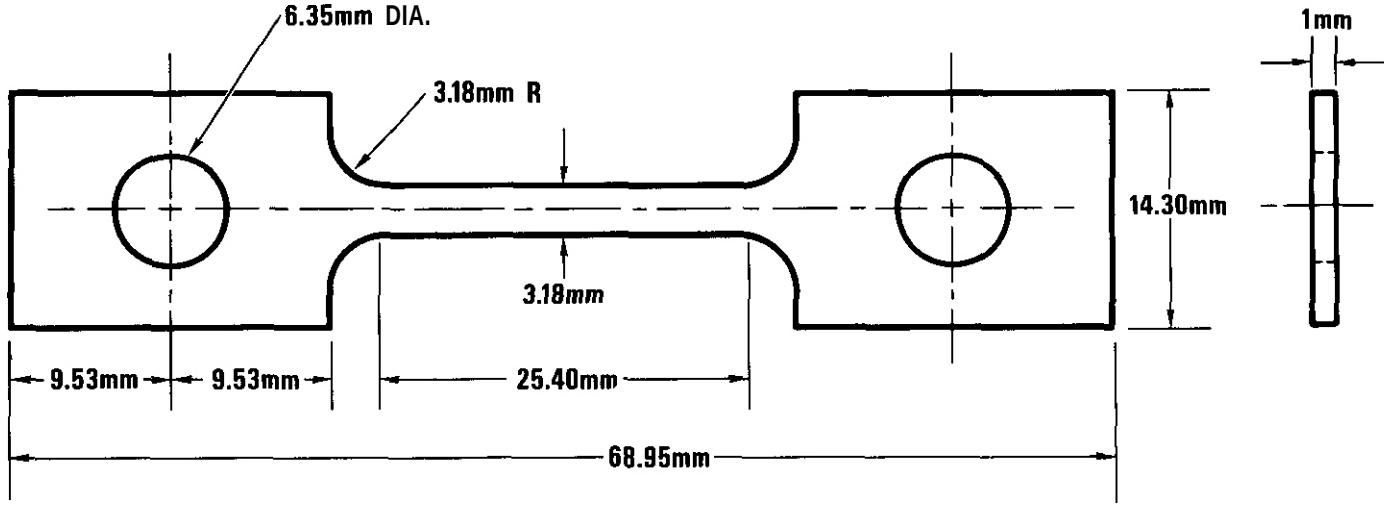

Fig. 7.7.1. Geometry of flat tensile specimens

7.7.4.3 Results and Discussion

The mechanical teste were performed on quenched and tempered specimens from 20°C to 650°C. Table 7.7.2 summaries the tensile properties of GA3X ferritic steel at elevated temperature?. The strain hardening exponent. determined from the log-log plots of true stress and true plastic strain. are as small as 0.10 at room temperature and drop to 0.06 at elevated temperatures above 400°C. The minimum value of uniform elongation **is** at temperatrure of 600°C. Although the uniform elongation **is** much smaller than the Strain hardening exponent obtained from the stress-atrain diagram, the changes of uniform elongation and strain hardening exponent versus test temperature have the same trend. The total elongation *is* a function of test temperature and the minimum value of the total elongation occurs 300°C. The yield strength and ultimate tensile strength decrease with increasing test temperature. The ratio of σ_{uts} over σ_{ys} is in the range of 1.27 to 1.09. An apparent drop of the ratio of σ_{uts}/σ_{ys} is observed at temperatures above 400°C which corresponds to **a** significant softening.

Table 7.7.2. The Elevated-Temperature Tensile Properties of GA3X steel

Test Temp. (°C)	Strain Hardening Exponent	Elongation Uniform (%)	Elongation Total (%)	*0.21* offset Yield Strength σys, MPa	Ultimate Tensile Strength σuts, MPa	The Ratio of σuts/σys
20°C	0.11	6.4	11.5	593	754	1.27
100°C	0.11	5.6	10.0	570	705	1.74
200°C	0.10	4.5	8.2	525	645	1.23
300°C	0.10	4.0	7.3	510	625	1.23
400°C	0.10	3.9	9.1	472	565	1.20
500°C	0.07	2.2	11.8	434	489	1.17
550°C	0.08	1.7	16.4	391	427	1.09
600°C	0.06	1.7	21.8	302	340	1.13
650°C	0.07	1.9	29.1	231	267	1.15

Hat microhardness and ductility parameter measurements were also performed on quenched and tempered specimens at temperatures from room temperature to 650°C. Three indentations. with holding time of 30 **s** and using a 500 gram load, were made at each temperature after the specimen soaked at test temperature for approximately 15 min. Figure 7.7.2 shows Vickere microhardness

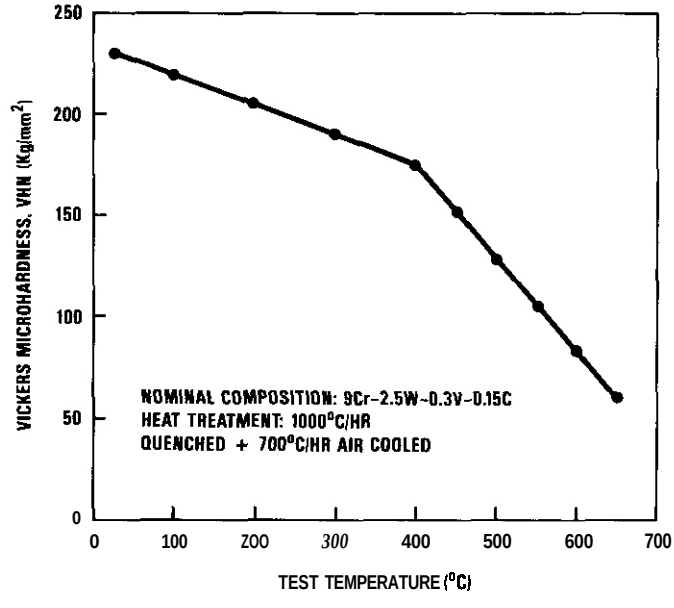

Fig. 7.7.2. Vickers microhardness result vs test temperature **for** GA3X ferritic steel

result of this ferritic steel versus test temperature. The standard deviation of microhardness number is within ±2%. The result shows that microhardness decreases as test temperature increase? and a rapid and disproportionate decrease in microhardness is observed at temperatures above 400°C. The hot-microhardness test shows a sensitive response to a significant softening occurred at temperatures above 400°C, consistent with the tensile test results.

The ductility parameter measurement of hot-hardness test is shown in Figure 7.7.3 along with the uniform elongation of the tensile test. The ductility parameter increases with increasing temperature and a maximum value is obtained at 600°C. The change of ductility parameter against test temperature has an opposite symmetry to the change of uniform elongation versus test temperature. An excellent agreement is obtained on the correlation of ductility parameter measurements with uniform elongation according to equation (5). The uniform elongation is approximately equivalent to the strain hardening exponent for work-hardenable metals. Therefore, the ductility parameter measurement of the hot-hardness test can be used as a means to monitor the strain-hardening characteristic of this ferritic steel at temperatures of interest.

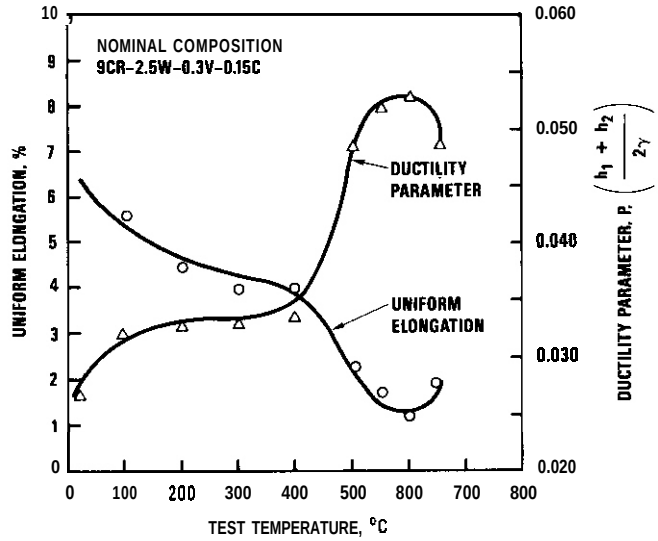

Fig. 7.7.3. Uniform elongation and ductility parameter measurements vs. test temperature on GA3X ferritic steel

Mancuso et al.,(Ref.9) studied the correlation between microhardness and tensile properties of irradiated ferritic steel at ambient temperature. An empirical equation for 0.2% offset yield strength was formulated as:

$$a_{ys}^{0.2\%} = 3.62\ (VHN) - 228\ MPa \qquad (7)$$

where VHN is the Vickers hardness number in the unit of Kg/mm^2. By using this equation, a good estimate of yield strength is obtained at temperatures up to 200°C, while a poor agreement is observed at test temperatures above 200°C.

A plot of ultimate tensile strength as a function of hot-microhardners values determined at the same temperature is shown in Figure 7.7.4. The solid and dashed lines are the calculated ultimate tensile strength employing equation (1) and using constant constraint factors of 3.0 and 2.51 respectively. It is apparent that equation (1) with a constraint factor of 3.0 (plastic-elastic model) would give an excellent agreement with experimental result at test temperatures from 20°C to 400°C. On the other hand, equation (1) with a constraint factor of 2.57 (plastic-rigid model) would also give an excellent agreement with experiment at 500°C, but would result in tensile strength higher than experimental data at temperatures from 550°C to 650°C. This observation for ferritic steel differs from the previous work on 304 austentic stainless steel (Ref.7), which indicated that the plastic-rigid model

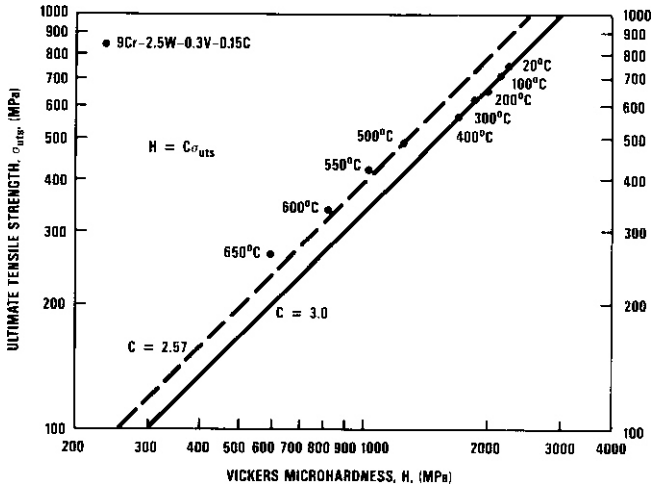

Fig. 7.7.4. Comparison of the calculated (σ = H/C) and experimental tensile strength of GA3X ferritic steel as function of the Vikers hot microhardness for each test temperature

would **give an** excellent agreement with experiment at temperatures up to 600°C while the plastic-elastic model was in excellent agreement with experiment at temperatures in the range of 800 to 1200°C.

The comparison of the calculated and experimental tensile strength? of GA3X steel is summarized in Table 7.7.3. The ultimate tensile strength calculated from equation (1) with C=2.57 is higher than experimental value? by the valuer of 16 to 23% at temperatures up to 400°C and **is** about 14 to 27% lower than experimental data using same equation with C=3.0 at temperature? above 400°C. By including the strain hardening characteristic of steel, equation (2) is shown to estimate the ultimate tensile strength to within 5% and equation (3) is shown to estimate yield strength to within 4% at temperatures up to 400°C. At test temperatures above 400°C, equations (2) and (3) are shown to result in the underestimation of tensile strength? by up to 30%. These preliminary results show that the ultimate tensile strength and 0.2% Offset yield strength can be correlated well with hot-microhardness values using equations (2) and (3) at test temperatures up to 400°C.

Table 7.7.3. The Comparison of Calculated and Experimental Tensile Strengths of GA3X Ferritic Steel

Test Temp. (°C)	VHN (H) (MPa)	0.2% offset Yield Strength Calc.[a] (MPa)	Exp. (MPa)	Exp: percent Discrepency	Ultimate Tensile Strength Calc.[b] (MPa)	Exp. (MPa)	Percent Discrepency C=f(n)[b]	C=2.57[c]	C=3.0[c]
20	2246	581	593	-2.0%	722	754	-4.2%	+15.9%	-1.0%
100	2157	558	570	-2.15	692	705	-1.85	+19.1%	+2.0%
200	2040	540	525	+2.8%	651	645	+1.0%	+23.1%	+5.4%
300	1873	498	510	-2.4%	598	625	-4.38	+16.6%	-0.1%
400	1726	457	472	-3.4%	552	565	-2.1%	+19.1%	+2.0%
500	1265	359	434	-17.35	403	489	-17.6%	+1.0%	-13.8%
550	1030	286	391	-26.95	328	427	-23.85	+6.15	-18.6%
600	834	242	302	-20.0%	266	340	-21.8%	+6.5%	-19.2%
650	598	170		-25.8%	191	267	-29.3%	-13.85	-26.2%

a : calculated basen on equation (3).
b : calculated based on equation (2).
c : calculated based on equation (1).

The fracture surface of the tensile tested specimens were examined by scanning electron microscopy. Figure **7.7.5** shows fractographs of specimens tested at temperatures indicated. A ductile dimple rupture caused by a void coalescence mechanism was observed for specimens tested up to 650°C. At temperatures above 400°C, the tensile tested specimens shoved an apparent change of dimple morphology from an equiaxed (tensile) dimple to an appearance of mixed equiaxed (tensile) and elongated (shear) dimple. The elongated shear dimples were usually indicated as ductile tearing (Ref.11). The shear dimples seem elongated parallel to the direction of the maximum shear stress. The evidence of the mixed dimple morphology suggests that there might have been a strong shear components and/or cross slip involved in the deformation at such high temperatures because temperatures of 500-650°C ($\geq 0.4\ T_m$) are probably in the time-dependent temperature region.

The hot-miorohardness test is very sensitive to the softening of metals. There are several reasons for the underestimation of tensile strengths by using equations (2) and (3). It is well known that grain size and crystallographic orientation of individual grains have a marked effect on the tensile strengths and strain hardening characteristics of metals. One may etch the specimen surface to determine whether some second phase or grain boundary may be in the region of the indentation to which would cause some of the scatter in the data. Still. the deviation of microhardness number is only within ±2% in this investigation. *So,* the metallurgical effects causing the underestimation o? tensile strengths is negligible. Another factor for scatter is that the deformation mode has changed at temperatures between 500-650°C, which is probably due to creep deformation under the loading condition of 500 grams and 30 s. It is known that Bickers and Knoop microhardness varies with load (Ref.12). There is first a tendency to increase (up to a Pew grams); then the microhardness value decreasess with increasing load. Thus, a hold time of 30 s with 500g load may be too long for the characterization of a short-time tensile test because time-dependent Stress-rupture plastic deformation might have been involved under this loading condition. The suggestion is that the discrepancy between the calculated and experimental strengths of this ferritic steel at temperatures above $0.4T_m$ can be probably reduced by selecting a proper loading condition (a smaller load and/or a shorter hold time). The proper selection of loading condition should receive a considerable attention for future investigation at temperatures higher than $\sim 0.4\ T_m$.

7.7.5 Conclusions

The hot-microhardness test gives a sensitive indication of the softening of metals, and the ductility parameter measurements correlate well with uniform elongation. The hardness-tensile property correlationship indicates that the Vickers hot-microhardness test and ductility parameter measurements can be used to monitor the strain-hardening characteristics of metals. The ultimate tensile strength and yield strength of CA3X ferritic steel can be correlated with hot-microhardness measurements at temperatures up to 400°C using Cahoon's expressions: $\sigma_{uts} = (H/2.9)\ (n/0.217)^n$ and $a_{ys} = (H/3)\ (0.1)^n$, respectively. The apparent discrepancy between the calculated and experimental tensile strengths at temperatures above 400°C is mainly attributed to the change of deformation mode, which may be avoided by selecting a proper loading condition. These preliminary results are very encouraging and suggest that the prediction of tensile properties of ferritic steel can be made using only a small amount of test material.

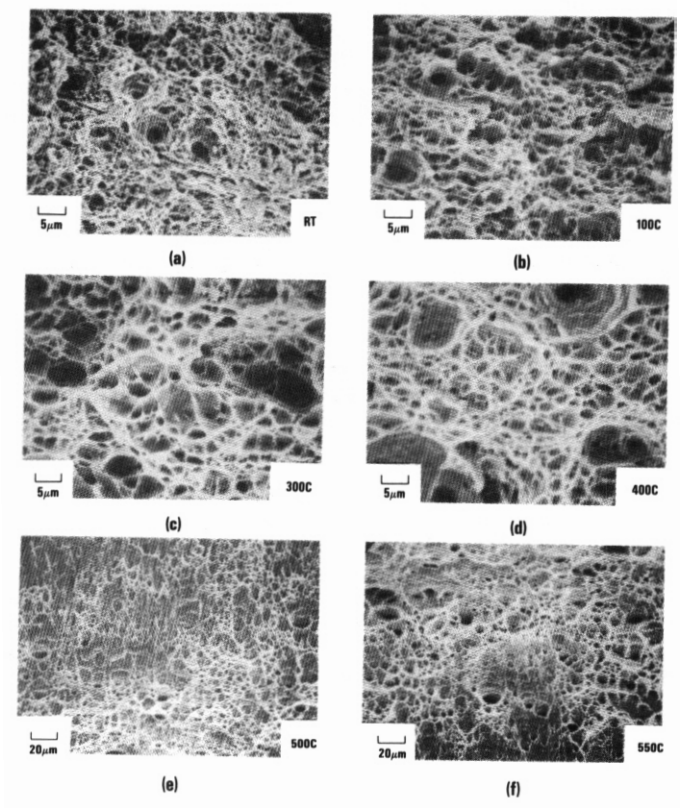

Fig. 7.7.5. Fractographs of the tensile tested specimens of GA3X steel tested at (a) 20°C, (b) 100°C, (c) 300°C, (d) 400°C, (e) 500°C and (f) 550°C

7.7.6 References

1. J. J. Gilman, in" The Science of Hardness Testing and Its Research Applications", J. H. Westbrook and H. Conrad. eds., pp. 51–74, American Society for Metals, Metals Park, Ohio. 1973.
2. M. C. Shau and G. J. Desalvo, Metals Eng. Quart.,1972, Vo1.12, pp.1-7.
3. M. C. Shau and G. J. Desalvo, Trans. ASME, 1970. Vo1.92, pp.469-79.
4. D. Tabor, J. Inrt. Metals, 1951, Vo1.79. pp. 1–18.
5. J. R. Cahoon, Met. Trans., 1972, Vo1.3, p. 3040.
6. J. R. Cahoon, W. H. Broughton, and A. R. Kutzak, Met. Trans., 1971, Vol. 2, pp. 1979-83.
7. J. Moteff, R. K. Bhargava, and W. L. McCullough, Met. Trans.. 1975. Vol.6A, pp. 1101–04.
8. R. Boklen, in "The Science of Hardness Testing and Its Research Applicationr", J. H. Westbrook and H. Conrad, eds.. pp. 109-116, American Society for Metals, Metals Park, Ohio, 1973.
9. J. F. Mancuso et. al., in Proc. of 10th Inter. Symposium on Effects of Radiation on Materials, June 1980, ASTM STP 725, pp.38-48.
10. J. L. Kamphouse, J. C. Blake and J. Moteff, Rev. Sci. Inrtrum., 1969. Vol. 40, pp. 321–25.
11. S. Bhattacharyya, V. E. Johnson, S. Agarual and M. A. H. Houer, "IITRI Fracture Handbook", IIT Research Institute, Chicago, Illinois. January 1979.
12. E. R. Petty, in Techniques of Metals Research, Vol. 5, Part. 2, R. F. Bunrhan (ed.), Wiley-Interscience, New York, 1971. p. 157.

7.8 MICROSTRUCTURE AND MECHANICAL PROPERTIES OF UNIRRADIATED LOW ACTIVATION FERRITIC STEEL - Chen-Yih Hsu and Thomas A. Lechtenberg (GA Technologies Inc.)

7.8.1 ADIP Task

The Department of Energy (DOE) Office of Fusion Energy (OFE), has cited the need to investigate ferritic alloys under the ADIP program task, Ferritic Steel Development (Path E).

7.8.2 Objective

The primary objective of this work is to develop low activation ferritic steels that exhibit mechanical and physical properties approximately equivalent to the commeroially available heat resistant alloys. HT-9 and modified 9Cr-1Mo, but which only contain elements that would permit near-surface disposal under 10CFR61 waste disposal criteria after exposure to fusion neutrons.

7.8.3 Summary

Transmission electron microscopic examination of quenched and tempered 9Cr-2.5W-0.3V-0.15C low activation ferritic steel revealed tempered lath-type martensite with precipitation of rod and plate-like $M_{23}C_6$ and MC carbides at lath and grain boundaries. Extraction replicas of precipitates were found to be predominantly $M_{23}C_6$ carbides analyzed by diffraction. The areal density and mean particle size of carbide precipitates were appreciably increased after thermal aging at 600°C for 100hrs. More rod-like $M_{23}C_6$ were found along prior austenite grain boundaries and martensite lath boundaries in the thermally aged specimens.

The elevated-temperature tensile strengths of this material were measured and are about 10% higher than the average tensile data of commercial heats of 9Cr-1Mo and modified 9Cr-1Mo steels up to a temperatrue of 650°C, with equivalent uniform elongation and -50% decrease in total elongation. The fracture toughness (K_{IC}) of this alloy is predicted to be about 10-20% lower than commercial heats of modified 9Cr-1Mo steel. but is comparable to some experimental heats of 9Cr-1MoVNb steel. The impact test results show a DBTT at -25°C and upper shelf energy of 1/3 size CVN precracked specimen at 2.2 Joules (37.2 J/cm^2 normalized fracture energy). Fractographic examination of tensile tested specimens shows a mixed mode of equiaxed dimple and elongated dimple at test temperatures above 500°C. The modification of the GA3X alloy composition for optimization of materials properties is discussed. However. the proposed low activation ferritic steel show the promise of improved mechanical properties over 9Cr-1Mo steels.

7.8.4 Progress and Status

7.8.4.1 Introduction

The available test data show that the 9-12%Cr ferritic/martensitic steels appear to be attractive materials for fusion reactor structural component applications. Commercially available alloys to be ueed for first wall/and blanket structural components will become activated during service and will pose a waste disposal problem after service. Guidelines (10CFR61) for the classification of nuclear wastes have been issued by the U.S. Nuclear Regulatory Commission. In 1982, DOE convened a panel to examine the issues and incentive? associated with the development of low activation material?. One Of the panel conclusions was that it was judged desirable and technically feasible to develop reactor materials Which fell within the 10CFR61 waste disposal criteria (low level waste) after fusion reactor irradiation. To achieve fusion's full potential as an environmentally attractive energy source, the residual activation of the materiala must be minimized.

The primary objective of this work is to develop low activation ferritic steel? with equivalent propertie? and performance in a fusion environment to the commercially developed alloy?. HT-9 and/or 9Cr-1Mo steel?. To achieve this, the elements Mo, Ni, Nb, and N, which are added for elevated temperature strength, must be reduced to very low levels. W and V can be used to substitute for Mo. In equal atomic fractions, W and MO show similar solid solution hardening characteristics and Fe-W-C alloy? develop analogou? precipitates with a similar precipitation sequence to Fe-Mo-C alloy?. So. it was suggested that the Cr-W steels offer promise for the development of a replacement for Cr-Mo steel?. An experimental heat (GA3X) of low activation ferritic steel was prepared with a nominal composition of 9Cr-2.5W-0.3V-0.15C steel. The addition of 0.3% V to Cr-W steels will result in a pronounced effect on the precipitate formation and on elevated temperature propertie?. The addition of V, however, may make the steel less weldable due to the formation of carbides. For this reason, the suggested carbon content is kept below 0.15% in Cr-W steel?. Ti is also a strong carbide former with an evidence of inhibiting grain coarrening while retaining good notch toughne??, so the addition of 0.1% Ti is also discussed as a modification to GA3X. This report summarizes the TEM examination and mechanical property evaluation of the unirradiated GA3X low activation ferritic steel compared to the commercial heat? of 9Cr-1Mo steel?, and also provides baseline data for a comparison with the irradiated GA3X steel.

7.8.4.2 Experimental Procedure?

The melting and fabrication practice of the GA3X heat of low activation ferritic steel were described in Ref. 1. The nominal and actual composition of this GA3X heat is shown in Table 7.8.1. The specimens discussed here were heat treated at Optimum condition (1000°C/1hr, water quenched + 700°C/1hr, air-cooled).

Table 7.8.1. The Nominal and Chemical Compositions of the Low Activation Ferritic Steel

Heat #		C	Cr	W	V	Ti	Mn	S
GA3X	Range	0.16 / 0.17	7.4 / 7.6	1.9 / 2.0	0.014 / 0.016	- =	0.002	0.005
	Nominal	0.15	9.0	2.5	0.3	-	-	-

A two-stage replication technique was used to prepare the carbon film extraction replicas of the precipitates. The specimen? were polished and slightly etched for a few seconds using the Titanium etch (10% HF, 5% HNO_3, 85% H_2O). The collodion/amyl acetate war ueed to extract precipitate? on the surface and was then deposited with carbon film by vacuum vapor deposition. Following this step. the plastic matter was dissolved in acetone and the remaining carbon film was placed an a copper supporting grid. In the preparation of thin-roil epecimenr. the sample was thinned mechanically to 0.076 mm (0.003in) and then punched into 3 mm diameter disks. The disks were electropolished in a solution of 50% ethyl alcohol, 45% butyl cellosolve, and 5% $HClO_4$, with polishing conditions of 150V and 15mA at temperature of -35°F. Carbon film extraction replica? and thin-foil microstructures were examined on a Philip 300M transmission electron microscope operating at 100KV.

The tensile tests were performed on flat tensile specimen? with dimensions as shown in Figure 7.8.1. The flat tensile specimens were dipped with toluene pretreat coating solution in Order to avoid any significant oxidation or decarburization during the tensile test, and were tested in an Instron tensile testing machine equipped with a resistance heating furnace at temperature range of 20°C - 650°C. The cross head speed was 0.5mm/min (0.02in/min) and the strain rate was about $3.5 \times 10^{-4} s^{-1}$. A fractographic examination of tensile tested specimens was performed on a scanning electron microscope.

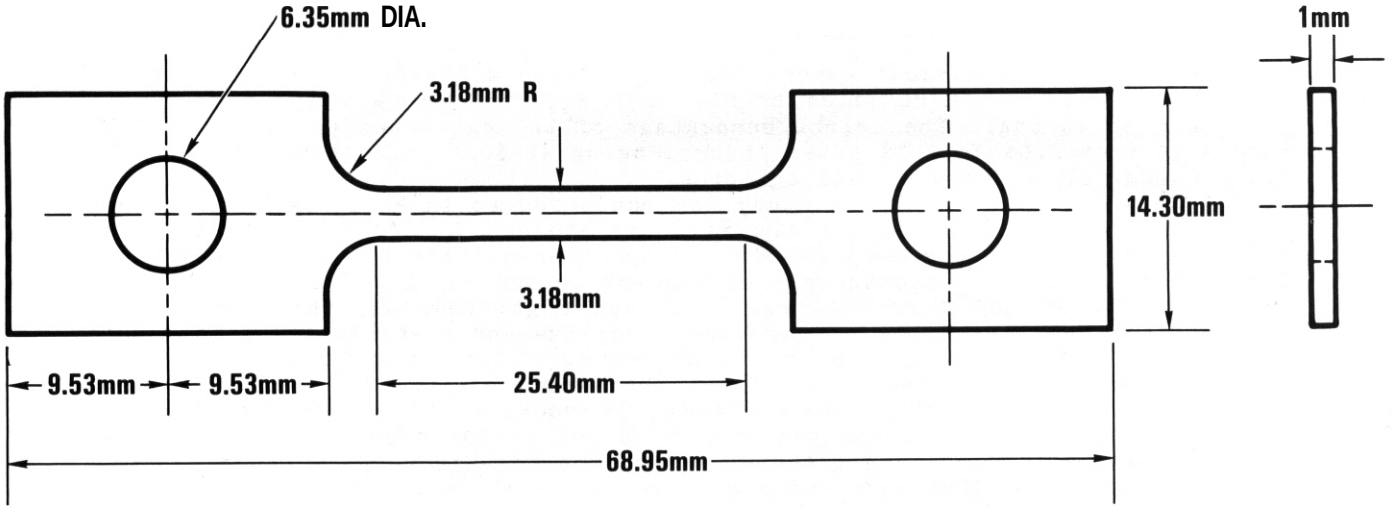

Fig. 7.8.1. Geometry of the flat tensile specimens

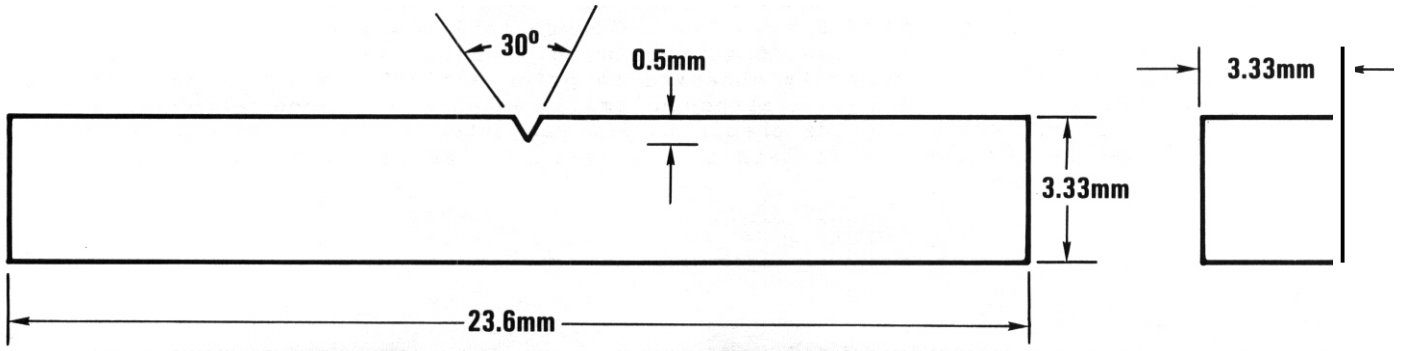

Fig. 7.8.2. Geometry of 1/3 size miniature Charpy impact specimen

The ductile brittle transition temperature (DBTT) and impact properties were determined Prom miniature Charpy v-notch specimen with dimensions shown in Figure 7.8.2. The miniature Charpy V-notch specimens were fatigue precracked with a stress intensity factor of no higher than 16 MPa√m. The precracked specimens were then tested in the instrumented impact testing machine by W. L. Hu, at the Hanford Engineering Development Laboratory. The fracture energy was electronically integrated from the load-line trace..

7.8.4.3 Results and Discussion

Metallographic Examination

In the last semiannual report (Ref. 2), X-ray diffraction analysis of the extracted precipitates revealed nearly 100% $M_{23}C_6$ carbides with a lattice parameter of 10.64Å. The weight percentage of the extracted precipitates was increased Prom 2.0% to 3.1% after thermal aging at 600°C for 100hrs and no Fe_2W type intermetallic compound was detected.

A detailed metallographic study was conducted to investigate the size and morphology of precipitates and the microstructure. Carbon film extraction replicas of precipitates were examined under transmission electron microscope. Figure 7.8.3 shows TEM micrographs of the extraction replica prior to and after thermal aging at 600°C for 100hrs. At high magnification, the extracted precipitates show two types of carbides, rod-like and plate-like shapes. This is similar to results reported by Lechtenberg, et al., for HT-9 (Ref. 3). Particles with a size leas than 0.1µm appeared only as small rod-shaped precipitates and coarser particles formed as rod-like or plate-like shapes. The selected area diffraction patterns Prom the isolated particles confirmed the carbides to be $M_{23}C_6$ and a Pew particles seem likely to be MC-type carbide. This is consistent with the X-ray diffraction analyses. The scarcity of MC-type carbide is due to very low V content (0.015%) and no Ti added in this steel. An appreciable amount of MC-type carbide should be detected if the target value of 0.3% V or Ti were added to this steel. The size of precipitates was typically in the range of 200A-7500A. The size distributions of carbide precipitates extracted prior and after thermal aging are shown in Figure 7.8.4. The mean particle size increased from 0.10µm to 0.14µm after thermal aging at 600°C for 100hrs and many more rod-like carbides were Pound in the thermally aged specimens than in the as-tempered specimens.

Electron transparent thin-Poil examination was also conducted on quenched and tempered specimens and thermally aged specimens. The thin-foil TEM micrographs Show lath martensite in the prior-austenite grain boundary, as shown in Figure 7.8.5. No significant amount of ferrite was seen. In both specimens, carbides were commonly observed on prior austenite grain boundaries and martensite lath boundaries although small amounts occurred within martensite laths. Heavy carbide precipitation was noted at the prior-austenite grain boundaries and martensite lath boundaries. The areal density of carbide

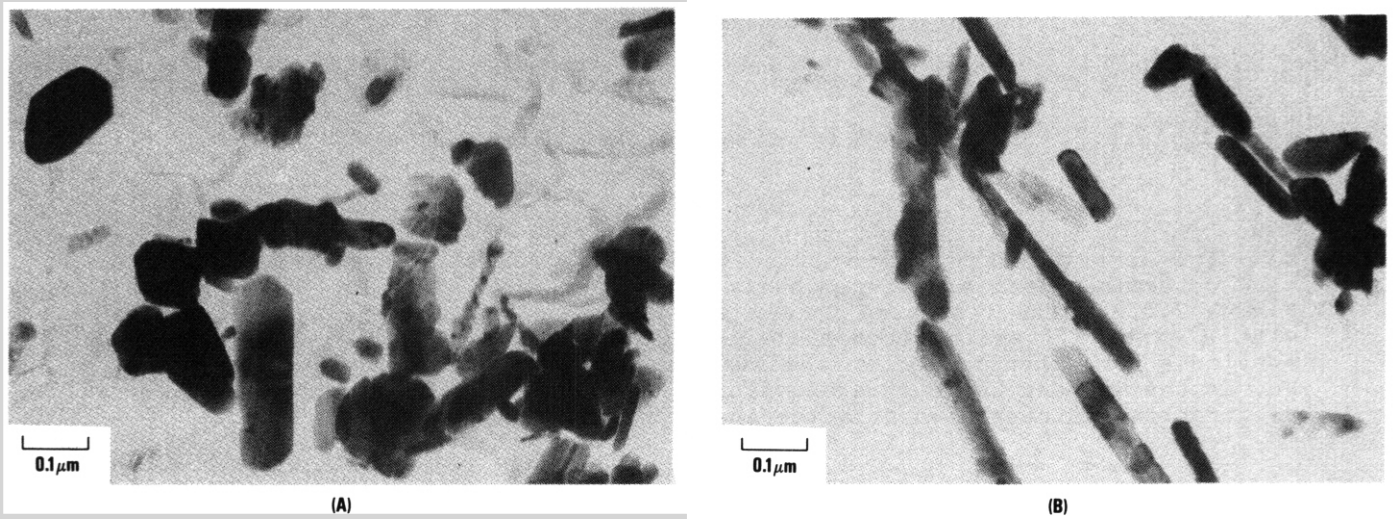

Fig. 7.8.3. TEM micrograph of carbon film extraction replica of GA3X steel, (a) quenched and tempered condition, and (b) condition (a) followed by thermal aging at 600°C/100 hr

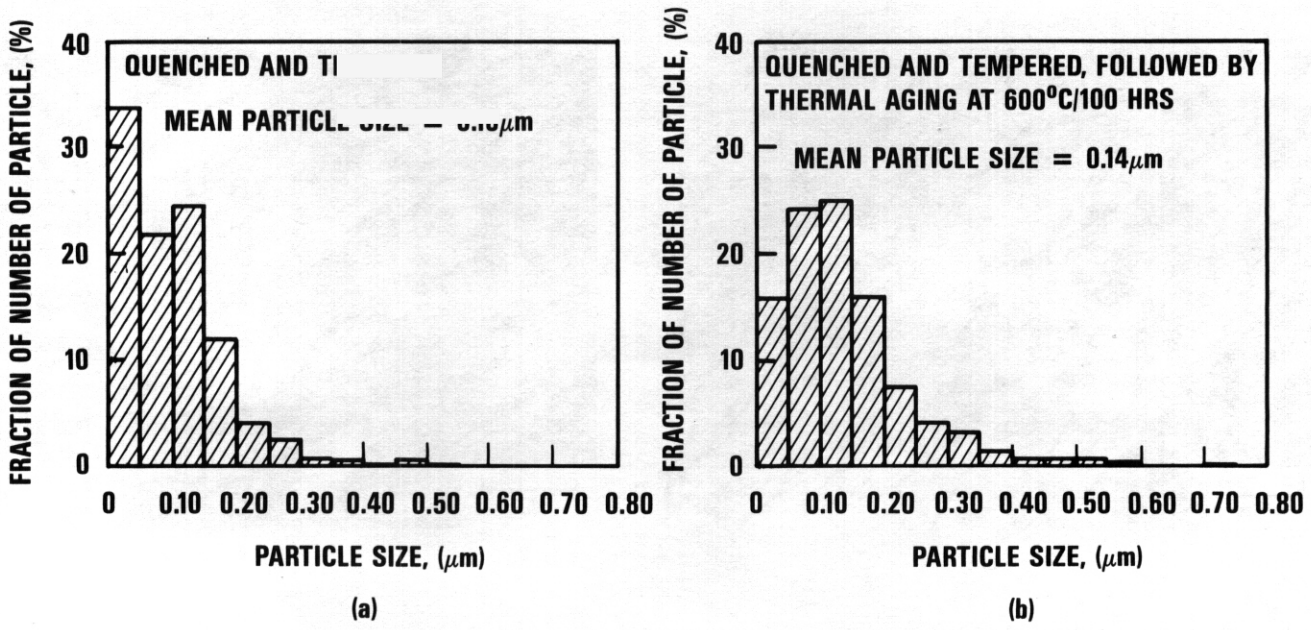

Fig. 7.8.4. Size distribution of the extracted precipitates of GA3X low activation ferritic steel, (a) quenched (1000°C/1hr) and tempered (700°C/1hr), (b) followed by thermal aging at 600°C/100 hrs

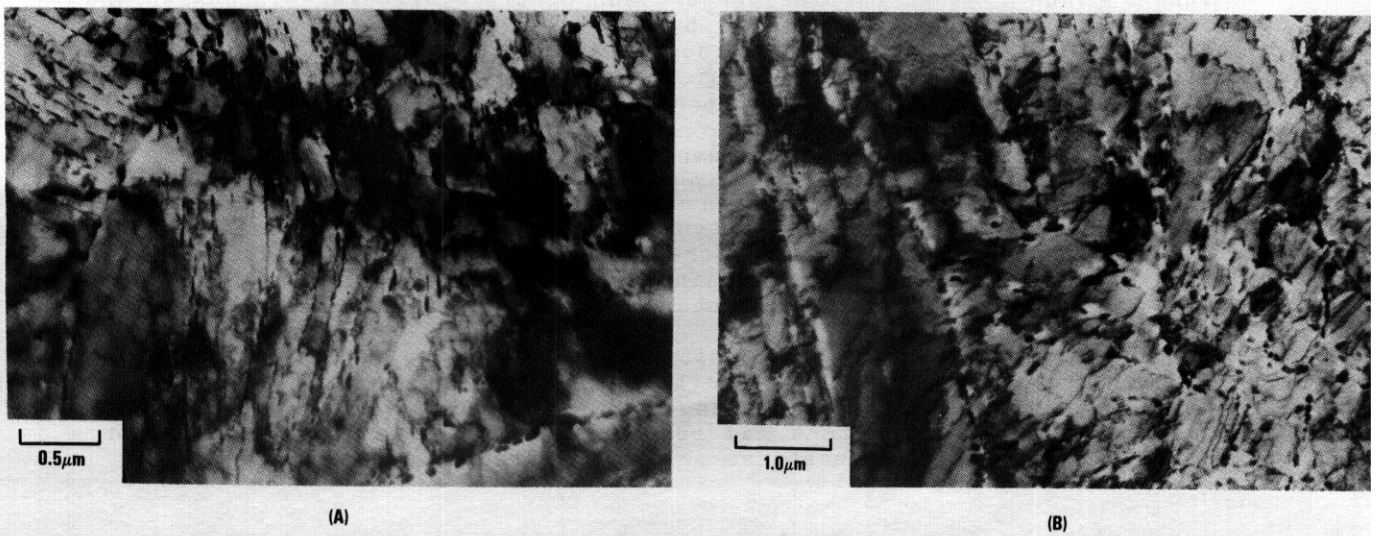

Fig. 7.8.5. TEM thin-foil micrographs of GA3X steel, (a) and (b) quenched and tempered condition, (c) and (d) followed by thermal aging at 600°C/100 hrs

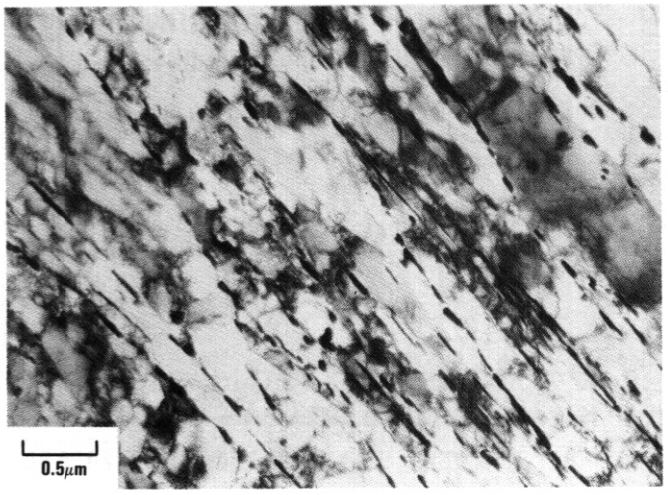

(C)

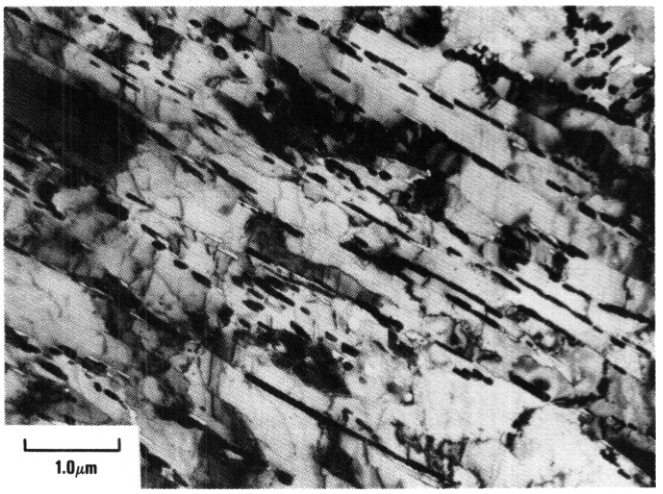

(D)

Fig. 7.8.5. (c) and (d)

precipitation is appreciably higher in the thermally aged specimen than in the as-tempered specimen as judged directly from the thin-Poi1 microstructural observation. In the thermally aged specimen, the particle size was increased, especially for particles appearing on grain boundaries and lath boundaries. Particle coalescence and an increase in the areal density of rod-like Carbides were found on austenite grain boundaries and martensite lath boundaries after the thermal aging treatment. This observation can be attributed to enhanced diffusion at grain + lath boundaries. It is indicated that the coarsening and precipitation of carbides was promoted by the thermal aging treatment.

The evidence is that carbide content and particle size were increased and particle morphology tended to change by the thermal aging treatment. The weight percent of precipitates was increased from 2.0% in the as-tempered condition to 3.1% after thermal aging at 600°C for 100hrs, and then remain fairly unchanged up to 1000hrs as reported in Ref. 2. This indicates that carbide precipitation was not complete after a one-hour tempering at 700°C. A double tempering or an increase of tempering temperature (750°C) may improve the phase stability under thermal aging or in a neutron environment. The influence of these precipitation phenomena may be an initial increase in tensile strength followed by a decrease when overaging occurs. The precipitation process and morphology change of particles and the increase of elongated rod-like carbides along grain boundaries and lath boundaries may influence the impact and fracture toughness and mechanical behavior of this steel.

In the quenched and tempered condition, dislocations are ordered producing irregular subgrains within the martensite laths. After thermal aging at 600°C for 100hrs there were no apparent changes in the dislocation sub-structures. Changes in dislocation structure may become more pronounced after prolonged thermal aging at service temperatures or during irradiation.

Mechanical Properties

The mechanical tests were performed on specimens after optimum heat treatment (1000°C/1hr, water quenched + 700°C/1hr, air-cooled). The elevated-temperature tensile strengths of this ferritic steel were measured from 20°C to 650°C. The ultimate tensile strength and 0.2% offset yield strength of this ferritic steel are compared with the average curves of 9Cr-1Mo and modified 9Cr-1Mo steels in Figures 7.8.6 and 7.8.7, respectively. Tensile strengths increased about 10% as compared to the average value for commercial heats of 9Cr-1Mo and modified 9Cr-1Mo steels. This was true over the entire range of

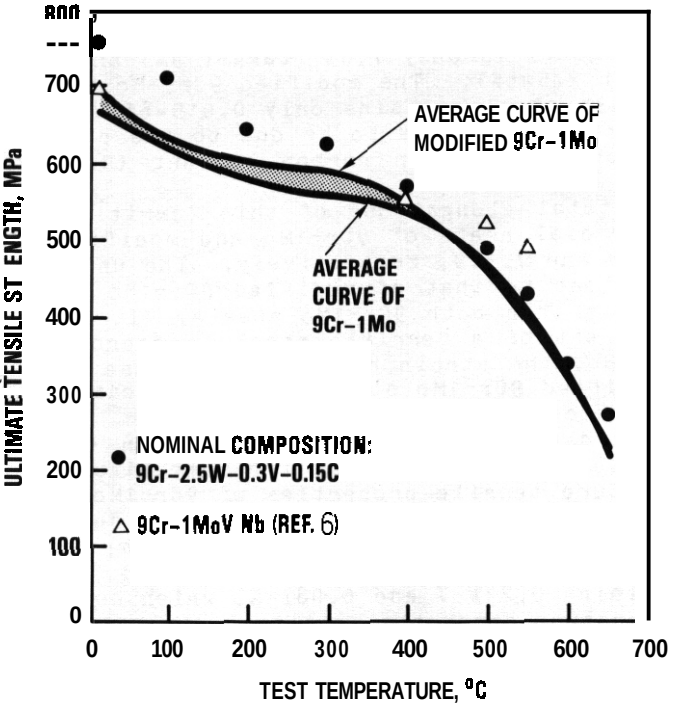

Fig. 7.8.6. The ultimate tensile strength of 9Cr-2.5W-0.3V-0.15C (GA3X) low activation ferritic steel compared to average curves of 9Cr-1Mo and modified 9Cr-1Mo steels (band)

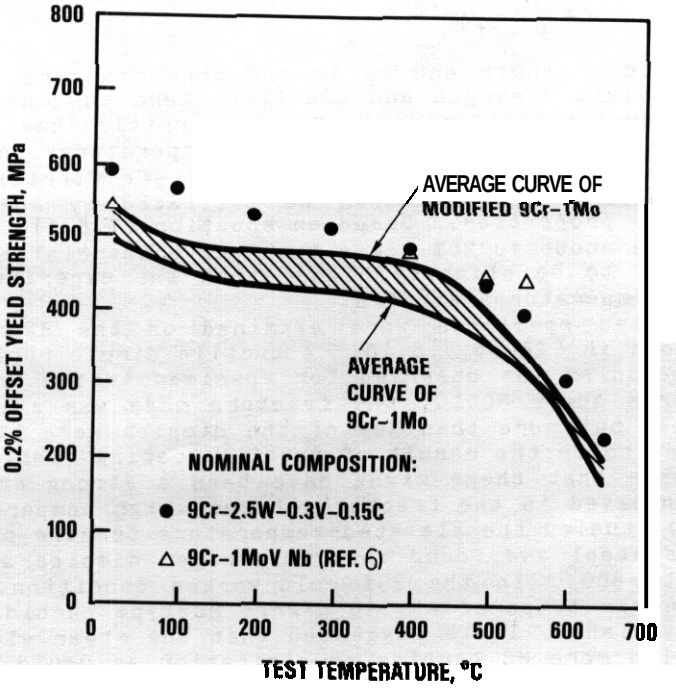

Fig. 7.8.7. The yield strength of 9Cr-2.5W-0.3V-0.15C (GA3X) low activation ferritic steel compared to the average curves of 9Cr-1Mo and modified 9Cr-1Mo steels (band)

test temperature (Refs. 4,5). This may be improved if the alloying concentrations had been closer to target in the GA3X heat. The actual Cr concentration of this steel is only 7.55 (target 9%) and the concentration of W is Only 2.0wt% (target 2.5wt%). The modified 9Cr-1Mo steel contains 0.21wt% V and 0.01wt% Ti and GA3X steel contains only 0.015wt% V. Hence, the enhanced tensile strength observed is likely to be due to the effect of a 0.17% carbon content, which is much higher than carbon content (0.1%) of both 9Cr-1Mo steels.

The uniform and total elongations of this ferritic steel along with the average data of commercial heats of 9Cr-1Mo and modified 9Cr-1Mo steels are shown in Figures 7.8.8 and 7.8.9, respectively. The uniform elongation of this steel is about equivalent to that of modified 9Cr-1Mo steel while the total elongation is ~50% less than both 9Cr-1Mo steels. It is well known that the strain hardening exponent of a ferritic steel is approximately equal to the uniform elongation. So, the strain hardening response of this ferritic steel is similar to the modified 9Cr-1Mo steels Which indicate Similar precipitation effects on dislocation movement and multiplication.

The tensile test data is alro compared with an experimental heat of unirradiated 9Cr-1MoVNb steel (Ref. 6) in the same figure. In oomparison with the elevated-temperature tensile properties of 9Cr-1MoVNb steel, the GA3X low activation ferritic steel shows higher strengths and ductility at temperatures from 20°C to 400°C, and becomes slightly weaker at temperatures above 500°C but maintains a higher ductility. In contrast to 0.0152 V in GA3X steel, the 9Cr-1MoVNb steel contains 0.245 V and 0.08; Nb which contributed significantly to the elevated temperature strengths. It is indicated that the low activation ferritic steel with a nominal composition of 9Cr-2.5W-0.3V-0.15C shows a promising potential of improved strength at elevated temperatures over those 9Cr-1Mo steels.

Changes in fracture toughness (K_{IC}) can be estimated by tensile behavior and the associated microstructural evolution of the steel (Refs. 7-13). Several models are available to correlate the toughness and tensile properties of irradiated metals. An excellent agreement between tensile-base prediction and K_{IC} Practure toughness measurements was obtained on irradiated stainless steel by using the modified Krafft correlation (Ref.12). In the case of low work-hardening coefficients, the modified Krafft correlation can be simplified as

$$K_{IC} = (\sigma_y \varepsilon_f)^{1/2} \qquad (7.8.1)$$

where σ_y is the yield Strength and ε_f is the true fracture strain. The opposing changes in yield strength and ductility tend to counterbalance each other. The work-hardening coefficients of GA3X ferritic steel determined from the tensile tests were as small as 0.1 at lower temperatures and were less than 0.1 at higher temperatures. In the same class of 9Cr ferritic steels. the variation of K_{IC} failure toughness can be estimated by comparing the differences of tensile properties. Based on equation (7.8.1), the plane-strain K_{IC} is predicted to be about 10-205 lower than the commercial heats of modified 9Cr-1Mo steel, and is to be slightly higher than the experimental heat of 9Cr-1MoVNb steel at temperatures studied.

The tensile tested specimens were examined on the SEM and their fractographs are shown in Figure 7.8.10. A ductile dimple rupture caused by a void coalescence mechanism was observed for specimen tested from 20°C up to 400°C. At temperatures above 500°C, the fracture mode war still ductile as shown by the dimples. but more than 30% of the dimples were elongated, which was usually indicated to be the result of ductile tearing (Ref.14). This mixed fracture mode suggests that there might have been a strong shear component and/or cross slip involved in the Practure at such high temperatures. Braski and Maziasz (Ref.15) studied the elevated-temperature tensile properties of PCA austenitic stainless steel and found shear-elongated dimples at test temperatures from 300°C to 600°C in the 255 cold-worked condition. Once the cold-worked specimen was tempered at 750°C/2hrs MC-type carbides precipitated and the mixed-mode vanished. It is suggested that the shear elongated dimples may be eliminated with more MC carbide precipitation as would be the case by increasing V and/or Ti concentrationr of GA3X steel. However, the reason for the formation of shear dimple is not yet fully understood and deserver further investigation.

The quenched and tempered 1/3 size Charpy specimenr were fatigue pre-cracked to approximately a/w=0.5, and then were tested in the instrumented impact terting machine at temperatures from -80°C to 100°C. The test results of this ferritic rteel are tabulated in Table 7.8.2 and is shown in Figure 7.8.11. The ductile-brittle transition temperature was determined to be -25°C

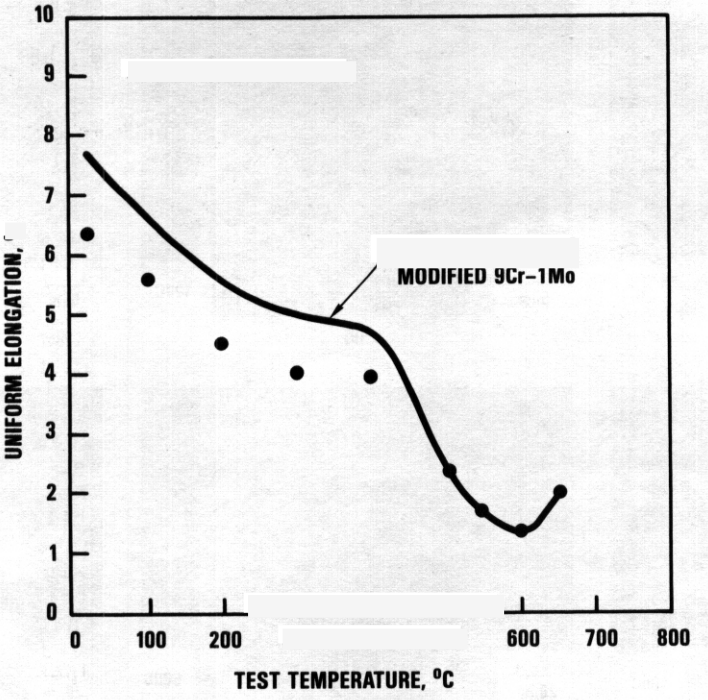

Fig. 7.8.8. Uniform elongation vs test temperature on GA3X low activation ferritic steel

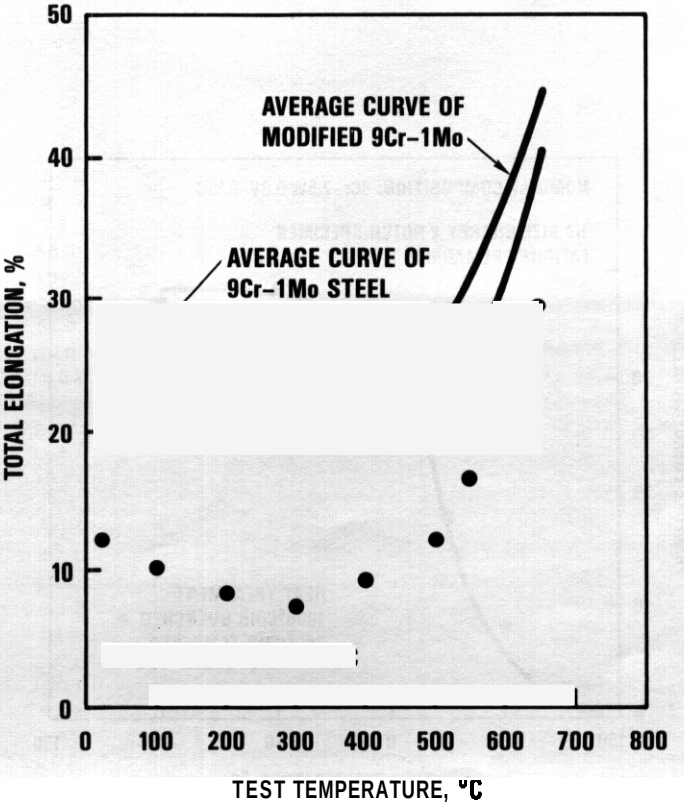

Fig. 7.8.9. Total elongation vs test temperature on GA3X low activation ferritic steel

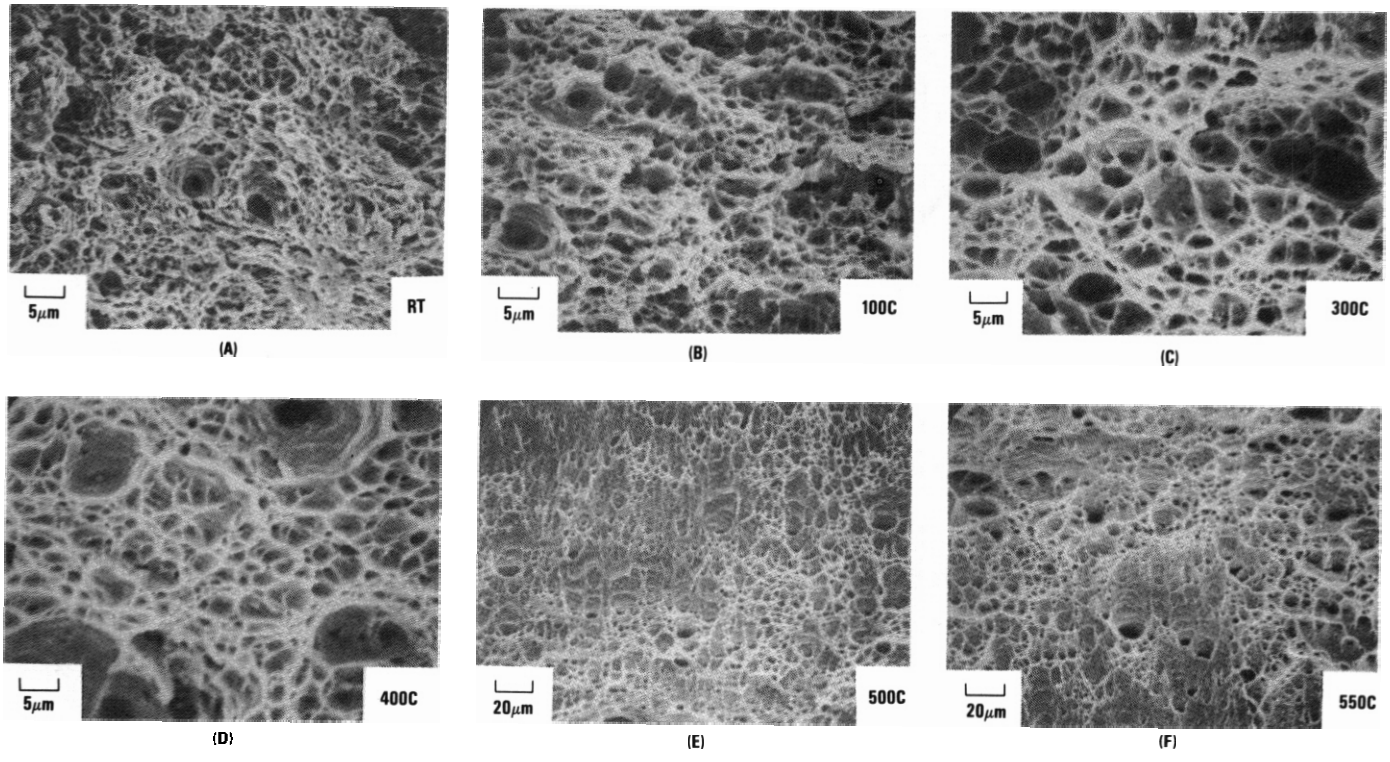

Fig. 7.8.10 Fractographs of the tensile tested specimens of GA3X steel tested at (a) 20°C, (b) 100°C, (c) 300°C, (d) 400°C, (e) 500°C and (f) 550°C

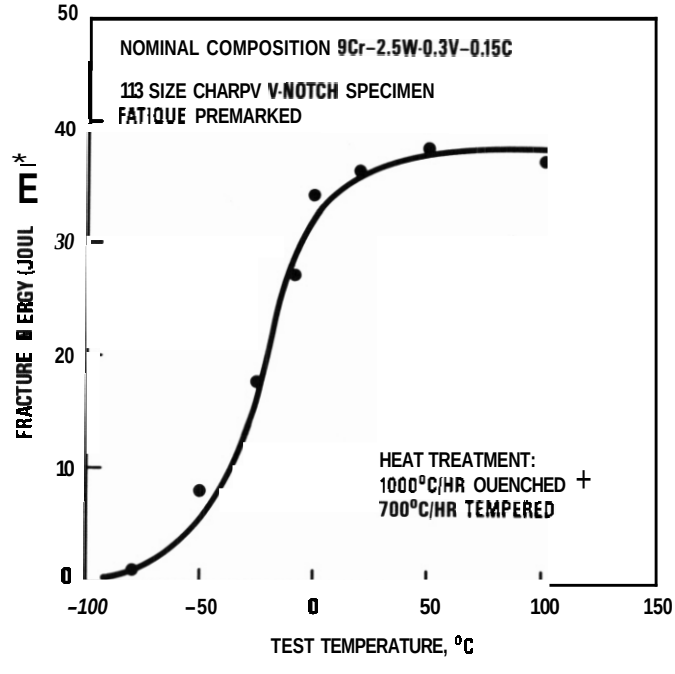

Fig. 7.8.11 The total fracture energy vs test temperature on the precracked 1/3 size miniature Charpy V-notch specimen of GA3X low activation ferritic steel

with an upper shelf energy of 2.2 Joules (37.2 J/cm^2 normalized fracture energy). The DBTT and impact energy of this low activation ferritic steel is very similar to the modified 9Cr-1Mo steels.

Table 7.8.2. The Impact Fracture Energy of the Precracked 1/3 Size Charpy Impact Specimens of GA3X Steel

Test Temperature (°C)	Fracture Energy (Joules)	Maximum Load (Kilo-Newtons)	Normalized Fracture Energy (Joules/cm^2)
100	2.225	0.645	37.56
50	2,499	0.733	38.29
21	2.264	0.693	36.11
0	2.180	0.726	34.10
-26	1.658	0.648	27.16
	1.113	0.574	17.73
-50	0.498	0.571	8.012
-80	0.050	0.536	0.852

While heat GA3X shows a 10% increase of tensile strengths and an estimated slight decrease in fracture toughness and duotility as compared to the commercial heats of both 9Cr-1Mo steels, the GA3X steel exhibits strengths and ductility very competitive to the experimental heat of 9Cr-1MoVNb steel. Anyhow, the experimental results provide some clues concerning optimum alloy composition. The mechanical properties of steel can be optimized by controlling microstructure through the processing and justification of alloy composition. For example, significant strengthening was contributed by the 0.17% carbon content. High carbon content can make the steel less weldable and increase particle coarsening which may degrade ductility and fracture toughness. The carbon content should be reduced to 0.15% or lower. The decrease in strength due to the lowering of carbon content can be supplementally improved by increasing Cr, V, and Ti alloying addition. The phase stability is a key concern for the justification of alloy composition. The Cr content should be maintained at a level of 9%. V and Ti are strong carbide formers. The addition of 0.3% V and <0.1% Ti could be made to control prior austenitic grain size and a low DBTT and to maintain high strengths at elevated temperatures. The increase in W may result in intermetallic precipitation, such as Fe_2W type Laves phase, after a prolonged thermal treatment or irradiation during service. The formation of intermetallic precipitation should degrade ductility and increase the DBTT. The extent of that degradation has not yet be determined. So, it is appropriate to maintain a W content at a level of 2.0% in order to reduce the Precipitation Potential of Fe_2W-type Laves phase during irradiation. However. the preliminary results point out that the proposed low activation ferritic steel Shows the promise of improved mechanical properties over both 9Cr-1Mo and modified 9Cr-1Mo steels.

7.8.5 Future Work

The evaluation of microstructure and mechanical properties of unirradiated GA3X low activation ferritic steel will continue. The post-irradiation microstructure and mechanical properties of GA3X steel will be evaluated at HEDL. More candidate alloys will be manufactured to meet the optimum and/or nominal compositions of 9Cr-2.5W-0.3V-0.15C and 11Cr-2.5W-0.3V-0.15C low activation ferritic steels.

7.8.6 Acknowledgement

The authors would like to express their appreciation to D.S. Gelles and W.L. Hu for their technical assistance on the impact testing of miniature Charpy specimens.

7.8.7 References

1. T. A. Lechtenberg, "Melting and Fabrication Aspect of Low Activation Ferritic Steels", P.111-119 in ADIP Semiannual Progress Report, March 31, 1985, DOE/ER-0045/14, U.S. DOE, Office of Fusion Energy.

2. Chen-Yih Hsu and T. A. Lechtenberg, "A Preliminary Evaluation of Microstructure and Mechanical properties on Low Activation Ferritic Steels". PP.120-128 in ADIP Semiannual Progress Report, March 31, 1985. DOE/ER-0045/14, U.S. DOE, Office of Fusion Energy.

3. T. Lechtenberg, W. M. Garrison and J. M. Hyzak, in Proceedings of Topical Conference on Ferritic Alloys for Use in Nuclear Energy Technologies, eds. J. W. Davis and D. J. Michel, published by AIME, 1984, pp. 365-370.

4. M. K. Booker, "Computation of Elevated Temperature Allowable Stress Values for Modified 9Cr-1Mo Steel", Presented to the ASME Working Group on Materials Behavior, New York, February 21, 1985.

5. V. K. Sikka, "Development of Modified 9Cr-1Mo Steel for Elevated Temperature Service". Proceedings of Topical Conference on Ferritic Alloys for use in Nuclear Energy Technology, eda. J. W. Davis and D. J. Michel. AIME, New York, 1984. pp. 317-327.

6. R. L. Klueh and J. M. Vitek, "Elevated Temperature Tensile Properties of 9Cr-1MoVNb Steel Irradiated In the EBR-II AD-2 Experiment. pp. 100-103 in ADIP Semiannual Progress Report, March 31, 1984, DOE/ER-0045/12, U.S. DOE. Office of Fusion Energy.

7. W. G. Wolfer and R. H. Jones, J. Nucl. Mater., Vol. 103 & 104. 1981. pp. 1305-1314.

8. J. M. Krafft, Appl. Matls. Res.. Vol. 3, 1964. p.88.

9. G. T. Hahn and A. R. Rosenfield. in Applications Related Phenomena in Titanium Alloys, ASTM STP432, Amer. Soc. for Test. and Matls, 1968. p.5.

10. F. H. Huang and G. L. Wire, "Irradiation Effects on the Fracture Toughness of 20% Cold-worked Type 316 Stainless Steel", in Proc. Int. Conf. on Dimensional Stability and Mechanical Behavior of Irradiated Metals and Alloys, British Nuclear Energy Society. Apr. 1983. Brighton. England, Vol.1, p.135.

11. F. H. Huang, "The Fracture Characterization of Highly Irradiated Type 316 Stainless Steel, Inter. J. of Fracture, 25 (1984) 181-193.

12. F. H. Huang and R. L. Fish, in Effects of Radiation on Materials: Eleventh Conference, ASTM STP 182. American Society for Testing and Materials, 1982, p. 701.

13. M. L. Hamilton, F. A. Garner and J. S. Yang, "Prediction of Fracture Toughness in Irradiated AISI 316 Based on a Tensile-Toughness Correlation", in Damage Analysis and Fundamental Studies Quarterly Progress Report, Oct.-Dec. 1984, DOE/ER-0046/20, U.S. DOE, Office of Fusion Energy.

14. S. Bhattacharyya, V. E. Johnson, S. Agarwal and M. A. H. Howes, "IITRI Fracture Handbook", IIT Research Institute, Chicago, Illinois, January 1979.

15. D. N. Braski and P. J. Maziasz, "Tensile Properties of Unirradiated PCA From Room Temperature to 700°C", Proc. of the 3rd. Topical Meeting on Fusion Reactor Materials. New Mexico, USA, September 1983, pp.338-342.

8. COPPER AND ITS ALLOYS

8.1 MICROSTRUCTURE OF COMMERCIAL COPPER ALLOYS IRRADIATED IN FFTF-MOTA AT 450°C - H. R. Brager and F. A. Garner (Hanford Engineering Development Laboratory)

8.1.1 AOIP Task

Not included in current ADIP Task Structure.

8.1.2 ADIP Task

The object of this effort is to determine the origin of radiation-induced alterations of the properties of copper alloys anticipated for use in fusion environments.

8.1.3 *Summary*

Electron microscopy of pure copper irradiated at ~450°C to 16 dpa revealed no unexpected behavior, showing both dislocation and void development. In the same experiment, however, the dispersion-hardened alloy A125 exhibited a remarkable insensitivity to irradiation. The precipitation-hardened alloy MZC also had no voids present but the precipitate microstructure was changed such that an apparent swelling of 1.03% occurred. Dependent on the heat-treatment employed the alloy CuBeNi showed various levels of voidage, particularly in those areas which suffered recrystallization and alteration of the precipitate structure.

8.1.4 Progress and Status

8.1.4.1 Introduction

In an earlier report the neutron-induced changes in electrical conductivity, tensile properties and density were measured for high purity copper and eight copper alloys after irradiation at 450°C to ~16 dpa in FFTF-MOTA.(1) In this report the microstructures induced in pure copper and three of the copper alloys are described after examination by transmission electron microscopy. The composition, heat treatment and bulk density change of these alloys are shown in Table 1.

8.1.4.2 MARZ Copper

This alloy was irradiated in the annealed condition using zone-refined 99.999% pure MARZ copper. The irradiation was conducted at ~450°C which represents a homologous temperature of 0.53. Thus one would expect a significant level of vacancy mobility at this temperature and a relatively low void density. Figure 1 shows that only a moderate density (~1 X 10^{14} cnr3) of quite large voids were observed. The average diameter of these voids was 90 nm and their shape was that of the usual truncated octahedra. The local swelling in the region shown in Figure 1 is ~4% compared to the measured change in bulk density of 6.5%. The difference probably reflects the region-to-region variability normally exhibited in foils with low to moderate void densities.

TABLE I

SWELLING OF VARIOUS COMMERCIAL COPPER ALLOYS IN MOTA-1B
RT ~450°C and 2.5 x 10^{22} n/cm^2 (E >0.1 MeV)

	Alloy Composition (wt.%)	Condition	% Swelling
Cu (MARZ)	cu (99.999%)	Annealed	**6.5**
CuNiße (1/2 HT)*	Cu-1.8 Ni-0.3 Be	20% CW & Aged (3 hr at 480°C)	1.70
CuNiBE (AT)*	Cu-1.8 Ni-0.3 Be	Annealed & Aged (3 hr at 480°C)	0.29
MZC	Cu-0.9 Cr-0.1 Zr-0.05 Mg	90% CW, Aged 1/2 hr at 470°C	1.03
Cu-A125	Cu-0.25 Al_2O_3	20% CW	0.13

* 1/2 HT and AT are industry designations for half-hard and tempered, and annealed and tempered, respectively.

The dislocation density in this region was also relatively low ($\sim 3 \times 10^{-9}$ cm^{-2}) and reflects both the purity of the copper and the high homolo ous temperature at which the irradiation was conducted. Also shown in Figure 1 is a low density ($\sim 10^{1}$ /cm^{3}) of small unidentified defect clusters. These clusters are not anticipated to have a significant effect on the electrical or mechanical properties when compared to the effect of the other microstructural components.

8.1.4.3 Dispersion-Strengthened Copper

The commercial alloy A125 was irradiated in the 20% cold-worked condition and is essentially pure copper strengthened with very small alumina particles formed by internal oxidation of a small amount of aluminum solute. In contrast to the pure copper which had large grains on the order of tens of microns, A125 contains grains and subgrains of micron and submicron sizes. In this particular alloy the Al_2O_3 is *0.25* percent by weight and is dispersed in particles ranging from 3 to 20 nm in size at a density of $\sim 3 \times 10^{16}$ cm^{-3}. As shown in Figure 2 both the particles and cold-worked dislocation density are relatively stable, not only after aging for 1000 hours at 700°C, but also after irradiation to 16 dpa at ~450°C.

A very careful examination of the microstructure after irradiation showed that this alloy was remarkably insensitive to irradiation, with no voids or bubbles observed and very few Frank loops, but only at small sizes (<10 nm). Examples of the void-free matrix and precipitate microstructure are shown in Figure 3. Figure 4 shows when different diffraction vectors are used to image the precipitates after irradiation, the black-white contrast vector is always parallel to the diffraction vector. This indicates that the precipitates have a radially-symmetric strain field.

8.1.4.4 Precipitation-Strengthened Cold-Worked Alloy

The MZC copper-base alloy contains small amounts of magnesium, zirconium and chromium which provide both solid solution strengthening and precipitation hardening. When combined with work hardening this alloy provides a good combination of high strength and high conductivity. The properties of the alloy are somewhat dependent on thermal-mechanical treatment. The recommended treatments are directed toward production of a high concentration of small precipitates which are rich in copper and zirconium. The purpose of introducing these precipitates is to stabilize the dislocation network at high temperatures. As shown in Figure 5 these precipitates were observed to be stable after aging for 1000 hours out-of-reactor at 400°C.

After a less detailed examination than that employed for the A125 alloy, it appeared that no voids had formed in the irradiated alloy. This is inconsistent with the reported density change of -1.03%. It is suspected that the apparent swelling is a consequence of a lattice parameter change of the matrix arising from precipitation. While Figure 6 shows that $\sim 5 \times 10^{16}$ cm^{-3} precipitates with sizes in the range 2-10 nm still exist after irradiation, there is a second population of precipitates at $\sim 10^{14}$ cm^{-3} which have much larger sizes (~50 nm). These were found to be rich in chromium. Experiments are now in progress to identify both precipitate populations. The dislocation density after irradiation was found to be marginally higher ($\sim 10^{11}$ cm^{-2}) than that of typical austenitic stainless steels (3-6 $\times 10^{10}$ cm^{-2}) irradiated at comparable homologous temperatures.

8.1.4.5 Precipitation-Strengthened Alloy

The CuBeNi alloy was irradiated in two conditions; the half-hard and tempered (1/2 HT) condition and the annealed and tempered condition (AT). Since beryllium in solution strongly reduces electrical conductivity, nickel is added to reduce the solubility of beryllium and induce precipitation of nickel-beryllium precipitates.

Figures 7 and 8 show that after aging of the 1/2 HT condition for 1000 hours at 400°C that the precipitates are quite stable but after aging at 700°C for the same time extensive recrystallization occurs along with strong coarsening of the precipitate structure. During irradiation at 450°C, however, recrystallization and coarsening also occurs. Figures 9 and 10 show that extensive recrystallization (~75% of grains) has occurred, with large precipitates and voids forming in the recrystallized zones. The unrecrystallized grains are largely free of voids and contain $\sim 5 \times 10^{16}$ cm^{-2} of small (~5 nm) precipitates of undetermined nature. There is some evidence that envelopes or halos of voids are formed around the large precipitates. Similar behavior has been observed in other alloys containing boron-rich precipitates.[2,3] It is assumed that these are a consequence of the $^{9}Be(n,2n)^{8}Be \rightarrow {}^{4}He + {}^{4}He$ reaction. The reaction energy is known to be broader in energy range and not as well defined as that of typical (n,σ) reactions, however, and the halo's are therefore broader and less distinct than that generated by (n, σ) reactions.

In the at condition, no recrystallization was observed after irradiation. In addition to the high density of small precipitates there were a very low density ($\sim 10^{12}$ cm^{-3}) of large voids, with sizes comparable to that observed in the pure copper.

8.1.5 Conclusions

Pure copper swells rather easily at 450°C but swelling can be delayed by solute additions, particularly when dense precipitate populations are introduced which are stable during irradiation. When the precipitate populations are unstable and when recrystallization occurs, then swelling can occur. This is particularly true in alloys which contain beryllium that transmutes to helium. It also appears that density change information must be supplemented by microscopy observations to determine whether decreases in density arise from voids and/or precipitation sequences.

The behavior of MZC and particularly of A125 during irradiation at 450°C is most promising and provides additional incentive for development of high-conductivity alloys for fusion service.

8.1.6 References

1. H. R. Brager, H. L. Heinisch and F. A. Garner, J. Nucl. Mater. 133 & 134 (1985) 675.
2. D. S. Gelles and F. A. Garner, J. Nucl. Mater., 85 & 86 (1979) 689.
3. A. Kumar and F. A. Garner, Radiation Effects, 82 (1984) 61.

8.1.7 Future Work

Additional microscopy will be performed on specimens irradiated at 16 dpa. Density change measurements on specimens irradiated to higher exposures will also be performed.

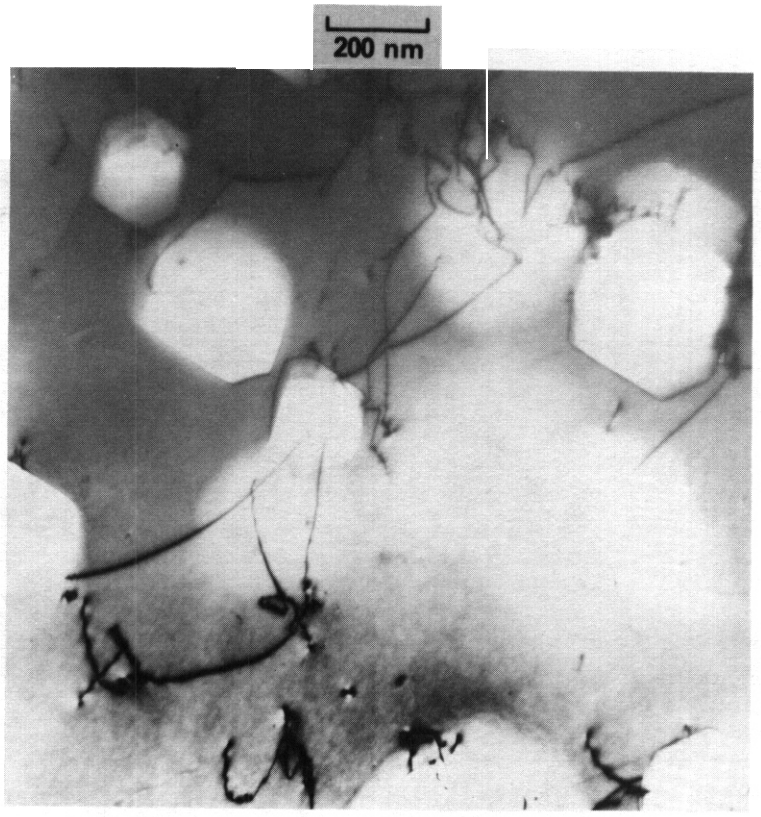

FIGURE 1. Large voids observed in MARZ copper after irradiation to 16 dpa at ∿450°C.

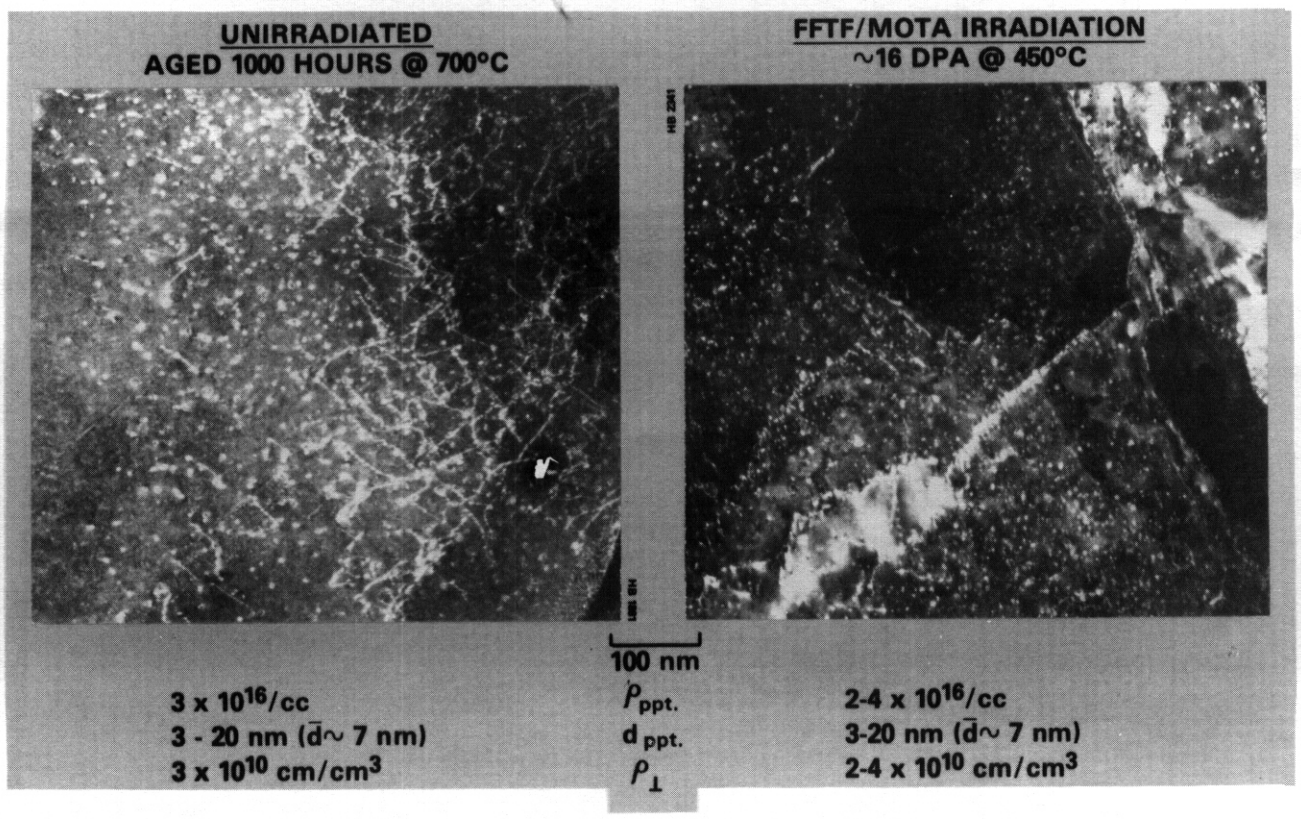

FIGURE 2. Comparison of microstructures of aged and irradiated A125 alloy.

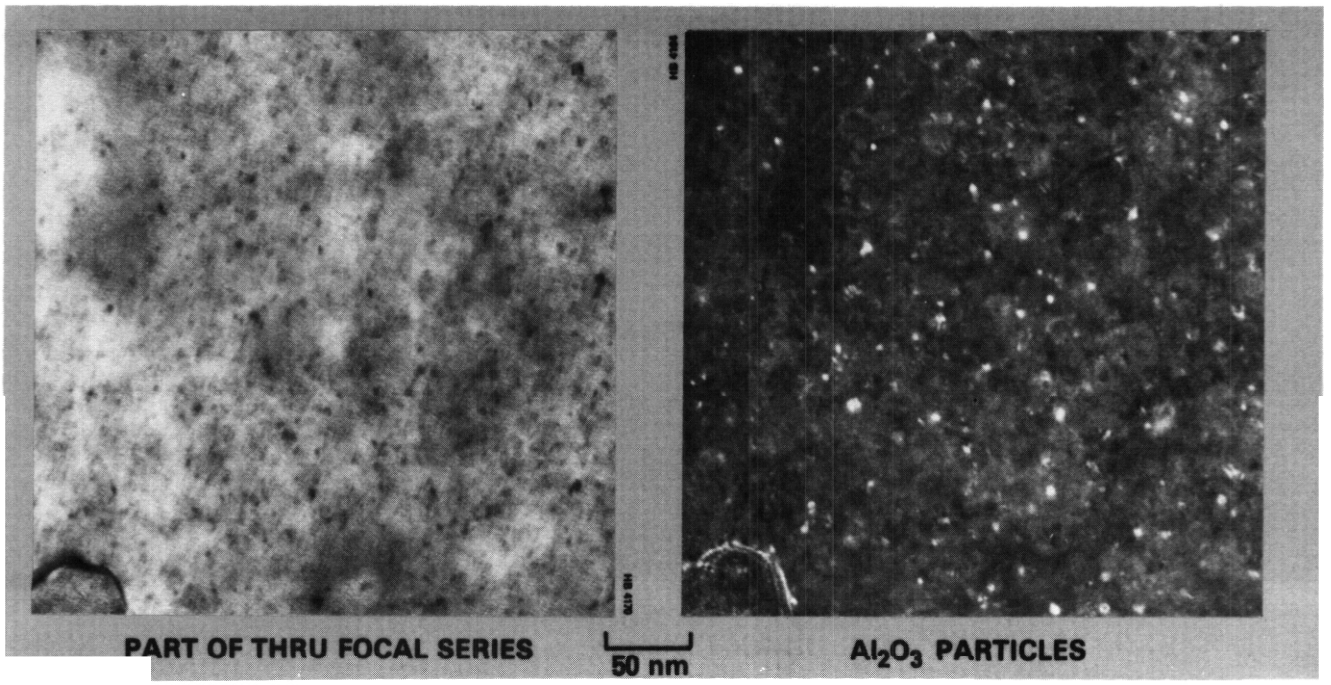

FIGURE 3. Illustration of absence of voids in irradiated A125 during careful thru-focal series of microscopy. Also shown is the fineness and distribution of Al_2O_3 dispersoids.

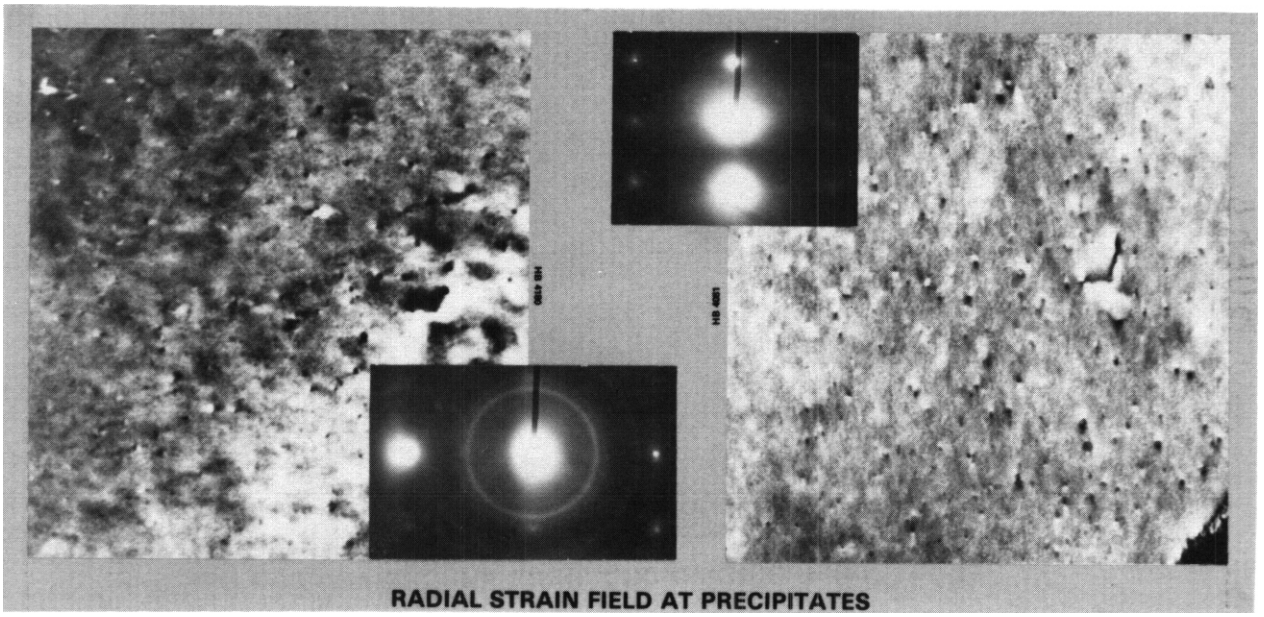

Figure 4. Illustration of the procedures used to establish the radially symmetric nature of the dispersoid particles in irradiated A125.

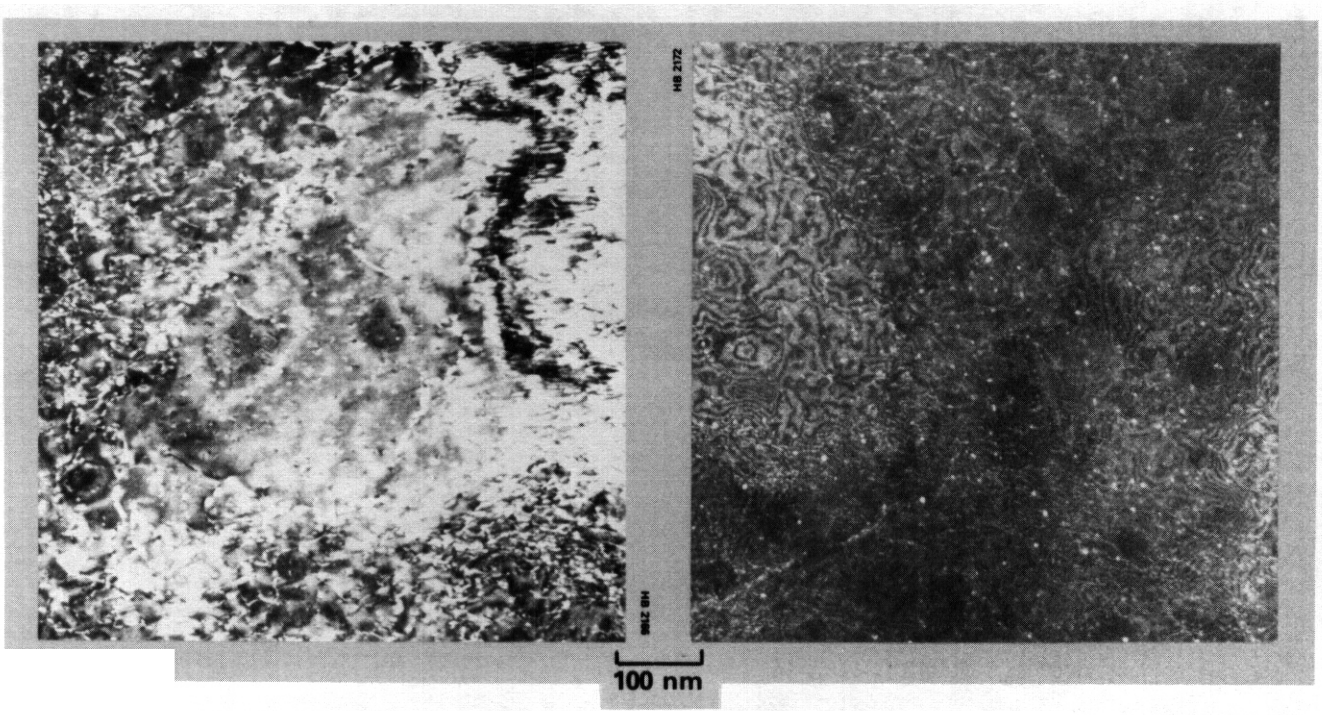

FIGURE 5. Micrographs demonstrating stability of small precipitates in MZC aged 1000 hours at 400°C.

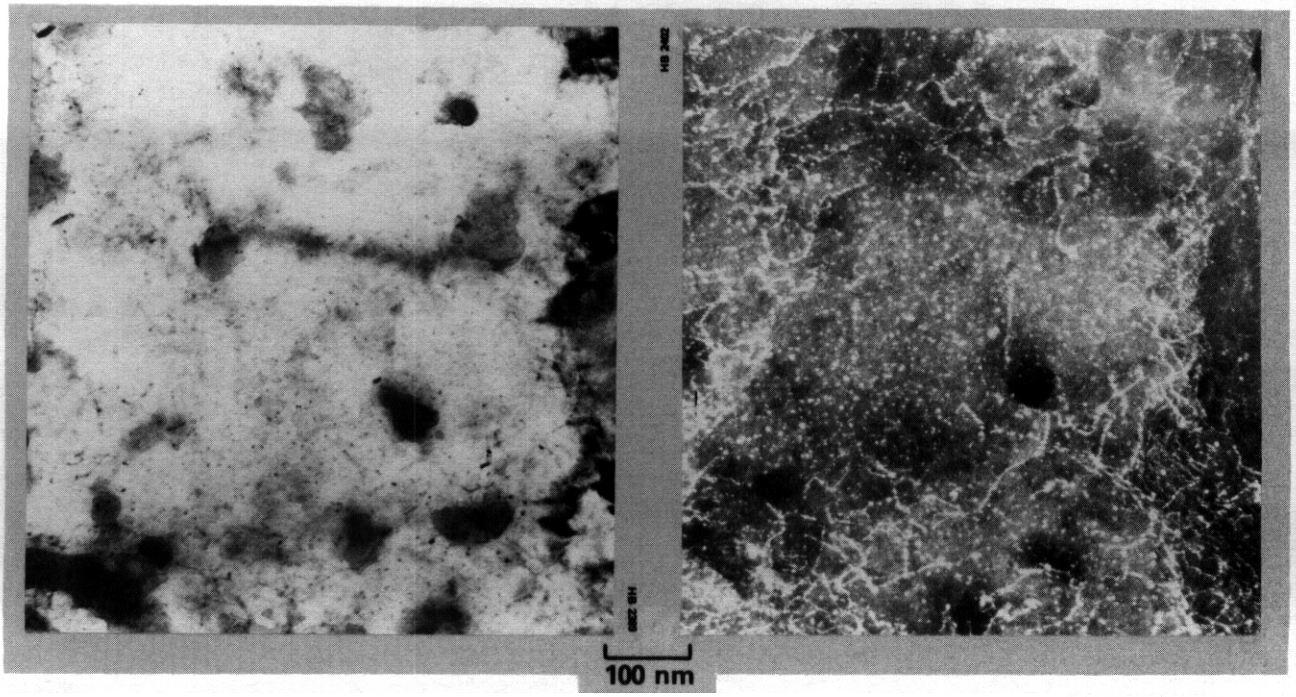

FIGURE 6. Bright-field and dark-field micrographs showing both large and small precipitates found in irradiated MZC.

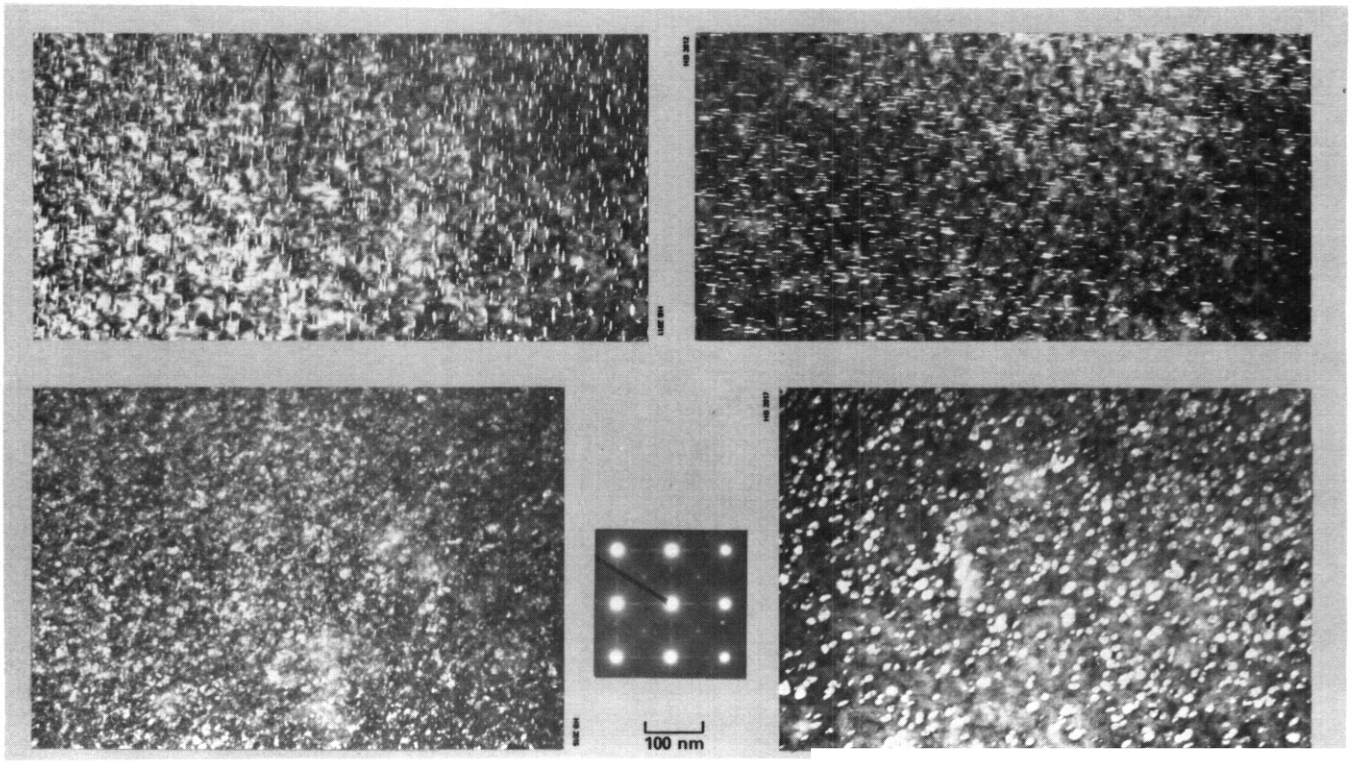

FIGURE 7. High density of small precipitates observed in CuBeNi (1/2 HT) after aging 1000 hours at 400°C, using different diffraction vectors.

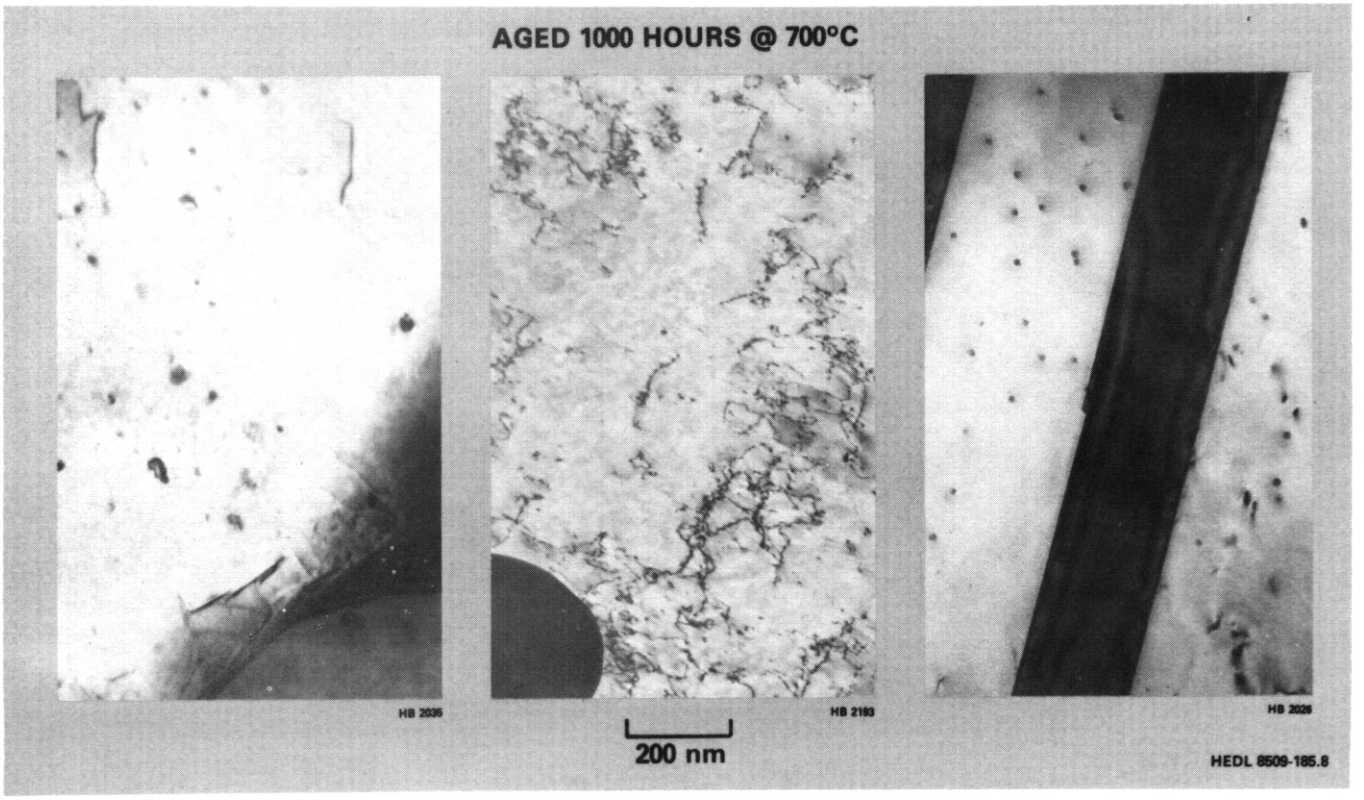

FIGURE 8. Recrystallized microstructures observed in CuBeNi (1/2 HT) after aging 1000 hours at 700°C.

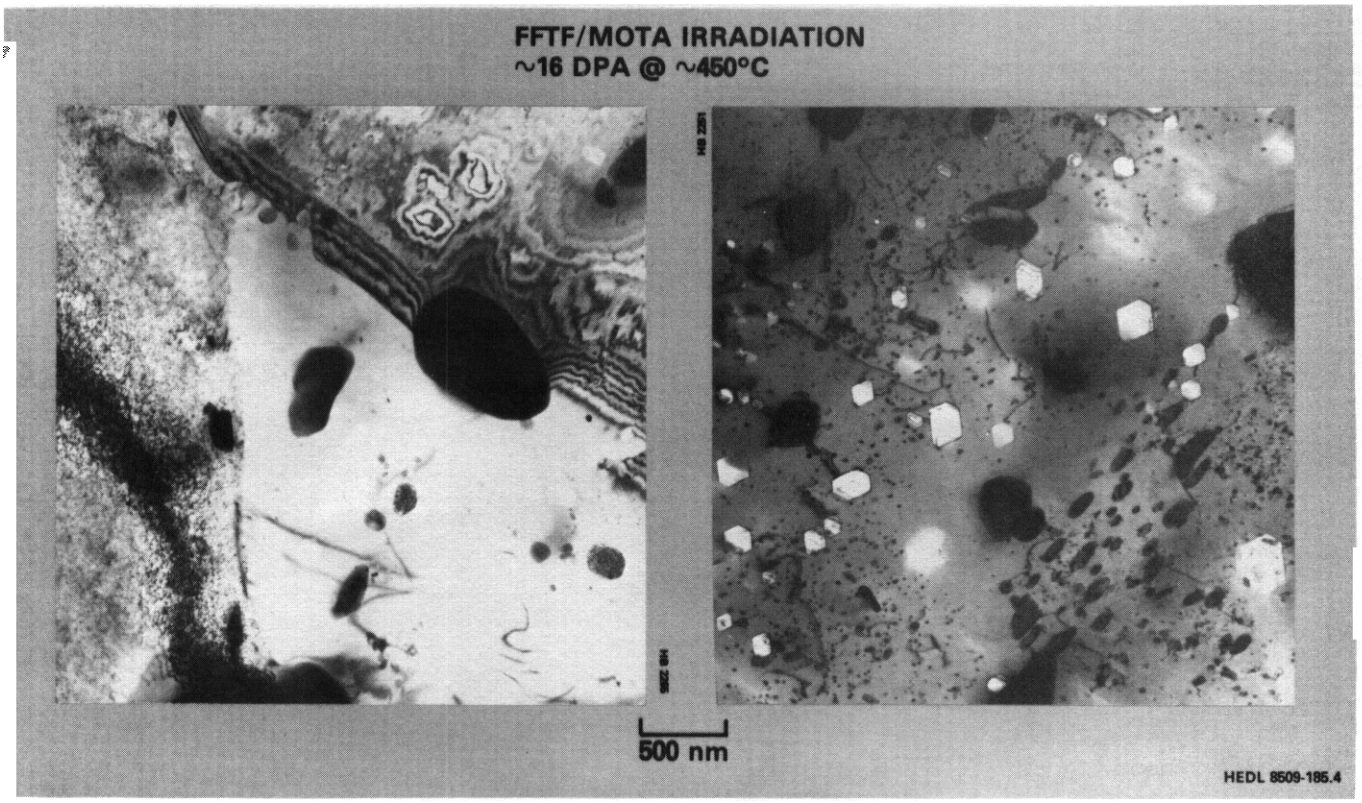

FIGURE 9. Adjacent grains in CuBeNi (1/2 HT) after irradiation, showing both recrystallized and unrecrystallized grains. Large precipitates and voids are found in in recrystallized areas.

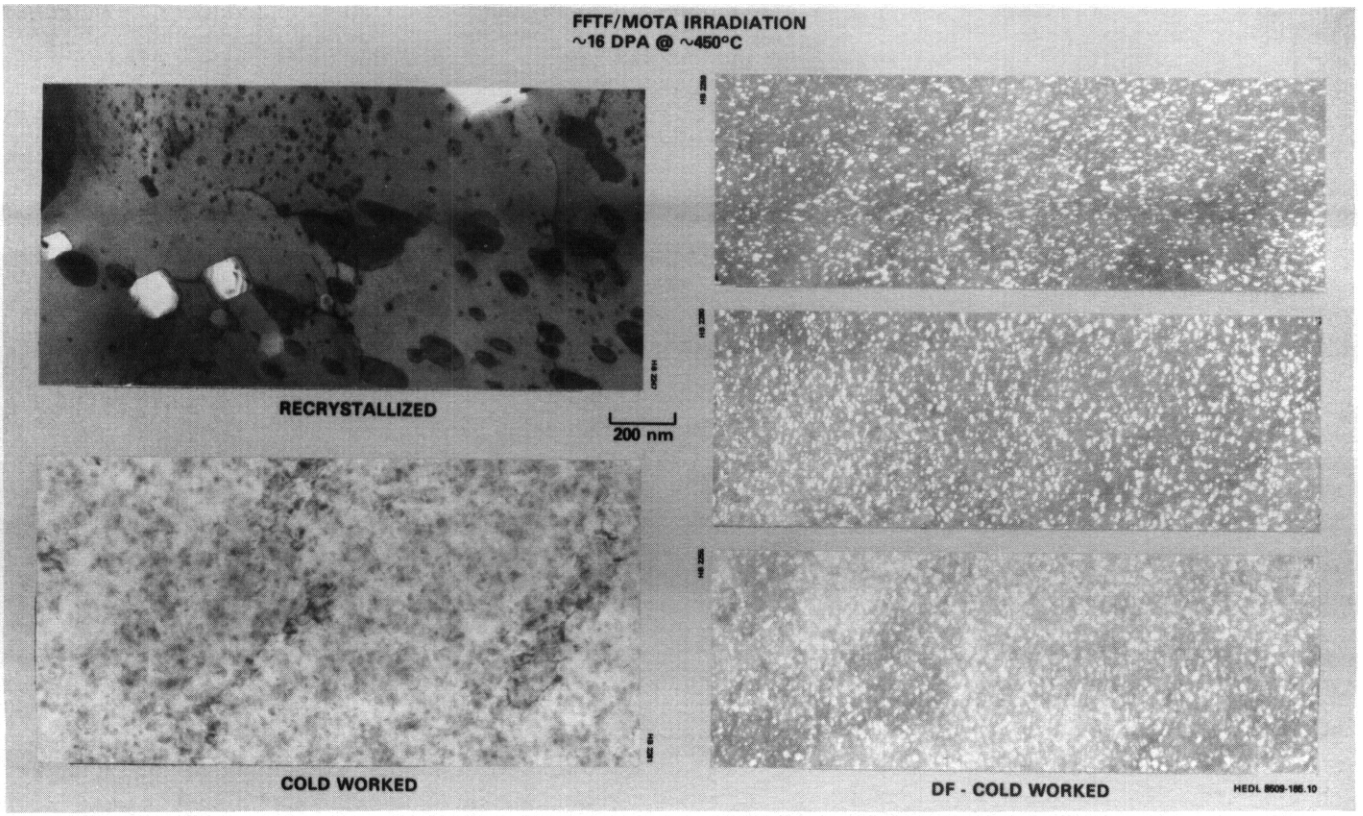

FIGURE 10. While the recrystallized areas of CuBeNi (1/2 HT) exhibit large voids and precipitates, the uncrystallized areas retain their original cold-work character.

9. MATERIALS COMPATIBILITY AND HYDROGEN PERMEATION STUDIES

9.1 ENVIRONMENTAL AND CHEMICAL EFFECTS ON THE PROPERTIES OF VANADIUM-BASE ALLOYS -- D. R. Diercks and D. L. Smith (Argonne National Laboratory)

9.1.1 ADIP Task

AOIP Task I.A.3, Perform Chemical and Metallurgical Compatibility Analyses.

9.1.2 Objective

The objective of this task is to experimentally evaluate the corrosion behavior of selected vanadium-base alloys in aqueous, liquid-metal, and gaseous environments and to investigate chemical effects on the mechanical and physical properties of the alloys. The results of these investigations will be used in the selection of appropriate vanadium-base alloys for structural applications in fusion reactors.

9.1.3 *Summary*

Exposures of V-15Cr-5Ti, V-20Ti, and VANSTAR-7 specimens to pressurized flowing water containing 0.03, 0.19, and 8 wppm dissolved O_2 at 288°C indicate that V-15Cr-5Ti has the best corrosion resistance at all three oxygen levels. Scanning Auger microprobe studies of impurity segregation in irradiated and ^3He implanted V-15Cr-5Ti indicate no clear correlation with observed embrittlement.

9.1.4 Progress and Status

9.1.4.1 Aqueous Corrosion Behavior of Vanadium-base Alloys

An initial series of experiments to determine the corrosion behavior of vanadium-base alloys in pressurized water at 288°C (550°F) and 8.3 MPa (1200 psi) containing various levels of dissolved oxygen in a refreshed autoclave system has been completed. The three exposed alloys are V-15Cr-5Ti, V-20Ti, and VANSTAR-7. Samples of all three alloys were obtained from the Fusion Power Program (FPP) materials inventory in the form of 0.76-mm (0.030-in.)-thick sheet, and additional samples of the first two alloys were obtained from the Argonne National Laboratory (ANL) LMFBR inventory in the form of 1.52-mm (0.060-in.)-thick sheet. These alloys were sheared into weight-change specimens approximately 7.1 cm (2.8 in.) long and 1 cm (0.4 in.) wide. Further experimental details, as well as the results of the first and second series of exposures in water containing 4 and 0.03 wppm dissolved O_2, respectively, are described in previous reports.[1-3]

During the present reporting period, this initial series of corrosion experiments was completed in which a third set of specimens was exposed to water with ~0.19 wppn dissolved O_2 in the effluent. This oxygen level is considered to be representative of that present in contact with the specimens. The test was conducted with high-purity distilled feedwater (conductivity ~0.15 μS/cm) containing approximately 2 wppm dissolved O_2 obtained by equilibrating the solution with a N_2-5% O_2 blanketing gas mixture. The flow rate through the autoclave sytem was ~11 cm^3/min, and the oxygen level in the effluent water was monitored on a more or less continuous basis with a Leeds and Northrup Model 7931 dissolved-oxygen meter. Spot checks of the oxygen level in the inlet water were made with the same meter, as well as with Chemetrics dissolved-oxygen ampules. During most of the test, the dissolved-oxygen level in the outlet water varied between 0.17 and 0.21 wppm, giving the average 0.19 wppn reported here. However, occasional excursions to oxygen levels as low as 0.14 wppm and as high as 0.26 wppm were experienced.

This third corrosion test was interrupted after exposure times of 206, 508, 1003, and 2001 h to weigh the specimens. The weight changes for the alloys from different heats are summarized in Table 9.1.1 and plotted in Figs. 9.1.1 and 9.1.2. In all cases, the specimens lost weight. As may be seen in Fig. 9.1.1, the V-20Ti and VANSTAR-7 specimens showed similar behavior, with no significant heat-to-heat variations for the V-20Ti. The corrosion kinetics are approximately linear, and weight losses after 2000 h are of the order of 19 to 22 mg/cm^2. Best-fit equations representing the data of Fig. 9.1.1 for each of the alloys are as follows:

$$\text{V-20Ti:}\quad W = 5.737 \times 10^{-3}\ t^{1.078},$$

and

$$\text{VANSTAR-7:}\quad W = 1.252 \times 10^{-2}\ t^{0.972},$$

Table 9.1.1. Observed weight losses for vanadium-base alloys from the FPP materials inventory and ANL LMFBR inventory exposed to water containing 0.19 ppm dissolved oxygen at 288°C and 8.3 MPa

Alloy	Source	Weight Loss/Unit Area (mg/cm^2) after Indicated Exposure Time			
		206 h	508 h	1003 h	2001 h
V-15Cr-5Ti	FPP	0.081	0.158	0.228	0.356
	FPP	0.159	0.257	0.353	0.511
	ANL	0.089	0.173	0.273	0.452
	ANL	0.120	0.211	0.308	0.496
V-20Ti	FPP	1.222	5.007	9.859	20.87
	FPP	1.303	4.639	10.16	20.00
	ANL	1.393	5.327	10.21	21.25
	ANL	1.338	4.937	9.627	20.72
VANSTAR-7	FPP	1.881	5.520	10.25	18.84
	FPP	2.059	5.631	10.62	21.52

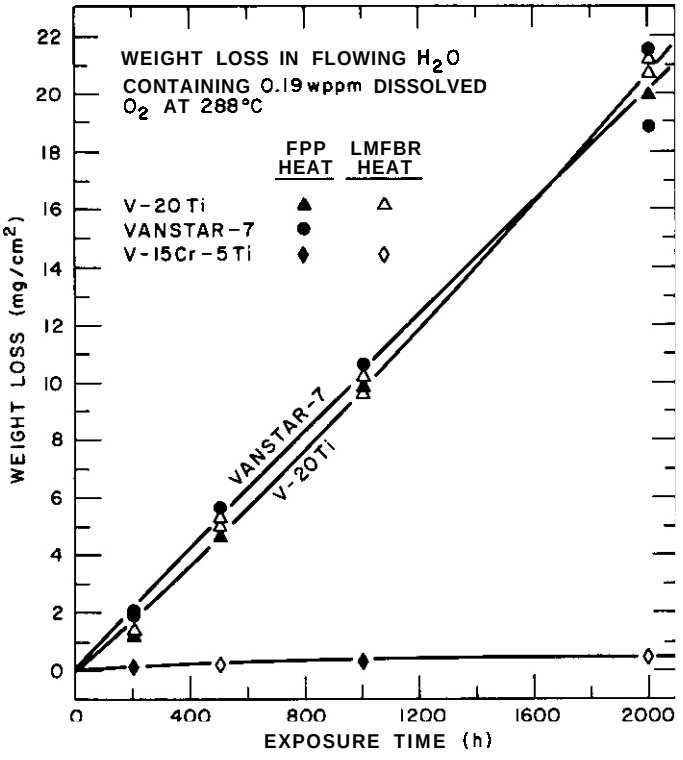

Fig. 9.1.1. Observed weight losses for V-20Ti and VANSTAR-7 exposed to water containing 0.19 wppm dissolved oxygen at 288°C.

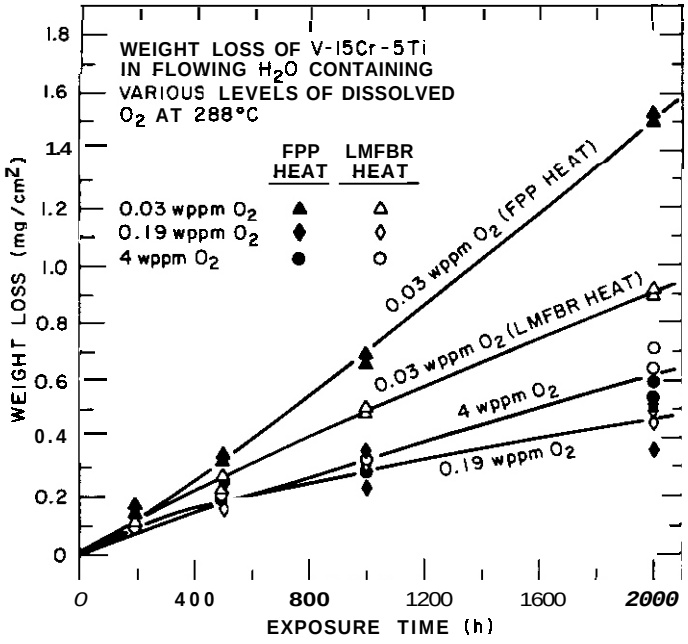

Fig. 9.1.2. Observed weight losses for V-15Cr-5Ti exposed to water containing 0.19 wppm dissolved oxygen at 288°C. The behavior of this same alloy in water containing 0.03 and 8 wppm oxygen is shown for comparison.

where W is weight loss in mg/cm^2, and t is time in hours. The weight losses for the V-20Ti and VANSTAR-7 alloys after 2000 h are factors of ~5 and ~3 lower, respectively, than those that were observed for the same alloys and heats after 2000 h obtained after exposure of the alloys to water containing 4 wppm dissolved oxygen.[2] On the other hand, the values are a factor of ~5 greater compared with those after 2000-h exposures to water containing 0.03 wppm dissolved O_2.[3]

The corrosion data obtained in this third test for the V-15Cr-5Ti specimens are plotted in Fig. 9.1.2 along with similar data obtained from exposures to water containing 4 and 0.03 wppm dissolved O_2.[2,3] Again, no significant heat-to-heat variations were seen, and the data obtained in water with 0.19 wppm dissolved oxygen yielded the relationship

$$\text{V-15Cr-5Ti:}\quad W = 2.837 \times 10^{-3}\, t^{0.6700}.$$

As can be seen in Fig. 9.1.2, the corrosion rates at the three oxygen levels show much less variation for this alloy than for the V-20Ti and VANSTAR-7 specimens described above. In addition, the highest corrosion rate was observed at the lowest dissolved oxygen level and the lowest rate at the intermediate level. This again contrasts with the behavior of the other two alloys, for which the corrosion rates increased monotonically with increasing oxygen level.

Wastage rates can be calculated on a linearly extrapolated basis from the observed 2000-h weight loss data of Table 9.1.1 assuming uniform corrosion and an approximate density of 6.16 g/cm^3 for each of the three alloys. These calculated wastage rates are about 0.003 mm/yr for V-15Cr-5Ti and about 0.14 mm/yr for the V-20Ti and VANSTAR-7 alloys. A maximum corrosion wastage rate of 0.005 to 0.020 mm/yr has been suggested for the fusion reactor first wall.[4] By way of comparison, the reported weight loss for Type 304 stainless steel under similar conditions is about 0.144 mg/cm^2 in 12 months, which translates to a wastage rate of about 0.0002 mm/yr.[5]

The nature of the oxide films formed on the surfaces of the exposed specimens was in general agreement with the observed corrosion behavior and with observations from the previous two tests. The V-15Cr-5Ti specimens, which showed the lowest corrosion rates and had decreasing corrosion rates with time, were covered by a thin, adherent, and apparently protective oxide. In contrast, the V-20Ti and VANSTAR-7 specimens, which had substantially higher weight losses and showed no tendency toward decreasing corrosion rate with time, were covered with heavier nonadherent oxide flakes or powder that appeared to offer little or no protection to the underlying metal.

The observation that the corrosion rate is lower for V-15Cr-5Ti in water with an intermediate dissolved oxygen content of 0.19 wppn than in solutions with either higher (4 wppm) or lower (0.03 wppm) oxygen content merits further comment. A qualitatively similar behavior is reported for carbon steels exposed to water containing various levels of dissolved oxygen in the temperature range from 200 to 300°C (392 to 572°F).[6] In this latter case, minimum corrosion rates are observed for dissolved oxygen levels in the range from about 0.1 to 10 wppm. Corrosion rates are found to increase by more than a factor of 10 when the oxygen concentration is varied by one order of magnitude in either direction from this range. This behavior is presumably associated with the formation of a stable protective oxide surface film for oxygen levels within the prescribed range. The available oxygen is apparently too low to form the film at lower levels, and the protection provided by the film is overwhelmed at higher levels. A similar effect appears to take place for the V-15Cr-5Ti alloy, although the range of optimum dissolved oxygen levels cannot be well defined on the basis of the present limited data. However, the 0.19 wppn dissolved oxygen level found to give the lowest corrosion rate for V-15Cr-5Ti is typical of that found in conventional boiling-water reactor coolant water as a consequence of radiolysis reactions as the water flows through the core.

9.1.4.2 Impurity Segregation in Vanadium-base Alloys

Previous reports[2,3] described results obtained in a series of scanning Auger microprobe (SAM) examinations of selected vanadium-alloy specimens fractured in situ at liquid nitrogen temperature after various thermomechanical treatments. Specimens from three heats of V-15Cr-5Ti, two heats of V-20Ti, and one heat of VANSTAR-7 were analyzed for the presence of segregated impurities on the fracture surfaces. Significant S segregation was observed on the intergranular fracture surface of an unirradiated V-15Cr-5Ti archival specimen (heat HSV-307, R1301) from the ORR-MFE-2 experiment. Less significant S, P, Si, and Cl segregation was sometimes observed on the intergranular fracture surfaces of other specimens examined. However, no clear correlation could be made between S and other impurity element segregation and such variables as alloy composition, thermomechanical condition, ductility, and bulk S content.

During the present reporting period, three untested tensile specimens of V-15Cr-5Ti were received for analysis from Oak Ridge National Laboratory (ORNL) as follows: (1) Specimen RA-143, which had been irradiated at 420°C to 6 dpa in FFTF, (2) Specimen RA-50, which was not irradiated but contained 300 appm ^3He implanted by the tritium trick, and (3) an unnumbered control specimen annealed at 1200°C. The specimens were received in the form of SS-3 type miniature sheet tensile specimens with an overall length of 31.75 mm (1.25 in.), a thickness of 0.25 mm (0.010 in.), and a gauge length of 12.7 mm (0.5 in.). It was conjectured that the brittle behavior of this alloy observed by ORNL after neutron irradiation or ^3He implantation might be related to impurity segregation to grain boundaries or other preferred fracture paths. The specimens were fractured in situ in the ANL "hot" SAM facility, and the fracture surfaces were analyzed for the possible presence of S, P, or other segregated impurities.

Specimen **RA-143**

The neutron-irradiated specimen **RA-143** was found to be extremely brittle, as was expected from previous testing conducted at ORNL. In fact, the specimen was inadvertently fractured outside the SAM during loading from the glovebox. Because the freshly fractured surface was exposed to the nitrogen environment of the glovebox, one would expect some possible contamination by N, as well as by O and C impurities present. However, contamination by S, P, and similar impurity elements of interest in this study would not be expected.

The fractured specimen was loaded into the SAM and examined, and the transgranular cleavage fracture surface present showed high levels of contamination by O and C at all three locations examined. This contamination apparently resulted from exposure of the fracture surface to the glovebox atmosphere. However, no S or P was detected. An attempt was made to clean the surface by sputtering with Ar ions, and examinations were made during and after sputtering. A typical Auger electron spectrum obtained from a region of transgranular cleavage fracture after sputtering is shown in Fig. 9.1.3. A small peak due to Ar picked up from the sputtering operation is seen, and substantial C and O peaks are also present. These peaks appear to be the result of recontamination of the freshly sputtered surface, a commonly observed phenomenon. Neither C nor Ar was observed in a spectrum obtained from a different location analyzed while simultaneously sputtering (see Fig. 9.1.4), but the spectrum was otherwise similar to that seen in Fig. 9.1.3. Again, no S or P was seen.

Specimen RA-50

The ^{3}He-implanted specimen RA-50 was successfully loaded into the SAM and fractured in situ at liquid nitrogen temperature. However, in contrast to the brittle behavior expected, the specimen was found to be relatively ductile. In fact, the first attempt to fracture the specimen using the pendulum arrangement in the SAM merely bent it, and it was necessary to remove and notch the specimen before it could be successfully fractured on the second try. The resulting fracture surface displayed predominantly transgranular cleavage and intergranular fracture regions, along with occasional areas of ductile dimpling.

Both intergranular and transgranular fracture regions were analyzed. Noticeable levels of S and P were detected at several intergranular regions; the spectrum obtained from the area having the largest observed concentrations is shown in Fig. 9.1.5. The irregular fracture surfaces and the lack of suitable calibration standards make quantitative analyses very difficult for these specimens. However, one might estimate the S and P levels indicated in the spectrum of Fig. 9.1.5 to be of the order of 1 wt % or so. A small C peak is also seen in Fig. 9.1.5, but this is probably due to normal contamination occurring during examination. Sulfur was detected at one transgranular fracture region (Fig. 9.1.6) and traces of C were occasionally seen in the transgranular spectra, but no P was found.

9.1.4.6 Control Specimen

The annealed control specimen was notched and successfully fractured in situ at liquid nitrogen temperature. The resulting fracture surface was largely transgranular cleavage, but occasional regions of intergranular fracture were noted. Three transgranular regions were analyzed, and no S or P was detected at any of them. Normal C contamination that increased with observation time was generally observed. Of the four intergranular areas analyzed, three showed small but detectable levels of S and P; a typical spectrum is shown in Fig. 9.1.7. The large peak at -50 eV in this spectrum is an anomaly caused by charging effects at the specimen surface. Significant C and O peaks associated with the buildup of contamination during examination were also generally seen in these intergranular regions.

9.1.4.7 Summary

The significant results and conclusions resulting from the analyses of the three V-15Cr-5Ti specimens may be summarized as follows:

1. The neutron-irradiated specimen **RA-143** was not embrittled due to impurity segregation to the fracture surface. This specimen failed almost entirely by transgranular cleavage, and no segregation to this transgranular surface was detected.

2. The ^{3}He-implanted specimen **RA-50** showed significant regions of intergranular fracture, and S and P were detected at several of these regions. However, the specimen was unexpectedly ductile in character, and so this impurity segregation did not appear to produce an embrittling effect.

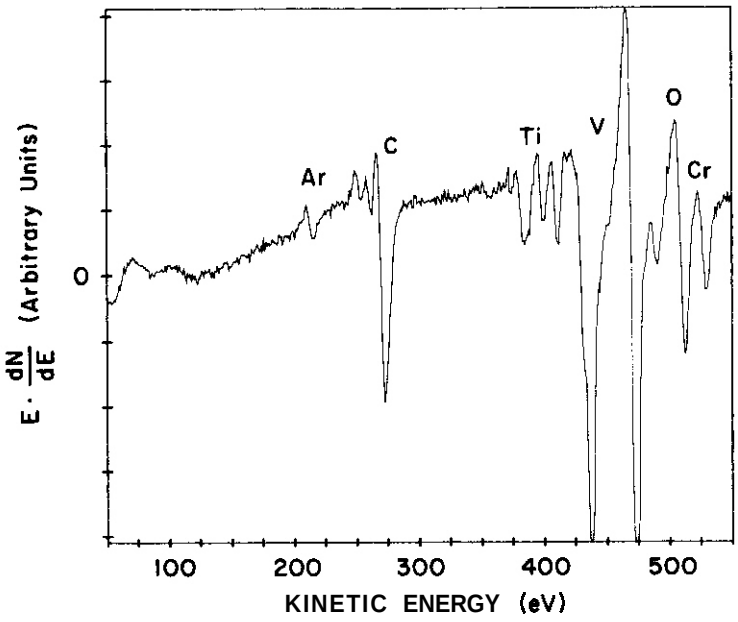

Fig. 9.1.3. Auger electron spectrum obtained from region of transgranular cleavage on fracture surface of neutron-irradiated specimen after sputtering.

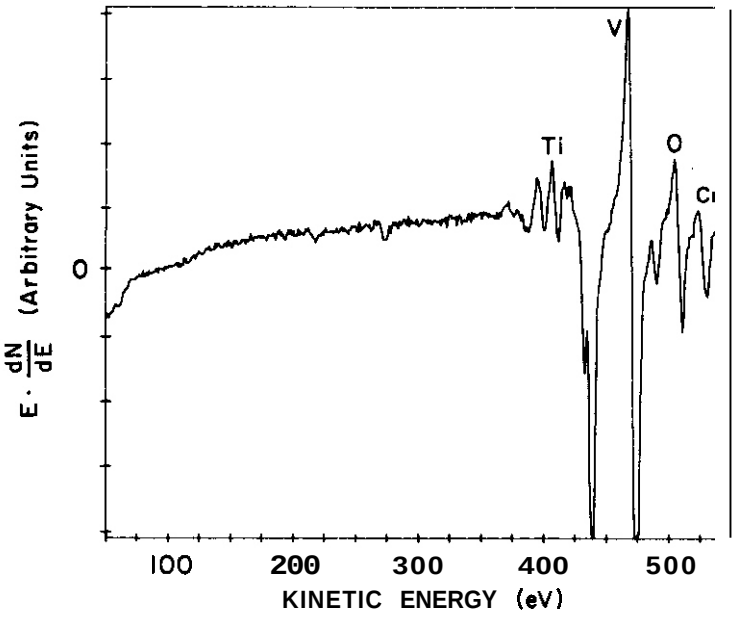

Fig. 9.1.4. Auger electron spectrum obtained from second transgranular cleavage region on fracture surface of neutron-irradiated specimen while simultaneously sputtering.

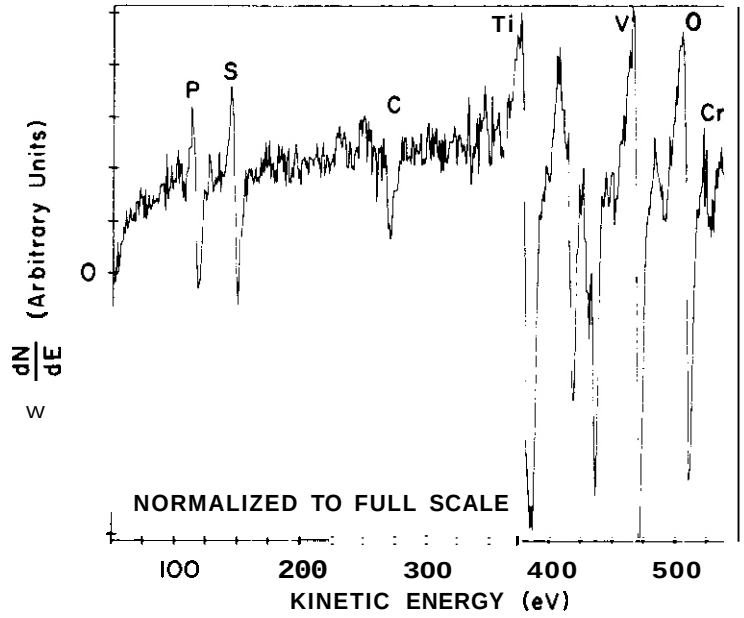

Fig. 9.1.5. Auger electron spectrum obtained from intergranular fracture region of ^3He-implanted specimen showing prominent S and P peaks.

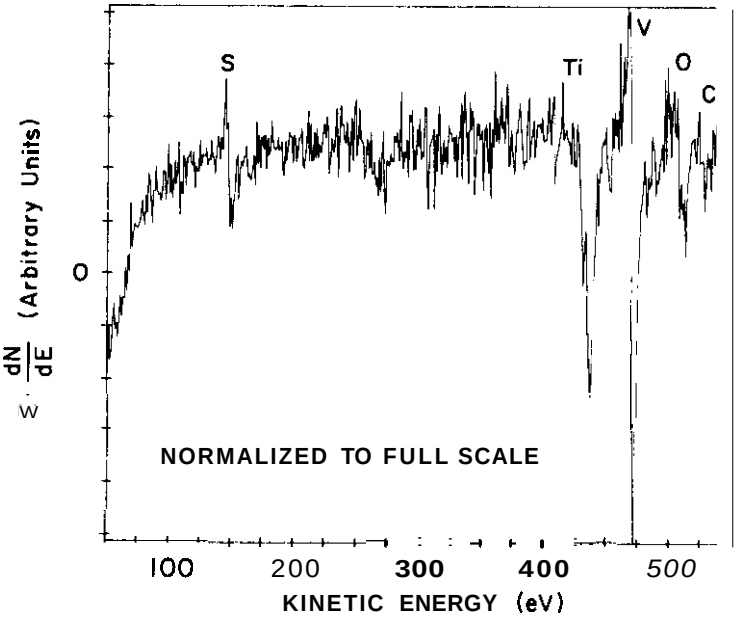

Fig. 9.1.6. Auger electron spectrum obtained from transgranular fracture region of ^3He-implanted specimen showing S peak.

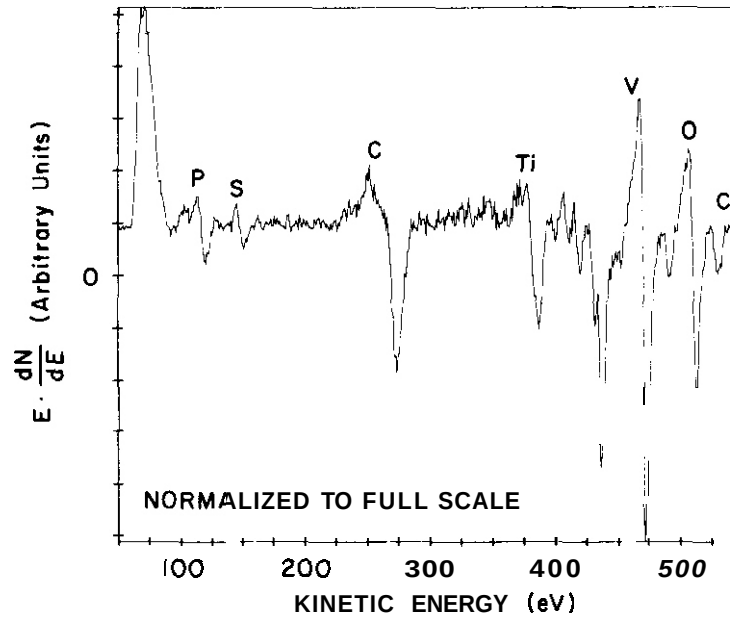

Fig. 9.1.7. Auger electron spectrum obtained from intergranular fracture region of annealed control specimen.

3. The annealed control specimen displayed a more or less brittle fracture with some intergranular regions, and S and P were found on most of the intergranular regions analyzed. However, the fracture mode was predominantly transgranular cleavage, where impurity segregation effects again appeared to play no role.

4. Overall, it appears that where the three specimens fractured intergranularly, impurity segregation was usually revealed. With one exception, however, no S or P was detected on any of the transgranular surfaces examined. This is in general agreement with previous ANL observations on other V-15Cr-5Ti fracture specimens. In the case of these three specimens, impurity segregation did not appear to significantly influence fracture behavior.

9.1.5 Conclusions

Exposures of V-15Cr-5Ti, V-20Ti, and VANSTAR-7 specimens for 2000 h to pressurized flowing water containing 0.19 wppn dissolved oxygen at 288°C have been completed. This completes an initial series of exposures at three different dissolved oxygen levels. The V-15Cr-5Ti specimens showed decreasing corrosion rates with time and had the lowest weight losses of the alloys tested. The V-20Ti and VANSTAR-7 specimens showed approximately linear corrosion rates and had weight losses greater by about a factor of 40 after 2000 h as compared with the V-15Cr-5Ti specimens. The V-15Cr-5Ti specimens formed a thin, adherent corrosion product, while that on the other two alloys was substantially thicker and less adherent. In evaluating the results obtained at all three dissolved oxygen levels, it is observed that the corrosion rates for the V-20Ti and VANSTAR-7 specimens increase monotonically with increasing level of dissolved oxygen. On the other hand, the observed corrosion rate for the V-15Cr-5Ti specimens was lower in water containing 0.19 wppm oxygen than in water containing either 0.03 or 8 wppm oxygen. This behavior is qualitatively similar to that observed by others for carbon steels under similar conditions, and appears to be associated with the formation of a stable, protective surface oxide under the appropriate conditions.

Three untested tensile specimens of V-15Cr-5Ti received fran ORNL were fractured in situ in the ANL "hot" SAM facility, and their fracture surfaces were analyzed for the possible presence of segregated impurities. The first specimen, which had been irradiated at 420°C to 6 dpa in FFTF, failed almost entirely by transgranular cleavage, and no segregation to this transgranular fracture surface was seen. The second specimen, which had been implanted with 300 appm ^3He by the tritium trick, showed significant regions of intergranular fracture, and S and P impurities were detected at several locations. However, no embrittling effect seemed to be associated with this segregation. A third annealed control specimen fractured primarily by transgranular cleavage, where impurity segregation appeared to play no role. Where the specimen fractured intergranularly, S and P were generally detected. Overall, impurity segregation did not appear to significantly influence the fracture behavior of these three specimens.

9.1.6 References

1. D. R. Diercks and D. L. Smith, "Environmental Effects on the Properties of Vanadium-base Alloys," pp. 75-19 in Alloy Development for Irradiation Perfonnance: Semiannual Progress Report for Period Ending March 31, 1984, DOE/ER-0045/12, Oak Ridge National Laboratory, Oak Ridge, TN, July 1984.

2. D. R. Diercks and D. L. Smith, "Environmental Effects on the Properties of Vanadium-base Alloys," pp. 209-213 in Alloy Developent for Irradiation Performance: Semiannual' Progress Report for Period Ending September 30, 1984, DOE/ER-0045/13, Oak Ridge National Laboratory, Oak Ridge, TN, March 1985.

3. D. R. Diercks and D. L. Smith, "Environmental Effects on the Properties of Vanadium-base Alloys," pp. 177-181 in Alloy Development for Irradiation Performance: Semiannual Progress Report for Period Ending March 31, 1985, DOE/ER-0045/14, Oak Ridge National Laboratory, Oak Ridge, TN, July 1985.

4. Blanket Comparison and Selection Study Final Report, ANL/FPP-84-1, Vol. 2, Argonne National Laboratory, Argonne, IL, pp. 6.2-17 and 6.2-18.

5. B. M. Gordon, M. E. Indig, R. B. Davis, A. E. Pickett, and C. W. Jewett, "Environmentally Assisted Cracking Resistance of BWR Structural Materials in Hydrogen-water Chemistry," presented at the 2nd International Symposium on Environmental Degradation of Materials in Nuclear Power System Water Reactors, Monterey, CA, September 9-12, 1985.

6. J. E. LeSurf, "The Water Chemistry of CANDU Reactors," pp. 177-186 in Proceedings of the International Conference on Water Chemistry of Nuclear Reactor Systems, Bournemouth, U. K., October 24-27, 1977, British Nuclear Energy Society, London, 1978.

9.2 ENVIRONMENTAL EFFECTS ON PROPERTIES OF STRUCTURAL ALLOYS IN FLOWING Pb-17Li -- O. K. Chopra and O. L. Smith (Argonne National Laboratory)

9.2.1 ADIP Task

ADIP Task I.A.3, Perform Chemical and Metallurgical Compatibility Analyses

9.2.2 Objective

The objective of this program is to investigate the influence of a flowing Pb-17 at. % Li environment on the corrosion behavior and mechanical properties of structural alloys under conditions of interest for fusion reactors. Corrosion behavior is evaluated by measuring the weight change and depth of internal corrosive penetration of alloy specimens exposed to flowing Pb-17Li for various times. The dissolution rates are determined as a function of temperature. Metallographic examination of the alloy surface is used to establish the mechanism and rate-controlling process for the corrosion reactions. Initial effort on mechanical properties is focused on tensile tests in a flowing Pb-17Li environment.

9.2.3 Summary

Corrosion data are presented for ferritic HT-9 and Fe-9Cr-1Mo steel and austenitic Type 316 stainless steel in flowing Pb-17Li at 465 and 482°C. The influence of temperature on the dissolution rate of the alloys is discussed. Tensile properties of HT-9 alloy in a flowing Pb-17Li environment are also reported.

9.2.4 Progress and Status

The effects of a flowing Pb-17Li environment on the corrosion behavior and mechanical properties of austenitic and ferritic steels are being investigated.[1-4] Tests are conducted under forced circulation of a Pb-17 at. % Li alloy in a loop consisting of a high-temperature test vessel with a heat exchanger section and a cold-temperature chamber. The total volume of the loop is ~2 L. Several analyses of the eutectic alloy show that the concentrations of O, H, and N are 260, 22, and <10 wppm, respectively.

Flat corrosion coupons, ~73 x 10 x 0.26 mm in size, of HT-9 alloy, Fe-9Cr-1Mo, and Type 316 stainless steel were exposed to flowing Pb-17Li, and the corrosion behavior was evaluated by measurements of weight loss and depth of internal corrosive penetration. Three corrosion test runs have been completed at maximum temperatures of 427, 454, and 482°C, respectively. For each test run, specimens were exposed at the maximum temperature position as well as at a downstream location. The temperature of the latter position was 15 to 25°C lower than the maximum temperature. The cold-leg temperature was maintained at 300°C and the Pb-17Li alloy was circulated at a rate of ~350 cm^3/min. The specimens were periodically removed from the loop for weight change measurements.

Constant extension rate tests (CERT) were conducted on normalized and tempered HT-9 specimens in a flowing Pb-17Li environment to investigate the possible embrittlement of the material. Cylindrical specimens, 2.54 mm in diameter and 10.2 mm in gauge length (ASTM Standard E8), were tested at temperatures between 270 and 450°C and strain rates of $5 \times 10^{-}$, 1×10^{-3}, and 1×10^{-2} s^{-1}.

9.2.4.1 Corrosion Behavior

The corrosion data for ferritic and austenitic steels in flowing Pb-17Li at 413, 427, and 454°C have been reported previously.[4] The results indicate that the weight losses for HT-9 and Fe-9Cr-1Mo ferritic steels increase linearly with time, whereas the annealed or 20% cold-worked (CW) Type 316 stainless steels achieve a steady-state dissolution behavior after an initial period of ~500 h characterized by very high dissolution rates. The weight losses for austenitic steels are an order of magnitude higher than for the ferritic steels. The large weight losses during the initial transient period are associated with the fotmation of a ferritic surface layer on the austenitic stainless steels.

The weight losses of ferritic HT-9 and Fe-9Cr-1Mo steel and the austenitic Type 316 stainless steel in flowing Pb-17Li at 465 and 482°C are shown in Fig. 9.2.1. The results are similar to those obtained previously at 427°C. The dissolution rates for ferritic steels are more than a magnitude lower than for Type 316 stainless steel. At both temperatures, the dissolution rate and weight loss for Fe-9Cr-1Mo steel are lower than for HT-9 alloy. However, both ferritic steels show significant weight losses after the initial 500-h exposure. Large initial weight losses were not observed for the ferritic steels in previous tests at a lower temperature.

The steady-state dissolution rates for HT-9, Fe-9Cr-1Mo, and annealed and 20% CW Type 316 stainless steel in flowing Pb-17Li are given in Table 9.2.1. The Arrhenius plots of the data are shown in Fig. 9.2.2. The slashed symbols represent the specimens that were located downstream from the maximum loop temperature position. The lines represent the best fit for the dissolution rates of HT-9 alloy and Type 316 stainless

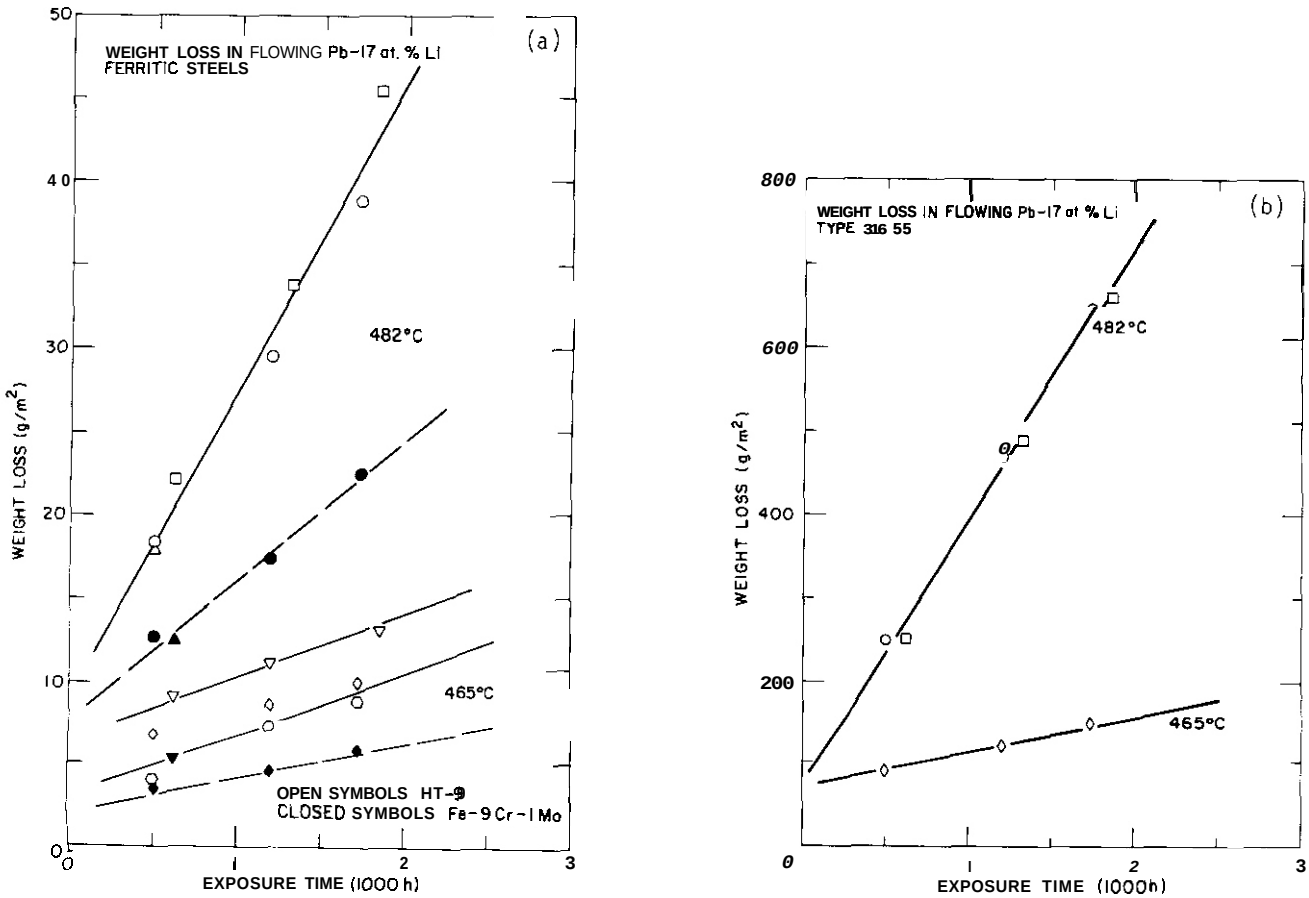

Fig. 9.2.1. Weight loss versus exposure time for (a) HT-9 and Fe-9Cr-1Mo ferritic steels and (b) Type 316 stainless steel exposed to flowing Pb-17Li at 482 and 465°C.

Table 9.2.1. Dissolution rates for ferritic and austenitic steels exposed to flowing Pb-17Li

Run Number	Temp. (°C)	Maximum Time (h)	Dissolution Rate (mg/m^2·h)			
			HT-9	9Cr-1Mo	316 SS	316 CW
1	454	3663	9.0	8.2	50.1	75.9
1	427[a]	3663	5.1	4.9	26.1	27.4
2	427	3808	7.4		55.1	58.6
2	413[a]	3808	2.6		23.9	31.1
3	482	1849	18.3	8.3	325.1	
3	465[a]	1849	3.8	1.9	45.0	

[a]Specimens were located downstream from the maximum loop temperature position.

steel (both annealed and 20% CW) obtained at the maximum loop temperature positions. For each test run, the specimens located at the lower temperature may be influenced by downstream effects; consequently, the data for these specimens (slashed symbols) were excluded from the analysis. The results yield activation energies of 17.2 and 28.6 kcal/mole for HT-9 alloy and Type 316 stainless steel, respectively. The activation energy for HT-9 alloy is comparable to the value of 16.3 kcal/mole obtained for ferritic steels in flowing lithium. However, the dissolution rates for the HT-9 alloy in Pb-17Li are more than an order of magnitude greater than in flowing lithium. Dissolution rate data obtained from other investigations[5-7] are also plotted in Fig. 9.2.3 and show good agreement with the results from the present study.

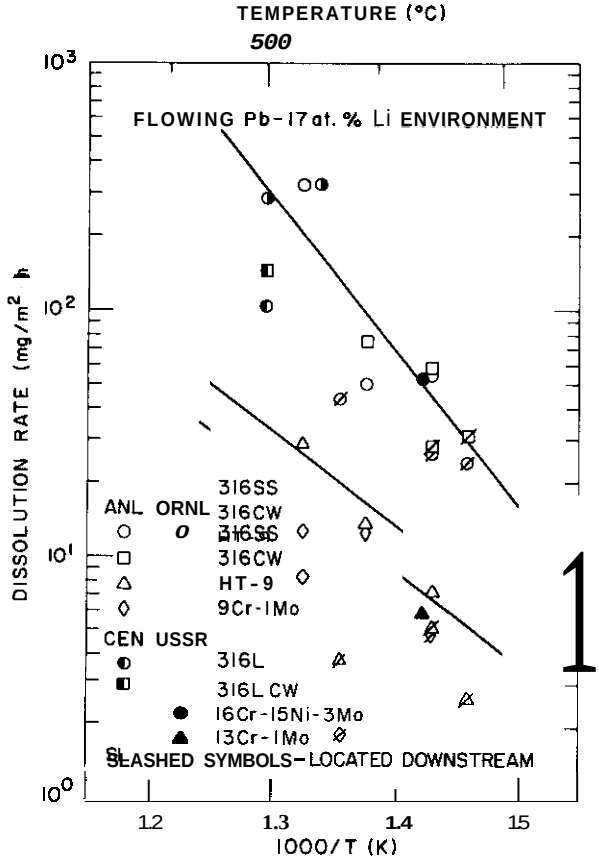

Fig. 9.2.2. Arrhenius plots of dissolution rate data for ferritic and austenitic steels exposed to flowing Pb-17Li.

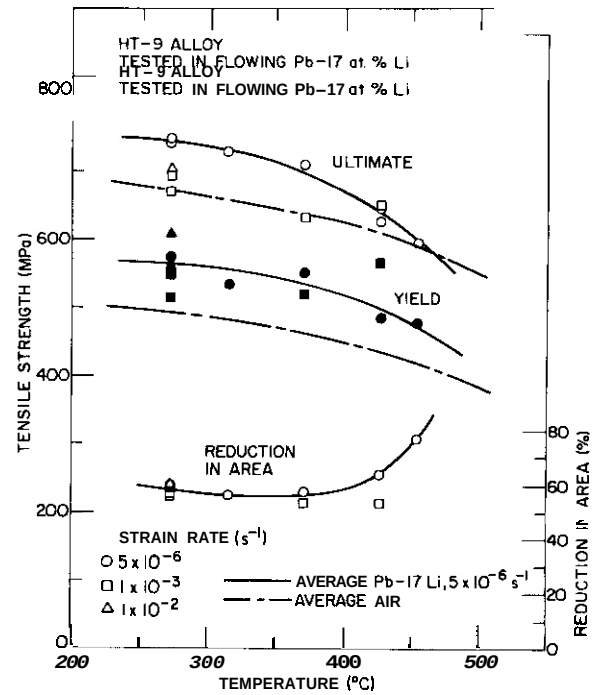

Fig. 9.2.3. Tensile properties of HT-9 specimens from constant extension rate tests in a flowing Pb-17Li environment at temperatures between 273 and 454°C.

9.2.4.2 Tensile Properties

Tensile properties of normalized and tempered HT-9 alloy at temperatures between 273 and 454°C and different initial strain rates in a flowing Pb-17Li environment are shown in Fig. 9.2.3. Prior to testing, all specimens were exposed for ~18 h to flowing Pb-17Li at 427°C to achieve complete wetting of the specimen surface. The results indicate that a Pb-17Li environment has no effect on the tensile properties of the HT-9 alloy at strain rates of $>5 \times 10^{-6}$ s^{-1}. The ultimate and yield strengths in Pb-17Li are comparable to the average values obtained in an air environment. An increase in initial strain rate decreases the ultimate strength at temperatures of <400°C whereas the yield strength and reduction in area are not significantly affected. At all temperatures and strain rates, the reductions in area are >50%. Tensile tests are in progress on HT-9 weldments and normalized and quenched HT-9 specimens to investigate the possible embrittlement of weld structures in a Pb-17Li environment.

9.2.5 Conclusions

Corrosion data in flowing Pb-17Li indicate that the dissolution rates for ferritic steels are an order of magnitude lower than those for austenitic steels. However, the rates in Pb-17Li are more than an order of magnitude higher than those in a flowing lithium environment. Arrhenius plots of the dissolution rate data yield activation energies of 17.2 and 28.6 kcal/mole for HT-9 alloy and Type 316 stainless steel. Data also indicate that downstream effects may also influence the dissolution behavior of alloys in a flowing Pb-17Li environment. Tensile data show that a flowing Pb-17Li environment has no effect on the tensile properties of normalized and tempered Hi-9 alloy.

9.2.6 References

1. O. K. Chopra and D. L. Smith. "Environmental Effects on Properties of Structural Alloys," pp. 216-200 in Alloy Development for irradiation Performance: Semiannual Progress Report for Period Ending September 30, 1983, DOE/ER-0045/11, Oak Ridge National Laboratory, Oak Ridge, TN, March 1984.

2. O. K. Chopra and D. L. Smith, "Corrosion of Ferrous Alloys in Eutectic Lead-Lithium Environment," J. Nucl. Mater. 122-123, 1219-1224 (1984).

3. O. K. Chopra and D. L. Smith. "Corrosion of Structural Alloys in Flowing Pb-17Li Environment," pp. 183-189 in Alloy Development for irradiation Performance: Semiannual Progress Report for Period Ending March 31, 1984, DOE/ER-0045/12, Oak Ridge National Laboratory, Oak Ridge, TN, July 1984.

4. O. K. Chopra and D. L. Smith, "Environmental Effects on Properties of Structural Alloys in Flowing Lithium," pp. 192-196 in Alloy Developnent for Irradiation Performance: Semiannual Progress Report for Period Ending March 31. 1985, DOE/ER-0045/14, Oak Ridge National Laboratory, Oak Ridge TN, July 1985.

5. P. [redacted] Tortorelli and J. H. DeVan, "Corrosion-of Type 316 Stainless Steel and 12Cr-1MoVW in Thermally Convective 19-17 at. % Li," pp. 205-207 in Alloy Development for Irradiation Performance: Semiannual Progress Report for Period Ending March 31, 1985, DOE/ER-0045/14, Oak Ridge National Laboratory, Oak Ridge, TN, Julv 1985.

6. P. Fauvet, J. Sannier, and G. Santarini, "Corrosion of 316L Stainless Steel in Flowing 17Li83Pb Alloy," 13th Symposium on Fusion Technology, Varese, Italy, September 1984.

7. V. [redacted] Nikitin et al., "Experimental Study of Selected Structural Materials Corrosion Resistivity in Pb-Li Eutectic," USSR Contribution to Phase IIA of the INTOR Workshop, October 1982.

9.3 CORROSION OF AUSTENITIC AND FERRITIC STEELS IN FLOWING LITHIUM ENVIRONMENT -- O. K. Chopra and D. L. Smith (Argonne National Laboratory)

9.3.1 ADIP Task

ADIP Task I.A.3, Perform Chemical and Metallurgical Compatibility Analyses.

9.3.2 Objective

The objective of this program is to investigate the influence of a flowing lithium environment on the corrosion behavior and mechanical properties of structural alloys under conditions of interest for fusion reactors. Corrosion rates are determined by measuring the weight change and depth of internal corrosive penetration as a function of time and temperature. These measurements, coupled with metallographic evaluation of the alloy surface, are used to establish the mechanism and rate-controlling process for the corrosion reactions. Initial effort on mechanical properties is focused on fatigue and tensile tests in a flowing lithium environment of controlled purity.

9.3.3 Summary

Corrosion data are presented for ferritic and austenitic steels in flowing lithium at 538°C. The lithium-exposed specimens were examined metallographically to evaluate the microstructural and compositional changes of the alloy surfaces. The influence of temperature on the dissolution behavior of the alloys is discussed.

9.3.4 Progress and Status

The corrosion behavior of several ferritic and austenitic steels is being investigated in a flowing lithium environment. The corrosion tests are conducted in a forced-circulation lithium loop consisting of three test vessels and a secondary cold-trap purification loop. A detailed description of the loop and the test procedure have been presented earlier.[1,2] The temperature and time of exposure and the loop operating conditions for the various corrosion tests are given in Table 9.3.1. Lithium was circulated at ~1 L/min in the primary loop, and the concentrations of C and H in lithium were ~10 and 120 wppm, respectively.

The corrosion data for HT-9 alloy, Fe-9Cr-1Mo, and Type 316 stainless steel in flowing lithium at 482, 427, and 372°C have been reported earlier.[2] The results indicate that the weight losses for ferritic steels follow a linear law with time and yield a constant dissolution rate after a relatively large weight loss during the initial ~500 h of exposure to lithium. The transient weight loss results from an "etching effect" of lithium and the specimen surfaces develop a dimpled appearance. The dissolution rates for ferritic steels decrease with a decrease in temperature. The austenitic Type 316 stainless steel shows a complex dissolution behavior in flowing lithium. The dissolution rates reach a steady state after a transient period of ~1500 h characterized by rapid dissolution. However, the steady-state dissolution rates are insensitive to changes in exposure temperature. The total weight loss of austenitic stainless steels in lithium is more than an order of magnitude greater than for the ferritic steels. During the current reporting period, corrosion tests were completed in flowing lithium at 538 and 482°C to evaluate the dissolution behavior of ferritic and austenitic steels at higher temperatures.

9.3.4.1 Corrosion Behavior of Ferritic Steels

The weight losses of HT-9 and Fe-9Cr-1Mo steel in lithium at 538°C (Run 6) are shown in Fig. 9.3.1. The results are similar to those observed earlier at lower temperatures, viz., the weight losses for both steels increase linearly with time after a relatively large initial weight loss. The dissolution rates for HT-9 and Fe-9Cr-1Mo steels at 538°C are higher than those observed at 482°C.

The corrosion specimens exposed at 482°C in the specimen exposure vessel (i.e., a location downstream from the specimens exposed at 538°C) showed very small weight loss. A total of eight different specimens of HT-9 and Fe-9Cr-1Mo steels exposed for 1500 to 2500 h in lithium at 482°C showed weight losses between 0.2 and 0.4 g/m^2 (i.e., actual weight loss of 0.1 to 0.2 mg). For these specimens, most of the weight loss occurred during the initial 500 h and the specimens showed little or no weight loss for longer exposures. Effects of specimen location were not observed during the earlier corrosion test runs. For example, specimens exposed at 427°C during Runs 4 and 5 showed identical dissolution behavior although the location of the specimens was different, i.e., specimens were placed at the maximum loop temperature in Run 5 while the specimens in Run 4 were located downstream in the specimen exposure vessel.

The surfaces of the corrosion specimens reflect the observed differences in the dissolution behavior at 538 and 482°C. Micrographs of the surface of HT-9 specimens exposed to lithium at 538 and 482°C during Run 6 are shown in Fig. 9.3.2. The specimen exposed at 538°C developed a pebbled or dimpled appearance similar to that observed earlier for specimens exposed to lithium at lower temperatures. Figure 9.3.3 shows

Table 9.3.1. Lithium loop operating conditions for various corrosion tests

Test Run	Loop Temperature (°C) Test Vessel	Spec. Exp. Vessel[a]	Supply Vessel	Cold Trap	N Content in Lithium (wppm)	Exposure Time (h) Test Vessel	Spec. Exp. Vessel
1	482	482	432	212	<50	1295	5000
2	4821427[b]	482	407	230[c]	~250	-	1997
3	427	482	407	230	~100	1100	-
4	482	427	410	212	<100	5521	6501
5	427	372	372	206	~100	5023	4955
6	538	482			~50	3655	3330

[a] Lithium flow was from test vessel to specimen exposure vessel.
[b] Test vessel temperature changed from 482 to 427°C after 1540 h.
[c] No flow occurred through cold trap after 890 h due to plugging. Plugged sections were replaced and flow started after an additional 480 h.

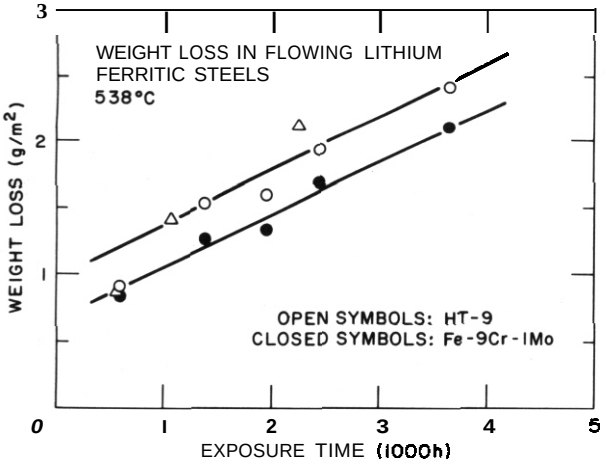

Fig. 9.3.1. Weight loss versus exposure time for HT-9 and Fe-9Cr-1Mo ferritic steel exposed to flowing lithim at 538°C, Run 6.

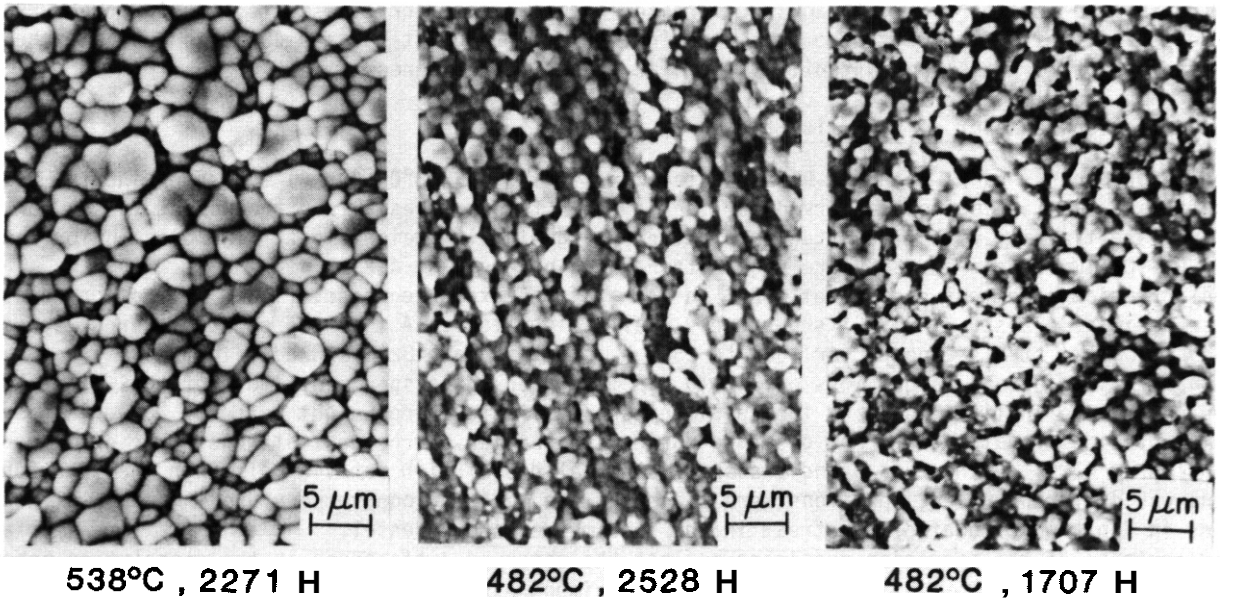

Fig. 9.3.2. Micrographs of HT-9 alloy surface exposed to flowing lithim at 538 and 482°C, Run 6.

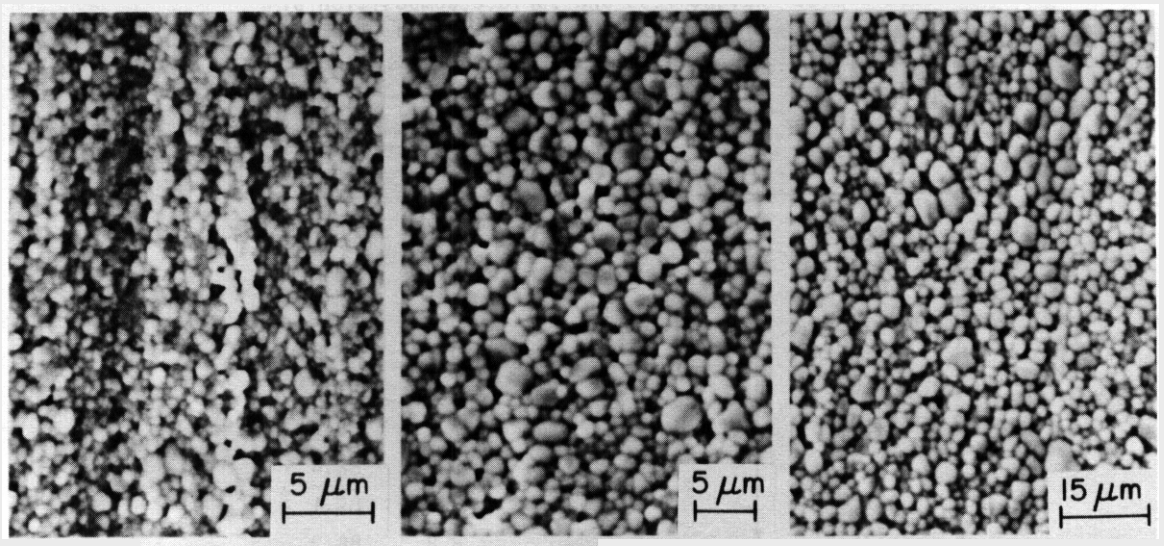

Fig. 9.3.3. Micrographs of HT-9 alloy surface exposed to flowing lithim for ~5000 h at 372, 427, and 482°C.

the micrographs of HT-9 alloy surface exposed to lithium for ~5000 h at 372, 427, and 482°C. Such dimples form during the initial 2000 h of exposure and their size does not change with additional exposure. However, the size of the dimples decreases with a decrease in exposure temperature, e.g., the size varies from 2-6 μm at 538°C to 0.5-2 μm at 372°C. The large weight losses observed during the initial stages of exposure may be attributed to the formation of the dimpled surface appearance.

Specimens exposed at 482°C during Run 6 (see Fig. 9.3.2) show surface deposits (i.e., the white particles on the surface), and the dimpled structure is not fully developed. These features were observed on all the HT-9 and Fe-9Cr-1Mo specimens exposed at 482°C, Run 6. The presence of deposits and the absence of a dimpled structure may account for the relatively small weight losses observed for these specimens.

Formation of a dimpled structure is associated with depletion of chromium from HT-9 and Fe-9Cr-1Mo specimens. Specimens that do not develop a dimpled structure exhibit little or no depletion of chromium from the alloy surfaces. Energy dispersive x-ray analyses (EDAX) were performed to determine the differences in surface composition of HT-9 alloy specimens exposed to lithium at different temperatures. The weight loss and concentrations of major elements for the specimens are given in Table 9.3.2. The results indicate that the concentration of chromium in the alloy surface decreases from ~12% to between 6 to 8%; the values after exposure at 538°C are lower than those at 372°C. Specimens exposed for short times, e.g., 1295 h at 482°C or 1100 h at 427°C, show a chromium content of ~11%, indicating that steady-state conditions are not attained after short-term exposure at these temperatures. Also, these specimens do not develop a dimpled structure. A similar behavior is observed for the specimens exposed at 482°C during Run 6, i.e., the specimen surfaces do not show a dimpled structure and the concentration of chromiun is higher than that for specimens from Runs 1 or 4.

Such differences in the dissolution behavior cannot be rationalized at present. Several factors, such as downstream effects, variations in lithium purity, etc.. may influence the dissolution process. The concentration of nitrogen in lithium, during Run 6, was 50 wppm compared to ~100 wppm for Run 4. The presence of surface deposits suggests downstream effects. The EDAX data indicate that the surface deposits are primarily iron. Thus, the higher chromiun concentrations are not due to the surface deposits. Dissolutionldeposition data at different temperatures, loop AT, lithium purity, etc., are required to resolve these issues.

9.3.4.2 Corrosion Behavior of Austenitic Steels

The weight losses of annealed and 20% cold-worked (CW) Type 316 stainless steel in lithium at 538 and 482°C (Run 6) are shown in Fig. 9.3.4. The results indicate some differences from data for other test runs at 482 and 427°C. In earlier tests, the austenitic steels showed large weight losses, i.e., 15 to 30 g/m^2, during the initial ~1000-h exposure at 482 or 427°C, and attained a steady-state dissolution rate for longer exposure times. The initial weight losses for most of the specimens from Run 6 are <15 g/cm^2. For example, three of the four specimens of annealed Type 316 stainless steel exposed at 538°C show ~3 g/m^2 weight loss

Table 9.3.2. Weight loss and surface composition of HT-9 alloy exposed to flowing lithium

Test Run	Time (h)	Temp. (°C)	Weight Loss (g/m^2)	Surface Composition (%) Cr	te
-	Unexposed		-	12.0	85.6
6	2271	538	2.13	5.8	93.3
1	1295	482	0.30	10.8	86.8
1	3000		1.35	62	91.8
1	5000		0.82	6.6	91.3
2	1997		2.93	7.1	88.5
4	5521		1.83	5.9	88.4
6	1707		0.28	8.6	89.1
6	2528		0.0	8.8	88.2
3	1100	427	0.22	11.0	87.0
4	5739		1.17	8.1	87.1
4	5739		1.11	8.7	84.8
4	6501		0.85	7.3	90.7
5	5023		1.37	6.5	88.4
5	4955	372	0.58	8.3	89.7
5	4955	372	0.65	8.0	87.8

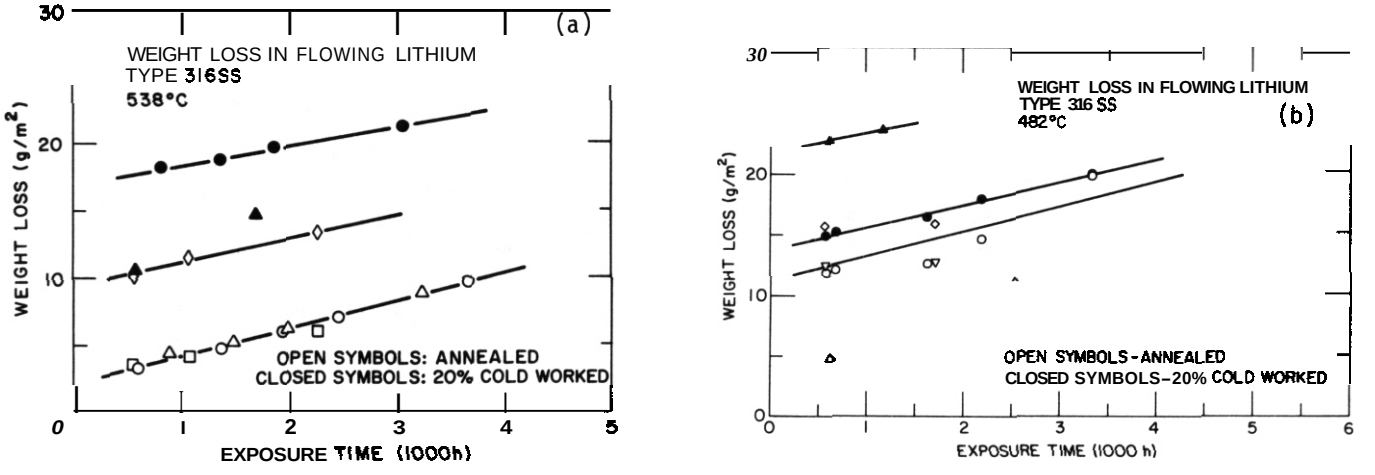

Fig. 9.3.4. Weight loss versus exposure time for annealed and 20% CW Type 316 stainless steel exposed to flowing lithim at (a) 538 and (b) 482°C.

after 500-h exposure (see Fig. 9.3.4a). The weight losses are larger, i.e., 15 to 20 g/m^2, for the 20% CW Type 316 stainless steel after similar exposure times. However, irrespective of the initial weight loss, the steady-state dissolution rates for all specimens are approximately the same, both at 538 and 482°C.

Micrographs of the surface of some of the specimens of annealed Type 316 stainless steel exposed to lithium at 538°C are shown in Fig. 9.3.5. The specimen with the largest weight loss (shown as diamond symbols in Fig. 9.3.4) developed a dimpled structure while the others, with smaller weight losses (shown as square and triangle symbols), exhibit a cellular structure. All specimens contain some surface cavities. A cellular structure is unusual for austenitic stainless steels exposed to lithium. Typical surface micrographs of annealed Type 316 stainless steel exposed to lithim at 372, 427, and 482°C for ~5000 h are shown in Fig. 9.3.6. A dimpled structure and surface cavities are observed at all temperatures. However, the size of the dimples is smaller at 372°C.

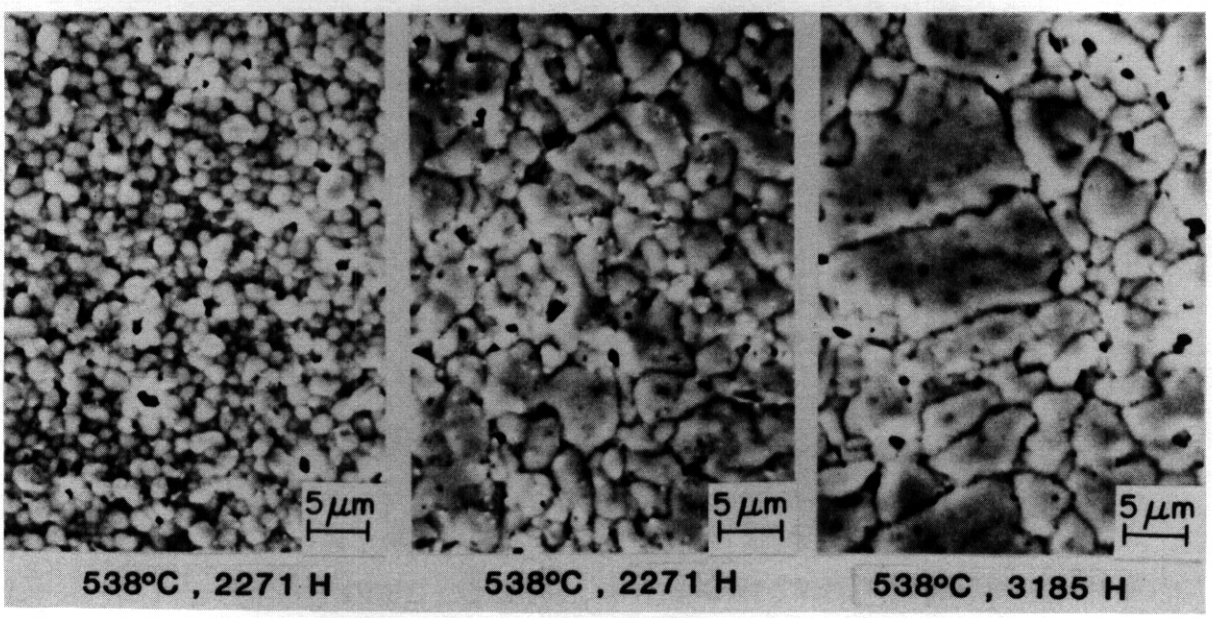

Fig. 9.3.5. Micrographs of the surface of annealed Type 316 stainless steel exposed to flowing lithium at 538°C, Run. 6.

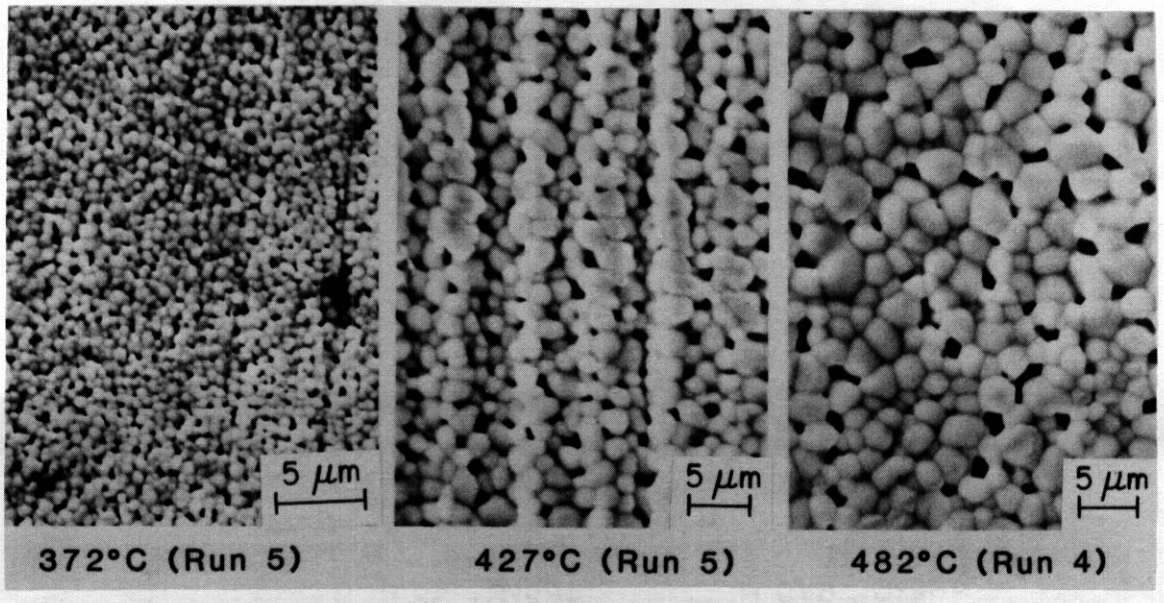

Fig. 9.3.6. Micrographs of the surface of annealed Type 316 stainless steel exposed to flowing lithium for ~5000 h at 372, 427, and 482°C.

Figure 9.3.7 shows surface micrographs of 20% CW Type 316 stainless steel exposed to lithium at 538 and 482°C (Run 6). The weight losses for these specimens were >15 g/m^2 and the specimens exhibit a dimpled structure. The specimens exposed at 482°C, however, contain surface deposits. Large surface deposits were also observed for annealed Type 316 stainless steel exposed at 482°C during Run 6 (see Fig. 9.3.8). For most specimens, the surface deposits were in the form of stringers parallel to the length of the specimens, while the deposits on some specimens had a distinct crystallographic orientation relative to the base metal.

The weight loss and concentration of major elements for Type 316 stainless steel exposed to lithium at different temperatures are given in Table 9.3.3. The results indicate that the depletion of nickel from the steel is quite rapid. The concentration of nickel decreases from 12.9 to <1% for specimens exposed for >2000 h at either 427 or 482°C. The nickel content is slightly higher, i.e., 1.5 to 2.5%, after exposure at 372°C and for some of the specimens exposed at 538°C. The latter exhibit a cellular surface structure. The depletion of chromium from the steel is slower and appears to depend on the nitrogen content in lithium.

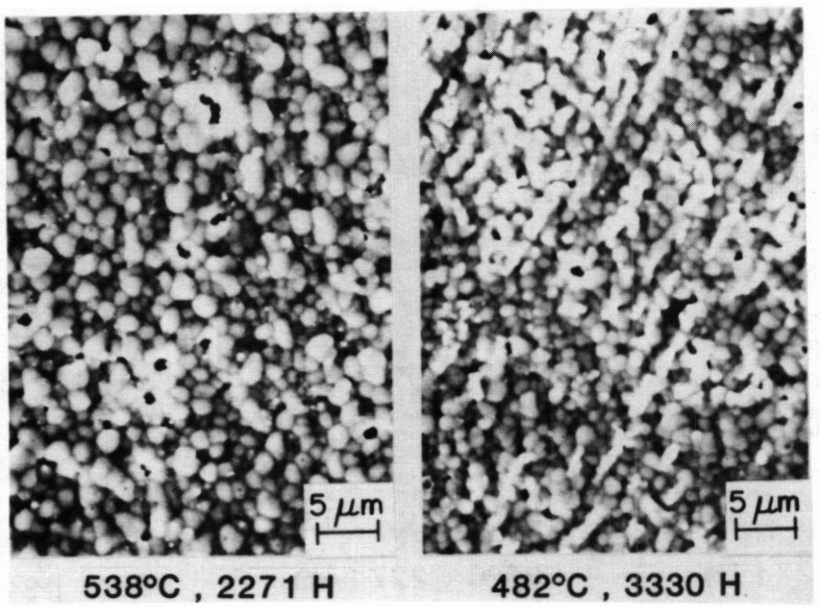

Fig. 9.3.7. Micrographs of the surface of 20% CW Type **316** stainless steel exposed to lithium at **538** and 482°C, Run **6.**

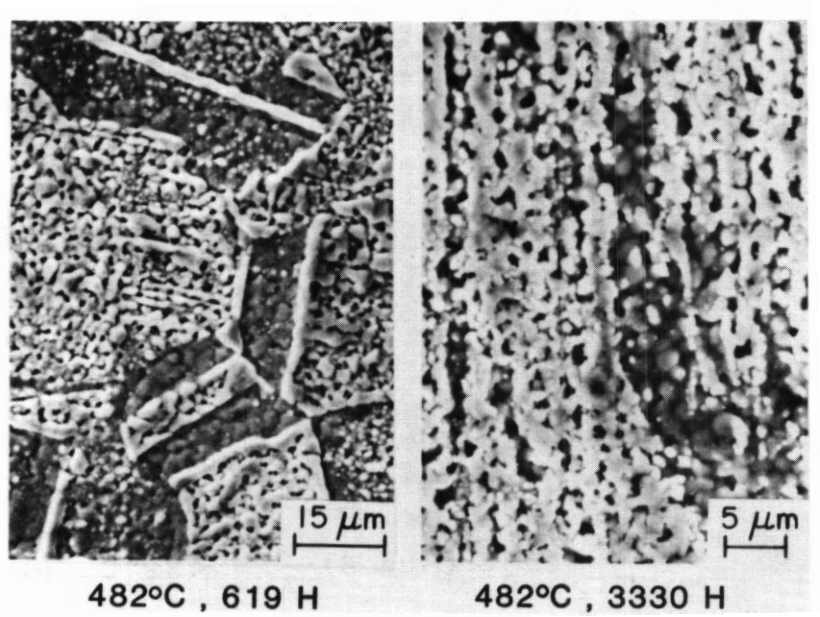

Fig. **9.3.8.** Micrographs of the surface of annealed Type **316** stainless steel exposed to flowing lithium at **482°C,** Run 6.

The chromium content decreases from **-18%** to between **8** and **10%** at all temperatures. However, specimens exposed at **482°C** to lithium containing **-250** wppn nitrogen (Run 2) show greater depletion of chromium than those exposed to lithium with <100 wppn nitrogen. In general, the specimens with greater depletion of chromium also show larger weight loss and internal penetration. The **EDAX** data indicate that the surface deposits observed on specimens exposed at **482°C** during Run **6** are rich in chromium. For these specimens, the concentration of chromium is >20%.

Table 9.3.3. Weight loss, depth of internal penetration, and surface compositions of Type 316 stainless steel exposed to flowing lithium

Test Run	Time (h)	Temp. (°C)	Weight Loss (g/m^2)	Penetration (μm)	Surface Composition (%) Cr	Fe	Ni
			Annealed Type 316 Stainless Steel				
-	Unexposed		-	-	17.5	64.9	12.9
6	2271	538	5.9	-	9.7	83.9	2.5
6	2271	↓	13.3	-	8.7	88.4	0.4
6	3185	↓	8.9	-	9.9	85.2	2.2
1	1295	482	6.7	13	12.2	81.6	1.2
2	1997	↓	21.0	25	6.2	90.9	1.1
4	5521	↓	31.8	37	9.7	84.0	0.7
6	619[b]	↓	4.8	-	22.0	68.7	2.3
6	619[a]	↓	4.8	-	15.4	73.4	6.0
6	1707[b]	↓	12.7	-	20.2	74.6	0.7
6	3330[b]	↓	19.8	-	20.1	73.0	0.8
3	1100[a]	427	17.2	21	18.7	77.1	1.8
4a	5739	↓	42.2	38	8.3	88.4	0.9
4b	5739	↓	41.5	37	8.1	86.6	0.8
5	5023	↓	57.2	31	8.0	90.6	0.6
5a	4955	372	14.1	9	10.6	86.0	1.4
5b	4955	372	12.9	13	9.7	87.3	1.5
			20% CW Type 316 Stainless Steel				
6	1701	538	14.7	-	8.6	88.5	0.3
1	1295	482	23.8	24	13.9	78.0	0.6
2	1997	↓	46.5	47	5.6	88.1	0.6
4	5521	↓	35.0	40	10.0	85.6	0.7
6	3330	↓	20.0	-	13.7	84.3	0.4
3	1100	427	24.9	25	14.3	82.6	1.3
4a	5739	↓	47.9	42	8.8	88.3	1.0
4b	5739	↓	51.6	40	8.6	86.8	0.9
4	6501	↓	52.9	46	7.3	87.9	0.8
5	5023	↓	46.0	38	8.5	89.4	0.6
5a	4955	372	16.3	14	-	-	-
5b	4955	372	15.5	13	10.2	86.5	1.4

[a] Large deposits of chromium observed on the specimen. The surface composition represents regions away from the deposits.
[b] Average composition of the surface with deposits.

9.3.4.3 Dissolution Rates

The steady-state dissolution rates of the various sets of ferritic steels and Type 316 stainless steel exposed to flowing lithium are given in Table 9.3.4. The Arrhenius plots of the data are shown in Fig. 9.3.9. The results indicate that the dissolution rates for HT-9 and Fe-9Cr-1Mo steel increase by a factor of ~2.5 with each 55°C increase in temperature. The Arrhenius plot for the dissolution rates yields an activation energy of 16.3 kcal/mole. However, the dissolution rates for Type 316 stainless steel are insensitive to changes in temperature. The steady-state dissolution rates range between 1.5 and 2.5 $mg/m^2 \cdot h$; the values are higher at lower temperatures.

9.3.5 Conclusions

Corrosion data for ferritic HT-9 and Fe-9Cr-1Mo steel in flowing lithium at temperatures between 372 and 538°C indicate that after an initial transient period of ~500 h, the weight losses for ferritic steels increase linearly with time and yield a constant dissolution rate. The dissolution rates increase with a increase in temperature. An Arrhenius plot of the dissolution rates yields an activation energy of 16.3 kcal/mole. The dissolution behavior of the two steels is identical. After exposure to lithium, the alloy surfaces develop a dimpled appearance. A dimpled surface structure is fully developed after ~2000 h

Table 9.3.4. Dissolution rates of ferritic and austenitic steels exposed to flowing lithium

Test Run	Specimen Location[a]	Temp. (°C)	Maximum Time (h)	Dissolution Rate (mg/m^2·h) HT-9	9Cr-1Mo	316 SS	316 CW
4	Test Vessel	482	5521	0.173	0.144	1.61	1.58
4	Spec. Exp. Vessel	427	5739	0.064	0.066	2.21	2.18
	Spec. Exp. Vessel	427	6501	0.070	0.070	-	-
5	Test Vessel[b]	427	5023	0.077	0.062	9.17	6.34
5	Spec. Exp. Vessel	372	4955	0.029	0.030	2.11	2.48
6	Test Vessel	538	3655	0.401	0.391	2.05	1.41
	Test Vessel	538	2271	-	-	1.75	-
6	Spec. Exp. Vessel'	482	3330	-	-	2.05	1.84

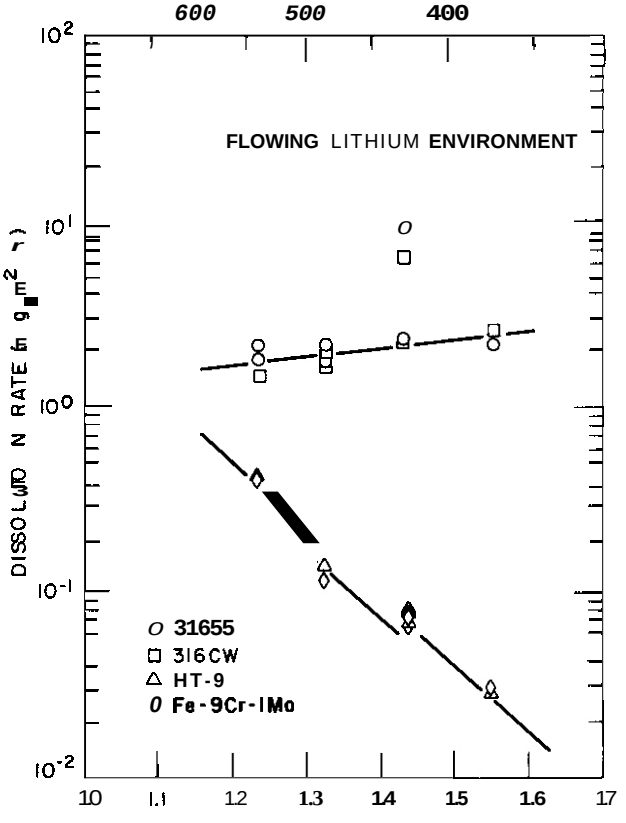

Fig. 9.3.9. Arrhenius plot of dissolution rate data for ferritic and austenitic steels exposed to flowing lithium.

of exposure and the size of the dimples does not change with additional exposure. However, the size of dimples decreases with a decrease in temperature. The formation of a dimpled structure is associated with depletion of chromium from the alloy surface and leads to significant weight loss during the initial period of exposure. Limited data (i.e., Run 6) indicate some downstream effects on the dissolution behavior of alloys. Iron-rich deposits were observed on the surface of HT-9 and Fe-9Cr-1Mo specimens located downstream (at 482°C) fran the maximum loop temperature position (538°C). These specimens showed little or no weight loss.

The dissolution rates for austenitic Type 316 stainless steel reach a steady state after an initial ~1500-h period characterized by rapid dissolution. The steady-state dissolution rates are relatively insensitive to variations in temperature. The dissolution rates for annealed or 20% CW Type 316 stainless steel exposed to lithium at temperatures between 372 and 538°C range from 1.5 to 2.5 mg/m2·h. The weight losses after the initial transient stage (i.e., 500- to 1000-h exposure) range between 15 and 30 g/m^2 after exposure at 427 or 482°C and between 3 and 15 g/m^2 after exposure at 372 or 538°C. The initial dissolution stage is associated with the formation of a ferritic surface layer due to depletion of nickel and, to some extent, chromium fcm the steel. This transient stage appears to play an important role in controlling the nature of the surface modifications and, consequently, in the overall dissolution behavior of austenitic steels. Specimens with large weight losses develop a well-defined dimpled structure and deep cavities. The surfaces of these specimens are depleted of nickel, and the chromiun content ranges from 8 to 10%. Specimens with small weight losses, i.e., <10 g/m^2, develop a very fine dimpled structure (e.g., at 372°C) or a cellular structure (e.g., at 538°C). For these specimens, the depletion of nickel is less and the concentration of chromium is higher. The influence of material and system parameters on the transient and steady-state dissolution of austenitic stainless steels cannot be established at present. Limited data indicate that an increase in nitrogen content in lithium from ~100 to 250 wppm increases the porosity in the ferrite scale and depletion of chromium from the alloy surfaces. Corrosion data from Run 6 suggest downstream effects on the dissolution behavior of austenitic steels. Specimens located downstream from the maximum temperature location showed large chromium-rich deposits on the surface.

9.3.6 References

1. O. K. Chopra and D. L. Smith, "Environmental Effects on Properties of Structural Alloys in Flowing Lithium," pp. 176-182 in Alloy Development for Irradiation Performance: Semiannual Progress Report for Period Ending March 31, 1984, DOE/ER-0045/12, Oak Ridge National Laboratory, Oak Ridge, TN, July 1984.

2. O. K. Chopra and D. L. Smith, "Environmental Effects on Properties of Structural Alloys in Flowing Lithium," pp. 182-191 in Alloy Development for Irradiation Performance: Semiannual Progress Report for Period Ending March 31, 1985, DOE/ER-0045/14, Oak Ridge National Laboratory, Oak Ridge, TN, July 1985.

9.4 CORROSION OF LOW ACTIVATION AUSTENITIC STEELS AND ORDERED ALLOYS IN THERMALLY CONVECTIVE LITHIUM — P. F. Tortorelli, J. H. DeVan, and C. T. Liu (Oak Ridge National Laboratory)

9.4.1 AOIP Task

AOIP Task I.A.3, Perform Chemical and Metallurgical Compatibility Analyses.

9.4.2 Objective

The purpose of this task is to determine the corrosion resistance of candidate first-wall materials to slowly flowing lithium in the presence of a temperature gradient. Corrosion and deposition rates are measured as functions of time, temperature, additions to the lithium, and flow conditions. These measurements are combined with chemical and metallographic examinations of specimen surfaces to establish the mechanisms and rate-controlling processes for dissolution and deposition reactions.

9.4.3 Summary

Completion of a second loop experiment with Cr-Mn steels in thermally convective lithium confirmed the nature of two competing reactions during the corrosion of these steels leading to observation of both dissolution and deposition reactions at hot leg surfaces. Analysis of long range ordered alloys exposed to thermally convective lithium revealed that corrosion-induced porosity was caused both by preferential depleti and redeposition of dissolved species.

9.4.4 Progress and Status

Because of their favorable neutronic (that is, activation) properties, manganese-containing austenitic stainless steels are currently being investigated as part of the fusion energy materials development effort. To assess the resistance of these alloys to liquid metal corrosion, a qualitative study of their reactions with molten lithium was initiated using a thermal convection loop. The loop circulated lithium between 500 and 350°C and was constructed of type 316 stainless steel which, because of prior operation with lithium and associated preferential leaching of nickel and chromium, was known to have a considerably higher iron concentration at hot leg surfaces than found in the starting material. The Mn-containing alloy specimens were exposed to lithium in a region of the loop near the top of the hot leg. Because of the nonisothermal nature of the loop, the temperatures of these specimens varied from 500°C [maximum loop temperature (T_{max})] to 485°C. Coupons of type 316 stainless steel were placed at the other normally-used specimen positions around the remainder of the loop. The specimens were removed from, and replaced into. the thermally convective lithium several times during the loop experiment.

The first loop experiment with Cr-Mn steels used specimens provided by Hanford Engineering Development Laboratory (HEOL). Weight change data and scanning electron microscopylenergy dispersive x-ray analysis results for these alloys, after a total of 3340 h, were reported in previous progress reports.[1,2] A second experiment with Mn-containing austenitic steels was conducted for 3096 h in the same loop and was completed during the current reporting period. The compositions of the latter specimens are listed in Table 9.4.1. The PCMA specimens are ORNL developmental alloys, while the others were supplied by HEOL. The specimens were weighed thrice after the start of exposure to lithium. The resulting weight changes as a function of exposure time are shown in Fig. 9.4.1. Note that some specimens gained weight while others exhibited a net weight loss over the 3096 h exposure period. However, as also seen in Fig. 9.4.1, almost every specimen actually gained weight during the last 2000 h of exposure.

Table 9.4.1. Compositions of Fe–Mn–Cr steels exposed to thermally convective lithium between 500 and 485°C in the second loop experiment

Alloy	Composition (wt %)						
	Mn	Cr	Ni	C	N	Si	Fe
Age 18–18+	18	18	0.5	0.1	0.4	0.6	Bal
R87	15	15	0.5	0.1	0.1	0.4	Bal
NIT-32	12	18	1.5	0.1	0.4	0.6	Bal
PCMA-2	17	15	0.01	0.06	0.001	0.04	Bal
PCMA-4	19	10	0.01	0.09	0.002	0.02	Bal
PCMA-6	14	16	0.01	0.18	0.003	0.02	Bal
PCMA-7	19	15	0.01	0.38	0.005	0.02	Bal
PCMA-9	18	20	0.01	0.26	0.006	0.03	Bal

As discussed previously,' the observation of mixed weight gains and losses for the steels containing 15 to 20% Mn indicates a competition between dissolution and deposition reactions. These reactions are thought to include concentration gradient chromium transport *among* the specimens *and* loop wall in the hot zone *as* well as thermal qradient mass transfer of manqanese to the cold zone. The differinq nature of these two types of mass iransfer processes can possibiy lead to a net weight gain if the amount of material deposited by concentration gradient mass transfer is greater than that lost by dissolution of manganese and other elements.

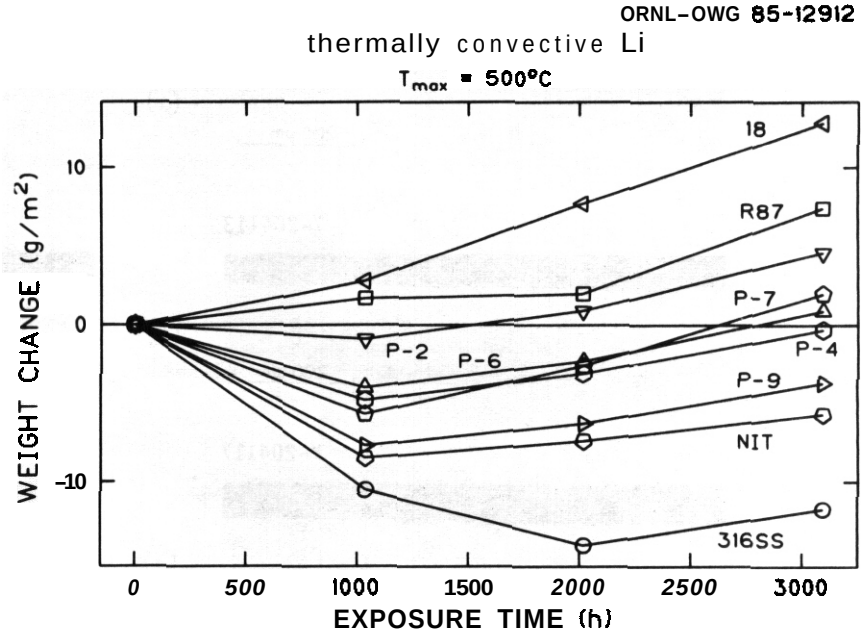

Fig. 9.4.1. Weight change versus exposure time for Cr–Mn Steels and type 316 stainless steel exposed to thermally convective lithium.

Such reactions are consistent with observations of manganese depletion and chromium enrichment in surface layers of corroded specimens exposed in the first loop experiment and from experiments in static lithium., While surface analyses of the second set of exposed coupons are not yet available, examination of polished cross sections of these coupons revealed evidence of both dissolution and deposition (see Fig. 9.4.2). Each of the specimens clustered in the 485 to 500°C zone of the lithium loop, including those with significant net weight gains, were found to have corrosion layers characteristic of the type caused by preferential dissolution of an alloy. These layers, containing dark-etching phases or pores, have characteristically been observed for Fe-Ni-Cr steels exposed to lithium.[4] In the present case, they appear to be related to the selective leaching of manganese, based on surface compositional analysis of specimens exposed in the first loop experiment. Indeed, the difference in contrast between the corrosion layer and the underlying matrix in the micrographs of Fig. 9.4.2 is consistent with the destabilization of austenite and transformation to ferrite in the surface layer due to loss of manganese. Such behavior is typically observed for Fe-Ni-Cr steels that undergo preferential loss of nickel in lithium.[4]

Evidence for the mass transfer of manganese to the cold zone is based on the formation of deposits on type 316 stainless steel specimens in the cold leg. A large measured weight gain (47.0 g/m^2) for the coupon located at the bottom of the loop's cold leg indicated substantial mass transport had occurred during the 3096 h of exposure to lithium and that most of the deposition was at the coldest point of the loop (near 350°C). This finding, which is similar to observations from the first loop experiment,[2] was corroborated by examination of polished cross sections of cold leg specimens (see Fig. 9.4.3). The specimen at the lowest temperature showed the greatest amount of deposition. It is expected that the upcoming compositional analyses of these coupon surfaces will show the deposits to consist of mainly manganese and nickel, as already has been shown for the earlier loop experiment.2

Referring to Figs. 9.4.1 and 9.4.2, the "dissolution zones" described above appeared to be thicker and more uniform for the alloys showing net weight losses. Conversely. the Cr-Mn steel with the largest weight gain after 3096 h (Age 18-18+, +12.8 g/m^2) showed a very thin dissolution zone, and the one with the next greatest increase in weight (R87, +7.4 g/m^2) showed a somewhat thicker, but very irregular corrosion layer. As shown in Fig. 9.4.2, deposits were observed on top of the dissolution zone on all Cr-Mn steels. The metallographic evidence thus supports a model of a corrosion process of competing dissolution and deposition reactions. Furthermore, given the trend of the weight change versus exposure time curves (see Fig. 9.4.1). it appears that manganese depletion makes the principal contribution to weight change during the early stages of exposure, while, after a Mn-depleted layer has been established, chromium transport and deposition becomes the dominant mechanism.

The exact nature of the transport reactions involving chromium is not known. However, as discussed previously,[1,2] the chromium reactions may be driven by the relatively high nitrogen concentrations of some of the Cr-Mn steels (see Table 9.4.1). Reactions between Cr and N and between Li, Cr, and N are possible[5,6] and could lead to increased dissolution and/or reaction product formation at specimen surfaces. Consequently, the next loop experiment in this series will involve only one composition of a Cr-Mn steel with a low nitrogen concentration (a PCMA alloy) and newly purified lithium. The data from this third experiment will then be compared to the results from the first two series of exposures to determine possible effects of nitrogen on the observed corrosion reactions.

Although long range ordered (LRO) alloys are no longer actively studied in the ADIP program, a further analysis of such specimens exposed earlier to thermally convective lithium was recently completed in order to (1) formally conclude our corrosion studies of this alloy system and (2) gain more information about some rather interesting corrosion reactions between lithiun and these alloys; in this way we hoped to increase our general understanding about liquid metal corrosion as part of our ongoing program with other AOIP alloys.

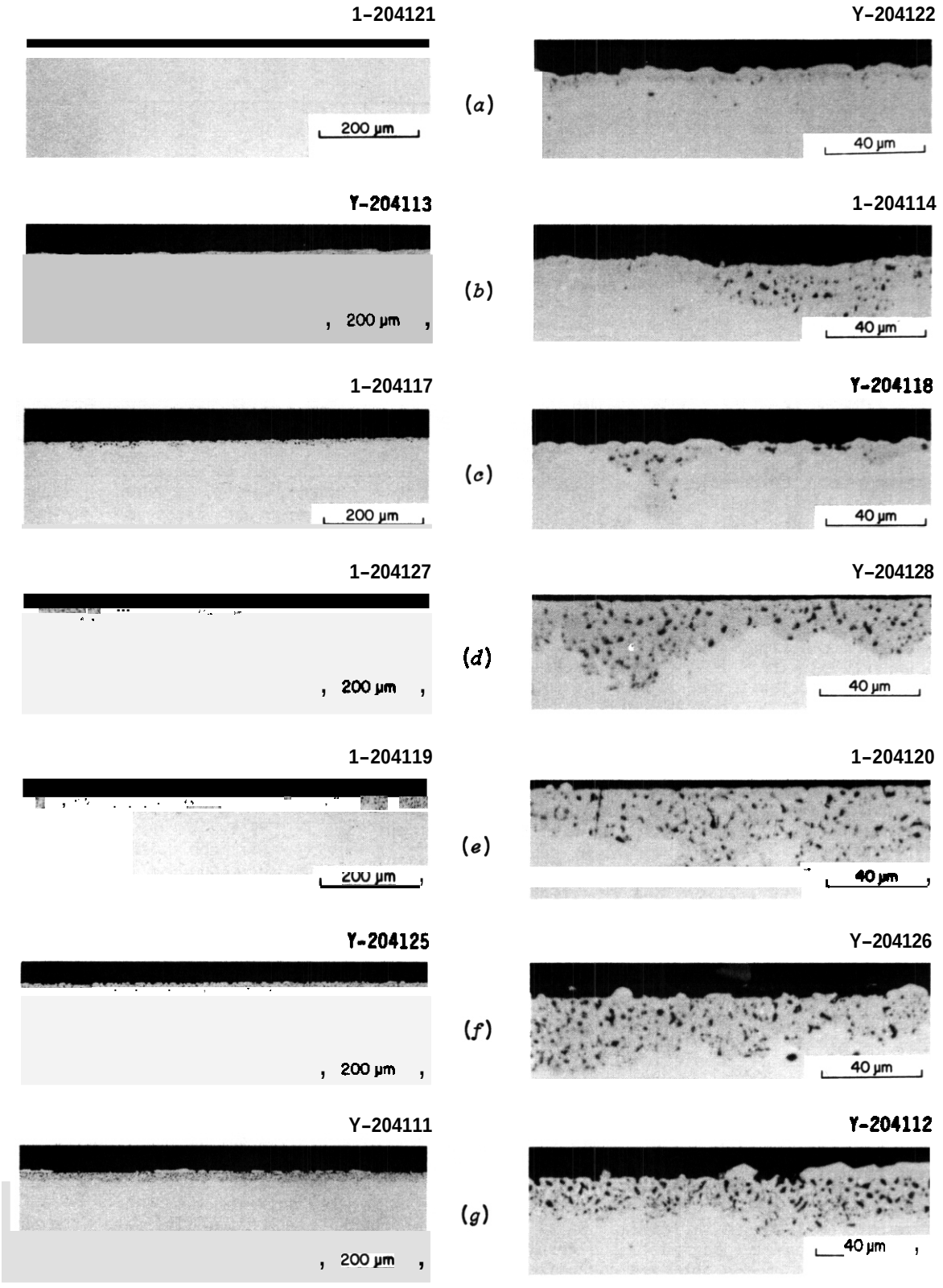

Fig. 9.4.2. Polished cross sections of alloys exposed to thermally convective lithium for 3095 h. (a) Age 18–18+, 490°C. (b) R87, 500°C. (c) PCMA-2, 495°C. (d) PCMA-4, 485°C. (e) PCMA-9, 495°C. (f) Nitronic-32, 485°C. (g) Type 316 stainless steel, 500°C.

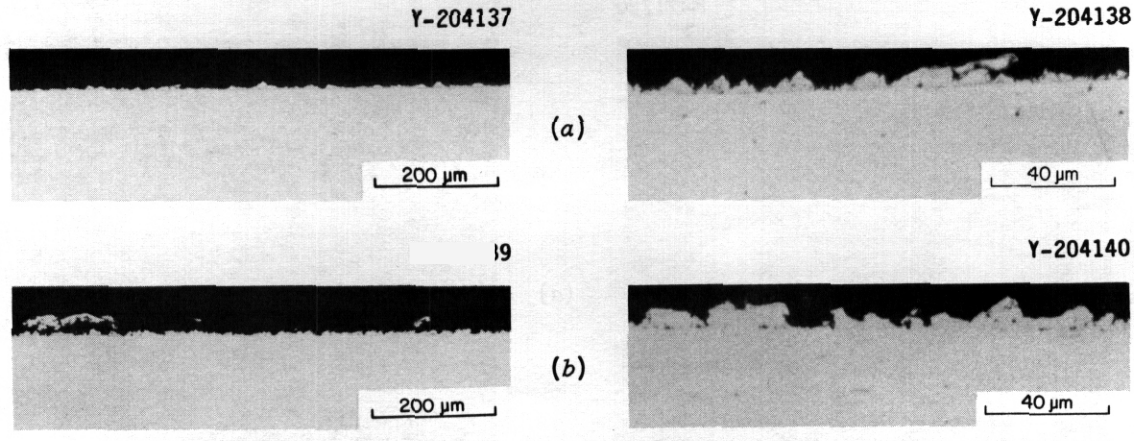

Fig. 9.4.3. Polished cross sections of type 316 stainless steel coupons located in the cold leg of a thermal convection loop that circulated lithium between 500 and 350°C for 3095 h and contained Cr–Mn steels in its hot leg. (*a*) 370°C. (*b*) 350°C.

We previously found[7,8] that the LRO-35 alloy (see Table 9.4.2) was essentially unaffected by exposure to static lithium at elevated temperatures, while Fe-Cr-Ni alloys with similar and higher nickel concentrations were readily attacked under the same exposure conditions. We therefore initiated experiments to assess the corrosion resistance of this and other LRO alloys to flowing lithium. Because of a lack of sufficient LRO material, the experiments were conducted in type 316 stainless steel TCLs similar to the one used to expose Cr-Mn alloys described above. The use of the stainless steel loop material imposed a severe chemical gradient between the LRO specimens and the loop wall, especially considering that surfaces of the loops' hot legs had been preferentially leached of nickel from prior exposures to lithium. Such an arrangement provides the worst case for the dissolution of the LRO alloys in thermally convective lithium. The LRO coupons were placed in the two hottest loop positions (600 and 570°C). The remainder of the coupon positions were occupied by type 316 stainless steel specimens. Th ΔT of the lithium circuit was 150°C.

Table 9.4.2. Long range ordered alloys that have been exposed to thermally convective lithium

Alloy designation	Composition (wt %)					
	Co	Fe	Ni	V	Ti	Al
LRO-1	Bal	16		23		
LRO-7	Bal	16		23		0.4
LRO-35		Bal	32	22	0.4	

Three different LRO alloy compositions, shown in Table 9.4.2, were exposed to thermally convective lithium in different loop experiments. While results from the analyses of the exposed LRO-35 specimens hav been reported previously,[9,10] further scanning electron microscopy and energy dispersive x-ray analyses of these LRO-35 specimens are presented below along with weight change and surface analytical results for LRO-1, LRO-7, and Ni_3Al. Earlier, we reported[9,10] that specimens of LRO-35 corroded very rapidly when exposed to flowing lithium at 600 and 570°C with the resulting surfaces being depleted in nickel and correspondingly enriched in iron and vanadium. Corrosion rates of the LRO alloys were much greater than those of type 316 stainless steel previously exposed in stainless steel lithium loops. However, dissimilar metal transfer of the nickel from the LRO coupons to the loop wall probably made a very significant contribution to the overall corrosio be less tha those measured in the present cas

During the current reporting period, further microstructural analysis of LRO-35 specimens revealed additional details about the corrosion process. Figure 9.4.4 shows scanning electron micrographs of polished cross sections of LRO-35 after 2500 and 7500 h of exposure to thermally convective lithium at 600°C. While the corrosion was much greater for the specimen exposed for the longer time period, the attack, even after 2500 h, was relatively severe. In both cases, two distinct corrosion zones can be observed: a very porous or open outer layer and a more compact, but still porous, inner zone next to the unaltered matrix. Analysis of the two zones by energy dispersive x-ray analysis showed that the outer one was primarily composed of iron, while the inner layer contained iron and vanadium. Nickel was essentially depleted from both layers while the composition of the matrix below the layers matched that of the starting material. X-ray data for both specimens are summarized in Table 9.4.3. The results for the specimen exposed for 2500 h confirmed earlier qualitative electron microprobe traces across its cross section.[9] Close examination of the inner corrosion zone revealed that the nonporous region was composed of two distinct "phases" (see Fig. 9.4.5). These two phases differed in secondary electron intensity; x-ray analysis showed the darker one to be enriched in vanadium relative to the other.

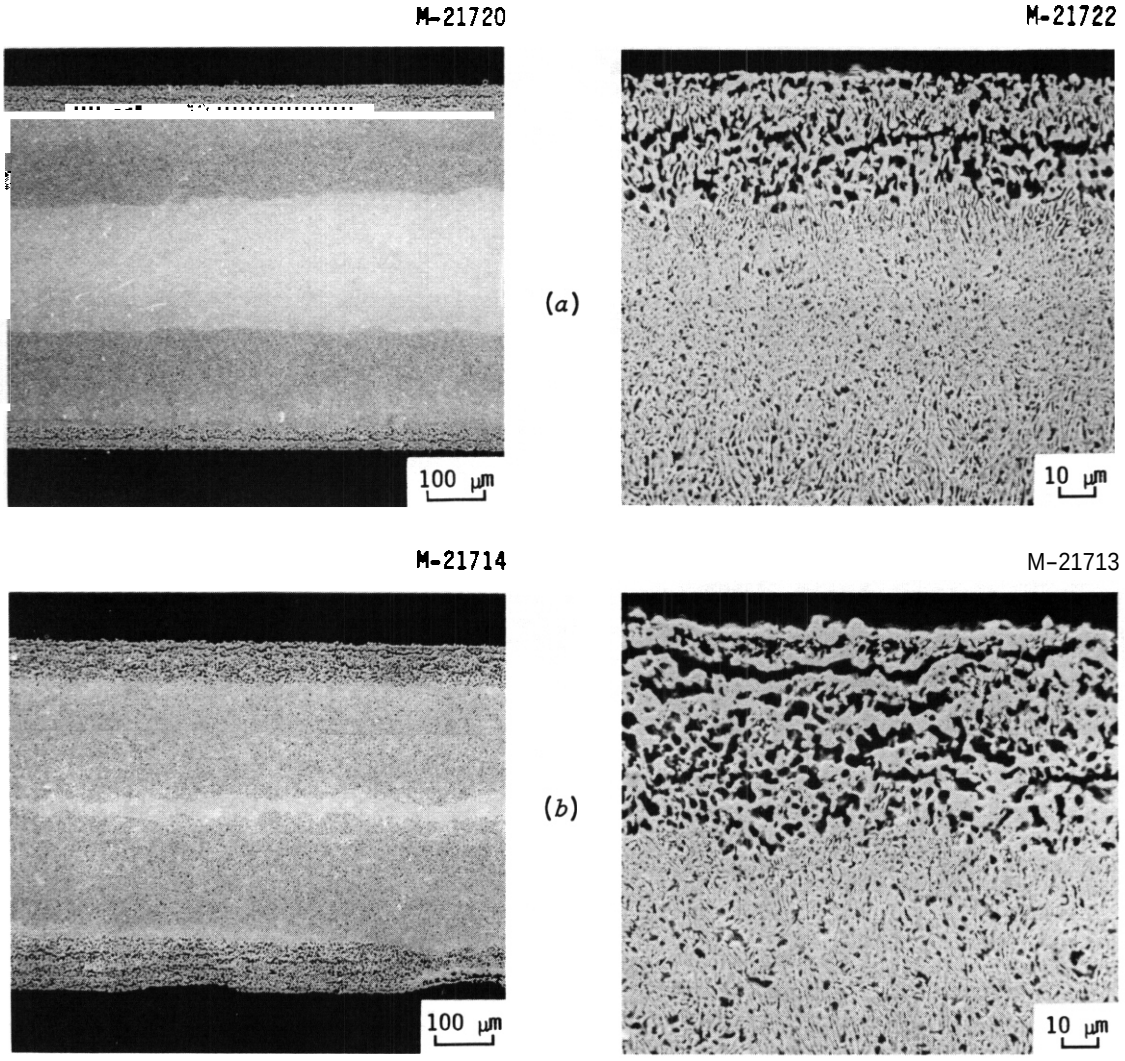

Fig. 9.4.4. Scanning electron micrographs of polished cross sections of LRO-35 exposed to thermally convective lithium at 600°C. (a) 2512 h. (b) 7495 h.

Consideration of the observed changes in morphology and composition suggests that the inner layer develops by dissolution of nickel and, to a lesser extent, iron, while the outer layer forms by redeposition of dissolved iron (during exposure or cool-down or both). We base this conclusion on the resistance of vanadium to dissolution in lithium compared to iron. The higher resistance of the former makes it improbable that it was preferentially depleted in the outer layer. Indeed, as shown in Table 9.4.3, vanadium is slightly enriched in the inner corrosion layer relative to the uncorroded matrix. It thus appears that, as observed in other nickel-containing alloys,[11] the nickel is preferentially dissolved from the alloy and then transported to the cold zone, while much of the iron is simply redeposited on the hot leg surface to form the very porous structure noted in the micrographs. It is interesting to note that, in another lithium loop experiment,[9] a loosely adherent surface layer on a LRO-35 specimen was found to be pure iron. In view of the present results. this layer must have consisted of the open outer zone of the duplex reaction layer.

Table 9.4.3. Compositional analysis of LRO-35 specimens exposed to thermally convective lithium at 600°C for 2512 and 7495 h

Analyzed area	Exposure time (h)	Concentration (wt %)[a]			
		Fe	Ni	V	Ti
Outer corrosion zone	2512	92	1	6	1
Outer corrosion zone	7495	93	1	4	1
Inner corrosion zone	2512	73	1	25	1
Inner corrosion zone	7495	67	1	30	0.5
Matrix	2512	46	31	22	0.5
Matrix	7495	46	31	22	0.5

[a]Averaged measurements based on standardless analysis using ZAF-corrected energy dispersive x-ray spectral data.

Examination of a LRO-1 specimen exposed to thermally convective lithium at 600°C for 2500 h revealed a different corrosion morphology than that observed for LRO-35 (see Fig. 9.4.6). Nevertheless, this examination also yielded evidence of redeposition, albeit under a different set of circumstances. Referring to the micrographs of the polished cross section of LRO-1 shown in Fig. 9.4.6, the corrosion process resulted in a very shallow, but open, surface layer. (Presumably, the parts that appear to be "detached" were actually connected to the specimen somewhere below or above the plane of polishing. In this sense, the "pore" size was much greater than in the case of LRO-35.) Energy dispersive x-ray spectra of some of these areas showed enrichment in iron and strong depletion in vanadium relative to the concentrations in the uncorroded matrix. Furthermore, some protrusions on the surface had a distinct overlying layer that differed in secondary electron intensity (see Fig. 9.4.7). X-ray spectra of these layers showed them to be similar in composition to those "detached" areas described above, while the underlying parts of the protrusions exhibited spectra like that of the uncorroded matrix. Table 9.4.4 lists the comoositions of these various parts of the micrograph shown in Fig. 9.4.7. Of the elements that compose LRO-1 (Co, Fe, and V), vanadium should be the most dissolution resistant. Therefore, these experfmental observations are again consistent with the assumption that the outer layer is a result of redeposition, in this case of iron and cobalt, since preferential dissolution of vanadium (which would result in a surface layer of iron and cobalt) is not a likely process. In this regard, it is interesting to note that a redeposition mechanism was considered, but rejected, as an explanation for porosity formation on Fe-Ni-Cr steels exposed to lithium because of the observation of dissolution-resistant molydenum nodules on the outer surface.[11] In that case, the presence of molydenum on the surface suggested lack of redeposition. while, for the present analysis, the lack of vanadium on the outer surface implied just the opposite.

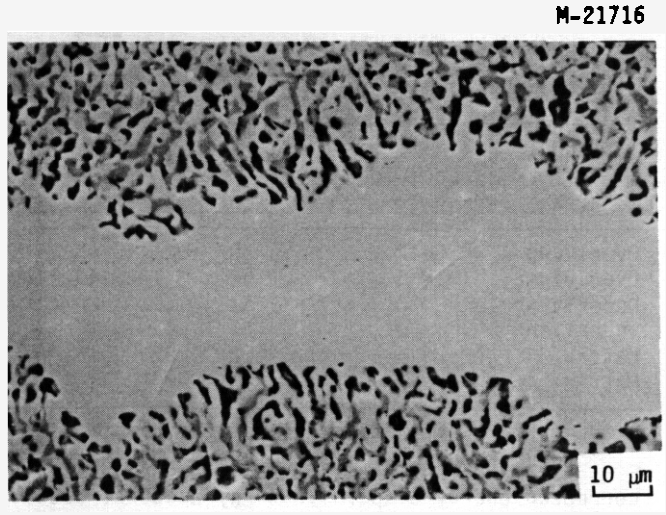

Fig. 9.4.5. Scanning electron micrograph of an area at the centerline of a polished cross section of LRO-35 exposed to thermally convective lithium at 600°C for 7495 h.

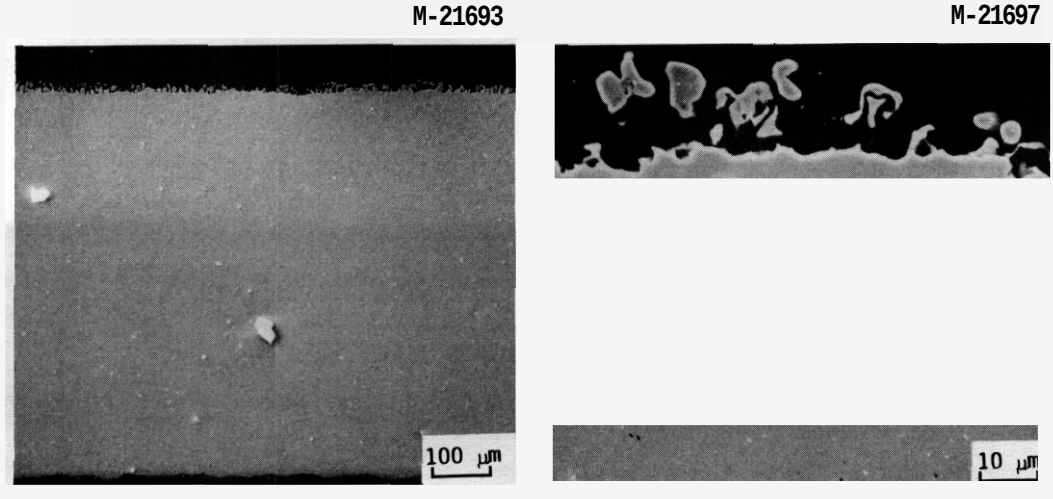

Fig. 9.4.6. Scanning electron micrographs of a polished cross section of LRO-1 exposed to thermally convective lithium at 600°C for 2721 h.

In order to determine if the severe corrosion of LRO alloys in thermally convective lithium could be reduced by the presence of aluminum in the starting alloy, specimens of LRO-1 and LRO-7 were exposed in successive loop experiments. The LRO-7 alloy is basically the same composition as LRO-1 except for the addition of 0.4 wt % Al (see Table 9.4.2). As shown by the weight change versus exposure time data in Fig. 9.4.8, the presence of aluminum had no effect on corrosion as measured by weight losses. In addition, as also shown in Fig. 9.4.8, a final lithium loop experiment with the ordered intermetallic alloy Ni_3Al revealed weight loss kinetics similar to those for the LRO alloys. This observation is in contrast to results for lead exposures,[12] which showed significantly less corrosion for Ni_3Al when compared to other nickel-containing alloys (presumably due to the lower nickel activity of the intermetallic alloy).

Table 9.4.4. Compositional analysis of LRO-1 exposed to thermally convective lithium for 2500 h at 600°C

Type of area	Location[a]	Concentration (wt %)[b]		
		co	V	Fe
Overlying	A	50	1	49
Overlying	B	52	1	49
Underlying	C	61	19	20
Underlying	D	61	22	17
Matrix	E	62	22	16
Matrix	F	61	23	16

[a]Letters refer to markings on Fig. 9.4.7.

[b]Standardless analysis based on ZAF-corrected energy dispersive x-ray spectral data.

M-21698

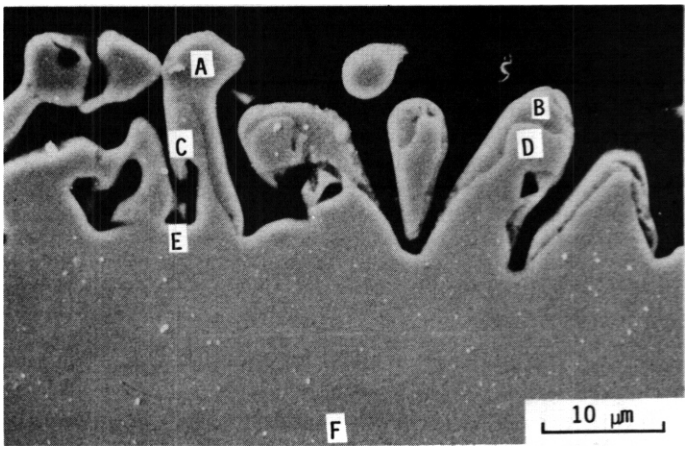

Fig. 9.4.7. Scanning electron micrograph of a polished cross section of LRO-1 exposed to thermally convective lithium at 600°C for 2727 h.

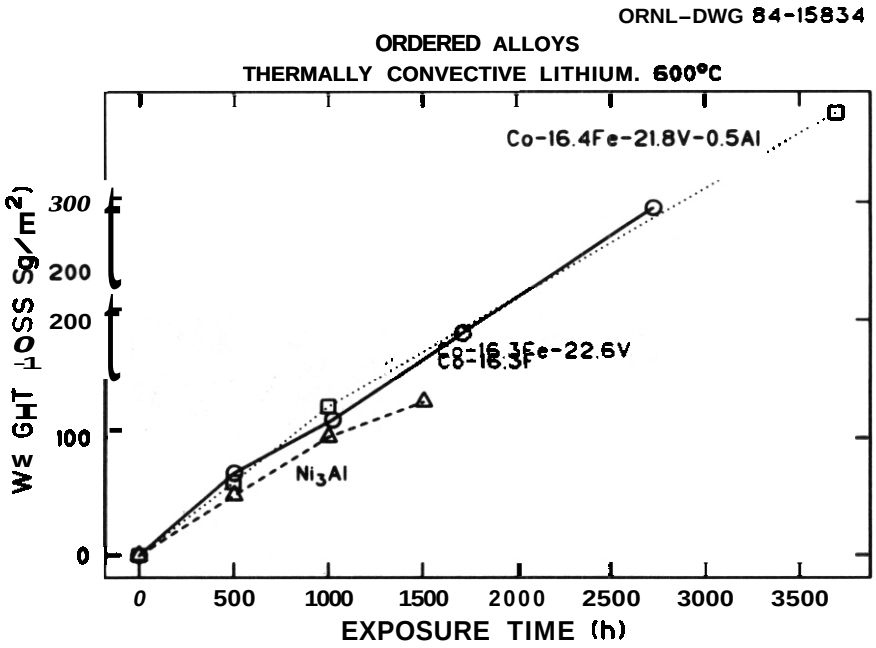

Fig. 9.4.8. Weight loss versus exposure time for ordered alloys exposed to thermally convective lithium at 600°C. (maximum loop temperature).

As stated above, the dissimilar metal gradient between the LRO specimens and the loop wall surely contributed to the severity of the corrosion of these alloys. However. the nature of the corrosion processes (particularly the extent of nickel depletion in response to a thermal gradient vis-a-vis an isothermal condition) does indicate that the Fe-Ni-V ordered alloys are not well suited for high temperature lithium containment under nonisothermal conditions. Furthermore, aluminum additions to nickel did not noticeably improve the corrosion resistance of these alloys in lithium under the current exposure conditions.

9.4.5 Conclusions

1. The exposure of Cr-Mn steels containing 15 to 20 wt % Mn to thermally convective lithium resulted in both dissolution and deposition reactions at 500°C. Although the relative extent of these competing reactions varied with alloy composition, all alloys suffered some dissolution. No exact correlation between extent of corrosion and composition was found.

2. An ordered Fe-Ni-V alloy was rapidly corroded in thermally convective lithium at 600°C. However, the extent of corrosion was exacerbated by concentration gradient mass transfer between the loop and the specimens.

3. Analysis of long range ordered alloys exposed to thermally convectfve lithium revealed two different types of corrosion-induced porosity: the inner layer was associated with preferential dissolution and the outer layer with redeposition of dissolved species.

9.4.6 References

1. P. F. Tortorelli and J. H DeVan. "Corrosion of Low Activation Austenitic Alloys and Standard Fe-12 Cr-1 MoVW Steel in Thermally Convective Lithium," pp. 189–95 in *ADIP Semiann. Frog. Rep.* **Sept. *30, 1384*** DOE/ER-0045/13, US. DOE, Office of Fusion Energy.

2. P. F. Tortorelli and J. H DeVan, "Thermal Convection Loop Studies of the Lithium Corrosion of Low Activation Austenitic Alloys and Standard Fe-12 Cr-1 MoVW Steel," pp. 197–204 in *ADIP Semiann. Frog. Rep. March* 31, *1385,* DOE/ER-0045/14, US. DOE, Office of Fusion Energy.

3. V. Coen and P. Fenici, "Compatibility of Structural Materials with Liquid Breeders — Review of Recent Work Carried Out at JRC, Ispra," *Nucl. Eng. and Design/Fus.* **1** (1984) 215–29.

4. O. K. Chopra and P. F. Tortorelli, "Compatibility of Materials for Use in Liquid-Metal Blankets of Fusion Reactors," *J. Nucl. Mater.* **122&123** (1984) 1201–12.

5. W. F. Calaway, "The Reaction of Chromium with Lithium Nitride in Liquid Lithium," pp. 18-8–18-26 in *Proc. Second Int. Conf. on Liq. Metal Technol. in Energy Production*, U.S. DOE, CONF-800401-P2, 1980.

6. M. G. Barker et al., "The Interaction of Chromium with Nitrogen Dissolved in Liquid Lithium," *J. Nucl. Mater.* **114** (1983) 143–49.

7. P. F. Tortorelli, J. H. DeVan, and C. T. Liu, "Compatibility of Static Lithium with a Long-Range-Ordered Fe-N-V Alloy and 2 1/4 Cr-1 Mo Steel," pp. 328–36 in *ADIP Quart. Prog. Rep. June 30, 1980*, DOE/ER-0045/3, U.S. DOE, Office of Fusion Energy.

8. P. F. Tortorelli and J. H. DeVan, "Corrosion of Fe-Ni-Cr and Fe-Ni-V Alloys in Static Lithium," pp. 152–57 in *ADIP Quart. Prog. Rep. Dec. 31, 1979*, DOE/ER-0045/1, U.S. DOE, Office of Fusion Energy.

9. P. F. Tortorelli, J. H. DeVan, and C. T. Liu, "Corrosion of Iron-Base Alloys in Flowing Lithium," pp. 312–20 in *ADIP Quart. Prog. Rep. Sept. 30, 1981*, DOE/ER-0045/7, U.S. DOE, Office of Fusion Energy.

10. P. F. Tortorelli, J. H. DeVan, and C. T. Liu, "Corrosion of Austenitic, Ferritic, and Long Range Ordered Alloys in Flowing Lithium," pp. 482–90 in *ADIP Semiann. Prog. Rep. March 31, 1982*, DOE/ER-0045/8, U.S. DOE, Office of Fusion Energy.

11. P. F. Tortorelli and J. H. DeVan, "Effects of a Flowing Lithium Environment on the Surface Morphology and Composition of Austenitic Stainless Steel," *Microstructural Sci.* **12** (1985) 215–26.

12. J. V. Cathcart and W. D. Manly, *The Mass Transfer Properties of Various Metals and Alloys in Liquid Lead*, Oak Ridge National Laboratory report ORNL-2008, October 1956.

9.5 CORROSION OF TYPE 316 STAINLESS STEEL AND 12 Cr-1 MoVW STEEL IN THERMALLY CONVECTIVE Pb-17 at. % Li — P. F. Tortorelli and J. H. DeVan (Oak Ridge National Laboratory)

9.5.1 ADIP Task

ADIP Task I.A.3, Perform Chemical and Metallurgical Compatibility Analyses.

9.5.2 Objective

The purpose of this task is to determine the corrosion resistance of candidate first-wall materials to slowly flowing Pb–17 at. % Li in the presence of a temperature gradient. Dissolution and deposition rates are measured as functions of time, temperature, and additions of minor elements to the lead-lithium. These measurements are combined with chemical and metallographic examinations of specimen surfaces to establish the mechanisms and rate-controlling processes for the dissolution and deposition reactions.

9.5.3 Summary

More extensive data from additional experiments with type 316 stainless steel and 12 Cr-1 MoVW steel in thermally convective Pb-17 at. % Li confirmed the results of earlier 500°C exposures. The 12 Cr-1 MoVW steel corroded uniformly, whereas the austenitic stainless steel suffered severe localized penetration and material loss.

9.5.4 Progress and Status

As discussed earlier,[1-4] lithium affords an effective solvent for removing lead-lithium from exposed stainless steel specimens. but its use leads to the partial or total stripping of corrosion layers. Therefore. in corrosion experiments involving lead-lithium, the specimen cleaning procedure can significantly affect weight loss determinations and surface analyses of exposed specimens. Accordingly, we have revised our experimental procedures for thermal convection loops (TCLs) circulating Pb-17 at. % Li. The loops are of the usual design[3,4] which allows corrosion coupons to be withdrawn and inserted without interrupting the lead-lithium flow. However, unlike loop experiments in lithium and earlier lead-lithium exposures, once a specimen is removed, it is not again exposed to the lead-lithium. Rather, four specimens are clustered at 500°C at the start of exposure and are selectively removed and replaced (with fresh coupons) at certain intervals to measure corrosion losses as a function of exposure time. In this way, the effects of specimen cleaning on subsequent re-exposure of the same coupon are avoided. With this selective replacement of loop coupons, corrosion data for seven different exposure periods will be obtained during the 10,000 h each loop operates with inserted specimens.

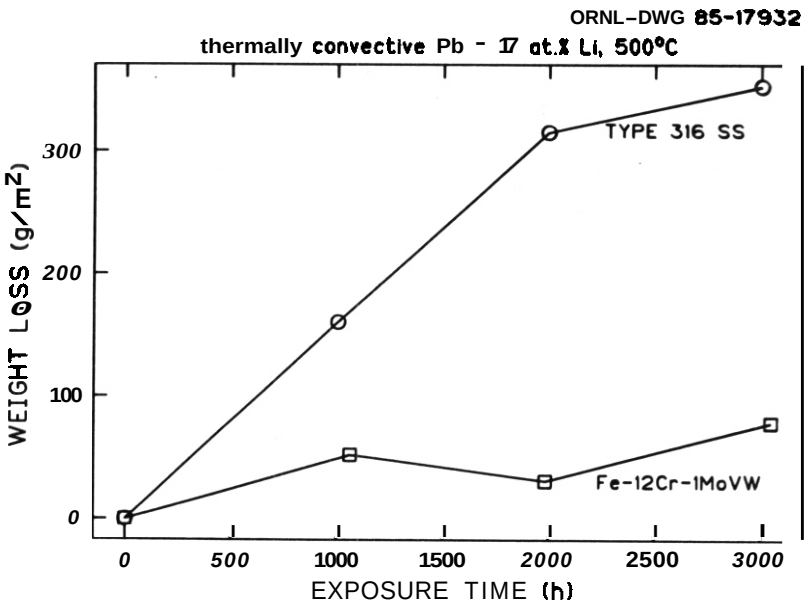

Fig. 9.5.1. Weight loss versus exposure time for type 316 stainless steel and 12 Cr–1 MoVW steel.

Two loop experiments of the type discussed above are currently in progress. In one loop, type 316 stainless steel coupons are contained in type 316 stainless steel piping that previously had circulated lithium for over 10.000 h. A second TCL contains 12 Cr-1 MoVW steel specimens and is made from 9 Cr-1 Mo steel. It had not seen previous service. Both loops are circulating Pb-17 at. % Li at a maximum temperature of 500°C, but the temperature differential is higher in the case of the 12 Cr-1 MoVW steel (150°C) than the type 316 stainless steel (100°C). (The details of the procedure for the preparation of the lead-lithium used in both loops were given previously.5)

The initial weight loss results for both alloys, shown in Fig. 9.5.1, confirmed earlier data[1,2] showing much greater susceptibility of type 316 stainless steel to corrosion by Pb-17 at. % Li relative to that of 12 Cr-1 MoVW steel. Furthermore, given the variability in the stripping of the corrosion layer during cleaning,' the latest weight losses measured for type 316 stainless steel at 500°C, as plotted in Fig. 9.5.1, agree rather well with previously reported4 values of 311 and 338 g/m² for this steel when similarly exposed for 2472 h. Consideration of the weight loss versus time curve for type 316 stainless

steel in Fig. 9.5.1 indicates a possible tendency for a decreasing rate of weight loss with exposure time. The data for 12 Cr-1 MoVW steel (as shown in Fig. 9.5.1) are not sufficient to even qualitatively determine the form of the weight loss curve at this stage of the study.

Metallographic examination of polished cross sections of the type 316 stainless steel coupons exposed in the latest loop test revealed that the specimen cleaning procedure, which did remove most of the residual lead-lithium, did not completely strip the extensive corrosion layer (see Fig. 9.5.2). However, based on the thicknesses of the corrosion layer and the sound metal remaining as a function of time, it appears, from Fig. 9.5.2, that a certain depth of the corrosion layer was removed either during loop exposure or during the cleaning process. The micrographs in this figure resemble those of a similarly exposed and cleaned type 316 stainless steel (500°C, 2472 h).[4] The severe attack and deep penetration by the lead-lithium are quite evident. This form of corrosion should be compared to the rather uniform weight loss process for 12 Cr-1 MoVW steel that occurs in Pb-17 at. % Li at 500°C. Despite a significant weight loss (see Fig. 9.5.1), the coupon exposed for 1009 h showed no signs of localized corrosion (see Fig. 9.5.3). This observation is similar to the one previously made for a specimen of this alloy exposed for 3078 h at 500°C.[4]

Given the difference in corrosion morphology, comparison of corrosion losses between the austenitic stainless steel and the 12 Cr-1 MoVW steel need to be based on the decrease in sound metal thickness rather than weight change, per se. A first attempt at these types of measurements for type 316 stainless steel is shown in Fig. 9.5.4. Since this nonuniform corrosion layer occurs only in the case of the austenitic stainless steel, measurement of corrosion loss by thickness changes would increase the difference in the susceptibilities of type 316 stainless steel and 12 Cr-1 MoVW steel relative to that obtained from the weight loss measurements. Furthermore, a determination of corrosion kinetics based on thickness measurements could be quite different from, and more appropriate than, that obtained from weight losses. Indeed, a comparison of Figs. 9.5.1 and 9.5.5 reveals that linear kinetics may be more appropriate for the corrosion of type 316 stainless steel in Pb-17 at. % Li. If confirmed by additional data, such kinetic behavior would be consistent with a porous nonprotective corrosion layer, as observed for this steel.

A type 316 stainless steel specimen exposed to Pb-17 at. % Li in a previous exposure series (500°C, 2472 h) was recently examined by scanning electron microscopy and energy dispersive x-ray analysis. Micrographs of the surface normal and cross sectional views are shown in Fig. 9.5.5. Compositional analysis indicated significant depletion in nickel and chromium. However, the severity of depletion, particularly for nickel, was not as great as was observed in lithium systems,[6] despite much larger corrosion losses. This observation can be related to the results of x-ray depth profiling (see Table 9.5.1), which revealed nonuniform variations in the concentrations of these elements below the exposed surface. Both observations indicate that the penetrating attack was very nonuniform and are consistent with the metallographic appearance near the surface shown in Fig. 9.5.2.

Table 9.5.1. Compositional analysis of type 316 stainless steel exposed to thermally convective Pb-17 at. % Li for 2472 h at 500°C

Area[a]	Concentration (wt %)[b]					Area[a]	Concentration (wt %)[b]				
	Fe	Cr	Ni	Mo	Si		Fe	Cr	Ni	Mo	Si
A	86	6	4	3	0.9	F	86	8	4	2	0.5
B	67	16	14	2	0.4	G	65	18	13	2	0.4
C	87	7	3	2	0.6	Corrosion layer[c]	82	8	6	3	0.5
D	72	13	12	2	0.4						
E	87	7	3	2	0.5	Matrix[d]	66	18	13	2	0.5

[a]X-rays generated from areas as indicated on micrograph shown in Fig. 9.5.5(*b*). Areas A–F are in corrosion layer; area G is in uncorroded matrix.

[b]As determined by ZAF standardless analysis of energy dispersive x-ray spectra. Concentrations do not sum to 100 due to rounding off.

[c]X-rays generated from scanning electron beam in corrosion layer.

[d]X-rays generated from scanning electron beam in uncorroded matrix.

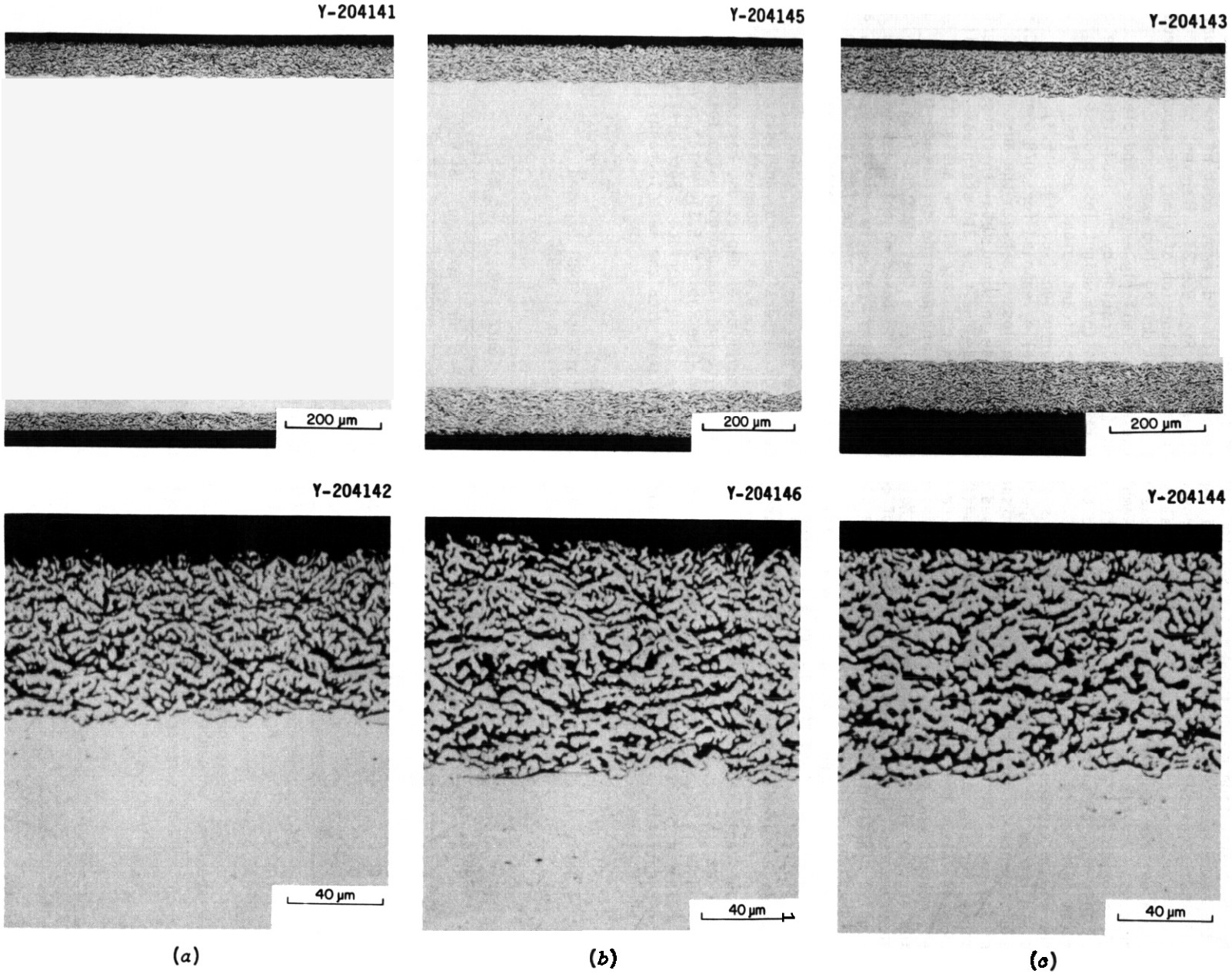

Fig. 9.5.2. Type 316 stainless steel exposed to thermally convective Pb-17 at. % Li at 500°C. (*a*) 1004 h. (*b*) 1997 h. (*c*) 3001 h.

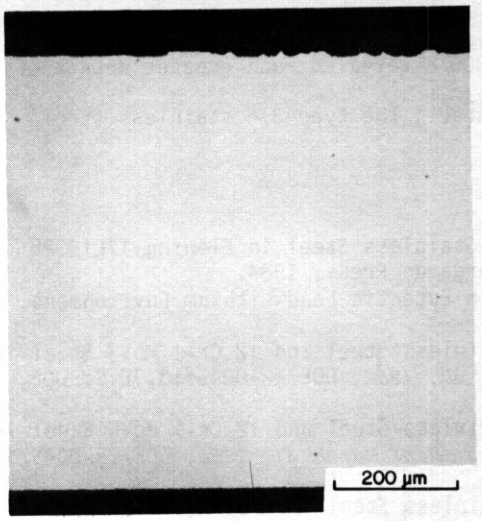

Fig. 9.5.3. 12-Cr-1 MoVW steel exposed to thermally convective Pb-17 at. % Li at 500°C for 1063 h.

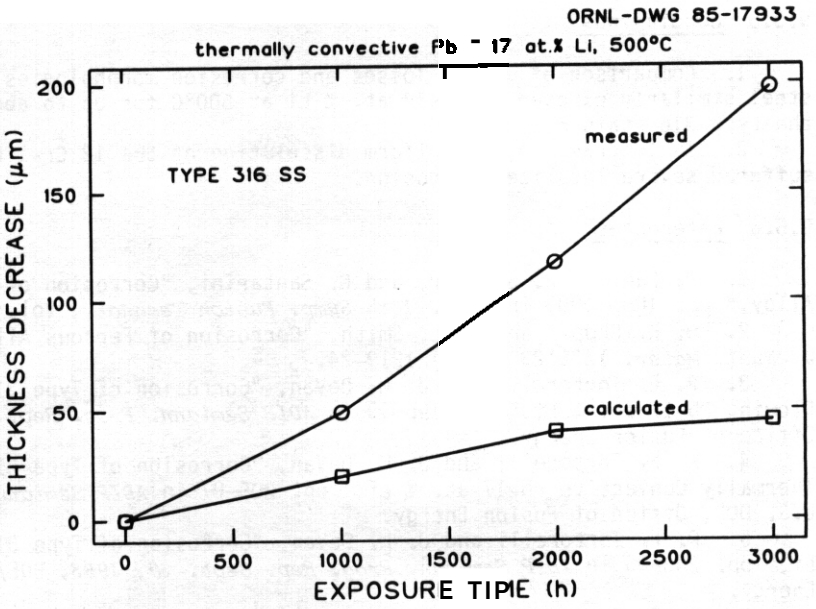

Fig. 9.5.4. Decrease in thickness versus exposure time for type 316 stainless steel. Calculated values are based on measured weight loss.

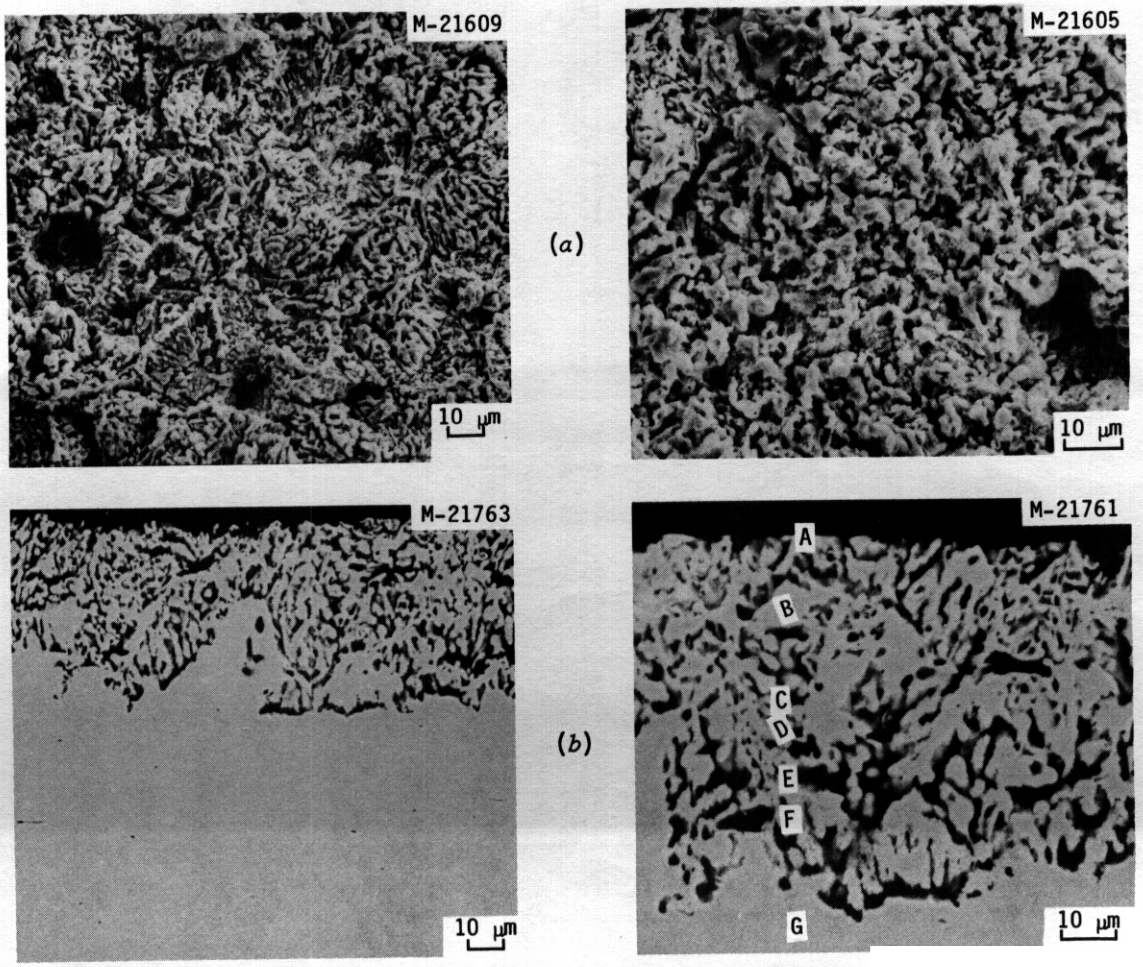

Fig. 9.5.5. Scanning electron micrographs of type 316 stainless steel exposed to thermally convective Pb-17 at. % Li for 2472 h at 500°C. (*a*) View of normal to corroded surface. (*b*) View of polished cross section.

9.5.5 Conclusions

1. Comparison of weight losses and corrosion morphologies of type 316 stainless steel and 12 Cr-1 MoVW steel similarly exposed to Pb-17 at. % Li at 500°C for up to about 3000 h revealed much greater attack of the type 316 stainless steel.
2. In contrast to the uniform dissolution of the 12 Cr-1 MoVW steel, the type 316 stainless steel suffered severe localized corrosion.

9.5.6 References

1. P. Fauvet, J. Sannier, and G. Santarini, "Corrosion of 316L Stainless Steel in Flowing 17Li83Pb Alloy," pp. 1003–1009 in *Proc. 13th Symp. Fusion Technol.*, Vol. 2, Pergamon Press, 1984.
2. O. K. Chopra and D. L. Smith, "Corrosion of Ferrous Alloys in Eutectic Lead-Lithium Environment," *J. Nucl. Mater.* 1226123 (1984) 1219–24.
3. P. F. Tortorelli and J. H. DeVan, "Corrosion of Type 316 Stainless Steel and 12 Cr-1 MoVW Steel in Flowing Pb-17 at. % Li," pp. 196–99 in *ADIP* **Semiann.** *Frog. Rep. Sept. 30, 1384,* DOE/ER-0045/13, U.S. DOE, Office of Fusion Eneray.
4. P. F. Tortorelli and J. H. DeVan, "Corrosion of Type 316 Stainless Steel and 12 Cr-1 MoVW Steel in Thermally Convective Pb-17 at. % Li," pp. 205–07 in *ADIP Semiann. Frog. Rep. March 31, 1985*, DOE/ER-0045/14, U.S. DOE, Office of Fusion Energy.
5. P. F. Tortorelli and J. H. DeVan, "Corrosion of Type 316 Stainless Steel in Flowing Pb-17 at. % Li," pp. 203–05 in *ADIP Semiann. Prog. Rep. Sept. 30, 1383,* DOE/ER-0045/11, U.S. DOE, Office of Fusion Energy.
6. P. F. Tortorelli and J. H. DeVan, "Effects of a Flowing Lithium Environment on the Surface Marphology and Composition of Austenitic Stainless Steel," *Microstructural Science*, Vol. 12 (1985) 215–226.

9.6 COMPATIBILITY OF VANADIUM ALLOYS IN HIGH TEMPERATURE WATER — P. F. Tortorelli (Oak Ridge National Laboratory)

9.6.1 ADIP Task

AOIP Task I.A.3, Perform Chemical and Metallurgical Compatibility Analyses.

9.6.2 Objective

The purpose of this task is to determine the compatibility of Path C vanadium alloys with high-temperature water for application to water-cooled fusion reactors. Candidate alloys are exposed to high-purity water in a stainless steel autoclave (with and without a hydrogen overpressure) to qualitatively determine (1) the extent of oxidation of the alloys and (2) the tendency for hydrogen uptake by these materials.

9.6.3 *Summary*

Initial results from slow strain rate testing of V-15 Cr-5 Ti and V-3 Ti-1 Si in 300°C water revealed little influence of a high temperature aqueous environment and hydrogen on the ductility of these alloys. A thin oxide film on exposed specimens is thought to prevent hydrogen uptake by these alloys.

9.6.4 Progress and Status

Previously, we reported1 that Path C vanadium alloys — specifically, in wt % V-20 Ti, V-15 Cr-5 Ti, and Vanstar-7 (V-9 Cr-3 Fe-1.2 Zr) — appeared to have fairly low oxidation rates in water at 300°C and that there was no discernible effect of a hydrogen overpressure of 83 kPa (12 psi) on the compatibility of the alloys. The influence of a hydrogen overpressure was the particular focus of this study since we wanted to examine the effects of oxygen suppressants, particularly hydrogen, on the oxidation rate in water and on the potential for hydrogen uptake by these vanadium alloys. This information is very pertinent to a recent fusion reaction design concept incorporating a self-cooled heavy water breeding blanket.*

The prior experiments were conducted by exposing tensile specimens of the vanadium alloys to deaerated, deionized water in a stainless steel autoclave for 100 h at 300°C with and without a hydrogen overpressure. In this way, pressurized water reactor conditions were partially simulated. The average steam pressure in the autoclave was about 9.0 MPa (1.3 ksi). After cooling from the exposure temperature, the specimens were removed from the autoclave, dried, and then immediately weighed and tensile tested in air at room temperature. Portions of the specimens were used for microhardness determination (within 12 h of removal from the autoclave) and hydrogen analysis (within 30 h). These analyses were performed as quickly as possible to avoid loss of hydrogen. Cross sections of the specimens were subsequently polished and etched for detailed metallographic examination.

Passivation of the vanadium alloys usually occurred, since weight gains were measured in most cases. These data are in contrast to recent results from a more detailed study of those alloys in high temperature (288°C) water,[3] where weight losses were measured. This difference in results may be attributed to several different experimental conditions. For example, while all our exposures were for 100 h, the weight changes measured in the more recent study were over a period of 2000 h with the earliest weighing at 192 h. All of our data are therefore short-term. As discussed below, our most recent measurements indicate most of the weight gain occurs within the first few hours. At much longer times, other processes could result in net weight losses. Furthermore, the oxidizing conditions in our static autoclave experiments could have been quite different from those of the other study, which used a refreshed autoclave system with controlled and monitored oxygen levels.

A more important result of our earlier study was that there was no significant hydrogen accumulation in the vanadium alloys as determined by postexposure chemical analyses and properties measurements. We postulated' that this lack of hydrogen uptake, despite a thermodynamic tendency for such, was due to thin oxide films acting as hydrogen permeation barriers, in accord with a study of hydrogen permeation through vanadium.'+ Such films are consistent with the measured weight gains, but such a thin oxide film has also been observed in V-15 Cr-5 Ti that suffered a net weight loss during exposure to high temperature water.3 In order to further investigate this phenomenon, in-situ straining experiments have been initiated during the current reporting period. A main purpose of this study is to avoid some of the problems related to post-exposure analysis by eliminating uncertainties about (1) the disposition of accumulated hydrogen during the long cool down periods after high temperature exposure and (2) the possible cracking of the thin oxide film while under strain (thereby compromising its effectiveness as a permeation barrier).

A high temperature, high pressure tensile testing system consisting of a Hastelloy C276* autoclave, a slow strain rate device, and a load cell, is being used for the in-situ study. A schematic drawing of the pressure vessel part of the system is shown in Fig. 9.6.1. Constant extension rates of about 10^{-4} to 10^{-7} s^{-1} are obtainable. During the current reporting period, pressure testing and calibration of the straining system were completed. Measurements of elongation and ultimate tensile strength for V-15 Cr-5 Ti at 300°C in argon were in relatively good agreement with published values.[5] We are, however, most interested in any relative difference in elongation (i.e., ductility) when vanadium alloys are exposed to 300°C water in the presence or absence of hydrogen. Experimental results to date are still quite limited.

---

*Trademark of Cabot Corporation.

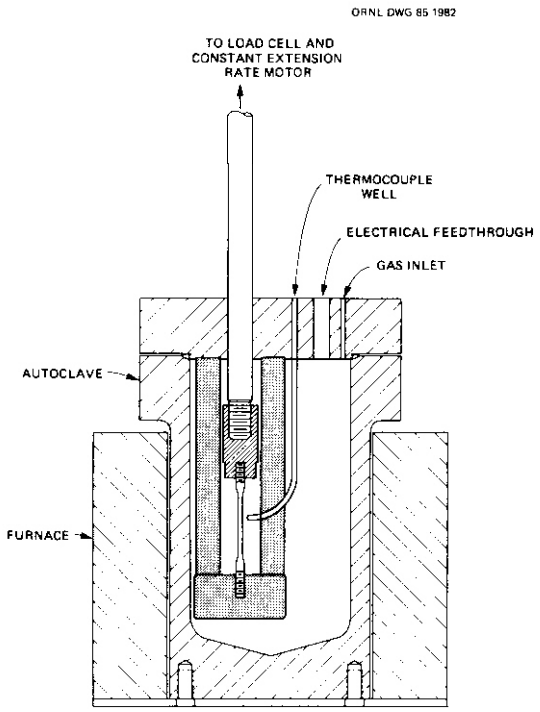

Fig. 9.6.1. Schematic drawing of constant extension rate pressure vessel system.

Table 9.6.1. Results of initial constant extension rate tests with vanadium alloys

Environment	Temperature (°C)	H_2 pressure (kPa)	Elongation[a] (%)
	V-15 Cr-5 Ti		
Ar	296	0	17
H_2O	292	0	23
H_2O	295	0	17
H_2O	296	90	18
	V-3 Ti-1 Si		
Ar	294	0	17[b]
H_2O	294	0	14
H_2O	308	0	16b

[a] At strain rate of $\sim 6 \times 10^{-5}$ s^{-1} except as noted.
[b] At strain rate of $\sim 1 \times 10^{-5}$ s^{-1}

However, as shown in Table 9.6.1, based on one test in a water plus hydrogen environment, there was no significant change in elongation of V-15 Cr-5 Ti relative to experiments conducted in 300°C water without a hydrogen overpressure. The data in Table 9.6.1 also show no susceptibility of either V-15 Cr-5 Ti or V-3 Ti-1 Si to ductility loss during straining in high temperature water and thus there is no initial evidence of aqueous stress corrosion cracking of these alloys under the present test conditions. While additional experiments are required to confirm these tentative findings, the preliminary data on a lack of a hydrogen effect are consistent with the results from our earlier study.[1] Furthermore, the weight gains of the exposed specimens were comparable to those reported earlier for 100 h exposures.[1] Although the specimens from the in-situ straining experiments were exposed for a much shorter time than the earlier exposures (~1 versus 100 h), the weight gains were of the same magnitude as at the longer times and indicate a rather rapid passivation rate in accordance with a study of vanadium in 25°C water.[6] The oxide film can thus form rapidly, and as discussed above, prevent hydrogen uptake by the vanadium alloys.

9.6.5 Conclusions

1. Preliminary results from slow strain rate testing of V-15 Cr-5 Ti and V-3 Ti-1 Si in 300°C water revealed little influence of a high temperature aqueous environment and hydrogen on the ductility of these alloys.
2. A rapid passivation rate of the vanadium alloys can lead to the development of a thin oxide film that prevents hydrogen uptake.

9.6.6 References

1. P. F. Tortorelli and J. H. DeVan, "Compatibility of Vanadium Alloys with High-Temperature Water," pp. 201–03 in *ADIP* Semiann. *Prog.* Rep. March *31, 1983*, DOE/ER-0045/10, U.S. DOE, Office of Fusion Energy.
2. D. Steiner et al., "A Self Cooled Heavy Water Breeding Blanket," paper presented at 11th Symp. on Fusion Engineering, Austin, Texas, Nov. 18-22, 1985.
3. D. R. Diercks and D. L. Smith, "Environmental Effects on the Properties of Vanadium-Based Alloys," pp. 177–81 in ADIP *Semiann. Prog. Rep.* March *31, 1985*, DOE/ER-0045/14, U.S. DOE, Office of Fusion Energy.
4. T. Namba et al., "Hydrogen Permeation Through Vanadium and the Effect of Surface Impurity Layer on It," *J.* Nucl. Mater. 105 (1982) 318–25.
5. R. E. Gold et al., "Technical Assessment of Vanadium-Base Alloys for Fusion Reactor Applications," Final Report, Vol. 2, report COO-4540-1. April 1978.
6. M. Pourbaix, Atlas *of* Electrochemical *Equilibria* in Aqueous Solutions, NACE, Houston 1974, pp. 234–45.

10. STATUS OF IRRADIATION EXPERIMENTS AND MATERIALS INVENTORY

10.1 FUSION PROGRAM RESEARCH MATERIALS INVENTORY — T. K. Roche, F. W. Wiffen (Oak Ridge National Laboratory), J. W. Davis (McDonnell Douglas Astronautics Company — St. Louis Division), and T. A. Lechtenberg (GA Technologies)

10.1.1 ADIP Task

ADIP Task I.O.1, Materials Stockpile for Magnetic Fusion Energy Programs.

10.1.2 Objective

Oak Ridge National Laboratory maintains a central inventory of research materials to provide a common supply of materials for the Fusion Reactor Materials program. This will minimize unintended material variations and provide for economy in procurement and for centralized record-keeping. Initially this inventory is to focus on materials related to first-wall and structural applications and related research, but various special-purpose materials may be added in the future.

The use of materials from this inventory that is coordinated with or otherwise related technically to the Fusion Reactor Materials program of the Department of Energy is encouraged.

10.1.3 Materials Requests and Release

Materials requests shall be directed to the Fusion Program Research Materials Inventory at ORNL (Attention: T. K. Roche). Materials will be released directly if (a) the material is to be used for programs funded by the Office of Fusion Energy, with goals consistent with the approved Materials Program Plans of the Materials and Radiation Effects Branch and (b) the reauested amount of material is available without compromising other intended uses.

Materials requests that do not satisfy both (a) and (b) will be discussed with the staff of the Reactor Technologies Branch, Office of Fusion Energy, for agreement on action.

10.1.4 Records

Chemistry and materials preparation records are maintained for all inventory materials. All materials supplied *to* program users will be accompanied by summary characterization information.

10.1.5 Summary of Current Inventory and Material Movement During Period April 1, 1985, through September 30, 1985

A condensed, qualitative description of the content of materials in the Fusion Program Research Materials Inventory is given in Table 10.1.1. This table indicates the nominal diameter of rod or thickness of sheet for product forms of each alloy and also indicates by weight the amount of each alloy in larger sizes available for fabrication to produce other product forms as needed by the program. No material was added to the inventory during this reporting period. Table 10.1.2 gives the materials distributed from the Inventory.

Alloy compositions and more detail on the alloys and their procurement and/or fabrication are given in this and earlier AOIP progress reports.

Table 10.1.1. Summary status of materials available in the fusion program research materials inventory

Alloy	Product form			
	Ingot or bar[a] weight (kg)	Rod diameter (mm)	Sheet thickness (mm)	Thin-wall tubing wall thickness (mm)
Path A Alloys				
Type 316 SS	900	16 and 7.2	13 and 7.9	0.25
Path A PCA[b]	490		1	0.25
USSR Cr-Mn steel[c]		16.5	1.6	
NONMAGNE 30[d]		18.5	10	

Table 10.1.1. (continued).

Alloy	Product form			
	Ingot or bar[a] weight (kg)	Rod diameter (mm)	Sheet thickness (mm)	Thin-wall tubing wall thickness (mm)
Path B Alloys				
PE-16	140	17 and 7.1	13 and 1.6	0.25
8-1	180			
8-2	180			
8-3	180			
8-4	180			
8-6	180			
Path C Alloys				
Ti-64			2.5 and 0.76	
Ti-6242S		63	6.3, 3.2, 0.76	
Ti-5621s			2.5 and 0.76	
Ti-38644			0.76 and 0.25	
Nb—1%Zr		6.3	2.5, 1.5, 0.76	
Nb—5%Mo—1%Zr		6.3	2.5, 1.5, 0.76	
V—20%Ti		6.3	2.5, 1.5, 0.76	
V—15%Cr—5%Ti		6.3	2.5, 1.5, 0.76	
VANSTAR-7		6.3	2.5, 1.5, 0.76	
Path D Alloy				
LRO-37[e]			3.3, 1.6, 0.8	
Path E Alloys				
HT9 (AOD fusion heat)	3400		28.5, 15.8, 9.5, 3.1	
HT9 (AOD/ESR fusion heat)	7000	25, 50, 75	28.5, 15.8, 9.5, 3.1	
HT9			4.5 and 18	
HT9 + 1%Ni			4.5 and 18	
HT9 + 2% Ni			4.5 and 18	
HT9 + 2% Ni + Cr adjusted			4.5 and 18	
T-9 modified9			4.5 and 18	
T-9 modified + 2% Ni			4.5 and 18	
T-9 modified + 2% Ni + Cr adjusted			4.5 and 18	
2 1/4 Cr-1Mo			h	

[a] Greater than 25 mm, minimum dimension.

[b] Prime candidate alloy.

[c] Rod and sheet of a USSR stainless steel supplied under the U.S./USSR Fusion Reactor Materials Exchange program.

[d] NONMAGNE 30 is an austenitic steel with base composition Fe—14%Mn—2%Ni—2%Cr. It was supplied to the inventory by the Japanese Atomic Energy Research Institute.

[e] LRO-37 is the ordered alloy $(Fe,Ni)_3(V,Ti)$ with composition Fe—39.4%Ni—22.4%V—0.43%Ti.

[f] Alloy 12Cr-1MoVW with composition equivalent to Sandvik alloy HT9.

BT-9 modified is the alloy 9Cr-1MoVNb.

[h] Material is thick-wall pipe, rerolled as necessary to produce sheet or rod.

Table 10.1.2. Fusion program research materials inventory disbursements April 1, 1985, through September 30, 1985

Alloy	Heat	Product form	Dimension[a] (mm)	Quantity (m^2)	Sent to
Path C Alloys — Reactive and Refractory Alloys					
V–15%Cr–5%Ti	CAM835A	Sheet	2.54	0.013	EG&G Idaho, Inc.
V–20%Ti	CAM833	Sheet	0.16	0.01	Radiation Effects Group, M&C Division, ORNL

[a]Characteristic dimensions: Thickness for plate and sheet, diameter for rod and tubing.

10.2 IRRADIATION EXPERIMENT STATUS AND SCHEDULE — M. L. Grossbeck (Oak Ridge National Laboratory)

A large number of planned, in-progress, and completed reactor irradiation experiments support the AOIP program. Table 10.2.1 summarizes the parameters that describe completed experiments. Experiments that have been removed from the reactor recently, that are now undergoing irradiation, or that are planned for future irradiation are shown in the schedule bar charts of Table 10.2.2.

Experiments were under way during the reporting period in the Oak Ridge Research Reactor (ORR) and the High Flux Isotope Reactor (HFIR), which are mixed-spectrum reactors, and in the Fast Flux Test Facility (FFTF), which is a fast reactor.

During the reporting period, the second HFIR capsule of the U.S./Japan cooperative program completed irradiation. This capsule was very similar to JP-1, removed last reporting period, and also received an exposure of 30 dpa. No other capsules were removed from the HFIR, reflecting a lower rate of removal resulting from the trend toward higher damage levels. However, two major ORR irradiation vehicles began irradiation in July 1985. These two experiments were also part of the U.S./Japan cooperative irradiation program. A comprehensive series of properties will be investigated by both participants, but the U.S. program has an increased emphasis on irradiation creep. There is also much interest in the low temperatures (60, 200°C) attained by ORR-MFE-6J.

Table 10.2.1. Descriptive parameters for completed AOIP program fission reactor irradiation experiments

Experiment	Major Objective	Alloy	Temperature (°C)	Displacement Damage (dpa)	Helium (at. ppm)	Duration (months)	Date Completed
		Experiments in ORB					
ORB-WE-1	Scope the effects of composition and microstructure on tensile. fatigue, and irradiation creep	Paths A, B, C	250–600	2	<10	4	6/78
ORR-MFE-2	Scope the effects of composition and microstructure on tensile. fatigue, and irradiation creep	Paths A, B, C	300–600	6	<60	15	*4/80*
ORR-MFE-5	In-reactor fatigue crack growth	Path A	325–460	1	<10	2	2/81
		Experiments io EBR-II					
Subassembly *X-264*	Effect of preinjected helium on microstructure, tensile properties and irradiation creep	316, PE-16, V–20%Ti, V–15%Cr–5%Ti, Nb–1%Zr	500–825	8	2–200	4	1/77
AA-X, Subassembly X-287	Effect of preinjected helium on microstructure, tensile properties, and irradiation creep	316, PE-16, V–20%Ti, V–15%Cr–5%Ti, Nb–1%Zr	400–700	20	2–200	23	12/78
AD-1, subassembly X-217D	stress relaxation Swelling, fatigue crack growth, and tensile properties	Ti alloys Ti alloys	*450* 370-550	2 *25*		I 14	1/78 9/79
AD-2, subassembly X344B	Tensile. fatigue, fracture toughness, Charpy, microstructure. and crack growth	Path E	390. 450. 500, 550	14,30		10,24	6/81, 4/83
		Experiments in HFIR					
HFIR-CTR-3	Swelling and tensile properties	PE-16. Inconel 600	300–700	4.3–9	350–1800	3	2/75
HFIR-CTR-4	Swelling and tensile properties	PE-16	300–700	2.2–4.5	100–350	2	3/77
HFIR-CTR-5	Swelling and tensile properties	PE-16. Inconel 600	300–700	4.3–9	350–1800	3	4/75
HFIR-CTR-6	Swelling and tensile properties	PE-16. Inconel 600	300–700	4.3–9	350–1800	3	4/75
HFIR-CTR-7	Swelling and tensile properties	PE-16	300–700	9–18	1250-3000	7	8/77
HFIR-CTR-8	Swelling and tensile properties	PE-16	300–700	9–18	1250–3000	7	8/77
HFIR-CTR-9	Swelling and tensile properties	316. 316 + Ti	280–680	10–16	400–1000	6	5/77
HFIR-CTR-10	Swelling and tensile properties	316. 316 + Ti	280–680	10–16	400–1000	6	5/77
HFIR-CTR-11	Swelling and tensile properties	316. 316 + Ti	280–680	10–16	400–1000	6	5/77
HFIR-CTR-12	swelling and tensile properties	316. 316 + Ti	280-680	7–10	200–500	4	2/77
HFIR-CTR-13	Swelling and tensile properties	316, 316 + Ti	280-680	7–10	200-500	4	2/77

Table 10.2.1. (continued)

Experiment	Major objective	Alloy	Temperature (°C)	Displacement Damage (dpa)	Helium (at. ppm)	Duration (months)	Date Completed
HFIR-CTR-14	Fatigue	316	430	9–15	400–1000	7	12177
HFIR–CTR–15	Fatigue	316	550	6–9	200–400	4	10/78
HFIR-CTR-16	Weld characterization, swelling, and tensile properties	316, PE–16, Inconel 600	55	6–9	150–2700	4	8/77
HFIR–CTR–I7	Weld characterization	316	280–620	7–13	180–460	5.5	10/77
HFIR–CTR–18	Swelling and tensile properties	316, PE–16	280–700	17–27	1600–5600	12	6/78
HEIR–CTR–19	Weld characterization	316	280-620	1–10	200–500	4	12/77
HFIR–CTR–20	Fatigue	316	430	6–9	200–400	4	1/78
HFIR-CTR-21	Fatigue	316	550	9–15	400–1000	7	7/78
HEIR–CTR–22	Fatigue	316	430	6–9	200–400	4	3/78
HFIR–CTR–23	Fatigue	PE–16	430	6-9	370–1000	3.5	2/79
HFIR-CTR-24	Temperature calibration and tensile properties	316	300–620	2.2	30	1	12/78
HFIR–CTR–26	Swelling and tensile properties	316	286-620	30	1900	10	4/80
HFIR-CTR-27	Swelling and tensile properties	316	286-620	56	3500	18	1/81
HFIR–CTR–28	Swelling and tensile properries	316	370–560	30	1900	10	12/80
HFIR–CTR–29	Swelling and tensile properties	316	370–560	56	3500	18	8/81
		Experiments in HPIR					
HFIR–CTR–30	Swelling, microstructure, and ductility	Paths A, B, C, D, and E	300–600	40	<15,000	14	11/81
HFIR-CTR-31	Swelling, microstructure, and ductility	Paths A, B, C. D, and E	300–600	20	< 7,500	8	5/81
HFIR-CTR-32	Swelling, microstructure, and ductility	Paths A, B, C, u, and E	300-600	10	< 3,000	4	12/81
HFIR–CTK–33	Swelling, tensile properties, and veld characterization	Paths A and E	55	10	< 510	4	10/80
HFIK–CTR–34	Charpy	Path E	3110, 400	10	w 7 5	4	5/82
HFIR-CTR-35	Charpy	Path E	300, 400	10	0–75	4	5/82
HFIK–CTR–36	Fatigue	316 PCA	430, 550	30	2,000	13	5/83
HFIR–CTK–39	Swelling and tensile properties	Path E	300–500	12	0–90	5	10/82
HFIR-CTR-40	Swelling and tensile properties	Path E	300–500	12	0–90	5	12/82
HFIR–CTR–4I	Swelling and tensile properties	Path E	300–500	12	0–90	5	1/83
HFIR–CTR–42	Swelling, tensile microstructure	Paths A, D	300–600	20	1100	8	6/83
HFIR-CTR-43		Similar to HFIR-CTR-42					
HFIR-CTR-44[a]	Swelling, tensile	Path A	25——00	10	50U	4	5/83
HFIK–CTR–45		Similar to HEIR–CTR–44					
HFIR–CTK–46	Charpy	Path E	300–400	10	75	4	6/83
HFIR–HFE–RBI	Swelling, microstructure. crack growth, fracture toughness, Charpy, tensile, and fatigue	Path E	55	10	90	8	7/82
HFIR-MFE-RB2	Swelling, microstructure, crack growth, fracture toughness, Charpy, tensile, and fatigue	Path E	55	2	200	17	7/83
HFIR-MFE-T1	Swelling, tensile fatigue	Path E	55	30	<300	12	8/82
HFIR-MFE-T2	Swelling and tensile fatigue	Path E	55	9	< 75	3	5/81
HFIR-MFE-T3	Impact properties	Path E	55	10	85	4	12/81

[a]Joint U.S./EC/JP.

Table 10.2.2. Objectives and schedule for current and planned ADIP program reactor irradiation experiments

Experiment designation	Major objective
A. Oak Ridge Research Reactor	
ORR-MFE-4	Effect of irradiation on tensile, fatigue, and irradiation creep of path A PCA (Prime Candidate Alloy) and path B base research alloys. Spectral tailoring to maintain correct He/dpa ratio.①
ORR-MFE-6J	Swelling, tensile, irradiation creep fatigue, crack growth, and microstructure of path A alloys. 60 and 200°C. Evaluated at 10 to 15 dpa intervals. Employs spectral tailoring to achieve fusion He:dpa value.
ORR-MFE-7J	Similar to ORR-MFE-6J but 300 and 400°C.
B. Fast Flux Test Facility (FFTF)	
FFTF MOTA Fusion Experiment	Microstructural and mechanical properties of Path A, C, and E alloys.

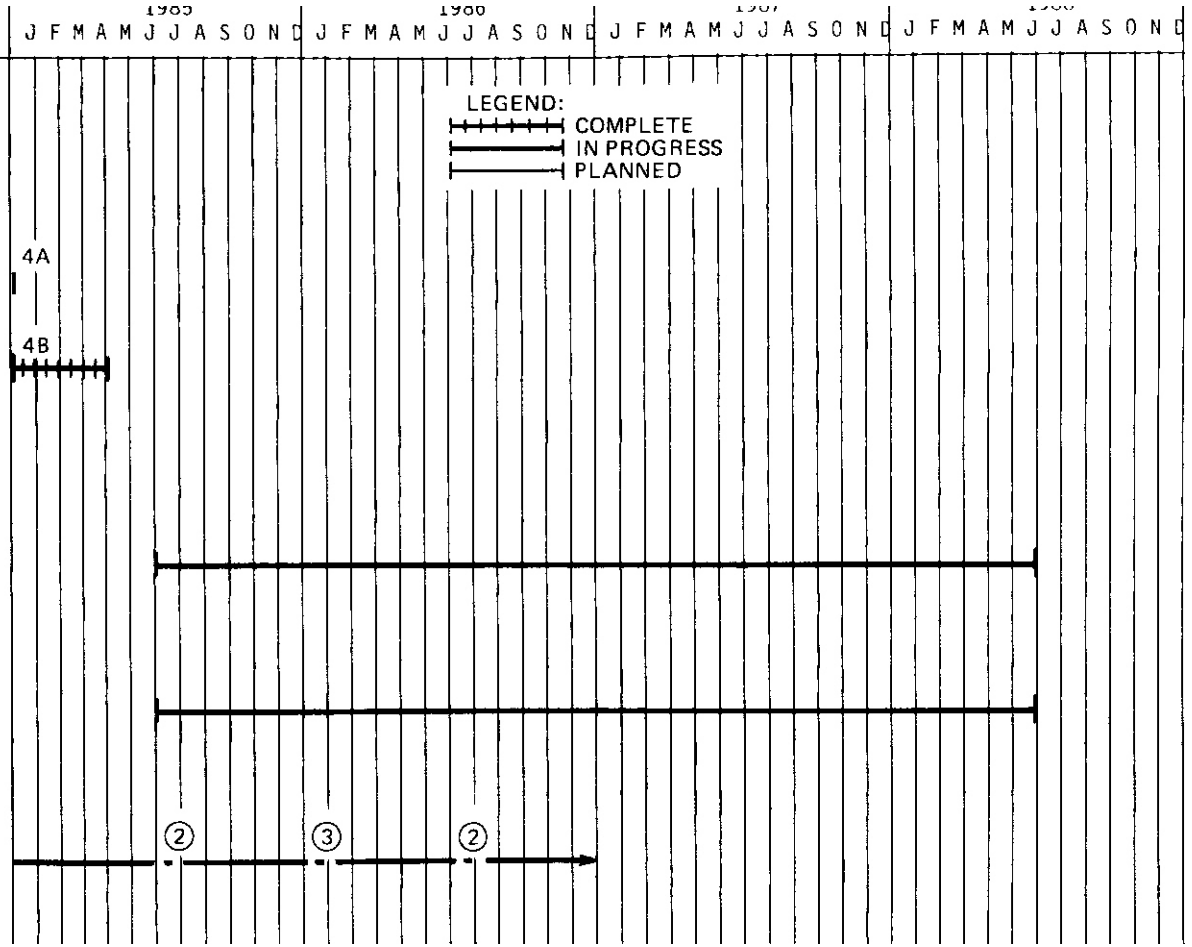

① MFE-4A operated at 330 and 400°C. MFE-4B operated at 500 and 600°C.

② Removed for specimen discharge.

③ Reactor down for refueling.

④ The HFIR-JP experiment series is a joint program shared by the U.S. and Japan Fusion Reactor Materials activities

Table 10.2.2. (continued)

Experiment designation	Major objective
C. High Flux Isotope Reactor (HFIR)	
HFIR-CTR-36	Fatigue properties of path A alloys. 30 dpa, 2000 ppm He.
HFIR-CTR-47	Impact properties of path E alloys. 40 dpa, 400 ppm He, 300 and 400°C.
HF R-CTR-48	Similar to HFIR-CTR-47.
HF R-CTR-49	Tensile properties and microstructure of path E alloys. 50 dpa, 70 to 500 ppm He, 300 to 500°C.
HFIR-CTR-50	Tensile, swelling, microstructure of path E alloys, 100 dpa, 150 to 1000 ppm He, 400, 600°C.
HFIR-CTR-51	Swelling, tensile properties of low-activation alloys. 20 dpa, 300–600°C
HFIR-CTR-52	Fatigue properties of 316 SS. 10 dpa, 500 ppm He 430°C. Joint experiment with European community and Japan.
HFIR-CTR-53	Impact properties of path E alloys. 10 dpa 75 ppm He, 200, 300°C, one-third size Charpy.
HFIR-CTR-54	Similar to HFIR-CTR-53
HFIR-CTR-55	Tensile swelling, microstructure of path E and low activation alloys. 50 dpa, 400 ppm He, 400, 600°C.
HFIR-CTR-56	Tensile, swelling microstructure of path E and low activation alloys. 100 dpa, 150–1000 ppm He, 400, 600°C.

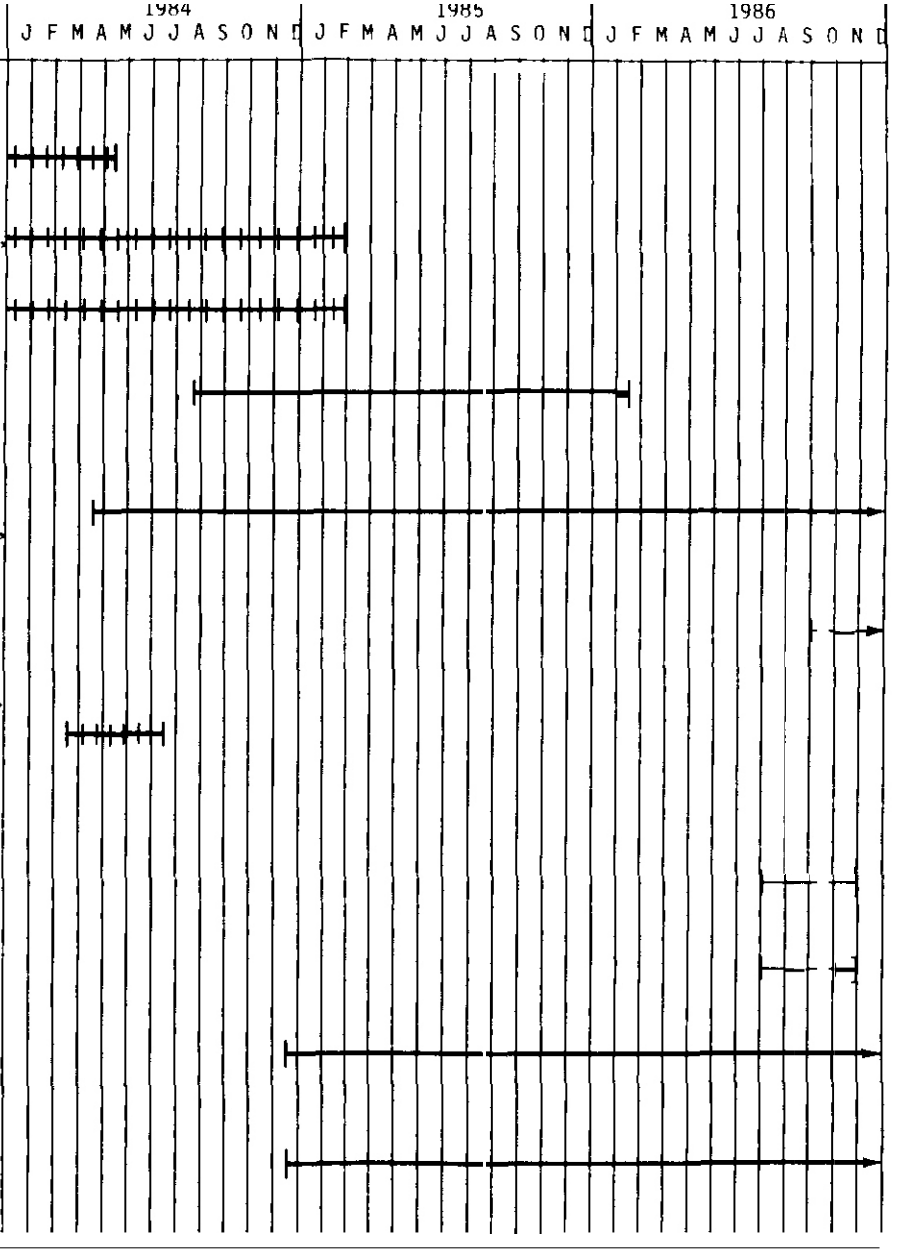

Table 10.2.2. (continued)

Experiment designation	Major objective	1983 J F M A M J J A S O N D	1984 J F M A M J J A S O N D	1985 J F M A M J J A S O N D	1986 J F M A M J J A S O N D
HFIR-JP-1(4)	Swelling, tensile and fatigue properties, and microstructure of path A alloys. 300–600°C, 30 dpa, 2000 ppm He.				
HFIR-JP-2	Similar to HFIR-JP-1 but to 50 dpa, 3500 ppm He.				
HFIR-JP-3	Similar to HFIR-JP-1.				
HFIR-JP-4	Swelling, tensile properties, and microstructure of path A alloys. 55°C, 50 dpa, 2000 ppm He.				
HFIR-JP-5	Similar to HFIR-JP-2.				
HFIR-JP-6	Similar to HFIR-JP-1.				
HFIR-JP-7	Similar to HFIR-JP-1.				
HFIR-JP-8	Similar to HFIR-JP-2.				

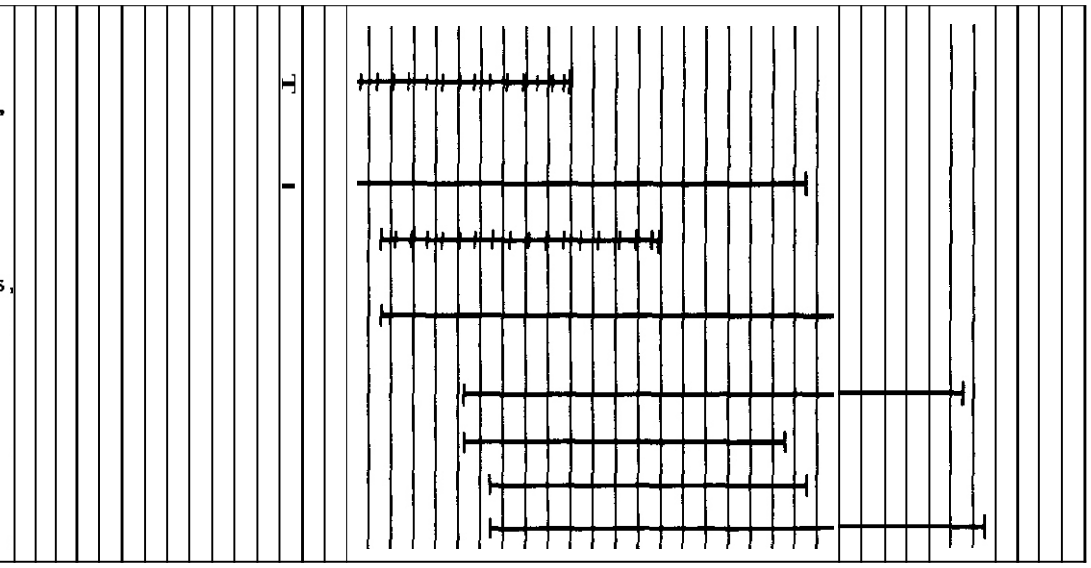

DOE/ER-0045/15
Distribution
Categories
UC-20, 20c

DISTRIBUTION

1–6. Argonne National Laboratory, 9700 South Cass Avenue, Argonne, IL 60439

L. Greenwood
B. A Loomis
V. Maroni
R. F. Mattas
D. L. Smith
H. Wiedersich

7. Auburn University, Department of Mechanical Engineering, Auburn, AL 36849

B. A Chin

8. Battelle-Pacific Northwest Laboratory, P.O. Box 999, Richland, WA 99352

J. L. Brimhall

9. Brookhaven National Laboratory, Upton, NY 11973

C. L. Snead, Jr.

10. Carnegie-Mellon University, Pittsburgh, PA 15213

J. C. Williams

11. Colorado School of Mines, Golden, CO BO401

G. R. Edwards

12–195. Department of Energy, Technical Information Center, Office of Information Services, P.O. Box 62, Oak Ridge, TN 37831

For distribution as shown in DOE/TIC-4500 Distribution Categories, UC-20 (Magnetic Fusion Energy), and UC-20c (Reactor Materials)

196–202. Department of Energy, Office of Fusion Energy, Washington, DC 20545

M. M Cohen
G. M. Haas
T. C. Reuther, Jr. (5 copies)

203. Department of Energy, Oak Ridge Operations Office, P.O. Box E, Oak Ridge, TN 37831

Office of Assistant Manager for Energy Research and Development

204. Energy Technology Engineering Center, P.O. Box 1449, Canoga Park, CA 91304

ETEC Library

205–206. GA Technologies, Inc., P.O. Box 81608, San Diego, CA 92138

T. A. Lechtenberg
D. L. Roberts

207–209. Lawrence Livermore National Laboratory, P.O. Box 808, Livermore, CA 94550

E.N.C. Dalder
M. Guinan
C. M Logan

210. Los Alamos National Laboratory, P.O. Box 1663, Los Alamos, NM 87545

R. J. Livak

211. Massachusetts Institute of Technology, 138 Albany Street, Cambridge, MA 02139

O. K. Harling

212. Massachusetts Institute of Technology, 77 Massachusetts Ave., Cambridge, MA 02139
N. J. Grant

213. McDonnell Douglas Astronautics Company, East, P.O. Box 516, St. Louis, MO 63166
J. W. Davis

214. National Materials Advisory Board, 2101 Constitution Ave.. Washington, DC 20418
K. M. Zwilsky

215–216. Naval Research Laboratory, Washington, DC 20375
Superintendent, Materials Science and Technology Division
J. A. Sprague

217. Northwestern University, Department of Materials Science and Engineering, Evanston, IL 60201
J. R. Weertman

218–254. Oak Ridge National Laboratory, P.O. Box X, Oak Ridge, TN 37831
Central Research Library (2 copies)
Document Reference Section
Laboratory Records Department (2 copies)
Laboratory Records Department, RC
ORNL Patent Section
L. A. Berry
E. E. Bloom
D. N. Braski
W. R. Corwin
J. H. DeVan
M. L. Grossbeck
S. Hamada
R. L. Klueh
R. A. Lillie
C. T. Liu
K. C. Liu
L. K. Mansur
P. J. Maziasz
C. J. McHargue
T. K. Roche
A. F. Rowcliffe (2 copies)
M. J. Saltmarsh
J. L. Scott
I. Siman-Tov
M. P. Tanaka
K. R. Thoms
P. T. Thornton (3 copies)
P. F. Tortorelli
J. M. Vitek
C. D. West
F. W. Wiffen
S. J. Zinkle

255. Princeton University, Plasma Physics Laboratory, P.O. Box 451. Princeton, NJ OB544
P. Bonanos

256–257. Rensselaer Polytechnic Institute, Troy, NY 12181
D. Steiner
N. Stoloff

258–259. Sandia National Laboratories, Livermore Division 8316, Livermore, CA 94550
W. Bauer
J. C. Lippold

260–261. Sandia National Laboratories, P.O. Box 5800, Albuquerque, NM 87185
M. J. Davis
W. B. Gauster

262. Science Applications, Inc., 1200 Prospect, La Jolla, CA 92037

H Gurol

263–265. University of California, Department of Chemical, Nuclear, and Thermal Engineering, Los Angeles, CA 90024

M. A. Abdou
R. W. Conn
N. M. Ghoniem

266. University of California, Santa Barbara, CA 93106

G. R. Odette

267. University of Missouri, Department of Mechanical and Aerospace Engineering, Columbia, MO 65211

M. Jolles

268. University of Virginia, Department of Materials Science, Charlottesville. VA 22901

W. A. Jesser

269. University of Wisconsin, 1500 Johnson Drive, Madison, WI 53706

G. L. Kulcinski

270. Westinghouse Electric Company, Advanced Energy Systems Division, P.O. Box 10864, Pittsburgh, PA 15236

W. A. Boltax

271–278. Westinghouse Hanford Company, P.O. Box 1970, Richland, WA 99352

H. R. Brager
D. G. Doran
A. M. Ermi
F. A. Garner
D. S. Gelles
E. C. Opperman
R. W. Powell
J. L. Straalsund

279. Westinghouse Research and Development Center, 1310 Beulah Road, Pittsburgh, PA 15235

J. A. Spitznagel

U S GOVERNMENT PRINTING OFFICE 1986631056/20246